Railway Bridge Monitoring with Minimal Sensor Deployment: Virtual Sensing and Resonance Curve-Based Drive-by Monitoring

Eisenbahnbrückenüberwachung mit minimalem Sensoreneinsatz: Virtuelle Sensoren und resonanzkurvenbasierte Überwachung im Vorbeifahren

Doctoral thesis

Steven Robert Lorenzen, M.Sc.

from Bad Soden am Taunus

submitted in fulfillment of the requirements for the degree of Doktor-Ingenieur (Dr.-Ing.)
at the Department of Civil and Environmental Engineering
of the Technical University of Darmstadt

First assessor: Prof. Dr.-Ing. Jens Schneider
Second assessor: Prof. Dr.-Ing. Danièle Waldmann-Diederich

Darmstadt 2023

Steven Robert Lorenzen
Railway Bridge Monitoring with Minimal Sensor Deployment: Virtual Sensing and Resonance Curve-Based Drive-by Monitoring

Darmstadt, Technical University of Darmstadt
Published online on TUprints in 2023
Date of oral exam: November 28, 2023

`URN`: urn:nbn:de:tuda-tuprints-264262
`URL`: http://tuprints.ulb.tu-darmstadt.de/26426

Creative Commons License (CC BY–SA 4.0 International), 2023.

Acknowledgement

This thesis was written during my time as a research assistant at the Institute of Structural Mechanics and Design (ISM+D) at the Technical University of Darmstadt. I would like to take this opportunity to thank all those involved.

Firstly, my deepest gratitude goes to my doctoral supervisor, Prof. Dr.-Ing. Jens Schneider. I thank him for providing the opportunity to pursue my Ph.D. at his institute, and for his continuous support and guidance throughout the entire process. His confidence in my work and the appreciation he showed me were a tremendous support. I am truly grateful for the time I spent working with him, as I have learned much from him – not just on academic subjects. This experience will be a lasting enrichment for my further professional and personal development.

I would also like to express my profound gratitude to both current and former colleagues from the Structural Dynamics Unit (SDU) at ISM+D. I am particularly grateful to Dr.-Ing. Andrei Firus, under whose supervision I was able to write my Master's thesis. It was with him that I first gained intensive experience in bridge dynamics and experimental dynamic analyses. I will forever be grateful to him for introducing me to this wonderful field of engineering.

Special thanks go to Hagen Berthold for our collaborative work. Without his extraordinary commitment in our joint research project ZEKISS, in the instrumentation of the Garather Bach bridge and the trains, this work would not have taken its current form.

I thank Antonia Kohl for enlightening discussions on railway bridge dynamics, particularly regarding vehicle-structure interaction, and for providing simulation results that enabled initial investigations into drive-by monitoring.

My thanks also go to Max Alois Fritzsche for his remarkable commitment in the instrumentation of the Garather Bach bridge and the ICE TD at the advanced TrainLab. Without his incredible effort, the measurement campaign would not have been as successful.

Of exceptional importance was my collaboration with my esteemed colleague Maximilian Michael Rupp. He was the first student to complete a thesis under my supervision during my time at the institute. I thank him for his consistent support and mutual enthusiasm. He was indispensable for the success of the ICE TD campaign at the advanced TrainLab.

For engaging discussions and enlightening explanations on data-driven methods and artificial intelligence topics, I thank Henrik Riedel. His high expertise in this field has been invaluable for the research project ZEKISS.

I would like to extend my thanks to Dr. Eftychia Apostolidi for her excellent leadership of our working group. She has managed to create a unique team out of the group. I also thank her for the extra effort she took to support me in writing this thesis.

I would also like to thank colleagues from the institute outside the SDU for their pleasant cooperation and collegial atmosphere over the years. Special mention goes to

Marcel Hörbert, for his invaluable commitment to the experiments I conducted, particularly for the work on the instrumentation of the Gatharer Bach bridge.

I am also deeply thankful to Kay Schuchmann for his extraordinary effort during the measurement campaign with the ICE TD at the advanced TrainLab. Without his commitment, the campaign would not have been conducted on such a scale.

I particularly thank Gregor Schwind for our collaborative work within the course of Structural Analysis IV. The discussions with him have helped deepen my understanding of plate and shell structures.

For excellent collaboration in joint research work, I thank Christian-Dominik Thiele and Jascha Brötzmann from the Institute for Numerical Methods and Informatics in Civil Engineering.

My thanks also go to our partners from Deutsche Bahn for their excellent cooperation, without which this work would not have been possible. In particular, I would like to thank Günter Grunert from DB Netz for successful collaboration on the ZEKISS research project. For the exchange and advice regarding train measurements, I thank Dr.-Ing. Klaus Ulrich Wolter from DB Systemtechnik. Finally, I thank Marcus Apitius from the advanced TrainLab for his commitment to our joint measurement campaign.

However, the most crucial support during this time came from my beloved family, who has supported me unconditionally. Our first daughter Nina was born two months before my first day at the institute. During my time there, Alexander and Julian were also born. Without the unconditional support and understanding of my beloved wife Larissa, this work would not have been possible. Thank you.

Oberursel, September 2023 *Steven Robert Lorenzen*

Abstract

The global railway bridge infrastructure is aging and exposed to increasing traffic loads. In Germany, the average lifespan of a railway bridge is 122 years. During this time, railway vehicles have evolved significantly, leading to higher axle loads and speeds. The urgent need to extend the lifespan of these bridges has prompted an intensive search for efficient methods to assess existing bridge structures.

One approach is vibration-based monitoring, which can be categorised into direct and indirect monitoring. In direct monitoring, sensors are installed directly upon the structure. Conversely, in indirect monitoring, a passing vehicle equipped with sensors is utilised, commonly referred to as drive-by monitoring.

Direct monitoring of bridges is still rare, and when bridges are instrumented, it is typically with a sparse deployment of sensors. Hence, methods are needed to extrapolate the measured structural responses to unmeasured locations. These methods are summarized under the term virtual sensing. Existing research on virtual sensing for railway bridges reveals gaps in long-term studies, especially considering different environmental and operational conditions. Notably, 95 % of all railway bridges in Germany are short-spanned with spans less than 30 m, and there is a significant lack of research in this segment. A main focus of this dissertation was to address this research gap.

The high effort in direct instrumentation currently does not allow for monitoring of the entire railway bridge network using available technology. A cost-effective approach to monitoring railway bridges is drive-by monitoring. Despite the potential of this approach, field tests and comprehensive experiments in the context of railway bridges are rare. There is a need for a robust methodology for frequency identification of railway bridges using drive-by monitoring, especially at regular operating speeds. The development and validation of a suitable methodology form the second focus of this work.

In this dissertation, three experimental investigations were conducted to explore both the direct and indirect monitoring methodologies. The HUMVIB bridge, the railway bridge over the Schmutter river with an instrumented ICE 4, and a railway bridge in Düsseldorf (Germany) with an instrumented ICE TD were thoroughly analysed.

During the investigations, modal expansion, a method that uses the structure's eigenmodes to reconstruct unmeasured structural responses, was confirmed as a suitable methodology for virtual sensing. The investigations under different operational and environmental conditions showed that the influence of operational conditions, such as train type and speed, is dominant over environmental conditions.

The experiments also validated the developed methodology for frequency identification using drive-by monitoring for two different trains and bridges.

This work aims to make contributions to the monitoring of railway bridges by providing practical, cost-effective, and reliable methods.

Zusammenfassung

Die weltweite Eisenbahnbrückeninfrastruktur altert und ist steigenden Verkehrslasten ausgesetzt. In Deutschland beträgt die durchschnittliche Lebensdauer einer Eisenbahnbrücke 122 Jahre. Während dieser Zeit haben sich die Eisenbahnfahrzeuge erheblich weiterentwickelt, was zu höheren Achslasten und Geschwindigkeiten führt. Der dringende Bedarf, die Lebensdauer dieser Brücken zu verlängern, hat zu einer intensiven Suche nach effizienten Methoden zur Bewertung bestehender Brückenstrukturen geführt.

Ein Ansatz dazu ist die schwingungsbasierte Überwachung. Diese wird typischerweise in direktes und indirektes Monitoring unterteilt. Bei der direkten Überwachung werden Sensoren direkt an der Struktur angebracht. Im Gegensatz dazu wird bei der indirekten Überwachung ein vorbeifahrendes Fahrzeug mit Sensoren verwendet, was üblicherweise als Drive-by-Monitoring bezeichnet wird.

Eine direkte Überwachung von Brücken ist derzeit noch die Ausnahme, und wenn Brücken instrumentiert sind, dann in der Regel mit einem spärlichen Einsatz von Sensoren. Daher werden Methoden benötigt, um die gemessenen Strukturantworten auf nicht gemessene Stellen zu extrapolieren. Diese Methoden werden unter dem Begriff Virtual Sensing zusammengefasst. Die vorliegenden Forschungen zum Virtual Sensing bei Eisenbahnbrücken zeigen Lücken in der Langzeituntersuchung, insbesondere unter Berücksichtigung verschiedener Umwelt- und Betriebsbedingungen. Besonders bemerkenswert ist, dass 95 % aller Eisenbahnbrücken in Deutschland mit Spannweiten kleiner als 30 m kurz gespannt sind, und es gerade in diesem Segment an Forschung mangelt. Ein Schwerpunkt dieser Dissertation war es, genau diese Forschungslücke anzugehen.

Der hohe Aufwand bei der direkten Instrumentierung erlaubt mit der zur Verfügung stehenden Technik derzeit keine Überwachung des Eisenbahnbrückennetzwerks. Ein kosteneffizienter Ansatz zur Überwachung der Eisenbahnbrücken ist das Drive-by Monitoring. Trotz des Potenzials dieses Ansatzes sind Feldtests und umfassende Experimente im Bereich der Eisenbahnbrücken selten. Es besteht ein Bedarf an einer robusten Methodik zur Frequenzidentifikation von Eisenbahnbrücken mittels Drive-by Monitoring, insbesondere bei regulären Betriebsgeschwindigkeiten. Die Entwicklung und Validierung einer geeigneten Methodik bildet den zweiten Schwerpunkt dieser Arbeit.

In dieser Dissertation wurden drei experimentelle Untersuchungen durchgeführt, um sowohl die direkte als auch die indirekte Überwachungsmethodik zu erforschen. Dabei wurden die HUMVIB-Brücke, die Eisenbahnbrücke über den Fluss Schmutter mit einem instrumentierten ICE 4 sowie eine Eisenbahnbrücke in Düsseldorf mit einem instrumentierten ICE TD detailliert analysiert.

Im Rahmen der Untersuchungen wurde die Modale Expansion, eine Methode, die die Eigenformen der Struktur zur Rekonstruktion der nicht gemessenen Strukturantworten verwendet, als geeignete Methodik für das Virtual Sensing bestätigt. Die Untersuchungen zu unterschiedlichen Betriebs- und Umweltbedingungen zeigen, dass der Einfluss der

Betriebsbedingungen, wie Zugtyp und gefahrene Geschwindigkeit, gegenüber dem der Umweltbedingungen dominant ist.

Mit den Experimenten konnte ebenfalls die entwickelte Methodik zur Frequenzidentifikation mittels Drive-by Monitoring für zwei unterschiedliche Züge und Brücken validiert werden.

Diese Arbeit hat als Ziel, Beiträge zur Überwachung von Eisenbahnbrücken zu leisten, indem sie praxisnahe, kosteneffiziente und zuverlässige Methoden liefert.

Contents

List of Figures xiii

List of Tables xxi

Glossaries xxv

1 Introduction 1

1.1 Motivation 1
1.2 Objectives 2
1.3 Own contributions 3
1.4 Structure of the thesis 3

2 Fundamentals 7

2.1 Singular value decomposition 7
2.2 Proper orthogonal decomposition 8
2.3 Linear system of equations and the pseudoinverse 9
2.4 Equation of motion 9
2.5 Modal analysis 11
  2.5.1 Modal decorrelation 11
  2.5.2 Mode shapes of a beam 12
  2.5.3 Strain mode shapes 14
  2.5.4 Determination of modal parameters from measurements 15
2.6 Structural modification theory 15
2.7 Resonance curves and vehicle-bridge interaction 17
2.8 Frequency range of bridge vibrations 18
2.9 Influence of higher eigenmodes 19
2.10 The signal of a moving sensor 20

3 State of the art 23

3.1 Virtual sensing of railway bridges 23
3.2 Drive-by monitoring of railway bridges 26

4 Methodology **33**
4.1 Virtual sensing 33
4.1.1 Modal expansion 33
4.1.2 Selection of modes and signal processing 34
4.1.3 Sensor placement 35
4.1.4 Leave-p-out validation and coefficient of determination 36
4.2 Resonance curves based drive-by monitoring 38
4.2.1 Frequency identification 39
4.2.2 Data acquisition and processing 40

5 Footbridge HUMVIB **43**
5.1 Experimental set-up and execution 44
5.2 System identification and structural model 46
5.2.1 Modal analysis 46
5.2.2 Beam and finite element (FE) model 46
5.2.3 Comparison of mode shapes 48
5.2.4 POD modes 50
5.3 Virtual sensing 53
5.3.1 Influence of the POD mode sets 53
5.3.2 Impact of considered modes and number of physical sensors 56
5.3.3 Evaluation of different sensor setups 61
5.3.4 Sample comparisons of signals from physical and virtual sensors 64
5.4 Conclusion 67

6 Railway bridge Schmutter **69**
6.1 Experimental set-up and execution 70
6.2 System identification and structural model 74
6.2.1 Modal analysis 74
6.2.2 Resonance curve 75
6.2.3 FE model 76
6.3 Virtual sensing 79
6.3.1 Coupled versus uncoupled model 79
6.3.2 Impact of train speed 83
6.3.3 Sample comparisons of signals from physical and virtual sensors 85
6.4 Drive-by monitoring 86
6.4.1 Influence of the cut-off frequency of the low-pass filter on the indirect resonance curve 87
6.4.2 Frequency identification 89
6.4.3 Comparison of indirect and direct resonance curves 94
6.5 Conclusion 98
6.5.1 Virtual sensing 98

6.5.2 Drive by monitoring 98

7 Railway bridge Garather Bach 101

7.1 Experimental set-up and execution 101

7.1.1 Bridge instrumentation 101

7.1.2 Train instrumentation 106

7.2 System identification and structural model 110

7.2.1 Modal analysis 110

7.2.2 POD modes 111

7.2.3 FE model 111

7.2.4 Comparison of mode shapes 111

7.2.5 Resonance curve 117

7.3 Virtual sensing 118

7.3.1 Impact of considered modes and number of physical sensors 118

7.3.2 Impact of train type and speed 119

7.3.3 Impact of signal amplitudes 120

7.3.4 Impact of environmental conditions 121

7.3.5 Evaluation of different sensor setups 123

7.3.6 Sample comparisons of signals from physical and virtual sensors 126

7.4 Drive-by monitoring 127

7.4.1 Influence of the cut-off frequency of the low-pass filter on the indirect resonance curve 128

7.4.2 Frequency identification 130

7.4.3 Comparison of indirect and direct resonance curves 136

7.5 Conclusion 141

7.5.1 Virtual sensing 141

7.5.2 Drive by monitoring 142

8 Conclusion and future research directions 145

8.1 Virtual sensing 145

8.1.1 Primary contributions and findings 145

8.1.2 Limitations 146

8.1.3 Recommendations for future research 148

8.2 Drive-by monitoring 148

8.2.1 Primary contributions and findings 148

8.2.2 Limitations 150

8.2.3 Recommendations for future research 150

8.3 Final remarks 151

Bibliography 153

Table of appendices **161**

List of Figures

1.1 Schematic presentation of the structure of the thesis. 5

2.1 Simplified modelling of the excitation by the resultant force of two bogies acting between two car bodies. 17
2.2 Comparison of calculated maximum accelerations at midspan for a moving-load model, a multi-body model, and a moving-load model with additional mass. 18

3.1 Virtual sensing flowchart 24

5.1 HUMVIB footbridge 43
5.2 Sensor positioning on the HUMVIB bridge. 45
5.3 Installed sensors on the HUMVIB footbridge 46
5.4 Comparison of simply supported beam model with fixed bearing with respect to torsion (left) and FE-model with vertically ridgid supports and elastic supports in lateral direction (right) 47
5.5 The first 7 vertical modes of the FE model divided into bending eigenmodes (B) and torsion eigenmodes (T) 48
5.6 Comparison of displacement mode shapes of FE model, beam model and stochastic subspace identification (SSI) 49
5.7 Comparison of strain mode shapes of FE and beam model 50
5.8 Comparison of proper orthogonal decomposition (POD) modes for accelerations ($\boldsymbol{\Psi}_{\mathrm{a},n}$) from four different mode sets 51
5.9 Comparison of POD modes for strains ($\boldsymbol{\Psi}_{\mathrm{s},n}$) from four different mode sets 52
5.10 Comparison of the maximum and minimum coefficients of determination at MP 1L for accelerations and strains for all 4 POD mode sets 57
5.11 Coefficients of determination of the leave-p-out validation, corresponding to the best and worst sensor combinations (s.c.), depending on the number of physical sensors and considered FE modes for each accelerometer. Negative values are marked with -. 59
5.12 Coefficients of determination of the leave-p-out validation, corresponding to the best and worst sensor combinations (s.c.), depending on the number of physical sensors and considered FE modes for each strain gauge. Negative values are marked with -. 60

5.13 Summary of the number of occurrences of each strain gauge in an optimal sensor combination to reconstruct a given measurement point using the POD 1.8 modes. Note that the sensor at MP 2R was defective and is therefore not included in the evaluation. 62

5.14 Summary of the number of occurrences of each strain gauge in an optimal sensor combination for reconstructing a given measurement point using the FE modes. Note that the sensor at MP 2R was defective and is therefore not included in the evaluation. 62

5.15 Summary of the number of occurrences of each accelerometer in an optimal sensor combination for reconstruction of a given measurement point using the POD 1.8 modes. 63

5.16 Summary of the number of occurrences of each accelerometer in an optimal sensor combination for reconstruction of a given measurement point using the FE modes 63

5.17 Exemplary comparisons of virtual sensor signals for the strains with those of the physical sensors for an arbitrarily chosen crossing to assess the coefficients of determination R^2. The number of FE modes considered and the sensor combination for the physical sensors were chosen to match the respective coefficients of determination. 65

5.18 Exemplary comparisons of virtual sensor signals for the acceleration with those of the physical sensors for an arbitrarily chosen crossing to assess the coefficients of determination R^2. The number of FE modes considered and the sensor combination for the physical sensors were chosen to match the respective coefficients of determination. 66

6.1 Instrumented railway bridge Schmutter with instrumented ICE 4 on it. 69

6.2 White ballast in the coupling joint. 70

6.3 Sensor positions on the Schmutter bridge. 71

6.4 Illustration of the sensor placement in cross-section. 72

6.5 Photoelectric sensors for axle detection and speed measurement. 72

6.6 Instrumentation of the ICE 4 with acceleration sensors on the axle boxes. 72

6.7 Axle configuration of the ICE 4. 73

6.8 Frequency of the first bending mode identified with SSI from the free decay signals of each passage. 74

6.9 Mode shapes identified with the SSI with the free decay signals after a passage in direction of Ulm with $v = 10\ \frac{\mathrm{km}}{\mathrm{h}}$. 75

6.10 Direct resonance curves, maximum absolute acceleration with a low-pass filter with a cut-off frequency of 8 Hz, as a function of train speed for the four mid-span sensors A6 to D6, separately for each direction. 76

6.11 Illustration of the FE model of the structure used. The cover plate of a box girder is hidden to illustrate the modelling of the interior........................ 77

6.12 Mode set of the selected bending and torsional modes of the coupled model. 78

6.13 Mode set of the selected bending and torsion modes of the uncoupled model towards Ulm. 78

6.14 Mode set of the selected bending and torsion modes of the uncoupled model towards Augsburg. 79

6.15 Comparison of the coefficients of determination for the coupled and the uncoupled model. For each sensor, the coefficients of determination of the leave-one-out validation are compared for all crossings.......................... 81

6.16 Differences in the coefficients of determination R^2 for the coupled and uncoupled model of the leave one out validation for each sensor. 82

6.17 Coefficients of determination R^2 of the leave-one-out validation as a function of train speed for each sensor, segregated by direction of travel and model type. 84

6.18 Exemplary comparisons of virtual sensor and physical sensor signals to assess the coefficients of determination... 86

6.19 Comparison of the contact periods for the resonance crossing in the direction of Ulm and Augsburg. 87

6.20 Comparison of the influence of the cut-off frequency of the low-pass filter on the indirect resonance curve of the sensor signal T_3 and the residual signal $T_3 - T_1$ for runs in the direction of Ulm..................................... 89

6.21 Indirect resonance curves for the runs towards Ulm with a cut-off frequency of $F_c = 8$ Hz. 91

6.22 Indirect resonance curves for the runs towards Augsburg with a cut-off frequency of $F_c = 8$ Hz. 92

6.23 Comparison of the identified frequencies for the two approaches: single sensor (top), residual signal with the preceding axle (bottom) separately for the crossings in the direction of Ulm and in the direction of Augsburg. The identified values are compared with the values identified with the bridge mounted sensors... 93

6.24 Comparison of the direct resonance curves of the signal sections in contact with the axle with which the indirect resonance curve was generated using residual signals in the direction of Ulm... 95

6.25 Comparison of the direct resonance curves of the signal sections in contact with the axle with which the indirect resonance curve was generated using residual signals in the direction of Augsburg.. 96

6.26 Percentage error of the residual signals compared to the measurement at the bridge for both directions of travel as a function of speed and as a function of bridge acceleration. 97

7.1 Garather Bach bridge.... 102
7.2 Sensor positions on the Garather Bach bridge a) side view b) top view c) cross-section.... 103
7.3 Installation of the axle load measuring points.... 103
7.4 Sensors installed on the main girders.... 105
7.5 Location of IDSSEL 60 and IDSSEL168 weather stations with distances to each other and to the bridge.... 106
7.6 Weather data from the IDSSEL60 weather station, with an indication of the time periods for which the monitoring data is available. 108
7.7 instrumented ICE TD passing the bridge of the track in the opposite direction (photo: Hagen Berthold). It should be noted that the investigations were carried out on the right bridge (directional track). 109
7.8 Instrumentation of the ICE TD with acceleration sensors on the axle boxes. 109
7.9 Axle configuration of the ICE TD. The length over the buffers is $l_{\mathrm{ob}} =$ 25.90 m. 109
7.10 First bending frequency identified by SSI analysis of free decay signals as a function of maximum amplitude, date and temperature. 113
7.11 POD modes for the Garather Bach bridge.... 114
7.12 FE model of the bridge 115
7.13 The six considered modes of the FE model, four bending modes and two torsional modes. 115
7.14 Comparison of four assigned FE modes with those of a SSI with ambient measurements and corresponding modal assurance criterion (MAC) values. 116
7.15 Comparison of three assigned FE modes with those of a SSI with free decay signals and corresponding MAC values. 116
7.16 Number of crossings for the five most frequent train types passing the bridge. 117
7.17 Experimental probability of the speeds of the trains for the four different types of train.... 117
7.18 Resonance curve from the acceleration signals of sensor A1 for the crossings of the five most frequent train types. The train type "Train 2" is included as 32 axle and 64 axle configuration.... 118
7.19 Resonance curve from the acceleration signals of sensors A2, A4, A7 and A8 for the crossings of the ICE TD.... 118
7.20 Summary of the number of occurrences of each strain gauge in an optimal sensor combination for reconstruction of a given measurement point using the FE modes. 124

7.21 Summary of the number of occurrences of each strain gauge in an optimal sensor combination for reconstruction of a given measurement point using the POD modes. 124

7.22 Summary of the number of occurrences of each accelerometer in an optimal sensor combination for reconstruction of a given measurement point using the FE modes. 125

7.23 Summary of the number of occurrences of each accelerometer in an optimal sensor combination for reconstruction of a given measurement point using the POD modes. 125

7.24 Exemplary comparisons of virtual sensor signals for the strains with those of the physical sensors for an arbitrarily chosen crossing to assess the coefficients of determination. The number of FE modes considered and the sensor combination for the physical sensors were chosen to match the respective coefficients of determination. 126

7.25 Exemplary comparisons of virtual sensor signals for the accelerations with those of the physical sensors for an arbitrarily chosen crossing to assess the coefficients of determination. The number of FE modes considered and the sensor combination for the physical sensors were chosen to match the respective coefficients of determination. 127

7.26 Contact periods of the instrumented axles of the ICE TD during resonance passage. 128

7.27 Exemplary compilation of the filter comparison for the last axle for the three approaches of a single sensor (top), the residual signal to the previous axle (middle) and the residual signal to the first axle (bottom). 129

7.28 Compilation of the indirect resonance curves and their maxima for the 'single-sensor' approach for the cut-off frequency of the low-pass filter of $F_c = 8.5\ Hz$. 132

7.29 Compilation of the indirect resonance curves and their maxima for the 'residual signal to preceding instrumented axle' approch for the cut-off frequency of the low-pass filter of $F_c = 8.5\ Hz$. 133

7.30 Compilation of the indirect resonance curves and their maxima for the 'residual signal to the first axle' approach for the cut-off frequency of the low-pass filter of $F_c = 8.5\ Hz$. 134

7.31 Comparison of the frequencies identified for the three approaches: single sensor (top), residual signal with the previous axle (middle) and residual signal with the first axle (bottom) for each of the sensors in comparison with the range identified with the bridge-mounted sensors 135

7.32 Comparison of the direct and indirect resonance curves for the contact periods of axle 1 to 16. For the indirect resonance curves, the residual signals to the first axle were used. All sigals were low-pass filtered with a cut-off frequency of 8.5 Hz. 138

7.33 Comparison of the direct and indirect resonance curves for the contact periods of axle 1 to 16. For the indirect resonance curves, the residual signals to the preceding axle were used. All sigals were low-pass filtered with a cut-off frequency of 8.5 Hz. 139

7.34 Percentage error of the maximum absolute values of the accelerations from the residual signals with the first axle $T_i - T_1$ and the residual signals with the preceding axle $T_i - T_{(i-1)}$ compared to the maximum absolute values of the sensors at bridge A2 and A7. 140

B.1 Comparison of the maximum and minimum coefficients of determination at MP 2L for accelerations and strains for all 4 POD mode sets 171

B.2 Comparison of the maximum and minimum coefficients of determination at MP 3L for accelerations and strains for all 4 POD mode sets 172

B.3 Comparison of the maximum and minimum coefficients of determination at MP 4L for accelerations and strains for all 4 POD mode sets 172

B.4 Comparison of the maximum and minimum coefficients of determination at MP 5L for accelerations and strains for all 4 POD mode sets 173

B.5 Comparison of the maximum and minimum coefficients of determination at MP 6L for accelerations and strains for all 4 POD mode sets 173

B.6 Comparison of the maximum and minimum coefficients of determination at MP 1R for accelerations and strains for all 4 POD mode sets 174

B.7 Comparison of the maximum and minimum coefficients of determination at MP 2R for accelerations and strains for all 4 POD mode sets 174

B.8 Comparison of the maximum and minimum coefficients of determination at MP 3R for accelerations and strains for all 4 POD mode sets 175

B.9 Comparison of the maximum and minimum coefficients of determination at MP 4R for accelerations and strains for all 4 POD mode sets 175

B.10 Comparison of the maximum and minimum coefficients of determination at MP 5R for accelerations and strains for all 4 POD mode sets 176

B.11 Comparison of the maximum and minimum coefficients of determination at MP 6R for accelerations and strains for all 4 POD mode sets 176

B.12 Influence of the cut-off frequency F_c on the resonance curve with the maximum absolute values of the accelerations for sensors T_1 to T_8 for runs in the direction of Ulm 178

B.13 Influence of the cut-off frequency F_c on the resonance curve with the maximum absolute values of the accelerations for sensors T_1 to T_8 for runs in the direction of Augsburg 179

B.14 Influence of the cut-off frequency F_c on the resonance curve with the maximum absolute values of the acceleration for the residual signals for runs in the direction of Ulm 180

B.15 Influence of the cut-off frequency F_c on the resonance curve with the maximum absolute values of the acceleration for the residual signals for runs in the direction of Augsburg 181

B.16 Coefficients of determination of the leave-p-out validation for the best and worst sensor combination (s.c.) depending on the number of physical sensors and considered FE modes for each strain gauge.......... 183

B.17 Coefficients of determination of the leave-p-out validation for the best and worst sensor combination (s.c.) depending on the number of physical sensors and considered POD modes for each strain gauge.......... 184

B.18 Coefficients of determination of the leave-p-out validation for the best and worst sensor combination (s.c.) depending on the number of physical sensors and considered FE modes for each accelerometer. 185

B.19 Coefficients of determination of the leave-p-out validation for the best and worst sensor combination (s.c.) depending on the number of physical sensors and considered POD modes for each accelerometer.......... 186

B.20 Inerquartile range of the coefficients of determination for the 5 most frequent train types and as a function of train speed, obtained by leave-one-out validation for each strain gauge using 3 FE modes. 187

B.21 Inerquartile range of the coefficients of determination for the 5 most frequent train types and as a function of train speed, obtained by leave-one-out validation for each strain gauge using 4 POD modes.......... 188

B.22 Inerquartile range of the coefficients of determination for the 5 most frequent train types and as a function of train speed, obtained by leave-one-out validation for each accelerometer using 6 FE modes.......... 189

B.23 Inerquartile range of the coefficients of determination for the 5 most frequent train types and as a function of train speed, obtained by leave-one-out validation for each accelerometer using 4 POD modes. 190

B.24 Inerquartile range and median of the coefficients of determination R^2 against the normalised amplitudes, obtained by leave-one-out validation for each strain gauge (S1 to S8) using 3 FE modes / 4 POD modes. 191

B.25 Inerquartile range and median of the coefficients of determination R^2 against the normalised amplitudes, obtained by leave-one-out validation for each strain gauge (S1 to S8) using 6 FE modes / 4 POD modes. 192

B.26 Interquartile ranges and median of the determination coefficients (R^2) for each strain sensor (S1 to S8), derived from Leave-One-Out validation results, are compared to the mean value recorded during the associated train passage using temperature sensors TC1 and TC2. Three FE modes were considered. 193
B.27 Interquartile ranges and median of the determination coefficients (R^2) for each strain sensor (S1 to S8), derived from Leave-One-Out validation results, are compared to the mean value recorded during the associated train passage using temperature sensors TC1 and TC2. Four POD modes were considered. 194
B.28 Interquartile ranges and median of the determination coefficients (R^2) for each accelerometer (A1 to A9), derived from Leave-One-Out validation results, are compared to the mean value recorded during the associated train passage using temperature sensors TC1 and TC2. Six FE modes were considered. 195
B.29 Interquartile ranges and median of the determination coefficients (R^2) for each accelerometer (A1 to A9), derived from Leave-One-Out validation results, are compared to the mean value recorded during the associated train passage using temperature sensors TC1 and TC2. Four POD modes were considered. 196
B.30 Influence of the cut-off frequency F_c on the resonance curve with the maximum absolute values of the accelerations of the singel senor signals 100 197
B.31 Influence of the cut-off frequency F_c on the resonance curve with the maximum absolute values of the accelerations of the singel senor signals 200 198
B.32 Influence of the cut-off frequency F_c on the resonance curve with the maximum absolute values of the accelerations of the residual signals to the preceding axle 100 199
B.33 Influence of the cut-off frequency F_c on the resonance curve with the maximum absolute values of the accelerations of the residual signals to the preceding axle 200 200
B.34 Influence of the cut-off frequency F_c on the resonance curve with the maximum absolute values of the accelerations of the residual signals to the first axle 100 201
B.35 Influence of the cut-off frequency F_c on the resonance curve with the maximum absolute values of the accelerations of the residual signals to the first axle 200 202

List of Tables

5.1 Material parameters of the FE model ... 47
5.2 Spring stiffnesses of the FE model ... 47
5.3 MAC values for the comparison of the displacement eigenmodes and those of the SSI ... 48
5.4 MAC values for comparison of strain mode shapes of FE and beam model . 49
5.5 MAC-values of the comparison of the POD modes for accelerations $\mathbf{\Psi}_{\mathrm{a},n}$ from the four different mode sets ... 51
5.6 MAC-values of the comparison of the POD modes for strains $\mathbf{\Psi}_{\mathrm{s},n}$ from the four different mode sets ... 53
5.7 Mean values of the coefficients of determination R^2 over the four passes with different frequencies for all acceleration sensors. ... 55
5.8 Mean values of the coefficients of determination R^2 over the four passes with different frequencies for all strain gauges. ... 55

6.1 Accelerometers installed on the Schmutter bridge. ... 73
6.2 Accelerometers installed on the ICE 4. ... 73
6.3 Summary of the mean and standard deviation for percentage errors: a comparison of the maximum absolute residual signal values derived from axle box accelerations on the ICE 4, with values recorded from sensors installed on the Schmutter bridge. ... 95

7.1 Pearson's correlation coefficient between the data from the IDSSEL 60 weather station and the IDSSEL168 weather station ... 106
7.2 Modes identified by analysing ambient measurements ... 110
7.3 Pearson correlation coefficients between the coefficients of determination R^2 of the leave one out validation and the environmental data of the IDSSEL 60 weather station for each starin gauge (S1 to S8). 3 FE modes and 4 POD modes are considered with a significance level of $\alpha = 0.001$. Insignificant results are indicated by n.s. ... 122
7.4 Pearson correlation coefficients between the coefficients of determination R^2 of the leave one out validation and the environmental data of the IDSSEL 60 weather station for each accelerometer (A1 to A9). 6 FE modes and 4 POD modes are considered with a significance level of $\alpha = 0.001$. Insignificant results are indicated by n.s. ... 123

7.5 Summary of mean and standard deviation for percentage errors: This compares the maximum absolute values derived from the residual signals to the first axle box accelerations on the ICE TD, with the values recorded from sensors on the Garather Bach bridge. 137

7.6 Summary of mean and standard deviation for percentage errors: This involves comparing the maximum absolute values derived from the residual signals related to the preceding axle box accelerations on the ICE TD, with the values recorded from sensors on the Garather Bach bridge. 137

A.1 Maximum and minimum coefficients of determination R^2 and the corresponding number of considered modes n_m for the leave-one-out validation for each accelerometer and 4 different sets of POD modes at a step frequency of 1.6 Hz. 163

A.2 Maximum and minimum coefficients of determination R^2 and the corresponding number of considered modes n_m for the leave-one-out validation for each accelerometer and 4 different sets of POD modes at a step frequency of 1.8 Hz. 163

A.3 Maximum and minimum coefficients of determination R^2 and the corresponding number of considered modes n_m for the leave-one-out validation for each accelerometer and 4 different sets of POD modes at a step frequency of 2.0 Hz. 164

A.4 Maximum and minimum coefficients of determination R^2 and the corresponding number of considered modes n_m for the leave-one-out validation for each accelerometer and 4 different sets of POD modes at a step frequency of 2.2 Hz. 164

A.5 Maximum and minimum coefficients of determination R^2 and the corresponding number of considered modes n_m for the leave-one-out validation for each strain gauge and 4 different sets of POD modes at a step frequency of 1.6 Hz. 164

A.6 Maximum and minimum coefficients of determination R^2 and the corresponding number of considered modes n_m for the leave-one-out validation for each strain gauge and 4 different sets of POD modes at a step frequency of 1.8 Hz. 165

A.7 Maximum and minimum coefficients of determination R^2 and the corresponding number of considered modes n_m for the leave-one-out validation for each strain gauge and 4 different sets of POD modes at a step frequency of 2.0 Hz. 165

A.8 Maximum and minimum coefficients of determination R^2 and the corresponding number of considered modes n_m for the leave-one-out validation for each strain gauge and 4 different sets of POD modes at a step frequency of 2.2 Hz. 165
A.9 Identified frequencies from the peaks of the indirect resonance curves compared to the value of the bridge measurements.......... 166
A.10 Sampling rates of the sensors in the different setups 167
A.11 List of the identified resonance peaks and the corresponding calculated frequencies for the accelerometers on the bridge 167
A.12 List of identified resonance peaks and corresponding calculated frequencies for the 'single sensor signal' approach compared to the mean value obtained with the sensors on the bridge.......... 168
A.13 List of identified resonance peaks and corresponding calculated frequencies for the 'residual preceding sensor' approach compared to the mean value obtained with the sensors on the bridge. 169
A.14 List of identified resonance peaks and corresponding calculated frequencies for the 'residual first sensor' approach compared to the mean value obtained with the sensors on the bridge.......... 170

Glossaries

Abbreviations

CWT	continuous wavelet transform
DBM	drive-by monitoring
EMA	experimental modal analysis
FE	finite element
FFT	fast Fourier transform
HHT	Hilbert–Huang transform
MAC	modal assurance criterion
ME	modal expansion
MOR	model order reduction
NDOF	*n*-degree of freedom system
ODE	ordinary differential equation
ODEs	ordinary differential equations
OMA	operational modal analysis
PDE	partial differential equation
PDEs	partial differential equations
POD	proper orthogonal decomposition
SHM	structural health monitoring
SSI	stochastic subspace identification
SSI-COV	covariance-driven stochastic subspace identification
SVD	singular value decomposition
VS	virtual sensing

Symbols: fundamentals

A	Amplitude of the track irregularities
A_n	Amplitude of the n-th mode
$\mathbf{A}$	Data matrix or constraint matrix
$\mathbf{a}_\square$	Column $\square$ of $\mathbf{A}$, representing 'snapshots'

B	Amplitude of bridge vibration
$\mathbf{b}$	Known vector in linear system
$\boldsymbol{\Delta}$	Change in matrices
E	Young's modulus
EI	Bending stiffness
$f_{\mathrm{B},n}$	Natural frequency of the n-th bending mode
$f_{\mathrm{T},n}$	Natural frequency of the n-th torsional mode
f_n	Natural frequency of the n-th mode
$\mathbf{f}$	Load vector
GI_T	Torsional stiffness of the cross section
$\mathbf{I}$	Identity matrix
I	Second moment of area
I_P	Polar moment of inertia
i	Index variable
l_ob	Length over buffers
L	Span length
λ	Eigenvalue
Λ	Diagonal matrix of modal damping ratios
$\mathbf{K}$	Stiffness matrix
M	Bending moment
$\mathbf{M}$	Mass matrix
μ	Mass per unit length
μ_T	Torsional mass per unit length
n	Mode number
n_m	Number of considered modes
Ω_n	Natural angular frequency of the n-th mode
ω	Angular frequency
ω_n	Natural angular frequency
ω_b	Natural angular frequency of the bridge
$\mathbf{p}$	External load on the body
Ψ_n	n-th POD mode
$\boldsymbol{\Psi}$	POD mode matrix
$\mathbf{r}$	Displacement field
q	Load perpendicular to the beam axis
q_n	Generalised coordinates of the n-th mode
r	Rank of truncated matrix
ϵ	Strain tensor
ε	Strain
ε_n	Strain of the n-th mode
σ	Normal stress

Σ	Diagonal matrix of singular values
t	Time
$\phi_{\mathrm{d},n}$	n-th displacement mode
$\phi_{\mathrm{s},n}$	n-th strain mode
$\mathbf{\Phi}$	Modal matrix
ϕ	Mode shape vector
φ	Mode shape function
ϕ_n	Mode shape of the n-th mode
$\mathbf{U}$	Left singular vector matrix
$\mathbf{u}$	Displacement vector
$\mathbf{V}$	Right singular vector matrix
v	Velocity
v_{res}	Resonance speed
w	Beam deflection
w_n	Beam deflection of the n-th mode
x, y, z	Spatial coordinates
x	Position along the beam
$\mathbf{x}$	Unknown vector in linear system
$\hat{x}$	Approximate solution vector
Ξ	Diagonal matrix of modal stiffnesses
z_{ti}	Track irregularity
$\ddot{z}_{\mathrm{b}}$	Accelerations caused by track irregularities
Θ_n	Mode shape for the n-th torsional mode
θ	Phase shift
$\tilde{\Box}$	Truncated $\Box$ matrix

Mathematical operators

∇	Gradient
$\ddot{\Box}$	Second time derivative of $\Box$
$\Box''$	Second spatial derivative of $\Box$
$\Box''''$	Fourth spatial derivative of $\Box$
$\Box^{+}$	Pseudoinverse of $\Box$
$\Box^{-1}$	Inverse of $\Box$
$\Box^{*}$	Conjugate transpose of $\Box$
$\Box^{\mathrm{T}}$	Transpose of $\Box$

1 Introduction

1.1 Motivation

The global railway bridge infrastructure is ageing and being subjected to increasing traffic loads. In Germany, the average service life of a railway bridge is 122 years (KNAPP, 2019), a period during which railway vehicles have significantly evolved. These advancements in railway vehicle design have led to increased axle loads and speeds, sometimes exceeding the structural design expectations of these aging bridges (FIRUS et al., 2018; KARIMI, 2020). Such developments are not unique to Germany but are also observed in countries like Japan, where the aging bridge inventory and the high-speed train network have led to resonance phenomena (SOGABE et al., 2005).

Germany's DB Netz AG operates 25,710 railway bridges (KNAPP, 2019), translating to 30,000 to 35,000 bridges when considering parallel superstructures [1]. Around 40 % of these bridges are over 80 years old (GEISSLER, 2014). Similar scenarios exist across the 212,000 km European rail network, which includes more than 300,000 bridges, with around 35 % being over a century old (VAGNOLI et al., 2018).

Economic and ecological considerations necessitate extending the service life of these structures as much as is feasibly possible. Additionally, the anticipated scarcity of skilled labour demands the creation of efficient techniques for assessing existing bridge structures (GEISSLER et al., 2019; LORENZEN et al., 2022a). Vibration-based methods serve as one approach to achieving objective evaluations of bridge structures.

Vibration-based monitoring of bridges is typically classified into direct and indirect monitoring (ZHU et al., 2014; MALEKJAFARIAN et al., 2015; TAN et al., 2017; LI et al., 2019). Direct monitoring involves the installation of sensors on the structure itself. Conversely, indirect monitoring utilises sensors attached to a passing vehicle. Therefore, indirect monitoring is also commonly referred to as drive-by monitoring.

Although direct monitoring provides a more accurate structural analysis, its implementation is often costly, time-consuming, and potentially hazardous (MALEKJAFARIAN et al., 2022). Consequently, it may be impractical to employ direct monitoring on a network level given the sheer number of bridges involved. As a result, indirect monitoring has emerged as a cost-effective alternative, attracting significant research interest (YANG et al., 2018). However, despite the potential of these drive-by technologies, more field validations are necessary to gain full acceptance and confidence from bridge operators (MALEKJAFARIAN et al., 2022).

---

[1] The difference in the number of bridges arises because DB Netz AG counts crossing points. A single crossing point comprises multiple parallel bridges.

The limited availability of sensors on structures necessitates the use of virtual sensing methods. These methods are employed to extrapolate the structural responses from the few accessible sensor-equipped locations to the multitude of unmeasured locations of the structure. This extrapolation is particularly critical for validating safety against fatigue failure (AZAM et al., 2022; MAES et al., 2021). However, like drive-by monitoring technologies, these virtual sensing methods require further validation on actual railway bridges. They also need long-term validation to account for changes in operational and environmental conditions. Undertaking this rigorous validation is essential to enhance the acceptance and confidence of bridge owners in these methodologies.

It is anticipated that both direct and indirect monitoring will continue to be employed in a complementary manner. While indirect monitoring is beneficial for network-level assessment, direct monitoring is needed when detailed information, such as realistic stress-time histories on individual components, is required. Technologies like drive-by monitoring and virtual sensing may play a crucial role in predicting the residual service life of bridges in the future.

The primary motivation of this work is to develop significant contributions to both direct and indirect monitoring of railway bridges. The aim is that the methods and concepts discussed in this thesis can be promptly applied in the field, thereby contributing immediately to the maintenance of the rapidly deteriorating railway bridge infrastructure.

1.2 Objectives

The main objective of this research is to enhance the monitoring of railway bridges by using vibration measurements with a minimal set of sensors. This comprehensive aim has been divided into two key sub-objectives:

(1) Identification and implementation of a suitable virtual sensing methodology for railway bridges, followed by its long-term validation. This process will entail studies on the impacts of various operational and environmental conditions on the method, providing an understanding of its performance under differing circumstances.

(2) Development and validation of a technique that identifies the resonance frequency of railway bridges using drive-by monitoring. This methodology was be thoroughly validated under realistic operating conditions.

The accomplishment of these objectives is expected to significantly contribute to the practical, cost-effective, and reliable monitoring of aging railway bridges.

To fulfill these objectives, measurements were taken from bridge structures and vehicles. The data utilized include both existing records from the Structural Dynamics Unit of the

Institute of Structural Mechanics and Design at the Technical University of Darmstadt and new measurements conducted during the duration of this research.

1.3 Own contributions

The specific scientific contributions to the body of knowledge made within the scope of this thesis are as follows:
Virtual Sensing:

- Provision of the first evidence of modal expansion for railway bridges exhibiting nonlinear system behaviour.
- Execution of the first long-term validation involving investigations under different operating and environmental conditions.
- The first validation for short-span bridges (less than 20 m) with ballasted superstructure.

Drive-by Monitoring:

- New approach: Resonance curve-based drive-by monitoring.
- Validation of the resonance curve-based drive-by monitoring, performed on two different structures and vehicles.

1.4 Structure of the thesis

At this point, an overview of the structure of the thesis is provided. A corresponding schematic illustration can be viewed in Figure 1.1.

The dissertation begins with **Ch.1: Introduction**. In this section, motivation for the study is established through a brief discussion of the socio-technical context and the problem statement. Building upon this, objectives of the study are defined and categorised into Objective 1 and Objective 2. An indication is given in the schematic illustration to show which objectives are addressed in wich subsection in subsequent chapters. Additionally, a brief enumeration of the specific scientific contributions made during the study is included. This chapter concludes with the present section, explaining the structure of the dissertation.

Following the introduction is the foundational layer of the work, consisting of Chapters 2 and 3.

In **Ch.2: Fundamentals**, essential theoretical foundations are succinctly laid out. Detailed derivations and explanations are intentionally omitted, and references to pertinent academic literature are cited for those seeking more in-depth information.

Ch.3: State of the Art summarises current research on virtual sensing and drive-by monitoring of railway bridges. Based on this compilation, existing gaps in the research are identified. This chapter is further divided into two subsections: section 3.1 addresses the state of science in virtual sensing of railway bridges, and section 3.2 focuses on drive-by monitoring.

Building upon the state of the art and theoretical foundations, the next layer of the dissertation is **Ch.4: Methodology**. Here, the methodology employed for analysing the experimental investigations is elucidated. This chapter is again divided into two subsections: section 4.1 for virtual sensing, and section 4.2 for drive-by monitoring.

The subsequent layer consists of experimental investigations conducted on three different bridge structures, each documented in a separate chapter.

The initial experimental investigations are described in **Ch.5: Footbridge HUMVIB**. Investigations on this structure were limited to virtual sensing only. Despite not being a railway bridge, this structure was chosen due to its easy accessibility and relative ease of modelling for preliminary virtual sensing investigations.

Ch.6: Railway Bridge Schmutter presents investigations on a double-track railway bridge coupled through ballast. Both the bridge and the traversing ICE 4 were equipped with sensors, facilitating studies in both virtual sensing and drive-by monitoring.

The final part of the experimental investigations is covered in **Ch.7: Railway Bridge Garather Bach**. Investigations on a single-track railway bridge with ballast are presented. A long-term monitoring system is installed on this bridge, and a measurement campaign using an instrumented ICE TD was conducted for frequency identification validation. Both long-term validation of virtual sensing and validation of drive-by monitoring were carried out.

The dissertation concludes with **Ch.8: Conclusion and Future Research Directions**. Primary contributions and findings of the study are summarised. Following this, limitations of the study are elucidated and recommendations for future work are presented. This is done separately for virtual sensing in section 8.1 and for drive-by monitoring in section 8.2. The chapter, and thereby the dissertation, is closed with final remarks (section 8.3).

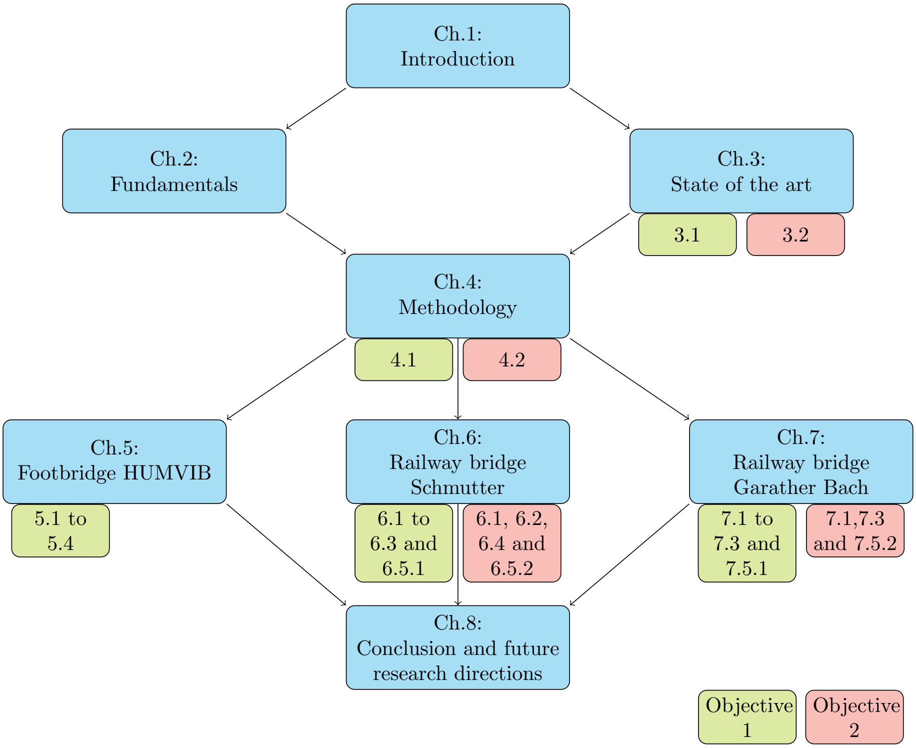
Ch.1:
Introduction
Ch.2:
Fundamentals
Ch.3:
State of the art
3.1
3.2
Ch.4:
Methodology
4.1
4.2
Ch.5:
Footbridge HUMVIB
5.1 to 5.4
Ch.6:
Railway bridge Schmutter
6.1 to 6.3 and 6.5.1
6.1, 6.2, 6.4 and 6.5.2
Ch.7:
Railway bridge Garather Bach
7.1 to 7.3 and 7.5.1
7.1,7.3 and 7.5.2
Ch.8:
Conclusion and future research directions
Objective 1
Objective 2

Figure 1.1 Schematic presentation of the structure of the thesis.

2 Fundamentals

This chapter provides the basic theoretical principles necessary for understanding the present work. The focus is placed on summarising key concepts and theories without delving into detailed derivations. For a more comprehensive presentation and additional details, the reader is referred to the relevant technical literature.

The first three sections of this chapter focus on the presentation of selected linear algebra concepts utilised in the context of this thesis. For a comprehensive explanation of the fundamentals of linear algebra, the reader is referred to STRANG (2006). Detailed presentations of the concepts briefly outlined below can be found in STRANG (2007)[1] and BRUNTON et al. (2019).

The remainder of this chapter is dedicated to significant elements of bridge dynamics, which are utilised in the current work. PETERSEN et al. (2018) provides a comprehensive description of the fundamentals of bridge dynamics and associated computational methods. For the study of vibrations in solid bodies under moving loads, FRÝBA (1976) is a recommended source. FRÝBA (1996) offers in-depth insights specifically tailored to the dynamics of railway bridges. A more recent and compact presentation can be found in THOMSEN (2021).

2.1 Singular value decomposition

The singular value decomposition (SVD) allows a unique decomposition of every complex-valued matrix $\mathbf{A} \in \mathbb{C}^{n\times m}$. If $\mathbf{A}$ is a data matrix representing measurements or simulation results, it may be arranged such that each column $\mathbf{a}_k$ represents a series of n measurements or simulation outcomes captured at the corresponding time k in the time series. Under this configuration, these columns are commonly termed as 'snapshots', where m denotes the total number of these snapshots. The SVD of the matrix $\mathbf{A}$ can be expressed as follows (BRUNTON et al., 2019):

$$\mathbf{A} = \begin{bmatrix} | & | & & | \\ \mathbf{a}_1 & \mathbf{a}_2 & \dots & \mathbf{a}_m \\ | & | & & | \end{bmatrix} = \mathbf{U}\mathbf{\Sigma}\mathbf{V}^* \tag{2.1}$$

---

[1] For the German translation, see STRANG (2012)

The matrices $\mathbf{U} \in \mathbb{C}^{n\times n}$ and $\mathbf{V} \in \mathbb{C}^{m\times m}$ are characterized by orthonormal columns. The columns of $\mathbf{U}$ are called left singular vectors, those of $\mathbf{V}$ right singular vectors. The matrix $\mathbf{\Sigma} \in \mathbb{R}^{n\times m}$ is a diagonal matrix which contains only non-negative entries – the so-called singular values (BRUNTON et al., 2019).

Many high-dimensional datasets reveal low-dimensional patterns that allow for data approximation in a reduced space. This characteristic is used in various fields, including image compression and model order reduction (MOR). The truncated SVD approximation is commonly written as (BRUNTON et al., 2019):

$$\mathbf{A} \approx \tilde{\mathbf{A}} = \tilde{\mathbf{U}}\tilde{\mathbf{\Sigma}}\tilde{\mathbf{V}}^{*} \tag{2.2}$$

Here, $\tilde{\mathbf{U}}$ and $\tilde{\mathbf{V}}$ represent the first r columns of $\mathbf{U}$ and $\mathbf{V}$, respectively, and $\tilde{\mathbf{\Sigma}}$ represents the first $r \times r$ block of $\mathbf{\Sigma}$.

2.2 Proper orthogonal decomposition

The POD is based on the SVD and provides a set of modes that are optimal for approximating simulation or measurement data in a low-dimensional subspace (BRUNTON et al., 2019). The POD originated in various research disciplines and was developed there under different names. Two of these are principal component analysis and Karhunen-Loeve decomposition. It has been shown that these methods are variants of the POD (EFTEKHAR AZAM et al., 2013).

The dominant modes for characterizing the dynamics of a system, from which the data matrix was recorded, are contained in the truncated matrix $\tilde{\mathbf{U}}$ (Equation 2.2) (BRUNTON et al., 2019):

$$\tilde{\mathbf{U}} = \mathbf{\Psi} = \begin{bmatrix} | & | & & | \\ \Psi_1 & \Psi_2 & \dots & \Psi_n \\ | & | & & | \end{bmatrix} \tag{2.3}$$

The POD modes $\mathbf{\Psi}$ of a structure differ from the eigenmodes as they are load-dependent (ZAYERI BAGHLANI NEJAD et al., 2021). In the special case where the mass matrix is proportional to the unit matrix, the eigenmodes and POD modes coincide. In the case of resonance, the dominant POD mode approaches the excited eigenmode (KERSCHEN et al., 2005).

2.3 Linear system of equations and the pseudoinverse

A linear system of equations can generally be expressed as (BRUNTON et al., 2019):

$$\mathbf{A}\mathbf{x} = \mathbf{b} \tag{2.4}$$

where $\mathbf{A} \in \mathbb{C}^{n \times m}$ is the constraint matrix, $\mathbf{b} \in \mathbb{C}^{n \times 1}$ a known vector and $\mathbf{x} \in \mathbb{C}^{n \times 1}$ an unknown vector. Three special cases can be distinguished (BRUNTON et al., 2019):

(1) If $\mathbf{A}$ is a square and invertible matrix, then for each given $\mathbf{b}$ there is a unique solution $\mathbf{x}$.

(2) In the underdetermined case, if $n < m$ and $\mathbf{A}$ has full column rank, there exists an infinite number of solutions $\mathbf{x}$ for each $\mathbf{b}$.

(3) In the overdetermined case, if $n > m$ and $\mathbf{b}$ is not in the column space of the matrix $\mathbf{A}$, the system is inconsistent and there is no solution.

In the overdetermined case, where no solution exists, there is often an interest in finding the solution $\hat{\mathbf{x}}$ that minimizes the quadratic error $|\mathbf{A}\hat{\mathbf{x}} - \mathbf{b}|_2^2$. This is referred to as the method of least squares. In the underdetermined case, when there are an infinit number of solutions, it may be advantageous to find the solution $\hat{\mathbf{x}}$ with the smallest norm $|\hat{\mathbf{x}}|_2$, such that $\mathbf{A}\hat{\mathbf{x}} = \mathbf{b}$ is fulfilled. This is referred to as the method of minimal norm. Both, the method of least squares and the method of minimal norm, can be calculated using the Moore-Penrose pseudoinverse. This is defined as (BRUNTON et al., 2019):

$$\mathbf{A}^{+} \triangleq \tilde{\mathbf{V}}\tilde{\mathbf{\Sigma}}^{-1}\tilde{\mathbf{U}}^{*} \tag{2.5}$$

This expression results from inverting the three matrices of the truncated matrix approximation of $\mathbf{A}$ according to Equation 2.2. Here, r is chosen so that all singular values are non-zero. Since $\mathbf{A}^{+}\mathbf{A} = \mathbf{I}$, the solution to Equation 2.4 is obtained by multiplying by $\mathbf{A}^{+}$ (BRUNTON et al., 2019):

$$\mathbf{A}^{+}\mathbf{A}\hat{\mathbf{x}} = \hat{\mathbf{x}} = \mathbf{A}^{+}\mathbf{b} \tag{2.6}$$

2.4 Equation of motion

Modelling in structural dynamics requires careful consideration of several factors. For example, the mass distribution can be considered either continuous or lumped. Time can be continuous or discrete. Furthermore, the system properties can be linear or non-linear, and time-variant or time-invariant. In terms of models, simplified planar models or more comprehensive 3D models are available. The choice of the model strongly depends on the specific application and the purpose of the calculation. Due to the challenges in determining the required parameters and the high computational times, it is generally recommended to use the simplest possible models (FRÝBA, 1996).

The focus of this section is exclusively on linear and time-invariant systems. Although system properties may change over time, for example due to temperature variations, these changes occur on long timescales compared to the bridge oscillations and crossing times. Therefore, the assumption of time invariance is justified for single crossings or short time intervals.

The oscillations of a three-dimensional body can usually be described by an operator equation. This relates the displacement field $\mathbf{r}(x,y,z,t)$ at a given position, characterised by the spatial coordinates x,y,z and the time t, to the external load $\mathbf{p}(x,y,z,t)$ on the body. The relationship is expressed in the form (FRÝBA, 1976):

$$L[\mathbf{r}(x,y,z,t)] = \mathbf{p}(x,y,z,t) \tag{2.7}$$

where the symbol L stands for a linear or non-linear differential operator. The behaviour of the body is determined by this equation, or by sets of such equations – usually in the form of partial differential equations – together with the boundary and initial conditions (FRÝBA, 1976).

A basic modelling of the structural behaviour of a bridge is the representation as a one-dimensional solid in the form of an undamped Euler-Bernoulli beam according to the first-order theory. The differential equation for the beam is as follows (PETERSEN et al., 2018, p.659) [2]

$$[EI(x)w(x,t)'']'' - \mu(x)\ddot{w}(x,t) = q(x,t) \tag{2.8}$$

In this equation, x represents the spatial coordinate along the beam axis, $w(x,t)$ the deflection, $EI(x)$ the bending stiffness of the beam and $\mu(x)$ the mass distribution per unit length, and $q(x,t)$ the load perpendicular to the beam axis.

For Equation 2.8 no analytical solution can be found except for a few special loading assumptions (PETERSEN et al., 2018). For the special case of a homogeneous beam, Equation 2.8 simplifies to a partial differential equation with constant coefficients:

$$EIw(x,t)'''' - \mu\ddot{w}(x,t) = q(x,t) \tag{2.9}$$

The equation for the homogeneous beam can be solved analytically for general load functions. However, this model is typically only suitable for simple cases or for basic vibration analysis of beam-like structures under transverse loading. Discretisation is required to model more complex systems. The equation of motion for a system with n degrees of freedom is then

---

[2] The notation has been modified for consistency.

$$\mathbf{M}\ddot{\mathbf{u}}(t)+\mathbf{C}\dot{\mathbf{u}}(t)+\mathbf{K}\mathbf{u}(t)=\mathbf{f}(t) \tag{2.10}$$

In this equation, $\mathbf{M}\in\mathbb{R}^{n\times n}$ is the mass matrix, $\mathbf{C}\in\mathbb{R}^{n\times n}$ is the damping matrix and $\mathbf{K}\in\mathbb{R}^{n\times n}$ is the stiffness matrix. $\mathbf{f}(t)\in\mathbb{R}^{n}$ is the load vector.

2.5 Modal analysis

Modal analysis is a methodology based on the determination of the inherent dynamic characteristics of a system such as natural frequencies, damping factors and mode shapes. The overall objective is to construct a mathematical model that adequately represents the dynamic behaviour of the system under consideration. The recorded modal parameters, which are determined by physical quantities such as mass, stiffness and damping, have a significant influence on the vibration behaviour of the system.

2.5.1 Modal decorrelation

Solving the eigenvalue problem of the free, undamped vibration leads to the determination of the eigenfunctions or eigenvectors of the system[3]. These will be uniformly referred to as mode shapes. Any sufficiently smooth displacement field $\mathbf{r}$ satisfying the boundary conditions can be represented by a weighted sum of these mode shapes (THOMSEN, 2021). The displacements in Equation 2.9 and Equation 2.10 can therefore be expressed as follows:

$$\begin{aligned} w(x,t) &= \sum_{n=1}^{\infty}\varphi_n(x)q_n(t) \\ \mathbf{u}(t) &= \sum_{n=1}^{N}\boldsymbol{\phi}_n q_n(t) \end{aligned} \tag{2.11}$$

This is called modal decorrelation (TARPØ et al., 2020). In this representation, $\varphi_n(x)$ and $\boldsymbol{\phi}_n$ represent the shape of the n-th displacement mode, where $n\in\mathbb{N}$. The terms $q_n(t)$ are referred to as generalised coordinates.

In the context of continuum modelling, mode shape expansion or modal decorrelation provides a simple and practical approach to transforming a partial differential equation (PDE) into a system of ordinary differential equations (ODEs). Each of these ODEs can be considered as a single degree of freedom system. This approach is also applicable to nonlinear[4] problems and higher dimensions, such as plate and shell problems (THOMSEN, 2021).

---

[3] For a presentation of the calculation of the eigenvalue solution see PETERSEN et al., 2018, p.518, 596, 682 or THOMSEN, 2021, p.6, 12.

When modelling as a linear n-degree of freedom system (NDOF), the coupled differential equations (Equation 2.10) are decoupled by modal decorrelation and can then also be solved as single-degree-of-freedom systems (THOMSEN, 2021). The equations are decoupled as follows.

The modal decorrelation can also be written in matrix notation as:

$$\mathbf{u} = \mathbf{\Phi q} \tag{2.12}$$

where $\mathbf{\Phi}$ is the modal matrix, with the n-th column consisting of the nth mode shape. Substituting the displacement in Equation 2.10 with the expression in Equation 2.12 and premultiplying with $\mathbf{\Phi}^T$ gives the decoupled equations (PETERSEN et al., 2018, p.517):

$$\mathbf{\Phi}^{\mathrm{T}}\mathbf{M\Phi\ddot{q}} + \mathbf{\Phi}^{\mathrm{T}}\mathbf{C\Phi\dot{q}} + \mathbf{\Phi}^{\mathrm{T}}\mathbf{K\Phi q} = \mathbf{\Phi}^{\mathrm{T}}\mathbf{f} \tag{2.13}$$

The modal analysis or modal model of the structure can also be used for model reduction. Since the dynamics of civil engineering structures are mainly relevant in the low frequency range, the dynamic behaviour can often be adequately approximated by a small number of considered mode shapes n_{m}:

$$\begin{aligned} w(x,t) &\approx \sum_{n=1}^{n_{\mathrm{m}}} \varphi_n(x) q_n(t) \\ \mathbf{u}(t) &\approx \sum_{n=1}^{n_{\mathrm{m}}} \boldsymbol{\phi}_n q_n(t) \end{aligned} \tag{2.14}$$

2.5.2 Mode shapes of a beam

The following section analyses the mode shapes and frequencies of a beam. Typically, the vibrations of a bridge are characterised by vertical motions caused by bending and torsional vibrations.

---

[4] In nonlinear problems, however, the ordinary differential equations generally remain nonlinearly coupled.

For the homogeneous beam, according to Equation 2.9, the following natural frequencies and angular frequency for bending vibrations result for a simply supported single span beam (Petersen et al., 2018, p. 596, 600):

$$\begin{aligned} f_{\mathrm{B},n} &= \frac{\pi}{2}\left(\frac{n}{l}\right)^2 \sqrt{\frac{EI}{\mu}} \\ \omega_{\mathrm{B},n} &= \left(\frac{n\pi}{l}\right)^2 \sqrt{\frac{EI}{\mu}} \end{aligned} \tag{2.15}$$

The associated mode shapes can be expressed as follows:

$$\varphi_n(x) = \sin\left(n\pi\frac{x}{l}\right) \tag{2.16}$$

where l represents the length of the beam and $x \in [0,l] \subseteq \mathbb{R}$.

The frequencies of the torsional vibration of a fork-supported single span beam are (Petersen et al., 2018, p. 710, 711):

$$\begin{aligned} f_{\mathrm{T},n} &= \frac{n}{2}\sqrt{\frac{GI_\mathrm{T}}{\mu_\mathrm{T} l^2}} \\ \omega_{\mathrm{T},n} &= \pi n\sqrt{\frac{GI_\mathrm{T}}{\mu_\mathrm{T} l^2}} \end{aligned} \tag{2.17}$$

The associated mode shapes are given by the following equation:

$$\Theta_n(x) = \sin\left(n\pi\frac{x}{l}\right) \tag{2.18}$$

Here, GI_T represents the torsional stiffness of the cross section, μ_T represents the torsional mass occupancy per unit length, and $\Theta_n(x)$ represents the twist angle of the cross section. The torsional mass is given by $\mu_\mathrm{T} = \mu I_\mathrm{P}$ where I_P is the polar moment of inertia.

The eigenvalues for various boundary conditions can also be found in Petersen et al. (2018).

For cross sections that are only singly symmetric and not doubly symmetric – i.e. the shear centre and the centre of mass do not coincide – the torsional vibration generates inertia forces that act perpendicular to the axis of symmetry (Petersen et al., 2018, p. 711). Thus a coupled flexural-torsional vibration problem arises for these cross sections. For a detailed treatment of the coupled problem and its solution, reference is made to the works of Senjanović et al. (2007) and Bercin et al. (1997). However, since the solution of the coupled system can be assumed to have the same form as the solution of the uncoupled system (Senjanović et al., 2007), and since no lateral vibrations are considered in the present work, the following discussion focuses exclusively on the mode shapes of pure bending and pure torsional vibrations.

At this point, however, the chosen solutions only illustrate that the frequencies depend on the stiffness, mass and length ratios. The mode shapes remain unchanged. This implies that changes in stiffness, e.g. due to temperature-dependent changes, will affect the frequencies but not the shapes, provided that the change in stiffness itself is homogeneous. This observation suggests that environmental influences have a significant effect on the natural frequencies but less on the mode shapes.

2.5.3 Strain mode shapes

To ensure the serviceability of bridges, the strains that occur under normal operating conditions are small. Therefore the strain field can be described by the linear strain tensor (LURIE et al., 2005). In general, therefore, the strains can be expressed in terms of the displacement field $\mathbf{r}(x,y,z,t)$ as follows:

$$\varepsilon(x,y,z,t) = \frac{1}{2}\left[(\nabla\mathbf{r})^{\mathrm{T}} + \nabla\mathbf{r}\right] \tag{2.19}$$

In this expression, the displacement field can be replaced by the weighted sum of the mode shapes:

$$\varepsilon(x,y,z,t) = \sum_{n=1}^{\infty} \underbrace{\frac{1}{2}\left[(\nabla\phi_n)^{\mathrm{T}} + \nabla\phi_n\right]}_{\equiv\,\phi_{\mathrm{s},n}} q_n(t) \tag{2.20}$$

where $\phi_{\mathrm{s},n}$ is the n-th strain mode. To distinguish between the displacement modes and the strain modes, they will be referred to as $\phi_{\mathrm{s},n}$ and $\phi_{\mathrm{d},n}$ respectively.

For the simple supported single span beam, the strain mode can be easily derived analytically. The bending mode shapes in Equation 2.16 describe the beam deflection in the n-th mode. With the moment curvature relation $w'' = -\frac{M}{EI}$, the formula for normal stresses in the beam $\sigma = \frac{M}{I}z$ and Hook's law $\sigma = E\varepsilon$ [5], the strains of the n-th bending mode are obtained as follows:

$$\varphi_{\mathrm{s},n}(x,z) = \left(\frac{n\pi}{l}\right)^2 \sin\left(n\pi\frac{x}{l}\right) z \tag{2.21}$$

where z is the distance to the neutral axis of the beam.

---

[5] For the derivation of the three formulae and further explanations, see GROSS et al. (2021)

2.5.4 Determination of modal parameters from measurements

Both theoretical and measurement based approaches to modal analysis are used (HE et al., 2001). Estimating modal parameters from measurements primarily employs two techniques: experimental modal analysis (EMA) and operational modal analysis (OMA), which are categorized based on the types of measurements involved. While OMA techniques measure only the output or structural responses, EMA techniques measure or know both the inputs (excitations) and the outputs (vibrations) (ZAHID et al., 2020).

EMA and OMA can be applied in two separate domains: time and frequency. Regardless of the domain difference, the informational availability remains the same. Though debates exist, time and frequency domain identification are theoretically considered equivalent (GATTULLI, 2016). A concise summary of EMA and OMA is available in ZAHID et al. (2020), and a comprehensive review and comparison are presented by REYNDERS (2012).

Artificially exciting civil engineering structures often demands substantial effort, and measuring excitations can pose significant challenges. Owing to these practical constraints, OMA is generally favored for modal analysis of such structures.

SSI, particularly its covariance-driven stochastic subspace identification (SSI-COV) variant, is commonly used within OMA due to its superior estimation accuracy and computational efficiency (ZAHID et al., 2020). Detailed descriptions of the theory, implementation, and applications of this method is given by VAN OVERSCHEE et al. (1996) and ZABEL (2019).

Displacement mode shapes can be determined using displacement, velocity, or acceleration measurements. However, due to their reference-free[6] nature and superior signal-to-noise ratio, acceleration signals are typically used for this purpose.

Strain mode shapes can be identified through strain measurements, yet accurately detecting the extremely small strains (sub-microstrains) that occur during environmental or operational excitation is challenging with current measurement methods. Nevertheless, Anastasopoulos et al. demonstrated the feasibility of identifying strain modes using fibre-optic Bragg grating (FBG) strain sensors (ANASTASOPOULOS et al., 2017).

Temperature variations can influence modal parameters, leading to potential experimental inaccuracies in their estimation from vibration responses. This effect is well-documented for natural frequencies, but not as extensively for mode shapes and modal strains (DE ROECK et al., 2018).

2.6 Structural modification theory

The structural modification theory forms a pivotal element in the theoretical foundation of this thesis. According to this theory, when the mass, stiffness, or damping parameters of a system are altered, the mode shapes of the original system continue to span the response of the modified system. This attribute is particularly crucial for modal expansion techniques, as demonstrated in section 3.1 and subsection 4.1.1. Due to its significance for the present study, this theory will be elaborated upon in the remainder of this section.

---

[6] This means that no additional reference point is required for the measurements, as is the case with displacement measurements.

With the orthonormal conditions (SESTIERI, 2000):

$$\begin{aligned}\mathbf{\Phi}^T\mathbf{M}\mathbf{\Phi} &= \mathbf{I}\\ \mathbf{\Phi}^T\mathbf{C}\mathbf{\Phi} &= \mathbf{\Lambda}\\ \mathbf{\Phi}^T\mathbf{K}\mathbf{\Phi} &= \mathbf{\Xi}\end{aligned} \tag{2.22}$$

Equation 2.13 can be rewritten as:

$$\ddot{\mathbf{q}}+\mathbf{\Lambda}\dot{\mathbf{q}}+\mathbf{\Xi}\mathbf{q} = \mathbf{\Phi}^T\mathbf{f} \tag{2.23}$$

For a NDOF system, as described by Equation 2.10, modifications indicated by $\mathbf{\Delta M}$, $\mathbf{\Delta C}$, and $\mathbf{\Delta K}$ lead to:

$$(\mathbf{M}+\mathbf{\Delta M})\,\ddot{\mathbf{u}}(t)+(\mathbf{C}+\mathbf{\Delta C})\,\dot{\mathbf{u}}(t)+(\mathbf{K}+\mathbf{\Delta K})\,\mathbf{u}(t) = \mathbf{f}(t) \tag{2.24}$$

Modal decorrelation, as shown in Equation 2.12, can be applied to this equation. When premultiplying by $\mathbf{\Phi}^{\mathrm{T}}$, the resulting expression is (SESTIERI, 2000):

$$\left(\mathbf{I}+\mathbf{\Phi}^{\mathrm{T}}\mathbf{\Delta M}\mathbf{\Phi}\right)\ddot{\mathbf{q}}+\left(\mathbf{\Lambda}+\mathbf{\Phi}^{\mathrm{T}}\mathbf{\Delta C}\mathbf{\Phi}\right)\dot{\mathbf{q}}+\left(\mathbf{\Xi}+\mathbf{\Phi}^{\mathrm{T}}\mathbf{\Delta K}\mathbf{\Phi}\right)\mathbf{q} = \mathbf{\Phi}^{\mathrm{T}}\mathbf{f}(t) \tag{2.25}$$

Since the matrices,

$$\begin{aligned}\mathbf{\Delta}\tilde{\mathbf{M}} &= \mathbf{\Phi}^T\mathbf{\Delta M}\mathbf{\Phi}\\ \mathbf{\Delta}\tilde{\mathbf{C}} &= \mathbf{\Phi}^T\mathbf{\Delta C}\mathbf{\Phi}\\ \mathbf{\Delta}\tilde{\mathbf{K}} &= \mathbf{\Phi}^T\mathbf{\Delta K}\mathbf{\Phi}\end{aligned} \tag{2.26}$$

are usually not diagonalised by the modal shapes of the original structure, the equations of motion remain coupled to the modal coordinates of the original structure. The corresponding undamped homogeneous problem can be written as (SESTIERI, 2000):

$$\left(\mathbf{I}+\mathbf{\Delta}\tilde{\mathbf{M}}\right)\ddot{\mathbf{q}}+\left(\mathbf{\Lambda}+\mathbf{\Delta}\tilde{\mathbf{K}}\right)\mathbf{q} = 0 \tag{2.27}$$

and the corresponding eigenvalue problem is (SESTIERI, 2000):

$$\left[\left(\mathbf{\Lambda}+\mathbf{\Delta}\tilde{\mathbf{K}}\right)-\lambda^I\left(\mathbf{I}+\mathbf{\Delta}\tilde{\mathbf{M}}\right)\right]\phi^I = 0 \tag{2.28}$$

The solution yields the new eigenvalues $\mathbf{\Lambda}^I$ and the new mode shapes $\mathbf{\Phi}^I$ that uncouple Equation 2.25. The new mode shapes can be expressed as (SESTIERI, 2000):

$$\tilde{\mathbf{\Phi}} = \mathbf{\Phi}\mathbf{\Phi}^I \tag{2.29}$$

Thus, it is shown that the new mode shapes are a linear combination of the mode shapes of the original system (SESTIERI, 2000).

2.7 Resonance curves and vehicle-bridge interaction

Understanding the principles of structural dynamics is crucial for the design and assessment of railway bridges, as a train crossing a bridge with a specific speed v_{res} can lead to resonant vibrations. These vibrations can affect the bridge's operability and train safety. Therefore, it is essential to anticipate resonant speeds and assess bridge dynamics. The resonance of the train-bridge system depends on numerous factors including the periodic loading and impact on the bridge due to wheel arrangements, track irregularities, and lateral movements caused by forces such as wind and vehicle deflections. These factors are speed-dependent, making their examination crucial in both theoretical and practical contexts (XIA et al., 2018).

The resonance of vertical modes is primarily driven by the regular excitation induced by the train's vertical axle loads. The axle loads may be simplified as resultant forces for two consecutive bogies belonging to two different car bodies as depicted in Figure 2.1.

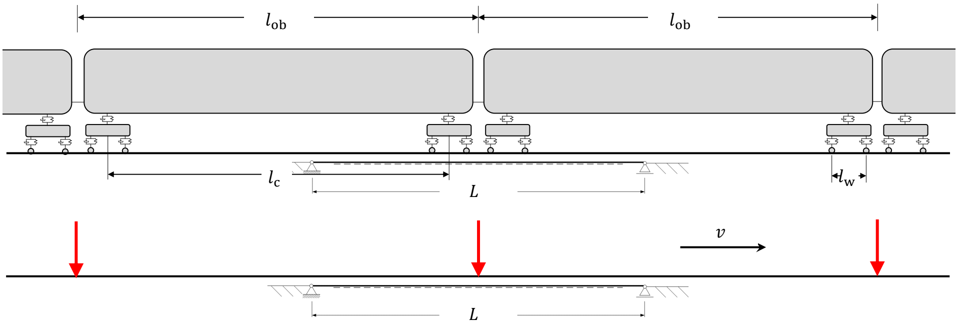

Figure 2.1 Simplified modelling of the excitation by the resultant force of two bogies acting between two car bodies. (XIA et al., 2018, p. 117, 115)

With this simplification of individual loads at a distance of l_{ob}, the resonance speed v_{res} can be determined analytically. For further details, the reader is referred to XIA et al. (2018, p.131). However, the solution is provided here:

$$v_{\text{res}} = \frac{f_n l_{\text{ob}}}{i} \, (i = 1, 2, 3, \ldots) \tag{2.30}$$

While this simplified approach offers a reasonable approximation of the structural dynamic response, it often results in an overestimation. When considering the vehicle-bridge interaction, two main effects are typically observed. First, a reduction in the structural response, which can be considered as additional damping, and second, a decrease in the bridge's resonant speed or frequency due to the additional mass (KOHL et al., 2023). A numerical example from KOHL et al. (2023), simulating an ICE 2 crossing a bridge with a span of $L = 15$ m, illustrating these effects is presented in Figure 2.2[7].

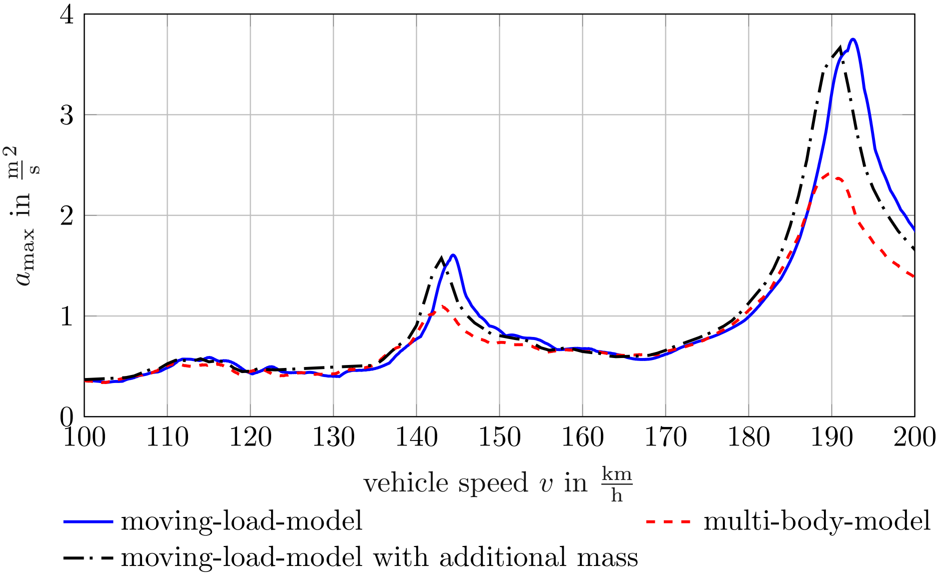

Figure 2.2 Comparison of calculated maximum accelerations at midspan for a moving-load model, a multi-body model, and a moving-load model with additional mass.

Besides resonance conditions, there are also cancellation conditions where the structural response is reduced (XIA et al., 2018, p.132). However, the cancellation effect significantly decreases with increased damping, thereby reducing the impact. It can also occur that resonance and cancellation conditions coincide, resulting in suppressed resonance, a phenomenon referred to as resonance disappearance (XIA et al., 2018).

2.8 Frequency range of bridge vibrations

The outcomes of an analysis of dynamic measurements are influenced by the chosen sampling rate of the signals and the considered frequency range. To maintain a consistent criterion for the choice of the frequency range under examination in this research, the regulation from DIN EN 1990:2021-10 A2.4.4.2.1 (4) (DIN, 2021) has been adopted. According to this regulation, in the event of a need for dynamic calculation to investigate vertical accelerations, all frequencies up to the highest of the following three values must be considered:

---

[7] In the original publication, a different axis section was depicted in the calculations. The author kindly provided the data for this study. The section has been adjusted to match the velocities investigated in this work.

(1) 30 Hz

(2) 1.5 times the frequency of the first eigenmode (fundamental vibration)

(3) the frequency of the third eigenmode

This criterion is applied within this work to determine the highest frequency to be examined.

2.9 Influence of higher eigenmodes

In this section, the increasing significance of higher eigenmodes near the supports is elucidated. For this purpose, the vibrations of a simply supported Euler-Bernoulli beam are examined.

Initially, attention is given to the displacement mode shapes of the beam, as detailed in Equation 2.16, and the strain mode shapes, as specified in Equation 2.21. It can be observed that the first maximum along the length of the n-th mode occurs at $x = \frac{1}{2n}L$. This suggests that as the order n of the modes increases, the first maxima move closer to the edges.

Another factor to consider is that the amplitude of the n-th mode undergoes greater amplification in accelerations compared to strains, as will be subsequently demonstrated. The strains and accelerations of the beam are first formulated in accordance with Equation 2.11, utilising the mode shapes for simply supported beams given in Equation 2.16 and 2.21:

$$\ddot{w}(x,t) = \sum_{n=1}^{\infty} \sin\left(\frac{n\pi}{L}x\right) \ddot{q}_n(t) \tag{2.31}$$

$$\varepsilon(x,z,t) = \sum_{n=1}^{\infty} \left(\frac{n\pi}{L}\right)^2 \sin\left(n\pi\frac{x}{L}\right) z q_n(t) \tag{2.32}$$

For free and undamped vibrations, the generalised coordinate $q(t)$ and its second time derivative can be expressed as follows:

$$q_n(t) = A_n \cos(\omega_n t + \theta) \tag{2.33}$$

$$\ddot{q}_n(t) = -\omega_n^2 A_n \cos(\omega_n t + \theta) \tag{2.34}$$

where A_n is the amplitude of the n-th mode and θ is the phase shift.

By employing Equation 2.15, the frequency of the first eigenmode is related to the fundamental frequency as follows:

$$\omega_n = \omega_1 n^2 \tag{2.35}$$

With this frequency relationship, the accelerations and strains are rendered as:

$$\ddot{w}_n(x,t) = -\omega_1 n^4 \sin\left(\frac{n\pi}{L}x\right) A_n \cos\left(\omega_n t + \theta\right) \tag{2.36}$$

$$\varepsilon_n(x,z,t) = -n^2 \left(\frac{\pi}{L}\right)^2 \sin\left(\frac{n\pi}{L}x\right) z A_n \cos\left(\omega_n t + \theta\right) \tag{2.37}$$

In this depiction, it becomes apparent that the amplitude of the generalised coordinate for accelerations is multiplied by n^4, whereas for strains of the same mode, it is multiplied only by n^2. This simple analysis elucidates why contributions from higher eigenmodes are more pronounced in accelerations than in strains towards the edges.

2.10 The signal of a moving sensor

The primary objective of this section is to illustrate two critical effects that are evident in the response of a moving sensor. For the purposes of this study, the sensor is attached to the axle boxes of a train, as described in the experimental section of this thesis.

The first effect of interest, mainly due to its significant impact on the sensor readings, concerns the measured acceleration resulting from track irregularities. Consider a periodic vertical track irregularity $z_{\text{ti}}(x)$, represented by a sine wave:

$$z_{\text{ti}}(x) = A \sin\left(\frac{\pi}{L_{\text{ti}}}x\right) \tag{2.38}$$

In this equation, A stands for the amplitude of the sine wave, while L_{ti} denotes half the period length of the vertical track irregularity.

Assuming that the sensor is rigidly connected with the track irregularity and travels at a constant speed v in the direction of x, where $x = vt$. Under this assumption, the track irregularities can be parameterised by time t. Applying double differentiation with respect to time to this parameterisation provides the acceleration of the moving sensor due to track irregularities. The following equation represents this:

$$\ddot{z}_{\text{ti}}(x) = -A \left(\frac{\pi}{L_{\text{ti}}}v\right)^2 \sin\left(\frac{\pi}{L_{\text{ti}}}vt\right) \tag{2.39}$$

Equation Equation 2.39 shows that there is a linear relationship between the frequency of acceleration caused by track irregularities and the speed. Additionally, the acceleration's amplitude demonstrates a quadratic relationship with speed increasing with the square of the speed.

The second important effect induced by the movement of the sensor relates to the recorded bridge vibration. Considering a scenario with a simply supported, undamped bridge, where only the free vibration of the first bending mode is active, and a sensor which is moved across the bridge at a constant speed v. Under these assumptions, and given that the initial deflection $w(x,t=0)=0$, the deflection of the bridge can be expressed as a function of position x and time t according to Equation 2.16:

$$w(x,t) = B\sin\left(\omega_\mathrm{b} t\right)\sin\left(\frac{\pi}{L}x\right) \tag{2.40}$$

Where B is the amplitude of the bridge vibration and ω_b is the natural angular frequency of the bridge. Double differentiation with respect to time gives the acceleration:

$$\ddot{w}(x,t) = -B\omega_\mathrm{b}^2\sin\left(\omega_\mathrm{b} t\right)\sin\left(\frac{\pi}{L}x\right) \tag{2.41}$$

It is assumed that there is a rigid connection between the sensor and the bridge. Consequently, the recorded acceleration for each instance is equal to the acceleration of the bridge at the position of the sensor. Considering $x = vt$, the sensor acceleration resulting from the bridge vibration can be represented as $\ddot{z}_\mathrm{b}$:

$$\ddot{z}_\mathrm{b}(t) = -B\omega_\mathrm{b}^2\sin\left(\omega_\mathrm{b} t\right)\sin\left(\frac{\pi}{L}vt\right) \tag{2.42}$$

This expression can be converted to:

$$\ddot{z}_\mathrm{b}(t) = -B\omega_\mathrm{b}^2\frac{1}{2}\left(\cos\left(\omega_\mathrm{b} t - \frac{\pi}{L}vt\right) - \cos\left(\omega_\mathrm{b} t + \frac{\pi}{L}vt\right)\right) \tag{2.43}$$

An important conclusion from this analysis is that the movement of the sensor across the bridge results in the sensor signal being composed of two frequencies. The bridge frequency is shifted by the so-called driving frequency $\omega_\mathrm{d} = \frac{\pi}{L}v$, which is subtracted for the first and added for the second of these frequencies.

3 State of the art

This chapter provides an overview of the current state of the art in virtual sensing and drive-by monitoring for railway bridges. Based on an analysis of previous research, existing gaps in research are identified and highlighted.

3.1 Virtual sensing of railway bridges

As described in the introduction to this thesis, the term virtual sensing (VS) summarises methods utilised for extrapolating measurements from the structure to unmeasured locations (MAES et al., 2021). The term is well-established[1], although the methods are also referred to as response reconstruction, response estimation, and response prediction[2].

Virtual sensors are known to generate signals by analysing the signals produced by physical sensors, in conjunction with a process model (TARPØ et al., 2020; TARPØ et al., 2021) (Figure 3.1).

VS methods can be divided into two categories. One category is based on models and analyses, while the other is based on empirical data. The former is referred to as analytical or model-based, while the latter is referred to as empirical or data-driven (KULLAA, 2019). The terms physics-based and data-centric are also used synonymously (AZAM et al., 2022).

Virtual sensors can either output the same physical quantity as the used physical sensors or estimate a different physical quantity at the same or a different location of the structure. For the process model, either a single physical quantity can be used, or several physical quantities can be combined (SARWAR et al., 2020; GULGEC et al., 2020).

Model-based methods use a structural-dynamic model of the monitored structure, usually a finite element model, to determine quantities of interest from the signals of physical sensors. Data-driven methods require at least a short-term measurement at the location of the virtual sensor and are suitable for replacing temporarily installed or failed sensors. They can also be used for sensor fault detection (KULLAA, 2019). In the case of data-driven methods, the model is generated using measurement data, with methods ranging from SVD (AZAM et al., 2022) to physics-based deep learning applications (YAO et al., 2020).

---

[1] (LIU et al., 2009; KULLAA, 2019; HENKEL et al., 2020; TARPØ et al., 2020; ERCAN et al., 2021; MAES et al., 2021; TARPØ et al., 2021; AZAM et al., 2022)

[2] (PAPADIMITRIOU et al., 2011; MAES et al., 2014; MAES et al., 2016; REN et al., 2017; PENG et al., 2019)

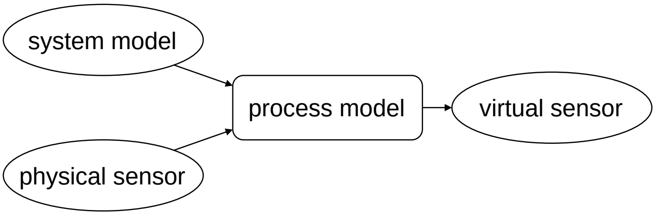

Figure 3.1 Virtual sensing flowchart according to TARPØ et al., 2021

One of the main applications of virtual sensing is the verification of safety against fatigue failure of components. The first work on stress or strain time history estimation began in the 1950s with investigations of analytical relationships between component response and strains in beams and plates (TARPØ et al., 2021). Currently, the most commonly used process models in the literature are the Kalman filter and the modal expansion (ERCAN et al., 2021; TARPØ et al., 2020). In 2005, the modal expansion technique was used to estimate the complete strain field of a laboratory structure and a lattice tower (GRAUGAARD-JENSEN et al., 2005).

In 2011, an adaptive Kalman filter was used for the first time to estimate the full strain field of a structure as part of a numerical simulation (PAPADIMITRIOU et al., 2011).

In 2016, three methods, the Kalman filter algorithm, the joint-input estimation and the modal expansion, were compared for strain estimation on an offshore monopile wind turbine in the Belgian North Sea. The authors of the study concluded that the three methods were comparable and interchangeable for this application (MAES et al., 2016). In another study based on numerical investigations, the authors also concluded that the use of the Kalman filter and modal expansion produce similar strain field estimates (REN et al., 2017).

Other authors have picked up on this and stated that the methods are interchangeable, without specifying the application for which this was concluded (TARPØ et al., 2020; TARPØ et al., 2021). However, this is not generally true, as the use of the Kalman filter typically assumes that external excitations are stationary broadband disturbances. However, this assumption is violated in some applications, in particular in the case of a train passing over a bridge (AZAM et al., 2022).

Since modal expansion makes no assumption about external excitation, it can also be used for train passages. Another aspect that makes modal expansion particularly interesting in the context of railway bridges is the possibility of substructuring (KULLAA, 2016).

Substructuring makes it sufficient to model only parts of the structure. Furthermore this method can be applied to non-linear systems (TARPØ et al., 2021).

A classification of VS methods into load model-based and load model-free methods seems reasonable, as the load makes the difference in applicability. The load model-based methods include all methods where an assumption is made about the type of loading. The load model-free methods, on the other hand, do not require any assumptions about the structure's loading.

So far, there are four studies on VS with measurements on railway bridges, investigating different bridge types (LUNDMAN et al., 2018; MAES et al., 2021; AZAM et al., 2022; FIRUS, 2023). All except AZAM et al. (2022) utilise load model based approches. LUNDMAN et al. (2018) investigated a single span truss bridge with a non ballasted superstructure, having a span of 33 metres. MAES et al. (2021) analysed a steel bowstring bridge with a span of 115 metres and a ballasted superstructure. AZAM et al. (2022) focused on a multi span continuous beam bridge with a span of 22 metres and a non ballasted superstructure. Lastly, FIRUS (2023) carried out an investigation on the Schmutter railway bridge, with the primary objective of reconstructing the axle loads of the train using measured structural responses. This study did not include evaluations on the quality of the reconstructions or on the influence of different trains and speeds.

However, all studies related to railway bridges are lacking long-term investigations that take into account different environmental and operational conditions.

In terms of span length, the majority of railway bridges are relatively short. For instance, 95 % of all railway bridges in Germany have spans of less than 30 metres, according to GEISSLER (2014). Similarly, in China, over 76.6 % of prestressed concrete bridges have spans of 32 metres or less. Additionally, simply-supported beams with small-and-medium spans are about 80 % of all railway bridges in China (XIA et al., 2018). Therefore, there is a lack of research on short span bridges, especially short-span bridges that have a ballasted superstructure. These represent a quasi-standard in the German railway network and exhibit non-linear system behaviour in the form of amplitude-dependent frequencies (subsection 6.2.1 and 7.2.1). The reliable modelling of the the structural and dynamic behaviour is a challenge for such structures.

The research gap therefore lies in the investigation of ballasted short span bridges, in particular the influence of different trains, speeds and environmental conditions on the quality of response estimation. This work aims to help to fill this gap. In the context of this thesis, only load model-free methods will be investigated, in particular modal expansion. Among the existing methods, this is particularly suitable for railway bridges as it does not use a full physical model including all modal parameters, but only the modes of the physical model. Using the example of a simply supported homogeneous Euler-Bernoulli beam, the resulting advantage can be easily illustrated. As discussed in section 2.5, the bending frequency of the beam varies with the mass and stiffness of the beam. However, the bending mode is always a half sine wave. In the case of non-homogeneous changes in stiffness and mass distribution, structural modification theory (section 2.6) can show that the structural responses still lie in the space spanned by the original modes of the system.

3.2 Drive-by monitoring of railway bridges

As introduced before, the term drive-by monitoring (DBM) can be described as a class of structural monitoring methods based on indirect vibration measurements. The term DBM is well established in the literature[3], but the term on-board monitoring (HOELZL et al., 2022) or simply the general term indirect monitoring is also used[4]. The concept of monitoring bridges using sensors on passing vehicles was initially proposed about 20 years ago by YANG et al. (2004) (LI et al., 2014; MALEKJAFARIAN et al., 2014; TAN et al., 2017). The aim was to determine the frequencies of bridges. Since then, the field has evolved from a conceptual level through theoretical work and numerical investigations to attempts at field validation. Although DBM initially aimed only to determine the natural frequency, over time the concept has been extended to include damage detection (MALEKJAFARIAN et al., 2015).

According to YANG et al. (2018), as well as MALEKJAFARIAN et al. (2022), the research field of DBM can be divided into two main categories: modal identification of bridges and condition monitoring of bridges. The modal identification of the bridge essentially aims to determine the modal parameters, i.e. natural frequencies, damping ratios and mode shapes of the bridge structure. The methods of the second category aim to evaluate the condition of the bridge based on measurements on the vehicle, e.g. measurements of the acceleration at the axles. A distinction is made between modal-based and non-modal-based approaches. The modal-based approaches provide a link between the two categories of DBM. In addition, MALEKJAFARIAN et al. (2022) divide the literature of both categories into theoretical, numerical and experimental studies, and whether the method uses single or multiple crossings.

It is not the intention here to summarise all areas of DBM, but to focus on the original task of frequency identification and its development with special consideration of railway bridges. For summaries of the whole field, the reader is referred to the reviews (MALEKJAFARIAN et al., 2015; YANG et al., 2018; MALEKJAFARIAN et al., 2022).

In addition to proposing the concept, YANG et al. (2004) demonstrated the fundamental feasibility of extracting bridge frequencies from vehicle measurements at a numerical level. They simulated crossings with a sprung mass crossing an undamped, simply supported Euler-Bernoulli beam at a constant speed. Only the first eigenmode of the beam was considered. Road roughness and track irregularities were not taken into account. The frequency was determined in the frequency domain using FFT.

---

[3] (OBRIEN et al., 2014; TAN et al., 2017; MATSUOKA et al., 2021; MATSUOKA et al., 2023)

[4] (ZHU et al., 2014; MALEKJAFARIAN et al., 2022; MALEKJAFARIAN et al., 2015; REITERER et al., 2022; ZHAN et al., 2021a)

One year later, LIN et al. (2005) provided the first experimental proof on a real bridge. The bridge was a prestressed concrete bridge with 6 spans of 30 m each. The test vehicle consisted of a light towing vehicle with two axles and a trailer with one axle. The measurement was carried out on the trailer axle. The authors concluded that in order to determine the bridge frequency, the dynamic characteristics of the test vehicle should be determined a priori and the speed should be reduced in poor road conditions. In addition, improvements should be made to the FFT resolution and measurement accuracy.

SIRINGORINGO et al. (2012) were the first to publish a successful experimental demonstration of the extraction of bridge frequency from a two-axle vehicle. A single span, simply supported steel box girder bridge with a span of 59 m was investigated. The deck consisted of a newly constructed steel concrete deck with a smooth surface. The authors showed that with previously known vehicle frequencies, the bridge frequencies could be extracted from the frequency spectrum at moderate speeds up to 30 km/h with a maximum error of 11.4 %.

In a review of frequency identification, MALEKJAFARIAN et al. (2015) concluded that the feasibility of extracting bridge frequencies from the response of a passing vehicle was well established through theoretical and experimental investigations. However, there were still challenges to overcome before the approach became reliable and effective. The main problems identified were the influence of the road profile on the vehicle response and the variation of the bridge frequency during vehicle induced vibrations. To successfully extract the bridge frequencies, speeds driven should be below 40 km/h and at least three bridge crossings at different speeds should be measured. Furthermore, the dynamic properties of the test vehicle or trailer should be either determined or calibrated in advance.

An approach to avoid the difficulties caused by vehicle vibrations has been proposed by YANG et al. (2017). Here, the response at the contact point is used to identify the modal parameters instead of the vehicle vibrations. The authors were able to show that the contact response is free of vehicle frequencies, which are particularly problematic on rough roads. In the study, YANG et al. (2017) also showed that the contact responses for the sprung mass can be calculated from the mass vibrations. Based on this, more recent studies have used the residuals of the contact point responses, i.e. the signal from one axle is subtracted from the subsequent axles (ZHAN et al., 2021a; ZHAN et al., 2021b; YANG et al., 2022), to minimise the influence of roughness.

The practical application of DBM is particularly problematic for system identification, as a large proportion of bridges have short spans. System identification based on vehicle measurements presents challenges for several reasons. Firstly, short bridges have a brief contact time with the vehicle. Secondly, these short bridges also have a high ratio of vehicle mass to bridge mass, especially when compared to longer bridges (YANG et al., 2018). Although it is known that frequency analysis using fast Fourier transform (FFT) leads to poor frequency resolution at short contact times (TAN et al., 2017), most frequency identification methods still use FFT (MALEKJAFARIAN et al., 2022).

As an alternative to FFT, existing OMA techniques can be used to determine bridge frequencies using DBM. This is the case even if the recording lengths recommended in the OMA literature cannot be achieved at normal traffic speeds (LOCKE et al., 2022). Thus, Yang et al. have adapted the SSI to account for the time-varying system caused by the vehicle-structure interaction (YANG et al., 2016). In a numerical study on a simply supported single span Euler-Bernoulli beam with a length of 30 m, Yang et al. were only able to identify the frequencies up to a speed of 2 m/s (7.2 km/h). At a speed of 4 m/s (14.4 km/h), identification was no longer possible. This is a very long contact time for railway traffic. Therefore, this method cannot be used during operation without affecting it.

The effect of the added mass of the vehicle during the crossing is particularly significant for short span bridges, therefore LOCKE et al. (2022) used a relatively light vehicle to evaluate the applicability of OMA techniques on a road bridge. The bridge consisted of four spans, each with a span of 9.14 m. They drove at a speed of almost 50 km/h (about 13.9 m/s). The authors concluded that the frequencies of the bridge can be determined using OMA techniques even for short span bridges, but it is important to use multiple crossings and it is beneficial to know the dynamic characteristics of the test vehicle. In addition, several OMA techniques should be combined to distinguish the physical modes from the spurious modes (LOCKE et al., 2022). The applicability of OMA techniques in the context of railway bridges is further limited by an additional time invariance in the form of sometimes strongly pronounced amplitude-dependent frequencies of the structures (subsection 6.2.1 and 7.2.1).

Much of the work in the field of DBM, especially the experimental work, is focused on road bridges. The larger spans of road bridges likely explain this trend. Specifically, the majority of road bridges in Germany have spans exceeding 30 m, whereas most railway bridges in Germany have spans less than 30 m (GEISSLER, 2014).

There is a lack of work that is explicitly related to railway bridges. Although DBM was initially introduced in 2004, it was not until 2021 that YANG et al. (2021) theoretically demonstrated its feasibility for railway bridges.

ZHAN et al. (2021) have extended the concept of DBM to bridges with high-speed trains (MALEKJAFARIAN et al., 2022). For this, the different signals from the preceding vehicles are combined to perform frequency identification using FFT. However, with this proposed method, the number of axles to be instrumented increases as the contact time decreases. Depending on the technology required, especially if it is to be wired, its use on existing trains is likely to be difficult due to the lack of space if they are to be used regularly. The proposed method has been treated analytically with single sprung masses crossing a simply supported single span Euler-Bernoulli beam at constant speed. The authors have numerically validated the method by modelling the train as a multi-degree-of-freedom system, with each car having ten degrees of freedom, but there is no experimental evidence to date.

In early 2023, ERDURAN et al. (2023) published a method for identifying bridge frequencies based on vibrations recorded by train-mounted sensors. The method uses a combination of FFT and continuous wavelet transform (CWT) to identify bridge frequencies. The method is validated with numerical simulations on a single span bridge with a span of 32.4 m. Within the simulation, frequencies could be identified for speeds up to 90 km/h (25 m/s) (ERDURAN et al., 2023).

There is a consensus in the literature that there is still an unmet need for field experiments to validate the methods[5]. Despite numerous theoretical and numerical investigations, there is a very limited number of experiments on DBM that have been performed on real structures (LOCKE et al., 2022; MALEKJAFARIAN et al., 2022). There are almost no field tests or full scale experiments of DBM for railway bridges (MATSUOKA et al., 2021). The few studies with field tests that exist are briefly reviewed here.

TSAI et al. (2015) published a study in 2014 in which they performed two vertical acceleration measurements on the axles of a train in Taiwan. The instrumented train crossed a three-span prestressed concrete bridge at 78.5 km/h (21.8 m/s), with each span 35 m long. They used a Hilbert–Huang transform (HHT)-based approach to analyse the signals, and the authors concluded that the vibration responses of the bridge, or their frequencies, would not be clearly identifiable unless a sophisticated method is used.

MATSUOKA et al. (2021) published a method for identifying resonant bridges. The method uses a vehicle equipped with a track irregularity measurement system, at the first and last bogie of the train. By comparing the two measurements it is then possible to identify vibrating bridges with spans between 20 m and 60 m. The authors validated the method on the Japanese high-speed network at speeds between 230 and 250 km/h (63.9 m/s - 69.4 m/s) in the target areas, and more than ten bridges were identified as vibrating on a route of approximately 250 km with 875 bridges. In the conclusion of the study, the authors emphasise that only ballastless tracks are available in Japan and that further investigations would be necessary to reliably apply the methodology to ballasted tracks.

REITERER et al. (2022) published a study that examined simultaneous measurements on a railway bridge and a train equipped with acceleration sensors. The aim of the study was to determine the fundamental frequency of the bridge using the signals from the sensors on the train. The bridge had a span of 33.3 m. The resonant frequency of the bridge was found to be 4.52 Hz using shakers. The authors show in the study the signals of the accelerations at the second bogie during the crossing at a speed of 135 km/h (37.5 m/s). This results in a contact time of about 0.89 s and thus a frequency resolution of the FFT of about 1.13 Hz. However, the signal shown is 3 s long. From a peak in the signal at 4.4 Hz, which is not the dominant peak, the authors conclude that the frequency was identified in good agreement with the measurements on the bridge using shaker excitation. However, no reference is made to the problematic resolution of the frequency range, although the authors address this as a known problem in the introduction to the paper. Overall, there is no convincing evidence that frequency identification using DBM is possible under practical operating conditions.

---

[5] (YANG et al., 2018; YANG et al., 2020; LOCKE et al., 2022; MALEKJAFARIAN et al., 2022)

LORENZEN et al. (2022) published an approach in which a neural network was trained using simulation data to identify the first eigenfrequency of the bridge from the contact signals of the acceleration sensors at the axle boxes. Transfer learning was used to adapt the trained network for use with real measurement data. For this purpose, data from a measurement campaign were used, featuring synchronous measurements on a bridge with a span of 19.5 m and an ICE 4 equipped with acceleration sensors. The dataset includes 52 recordings of crossings at speeds ranging from 10 to 200 km/h. In the course of this study it was shown that a resonance curve can be constructed from the sensor signals, from which the resonance frequency can then be calculated. The resonance curve approach based on the bridge sensors yielded a resonance frequency of 4.95 Hz, while the resonance curves produced by the train sensors yielded values between 4.99 Hz and 5.11 Hz, depending on the sensor. This study therefore provides the first evidence that the bridge frequency can be measured on the train under real operating conditions. The use of resonance curves is a practical approach that avoids the problems of frequency resolution in signal processing, as in the FFT, and allows the identification of the bridge frequency even with very short contact times.

Shortly afterwards, a study was published by MALEKJAFARIAN et al. (2022) on the identification of the frequencies of a multi span bridge using DBM. In the study, a 175 m long viaduct was crossed 41 times at speeds between 85 and 120 km/h (23.6-33.3 m/s). The first two of a total of twelve spans are 12.2 m long at each end, all other spans are 15.85 m long. The Ensemble Empirical Mode Decomposition (EEMD) method was used for frequency identification, in which the signals are decomposed into several intrinsic modes. The instantaneous frequencies can be determined from these modes. Since only one frequency is available for each span, the instantaneous frequency is averaged over the entire span length. The authors conclude that it is necessary to know a priori a range in which the bridge frequencies lie in order to apply the method. For the case studied, the method gives reasonable results, although the results are significantly worse for the shorter spans. However, no quantification of the accuracy is performed, so the assessment of the accuracy is limited. However, given the similar trend in directly and indirectly determined frequencies across the different spans, the study demonstrates that at least the relative frequency variations between individual spans of a multi span bridge can be identified.

The most recent field tests have been carried out by MATSUOKA et al. (2023) [6]. In this publication they proposed a DBM method for estimating the deflection of simply supported single span beam bridges. The track irregularity measurements of the first and last vehicles are compared. The method has been validated on six bridges with spans between 21 m and 58.2 m. The method is designed for quasi-static deformations, so slow speeds are required for application. The authors were able to show that up to about 100 km/h (27.8 m/s) the deflection can be determined with an error of less than 10 % compared to ground measurements. Like MATSUOKA et al. (2021), the authors point out that all the bridges had a ballastless track. Investigations are therefore required to assess whether the method can be applied to ballasted tracks and which adjustments may be required.

---

[6] As of April 2023

In summary, there is a need for a suitable methodology for the frequency identification of railway bridges using DBM. The method should also be applicable at regular operating speeds and the associated short contact times. In addition, it should not be necessary to determine the dynamic characteristics of the vehicle in order to apply the method, as this would be very costly. Due to the small number of field tests, there is a great need for further field tests to validate the methods of DBM. In addition to the great benefit for model calibration, the determined resonance frequency can be used to avoid resonance crossings. The impact on rail operations would be minimal, as a few km/h more or less have a large effect on the dynamic amplification of structural responses. This could have a significant impact on the extension of the service life of bridge structures.

4 Methodology

This chapter describes the methodology used in the experimental investigations of this thesis. The chapter is divided into two subsections, the first of which describes the methodology of the virtual sensing investigations. The second subsection is dedicated to the drive by monitoring methodology.

4.1 Virtual sensing

As described in section 3.1, modal expansion is particularly suitable for implementing virtual sensing on railway bridges. This section describes the methodology and explains how to extrapolate measured structural responses to unmeasured locations.

4.1.1 Modal expansion

As outlined in section 2.5, modal decorrelation is commonly used to create a reduced order model with fewer degrees of freedom. This technique also establishes a mathematical link between the retained and omitted degrees of freedom in relation to the original FE model (KAMMER, 1987). The validity of these relations primarily refers to linear time-invariant systems. However, as shown in section 2.6, the structural response of a system where the masses, stiffnesses or damping are changed lies in the space spanned by the modes of the original system. In a laboratory experiment, TARPØ et al. (2021) have shown that, at least for subsystems of a mechanically non-linear system, virtual sensing can be achieved with the linear mode shapes of the structure. Since the strains and displacements in the bridge structure during operation are small, the structural response can be well approximated even if the overall mechanical system behaviour of the bridge, track, and vehicle is time-varying or non-linear.

Besides the expansion of the eigenmodes of the structure, it is possible to use the POD modes presented in section 2.2 for expansion. In the following, a unified description is given for the expansion of the eigenmodes and the POD modes.

The structural response of a NDOF is expressed through modal decorrelation, as shown in Equation 2.13:

$$\mathbf{Y} = \begin{Bmatrix} \mathbf{y}_{\mathrm{m}} \\ \mathbf{y}_{\mathrm{u}} \end{Bmatrix} = \mathbf{\Theta}\mathbf{q} = \begin{bmatrix} \mathbf{\Theta}_{\mathrm{m}} \\ \mathbf{\Theta}_{\mathrm{u}} \end{bmatrix} \mathbf{q} \tag{4.1}$$

Using this, the quantities of interest at unmeasured locations, or the readings from virtual sensors, can be deduced as:

$$\hat{\mathbf{Y}} = \begin{Bmatrix} \hat{\mathbf{y}}_{\mathrm{m}} \\ \hat{\mathbf{y}}_{\mathrm{u}} \end{Bmatrix} = \mathbf{\Theta}\hat{\mathbf{q}} = \mathbf{\Theta}\mathbf{\Theta}_{\mathrm{m}}^{+}\mathbf{y}_{\mathrm{m}} \tag{4.2}$$

To clarify the terms used:

- $\mathbf{Y} \in \mathbb{R}^{N \times t}$: The response matrix. It stores quantities of interest for all N degrees of freedom from either the FE model or the POD modes, which are sourced from short-time measurements. t is the total number of samples.
- Splitting the structural response:
  - $\mathbf{y}_{\mathrm{m}} \in \mathbb{R}^{a \times t}$: Represents the measured degrees of freedom.
  - $\mathbf{y}_{\mathrm{u}} \in \mathbb{R}^{(N-a) \times t}$: Represents the unmeasured degrees of freedom. Here, a denotes sensor channels or measurements per time step.
- $\mathbf{\Theta} \in \mathbb{R}^{N \times n_{\mathrm{m}}}$: This matrix encompasses the modes. n_{m} signifies the considered number of modes.
  - $\mathbf{\Theta}_{\mathrm{m}} \in \mathbb{R}^{a \times n_{\mathrm{m}}}$: The measured degrees of freedom.
  - $\mathbf{\Theta}_{\mathrm{u}} \in \mathbb{R}^{(N-a) \times n_{\mathrm{m}}}$: The unmeasured degrees of freedom.
- $\mathbf{q} \in \mathbb{R}^{n_{\mathrm{m}} \times t}$: Weights for approximating the structural response.
- $\hat{\mathbf{Y}}$: An approximation of the responses. It's based on the least squares estimation of the weights $\hat{\mathbf{q}}$. Within this, $\mathbf{\Theta}_{\mathrm{m}}^{+}$ represents the Moore-Penrose pseudoinverse of $\mathbf{\Theta}_{\mathrm{m}}$.

To obtain meaningful outcomes and to circumvent overfitting, an overdetermined system of equations should be formulated. For this to be true, the number of physical sensors must exceed the number of modes considered.

4.1.2 Selection of modes and signal processing

As discussed in section 2.8, measurements of structural responses depend on the sampling rate and, more importantly, the considered frequency range. Therefore, the regulation according to DIN EN 1990:2021-10 A2.4.4.2.1 (4) (DIN, 2021) is applied in this study. For all structures investigated, it follows that all structural frequencies up to 30 Hz must be considered.

In addition to the number of considered modes, the question of which modes should be considered is also important. In this study, only vertical vibrations of bridges are analysed, so it is reasonable to assemble the set of modes from bending and torsion modes. For modal expansion, it is particularly important to use global modes, i.e., not those where only small parts or sections of the structure vibrate[1]. For this purpose, a metric has been proposed in (JUNG et al., 2015) that allows classification into local and global modes.

However, applying this metric, all global modes are kept, not just the vertical ones. Therefore, the calculated modes were examined, and the selection of bending and torsion modes was made manually through visualization in the software. The set of bending and torsion modes up to 30 Hz then formed the modal matrix for the investigations on modal expansion.

For signal preprocessing all signals were down-sampled to 120 Hz and a 4th order Butterworth low-pass filter with a cut-off frequency at 30 Hz was applied. In addition, the offset of the signals has been removed where present.

The processed signals were used to determine the POD modes according to the description in section 2.2. Since these modes are already sorted by their contributions to the overall signal, searching for combinations is unnecessary; logically, all modes are used from the first to the number of considered modes n_{m}, as omitting any would worsen the results.

For FE modes, however, there are better and worse combinations. In this thesis, the modes were chosen from the set of bending and torsion modes without omission. That is, the first n_{m} modes of the mode set were always chosen. This approach was taken to limit the number of combinations investigated.

4.1.3 Sensor placement

In the context of virtual sensing, a natural question arises regarding where the physical sensors should be placed to enable the optimal reconstruction of structural responses at unmeasured points. While this question is beyond the scope of this thesis, a recent methodology for optimal sensor placement in modal expansion has been made available (ERCAN et al., 2021). A general review of sensor placement strategies, particularly relevant to structural health monitoring, can be found in (BARTHORPE et al., 2020). When a large number of sensors are involved, complex optimisation problems arise for which sophisticated strategies are required to approximate optimal setups.

The experiments in this work were not conducted solely for the purpose of validating virtual sensing, so no optimisation was undertaken to meet the requirements of virtual sensing. In the experiment detailed in chapter 7, used for long-term validation of virtual sensing, behaviour of the measurement points had to be operationally adapted on-site due to the limited accessibility of the structure (no lifting platforms or scaffolding were available).

However, in the context of this work, the performance of different sensor setups selected from the available instrumentation is investigated within the framework of a leave-p-out validation.

---

[1] If the virtual sensing is to be done in a local area and not globally, the use of local modes can of course be useful.

4.1.4 Leave-p-out validation and coefficient of determination

To investigate the quality of the virtual sensor signals, leave-p-out validations are performed with the given sensor setups. This means that from a total set of a sensors, k sensors are chosen as physical sensors for the reconstruction of the structural response. The remaining $a-k=p$ sensors can then be used to assess the quality of the reconstruction. For this purpose, all p sensors are considered as a virtual sensor and compared with the actual measurement.

The individual signals from the bridge oscillations also pass through zero, making percentage error inappropriate. The coefficient of determination, R^2, is a commonly used metric for model validation. or the purposes of this study, it has the advantage of taking into account both amplitude discrepancies and the overall magnitude of the reference signal. It can be determined as follows (TARPØ et al., 2020):

$$R^2 = 1 - \frac{\mathrm{E}\left[(\mathbf{y}_i - \hat{\mathbf{y}}_i)^2\right]}{\mathrm{Var}\left(\mathbf{y}_i\right)} \tag{4.3}$$

where:

- $\mathbf{y}_i \in \mathbb{R}^t$ represents the signal from the i-th sensor,
- $\hat{\mathbf{y}}_i$ is its estimation,
- and $R^2 \in [-\infty, 1]$.

To elaborate further on this metric: An R^2 of 1 indicates the model perfectly explains the variability of the dependent variable; an R^2 of 0 means it explains none of the variability, and a negative R^2 suggests the model performs worse than just predicting the mean.

The selection of the k sensors leads to $c = \binom{a}{k}$ combinations. For all of these c possible combinations, the coefficient of determination R^2 is determined for each $n_\mathrm{m} \in [2, k-1] \cap \mathbb{N}$.

For the evaluation of a large number of passages and their joint analysis, the coefficients of determination are arranged in a five-dimensional array $\mathbf{R}_{m,i,j,r,s}$ derived from each sensor and all sensor combinations that result from $k \in \mathbb{N} \cap [2, a-1]$ physical sensors and $n_\mathrm{m} \in \mathbb{N} \cap [1, k-1]$ considered modes. In this array:

- m is the index of the number of considered modes,
- i is the index of the sensor adopted as a virtual sensor (from the p left out),
- j is the index of the sensor combination,
- r is the index of the passage, and
- s is the number of physical sensors utilised to fit the model.

The selection of the k sensors results in $c = \binom{a}{k}$ combinations. Consequently, the number of combinations increases rapidly with the number of sensors, becoming impractical to examine. For instance, in the experiment conducted at the Garther Bach bridge detailed in chapter 7 with nine sensors, there are a total of 510 combinations; in the experiment conducted at the HUMVIB described in chapter 5 with twelve sensors, there are a total of 4094 combinations; and in the experiment conducted at the Schmutter bridge as outlined in chapter 6 with 37 sensors, there are 1.3744×10^{11} (137.44 trillion) combinations. Due to the vast number of combinations, only the possible combinations for the first two experiments have been examined. For the last-mentioned experiment, only a leave-one-out validation was conducted.

The array $\mathbf{R}_{m,i,j,r,s}$ cannot be fully populated as not all combinations are possible. Therefore, the array $\mathbf{R}$ is initially filled with entries of NaN (not a number). This must be taken into account during evaluations, such as when calculating a mean value.

Thus, calculation of the mean value for e.g. all crossings is defined as follows:

$$\bar{\mathbf{R}}_{m,i,j,s} = \frac{1}{\#(\mathbf{R}_{m,i,j,r,s} \neq \mathrm{NaN})} \sum_{r=1}^{P} \mathbf{R}_{m,i,j,r,s} \cdot \mathbb{I}(\mathbf{R}_{m,i,j,r,s} \neq \mathrm{NaN}) \tag{4.4}$$

In this equation:

- $\bar{\mathbf{R}}_{m,i,j,s}$ is the mean value of the coefficient of determination for a given set of sensor combinations, modes, and physical sensors, averaged over all passages.

- $\#(\mathbf{R}_{m,i,j,r,s} \neq \mathrm{NaN})$ denotes the count of non-NaN entries of the array $\mathbf{R}_{m,i,j,r,s}$ over all passages.

- $\mathbb{I}(\mathbf{R}_{m,i,j,r,s} \neq \mathrm{NaN})$ is the indicator function, which is equal to 1 if the entry is not NaN, and 0 otherwise.

- P represents the total number of passages.

The sum is calculated over all passages, but only non-NaN entries are included, as indicated by the indicator function. The mean value $\bar{R}_{m,i,j,s}$ is computed by dividing the sum by the count of non-NaN entries.

The array $\bar{\mathbf{R}}_{m,i,j,s}$ can be used, for example, to determine the best and the worst sensor combination with respect to all passages for all numbers of considered modes n_m and all given numbers of physical sensors k.

To find the minimum and maximum values of R^2 along the combination dimension in the array $\bar{R}_{m,i,j,s}$, the following operations can be applied:

The minimum value of R^2 for a given of combination mode, virtual sensor, and physical sensor set, averaged over all passages, is given by:

$$\min_j \bar{\mathbf{R}}_{m,i,j,s} = \min_{\substack{j=1 \\ \bar{\mathbf{R}}_{m,i,j,s} \neq \mathrm{NaN}}}^{C} \bar{\mathbf{R}}_{m,i,j,s} \tag{4.5}$$

Similarly, the maximum value of R^2 among the non-NaN entries is given by:

$$\max_j \bar{\mathbf{R}}_{m,i,j,s} = \max_{\substack{j=1 \\ \bar{\mathbf{R}}_{m,i,j,s} \neq \mathrm{NaN}}}^{C} \bar{\mathbf{R}}_{m,i,j,s} \tag{4.6}$$

In these equations:

- C represents the total number of combinations (index j).
- The subscript in the min and max functions indicates that only non-NaN entries of the array $\bar{\mathbf{R}}_{m,i,j,s}$ are considered in finding the minimum and maximum values.
- $\min_j \bar{\mathbf{R}}_{m,i,j,s}$ are the minimum values of the coefficient of determination among all non-NaN combinations for a given mode, virtual sensor, and physical sensor set.
- $\max_j \bar{\mathbf{R}}_{m,i,j,s}$ are the maximum values of the coefficient of determination among all non-NaN combinations for a given mode, virtual sensor, and physical sensor set.

4.2 Resonance curves based drive-by monitoring

One of the objectives of this work is to develop and experimentally validate a methodology for the resonance frequency identification of railway bridges under normal operating conditions with regularly scheduled trains. To this end, a methodology has been developed with a new approach based on resonance curves[2]. Acceleration measurements at the axle boxes of the train are used to record the maximum accelerations for different crossing speeds. The measured accelerations is expected to increase with increasing bridge acceleration so that a resonance curve can be generated from these signals. Rupp et al. introduced the terms direct resonance curve and indirect resonance curve to distinguish them from resonance curves generated by sensors on the bridge structure (RUPP et al., 2023).

---

[2] see section 2.7

4.2.1 Frequency identification

This subsection elaborates on the methodology of bridge frequency identification proposed in this research. The process of frequency identification, particularly through DBM in the context of railway bridges, presents a significant challenge, as previously mentioned in section 3.2. This challenge arises from the limited contact time between the train and the short-span bridges, particularly at high speeds typical of regular train schedules. This short contact time often leads to inadequate frequency resolution. To address this problem, the proposed methodology leverages the use of resonance curves.

In the context of beam-like, single span bridges, it is generally assumed that the structural response of the bridge measured at the train is dominated by the first bending mode (PETERSEN et al., 2018, p.1193).

For the resonance condition (Equation 2.30), the variable i is considered to take values between 1 and 4 (REITERER et al., 2021). With a well-determined resonance curve that exhibits at least two peaks, the resonance frequency can be determined.

Therefore, a set of ratios needs to be defined as the set of all possible resonance speeds resulting from the given values of i:

$$R = \left\{ r_{ij} = \frac{i}{j} : i, j \in \{1,2,3,4\}, i \neq j, i < j \right\} \tag{4.7}$$

Additionally the actual ratio of measured resonance speeds is calculated:

$$V = \frac{v_{\text{res},1}}{v_{\text{res},2}}, \quad \text{where} \quad v_{\text{res},1} < v_{\text{res},2} \tag{4.8}$$

Based on this, find the pair (i, j) that best matches the measured speed ratio V, i.e. minimises the absolute difference between V and the elements in R:

$$(\hat{\imath}, \hat{\jmath}) = \arg\min_{r_{ij} \in R} \left| V - r_{ij} \right| \tag{4.9}$$

It should be noted that an issue arises due to the equality of ratios, when $i = 1$ and $j = 2$ as well as when $i = 2$ and $j = 4$. As a consequence of this equality, these two cases become indistinguishable. To resolve this ambiguity and to unambiguously determine the frequency without resorting to estimation, identification of another peak on the resonance curve is imperative.

With these known values for i and the corresponding resonance speed, the resonance condition (Equation 2.30) to determine the resonance frequency can be rearranged as follows:

$$f = \frac{v_{\text{res}} i}{l_{\text{ob}}} \tag{4.10}$$

Here, only one peak needs to be determined with relative precision to allow accurate identification of the frequency. The approximate position of the peak can be used to determine the values $(\hat{\imath}, \hat{\jmath})$.

If only one resonance speed has been determined or a second cannot be detected, the determination of the frequency is possible, provided that the frequency range can be sufficiently limited so that the choice of i for the speed is unique.

It should be noted that the methodology assumes a constant speed for the train passing over the bridge. This assumption is justified because the potential variations in speed are limited. Furthermore, the sections of the signal relevant to the analysis of the bridge are relatively short. Therefore, except in extreme cases, this assumption should be considered well justified.

4.2.2 Data acquisition and processing

Data collection

Since the resonance curves represent the maximum structural responses as a function of speed, several runs are required. Two cases have to be distinguished in the data collection for the proposed method: In the first case, measurements are made in the context of a measurement campaign, where a train is not used in regular operation, but separately. This means that the speeds are travelled can be explicitly specified, but the number of runs must be kept to a minimum for economic reasons. For this purpose, Rupp et al. have published a methodology to find the resonance peaks with a minimum number of passages (RUPP et al., 2023). The second case is to collect data on regular scheduled trains over a longer period of time. In this case it is not necessary to specify the speeds explicitly. The speeds are not evenly distributed, but after some time of operation the speed band is sufficiently densely sampled[3].

Signal filtering

In the context of this work, it is assumed that the fundamental frequency of the bridge can be estimated a priori. This can be well justified as there are studies on the fundamental frequency of bridges depending on the type of construction and span, which allow a good estimation (KARIMI et al., 2022). This is necessary in order to set the filter to only consider the frequency range of the signal that includes the bridge vibration, so a reasonable guess is required. However, it is plausible that an algorithmic approach with varying filter settings could overcome this problem, but this is beyond the scope of this work.

In the proposed method, the signal needs to be filtered with a low-pass filter based on the estimated fundamental frequency[4]. To ensure that the signal from the bridge remains contained, the cut-off frequency F_c should be chosen at a distance from the estimated fundamental frequency $\hat{f}_0$.

---

[3] This can also be observed in the long-term evaluation of measurements on the Garther Bach railway bridge, as shown in Figure 7.17 and 7.18.

[4] A band-pass filter would also be applicable, but the application of low-pass filters was sufficient within the scope of this work.

In the context of DBM, it can be advantageous to transform acceleration signals recorded in the time domain into the spatial domain using the simultaneously recorded positions. As the signal no longer exists in the time domain, the filtering limit is now denoted by the wavenumber f_L. The relationships between frequency f, wavenumber f_L and wavelength L_w are as follows (LUBER, 2011):

$$\begin{aligned} f &= f_L v \\ f_L &= \frac{1}{L} \end{aligned} \tag{4.11}$$

To overcome the problems of the edge effect[5] in filtering, a longer sequence is filtered. This puts the edges further out and allows them to be removed without affecting the relevant signal.

Elimination of the effects of track irregularities and speed

The influence of track irregularities and the driven speed described in section 2.10 leads to well known problems for the DBM as described in section 3.2. As also described in section 3.2, a common approach to counter this is to use residual signals, i.e. the signal of one sensor is subtracted from the signals of the following axles. Ideally, the first axle is available for this purpose, as the vibrations of the bridge are expected to be very low for this axle and thus track irregularities have the greatest influence on the acceleration signals.

---

[5] Explanations of the well known effect can be found in (ALESSIO, 2016).

5 Footbridge HUMVIB

In this chapter, experimental investigations conducted on the HUMVIB bridge are presented. This footbridge, constructed by the Institute of Mechanics and Design (ISM+D) at TU Darmstadt, Campus Lichtwiese, serves as a platform for the study of human-structure interaction. The HUMVIB Bridge (Figure 5.1) was used in a single-span configuration with a span of 13.24 m. The bridge is composed of two parallel arranged HEB 240 steel beams set at a distance of 1.80 m, which are supported at their ends on load cells supplied by Induk GmbH, Model UC 350 (Figure 5.1b and 5.1c).

On these steel beams, 13 reinforced concrete slabs (250/100/12 cm) were laid on an elastomer interlayer. A rough distance of 2 cm between the slabs was maintained. By this construction, it is ensured that the load distribution in the longitudinal direction of the bridge is carried out via the steel beams. A relatively simple model formulation was facilitated by this design, in contrast to the more complex models required for the railway bridge Schmutter in chapter 6 and the railway bridge Garather Bach in chapter 7.

The ease of accessibility and straightforward model formulation were considered decisive for the initial experiments related to virtual sensing to be conducted on this bridge, despite the fact that it is not a railway bridge.

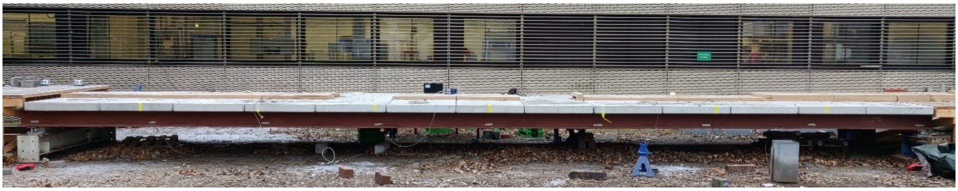

(a) side view

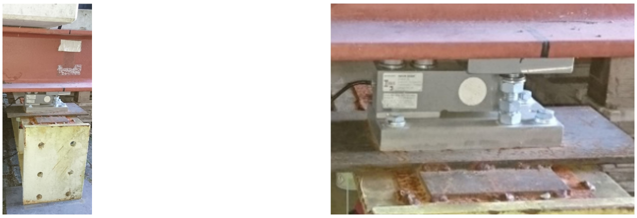

(b) detail support

(c) close-up load cell

Figure 5.1 HUMVIB footbridge (Photos: Maximilian Rupp)

5.1 Experimental set-up and execution

On the 22nd of January 2019, measurements were carried out on the HUMVIB Bridge, with an external temperature of approximately 0 °C (RUPP, 2019). Each main girder was equipped with six measurement points, at which the vertical accelerations and strains in the longitudinal direction of the beams were recorded. The instrumentation was chosen to primarily capture the vertical vibrations, that is, vertical bending and torsion. Considering lateral vibrations would have required additional channels and sensors that were not available. However, lateral vibrations were of minor importance given the load applied in the study, justifying their omission.

PCB 393 B04 sensors (PCB Synotech GmbH, 41836 Hückelhoven, Germany) were employed as acceleration sensors. The strain gauges applied were of type HBM1-LY61-6 and were mounted using the rapid adhesive Z70 from HBK, which is suitable for use at low temperatures. The strain gauges were covered with ABM75, a permanently plastic putty with aluminium foil. The sensors were connected to Quantum MX840A and MX840B amplifiers. The Catman AP data acquisition software was utilised for recording (all these products are from Hottinger Brüel & Kjaer GmbH, 64293 Darmstadt, Germany).

To prepare for the strain gauge application, the measurement points underwent a sanding process to strip off the protective coating from the girders. Special attention was paid to ensure even removal and to retain a flat surface. Following the sanding, the sites were cleaned using acetone to rid them of any residual dirt and grease. Considering the cold external temperatures, the steel carrier was preheated using a hot air device before the adhesive process. Teflon strips were then placed over the strain gauge, which were subsequently secured using a press, allowing them to cure for a minimum of two minutes. The purpose of the Teflon strips is to prevent the adhesive from bonding with the strain gauge, ensuring the measurement point remains undamaged during the removal of the press. To avoid potential delamination at the strain gauges, cables were soldered to them, maintaining a temperature of <350 °C and limiting exposure to less than one second (see Figure 5.3 a)). After validating the functionality of each measurement point via preliminary tests, they were sealed using ABM75.

The acceleration sensors were attached to the downside of the bottom flanges using magnets (see Figure 5.3 b)).

With the measurement setup described, twelve passages of a test subject with a weight force of approximately 900 N were recorded. The walking frequency was varied between 1.6 Hz and 2.2 Hz in 0.2 Hz increments, resulting in three recorded passages for each frequency. The walking frequency for the subject was regulated using a metronome. The subject synchronized with the metronome's beat on a starting platform before entering the structure. Before the start of each passage, care was taken to ensure that any vibrations within the structure had subsided. All sensor signals were recorded at a sampling rate of 1,200 Hz. At the start of each measurement, all channels were zero-adjusted.

To enable a modal analysis of the structure using SSI, accelerations of the structure in its ambient state were also recorded over a 600-second interval.

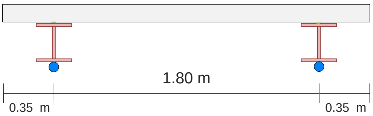
1.80 m
0.35 m
0.35 m

(a) cross section

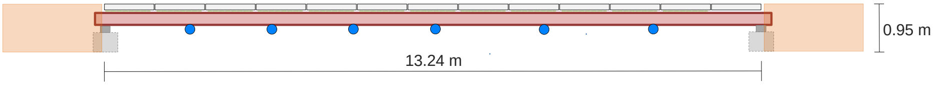

(b) side view

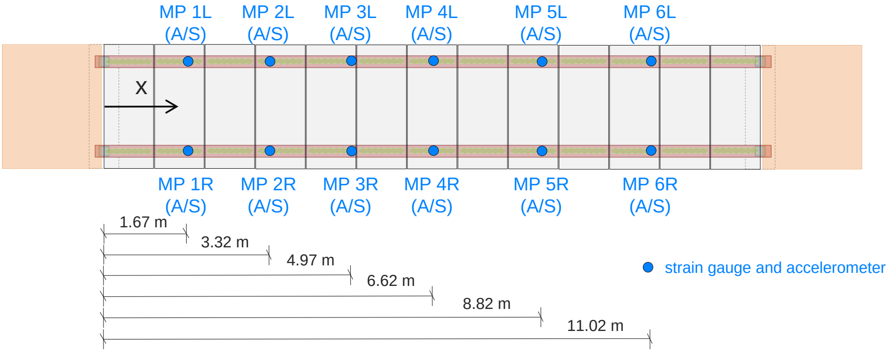
MP 1L (A/S)
MP 2L (A/S)
MP 3L (A/S)
MP 4L (A/S)
MP 5L (A/S)
MP 6L (A/S)
X
MP 1R (A/S)
MP 2R (A/S)
MP 3R (A/S)
MP 4R (A/S)
MP 5R (A/S)
MP 6R (A/S)
1.67 m
3.32 m
4.97 m
6.62 m
8.82 m
11.02 m
● strain gauge and accelerometer

(c) top view

Figure 5.2 Sensor positioning on the HUMVIB bridge.

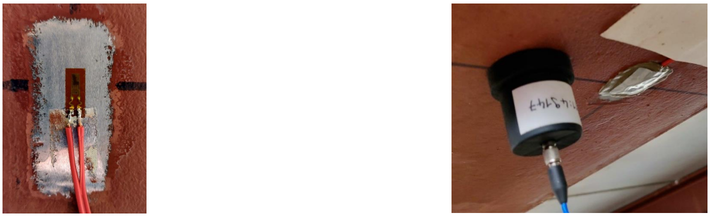

(a) strain gauge before installation of the cover

(b) installed acceleration sensor and strain gauge

Figure 5.3 Installed sensors on the HUMVIB (photos: Maximilian Rupp)

5.2 System identification and structural model

This section presents the structural model of the bridge used and describes the results of the system identification. For the system identification, the acceleration signals were used to apply the SSI. In addition, it is explained how the POD modes were extracted from the measured data.

5.2.1 Modal analysis

The modal analysis was conducted using the software Macec (Reynders et al., 2021). As a first step in signal pre-processing, the signal offset was removed using the Matlab function *detrend()*. Then the Matlab function *decimate()* was used to reduce the sampling rate of the signals by a factor of 10 from 1200 Hz to 120 Hz. The processed signals were then filtered with a 4th-order Butterworth bandpass filter in the range of 0.5 Hz to 50 Hz. From the whole processed signal, the middle 200 s of the recording were cut out to be analysed with the Data-Driven-SSI. The two free parameters were chosen as $i = 33$ and $n = 100$. For details on the choice of parameters, please refer to the instructions of the Macec software (Reynders et al., 2021, p. 42).

5.2.2 Beam and FE model

In the modal expansion (ME), the structural model is reduced to the eigenmodes. Two different structural models were used to obtain the eigenmodes of the structure. On the one hand, the analytical bending and torsion eigenmodes of a homogeneous beam were used[1]. On the other hand, the eigenmodes of a 3D FE model were used. A comparison of the two models is shown in Figure 5.4. For simplicity, the beam model was assumed to be a double-symmetric cross section, so that the shear centre and the centre of gravity coincide and there are no coupled flexural-torsional modes. This means that the eigenmodes of the

---

[1] see subsection 2.5.2

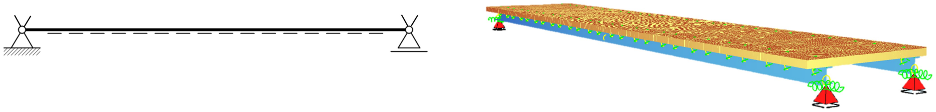

Figure 5.4 Comparison of simply supported beam model with fixed bearing with respect to torsion (left) and FE-model with vertically ridgid supports and elastic supports in lateral direction (right)

Table 5.1 Material parameters of the FE model

	Young’s modulusl [N/m²]	Poisson’s ratio [-]	specific weight [N/m³]
concrete	$3.10 \cdot 10^{10}$	0.2	25000
steel	$2.10 \cdot 10^{11}$	0.3	78500

simple supported Euler-Bernoulli beam and the torsional modes of a fork supported beam can be used. Since no frequencies are to be determined, but only the eigenmodes of the model are used, their quantification can be omitted if a homogeneous distribution of masses and stiffnesses is assumed[1].

The FE model was created using the Sofistik software according to the description of the structural model in (Firus et al., 2022). The model has a total of 89,912 degrees of freedom. The two steel beams are modelled as beam elements, while the reinforced concrete slabs are modelled as shell elements. The steel beams have ridigd supports at the ends in the vertical direction and are elastically supported in the lateral directions. The shell elements are connected to the beam elements at four points per slab (two per beam). This connection consists of translational springs in all three directions and a rotational spring around the longitudinal axis of the steel beams. The material parameters used are listed in Table 5.1. The spring stiffnesses have been set for the model according to the values determined in (Firus et al., 2022) via model update (Table 5.2).

A modal analysis was performed with the model to calculate the modal displacements and strains at the bottom sides of the beams and thus also at the measurement points. The

Table 5.2 Spring stiffnesses of the FE model

support		connections			
[N/m]		translation [N/m]			rotation [Nm]
x	y	x	y	z	r
$1.26 \cdot 10^{7}$	$1.07 \cdot 10^{7}$	$1.11 \cdot 10^{7}$	$2.52 \cdot 10^{6}$	$1.82 \cdot 10^{7}$	$1.20 \cdot 10^{7}$

Table 5.3 MAC values for the comparison of the displacement eigenmodes and those of the SSI

	B1	**T1**	**B2**	**T2**	**B3**	**T3**	**B4**
FE / Beam	1.000	1.000	1.000	1.000	1.000	1.000	1.000
FE /SSI	1.000	0.987	0.992	0.990	0.991	0.954	0.884
Beam / SSI	1.000	0.987	0.992	0.990	0.992	0.955	0.886

selection of modes according to the description in subsection 4.1.2 resulted in a total of seven modes, including four bending modes and three torsional modes (see figure 5.5).

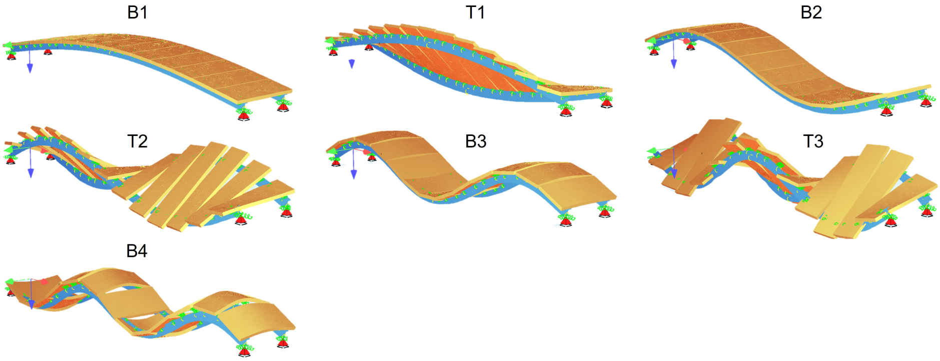

Figure 5.5 The first 7 vertical modes of the FE model divided into bending eigenmodes (B) and torsion eigenmodes (T)

5.2.3 Comparison of mode shapes

In order to compare the mode shapes, they have been scaled to the same amplitudes (Figure 5.6). There is excellent agreement between the displacement mode shapes of the FE and the beam model. This is also evident from the calculated MAC values summarised in table 5.3. The model based displacement mode shapes agree very well with the mode shapes obtained using SSI. Only the third torsional mode (T3) and the fourth bending mode (B4) show less agreement. Since the strain mode shapes cannot be determined experimentally due to the poor signal-to-noise ratio of the strain gauge[2], only a comparison between the shapes of the FE model and those of the beam model is possible for the strain mode shapes (see Figure 5.7). Also for the strains, a very good agreement of the modes of the two models is shown. Only for the torsional modes T1 and T2 small deviations can

---

[2] see subsection 2.5.4

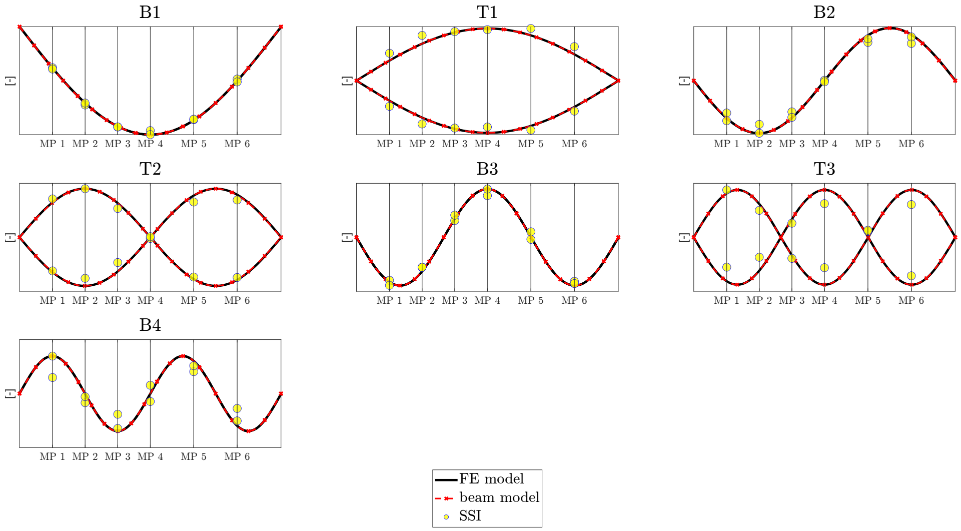

Figure 5.6 Comparison of displacement mode shapes of FE model, beam model and SSI

Table 5.4 MAC values for comparison of strain mode shapes of FE and beam model

	B1	**T1**	**B2**	**T2**	**B3**	**T3**	**B4**
FE / beam	1.000	0.998	1.000	0.998	1.000	1.000	1.000

be observed. These can be attributed to the discretely distributed coupling springs (two connection points per concrete slab and beam). The good agreement of the modes is also confirmed by the MAC values close to 1.0 (see Table 5.4).

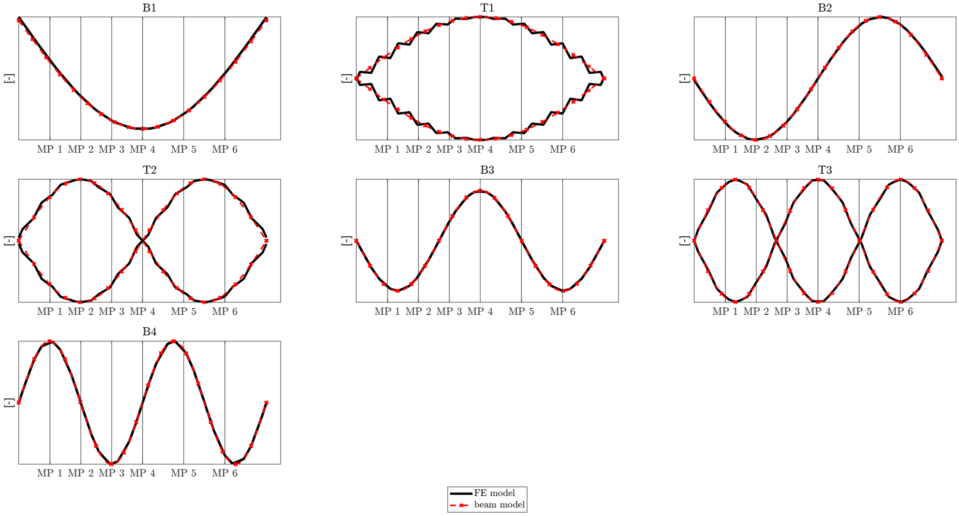

Figure 5.7 Comparison of strain mode shapes of FE and beam model

5.2.4 POD modes

Since the POD modes $\boldsymbol{\Psi}$ are load dependent[3], data from the first run were used for each step frequency of the trial (1.6 Hz, 1.8 Hz, 2.0 Hz and 2.2 Hz): The objective was to use these four sets of POD modes to verify whether the extracted POD modes are able to effectively approximate the structural responses under different loading scenarios. For a comparative plot, the amplitudes of the modes were scaled to $+1$.

A comparison of the acceleration modes (Figure 5.8) illustrates that the modes derived from different step frequencies differ from each other. Nevertheless, the first mode, which is affine to the first bending mode of the system, remains almost constant across all POD mode sets. The second mode is also affine to the second bending mode of the system in all sets, but the mode set obtained from the pass at 1.6 Hz shows a lower affinity.

To quantify the agreement between the different modes, the MAC values were calculated. The results are summarised in Table 5.5. For easier interpretation, the cells corresponding to the MAC values are highlighted with a two-colour colour scale, with values varying between 0/white and 1/blue.

The strain modes show a similar affinity of the first and second modes to the first and second bending mode shapes, respectively, as the acceleration modes (Figure 5.9). However, in contrast to the acceleration modes, neither set of modes in these two strain modes shows significant differences from the other modes. This is also confirmed by the calculated MAC values summarised in Table 5.6.

---

[3] see chapter 2,section 2.2 on page 8

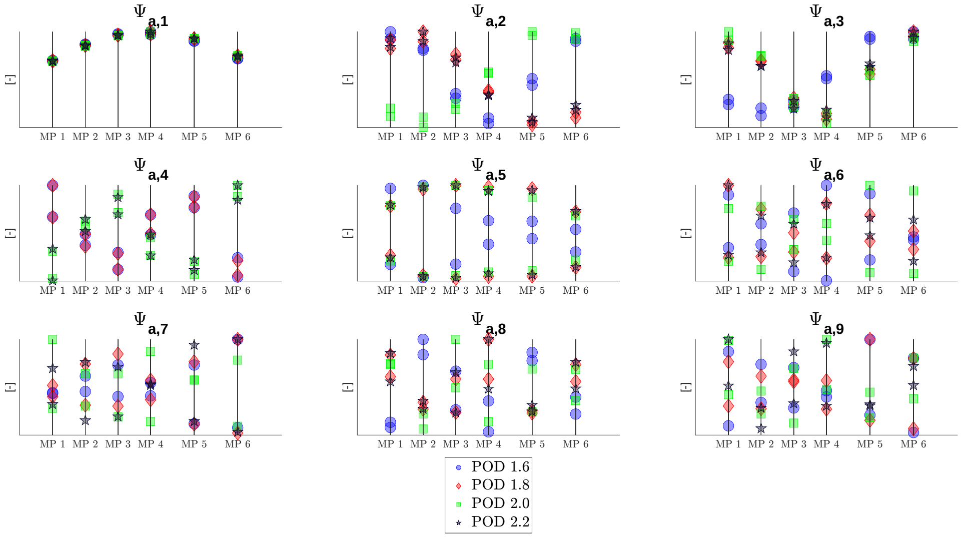

Figure 5.8 Comparison of POD modes for accelerations ($\mathbf{\Psi}_{\mathrm{a},n}$) from four different mode sets

Table 5.5 MAC-values of the comparison of the POD modes for accelerations $\mathbf{\Psi}_{\mathrm{a},n}$ from the four different mode sets

POD set	compared to	$\Psi_{a,1}$	$\Psi_{a,2}$	$\Psi_{a,3}$	$\Psi_{a,4}$	$\Psi_{a,5}$	$\Psi_{a,6}$	$\Psi_{a,7}$	$\Psi_{a,8}$	$\Psi_{a,9}$	$\Psi_{a,10}$	$\Psi_{a,11}$	$\Psi_{a,12}$
1.6	1.8	1.00	0.06	0.06	1.00	0.67	0.71	0.94	0.83	0.79	0.11	0.13	0.34
	2.0	1.00	0.02	0.02	0.98	0.74	0.18	0.30	0.09	0.30	0.02	0.31	0.58
	2.2	1.00	0.12	0.12	0.99	0.71	0.69	0.82	0.78	0.26	0.13	0.20	0.60
1.8	1.6	1.00	0.06	0.06	1.00	0.67	0.71	0.94	0.83	0.79	0.11	0.13	0.34
	2.0	1.00	0.99	0.98	0.98	0.99	0.21	0.21	0.00	0.11	0.22	0.06	0.08
	2.2	1.00	0.99	0.98	0.99	1.00	0.92	0.93	0.96	0.02	0.01	0.00	0.01
2.0	1.6	1.00	0.02	0.02	0.98	0.74	0.18	0.30	0.09	0.30	0.02	0.31	0.58
	1.8	1.00	0.99	0.98	0.98	0.99	0.21	0.21	0.00	0.11	0.22	0.06	0.08
	2.2	1.00	0.95	0.95	0.99	0.99	0.05	0.04	0.00	0.03	0.42	0.89	0.91
2.2	1.6	1.00	0.12	0.12	0.99	0.71	0.69	0.82	0.78	0.26	0.13	0.20	0.60
	1.8	1.00	0.99	0.98	0.99	1.00	0.92	0.93	0.96	0.02	0.01	0.00	0.01
	2.0	1.00	0.95	0.95	0.99	0.99	0.05	0.04	0.00	0.03	0.42	0.89	0.91

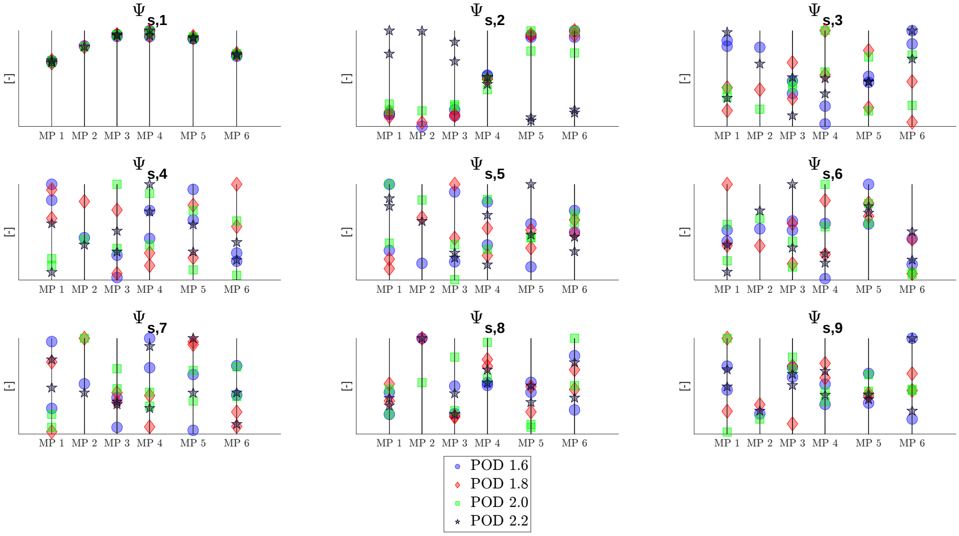

Figure 5.9 Comparison of POD modes for strains ($\boldsymbol{\Psi}_{s,n}$) from four different mode sets

The MAC values show that for the strain modes, only the first modes of the different sets agree well; in contrast, the first five modes show good agreement between the different sets for the acceleration modes. However, a lower number of matching modes is to be expected, given the poorer signal-to-noise ratio of the strain gauge compared to the accelerometers.

Despite the load dependence of the POD modes, the dominant modes, apart from the second acceleration mode from the excitation at 1.6 Hz, show a clear agreement under the different loading conditions. This suggests that an efficient reconstruction of the structural responses might be possible over a spectrum of excitations that are of similar type [4].

In the following section, the capability of the different sets of POD modes to project the structural responses onto the subspaces spanned by them is investigated. Therefore, the influence of the used mode sets on the reconstruction quality is investigated.

---

[4] meaning here e.g. moving concentrated loads

Table 5.6 MAC-values of the comparison of the POD modes for strains $\Psi_{\mathrm{s},n}$ from the four different mode sets

POD set	compared to	$\Psi_{\mathrm{s},1}$	$\Psi_{\mathrm{s},2}$	$\Psi_{\mathrm{s},3}$	$\Psi_{\mathrm{s},4}$	$\Psi_{\mathrm{s},5}$	$\Psi_{\mathrm{s},6}$	$\Psi_{\mathrm{s},7}$	$\Psi_{\mathrm{s},8}$	$\Psi_{\mathrm{s},9}$	$\Psi_{\mathrm{s},10}$	$\Psi_{\mathrm{s},11}$
1.6	1.8	1.00	0.99	0.40	0.01	0.09	0.41	0.24	0.40	0.00	0.21	0.16
	2.0	1.00	0.94	0.31	0.05	0.30	0.11	0.00	0.00	0.16	0.12	0.17
	2.2	1.00	0.95	0.48	0.01	0.08	0.29	0.31	0.82	0.79	0.83	0.93
1.8	1.6	1.00	0.99	0.40	0.01	0.09	0.41	0.24	0.40	0.00	0.21	0.16
	2.0	1.00	0.95	0.01	0.01	0.05	0.30	0.10	0.10	0.24	0.07	0.92
	2.2	1.00	0.93	0.02	0.03	0.45	0.07	0.01	0.75	0.04	0.11	0.24
2.0	1.6	1.00	0.94	0.31	0.05	0.30	0.11	0.00	0.00	0.16	0.12	0.17
	1.8	1.00	0.95	0.01	0.01	0.05	0.30	0.10	0.10	0.24	0.07	0.92
	2.2	1.00	0.86	0.11	0.37	0.17	0.00	0.00	0.04	0.10	0.15	0.25
2.2	1.6	1.00	0.95	0.48	0.01	0.08	0.29	0.31	0.82	0.79	0.83	0.93
	1.8	1.00	0.93	0.02	0.03	0.45	0.07	0.01	0.75	0.04	0.11	0.24
	2.0	1.00	0.86	0.11	0.37	0.17	0.00	0.00	0.04	0.10	0.15	0.25

5.3 Virtual sensing

In this section, investigations into the data-driven and model-based VS at the HUMVIB are presented. Initially, the influence of various POD mode sets, resulting from different excitation frequencies, is examined using the leave-one-out validation method. Subsequently, the effect of different sensor configurations and the consideration of various mode numbers are explored during the leave-p-out validation for the various measured quantities. This is conducted both with the model-based modes and with the POD modes.

5.3.1 Influence of the POD mode sets

To investigate the influence of the POD mode set selection, a leave-one-out validation was conducted. In this method, one sensor was removed from the data matrix, while the remaining sensors were used to reconstruct the removed sensor as a virtual sensor. The outcome can then be compared with the actual measurement data of the removed sensor.

This validation method eliminates the need to compare different sensor setups with each other and isolates the number of considered modes n_{m} as the only remaining influencing factor. Therefore, the coefficient of determination R^2 was calculated for both the acceleration sensors and the strain gauge for $\{n_{\mathrm{m}} \in \mathbb{N} \mid 1 \leq n_{\mathrm{m}} < k-1\}$.

The minimum and maximum values of the coefficient of determination, along with the associated number of considered modes, were summarised in a tabular form. The detailed results for each excitation frequency are found in the appendix tables (Table A.1 to A.8).

In Table 5.7 and 5.8, the mean values of these results, aggregated across all excitation frequencies, are presented[5].

The analysis of both accelerations and strains reveals that the choice of the POD mode set has a minor effect on the maximum coefficients of determination in the leave-one-out validation. However, differences are observed in the minimum values.

In the context of accelerations, the impact of the selected mode set is overall marginal. A significant discrepancy is only discernible in the mode set resulting from the 1.6 Hz excitation, especially at the measurement points MP 5L, MP 6L, and MP 6R. This result corresponds with the previously observed deviations of this mode set from the others.

The minimum coefficients of determination for strains exhibit a notably larger variance, depending on the selection of the POD mode set. When examining the relationship of the minimum coefficients of determination to the number of considered modes n_m, it becomes evident that, for accelerations, generally fewer modes were taken into account compared to the maximum values. The sole exception is the mode set from the 1.6 Hz excitation, and this is only true for the sensors MP 5L and MP 1R.

In the context of strain measurements, it is often observed that a larger number of modes is considered for the minimum values compared to the maximum values. One plausible reason for this is that the poorer signal-to-noise ratio of the strain gauges compared to the accelerometers results in noisier modes, especially in the higher modes. Therefore, the reconstruction quality may decrease when a greater number of modes is incorporated.

For acceleration data, the leave-one-out validation indicates that the choice of the POD mode set has little influence. However, for strain data, the situation concerning the minimum values is more complex, as there is no clear relationship between the number of considered modes and the reconstruction quality. The effects of the number of considered modes will be further examined in a subsequent leave-p-out validation.

---

[5] The absence of the number of considered modes n_m in the tables presenting mean values (Table 5.7 and 5.8) is due to the fact that these mean values are aggregated across various excitation frequencies. In this aggregation process, the minimum and maximum values are derived from different numbers of considered modes, making it unfeasible to specify a single n_m in these summary tables. For detailed information regarding n_m for each excitation frequency, the reader is referred to the tables in the appendix (Table A.1 to A.8).

Table 5.7 Mean values of the coefficients of determination R^2 over the four passes with different frequencies for all **acceleration sensors**.

POD		MP 1L	MP 2L	MP 3L	MP 4L	MP 5L	MP 6L	MP 1R	MP 2R	MP 3R	MP 4R	MP 5R	MP 6R
1.6	max	1.00	1.00	1.00	1.00	1.00	1.00	1.00	1.00	1.00	1.00	1.00	0.99
	min	0.74	0.88	0.95	0.94	0.52	0.69	0.66	0.85	0.92	0.94	0.86	0.67
1.8	max	1.00	1.00	1.00	1.00	1.00	1.00	1.00	1.00	1.00	1.00	1.00	0.99
	min	0.74	0.88	0.95	0.94	0.88	0.72	0.65	0.85	0.92	0.94	0.86	0.71
2	max	1.00	1.00	1.00	1.00	1.00	1.00	1.00	1.00	1.00	1.00	1.00	0.99
	min	0.74	0.88	0.95	0.94	0.88	0.72	0.65	0.85	0.92	0.94	0.86	0.71
2.2	max	1.00	1.00	1.00	1.00	1.00	1.00	1.00	1.00	1.00	1.00	1.00	1.00
	min	0.74	0.88	0.95	0.94	0.88	0.72 .	0.65	0.85	0.92	0.94	0.86	0.71

Table 5.8 Mean values of the coefficients of determination R^2 over the four passes with different frequencies for all **strain gauges**.

POD		MP 1L	MP 2L	MP 3L	MP 4L	MP 5L	MP 6L	MP 1R	MP 3R	MP 4R	MP 5R	MP 6R
1.6	max	0.95	0.99	0.99	0.99	0.99	0.96	0.94	0.99	0.99	0.99	0.98
	min	0.78	0.13	0.97	0.97	0.95	0.36	0.84	0.97	0.99	0.97	0.37
1.8	max	0.93	0.99	0.99	0.99	0.99	0.95	0.95	0.99	0.99	0.99	0.98
	min	0.38	0.78	0.92	0.97	0.95	0.87	0.15	0.89	0.98	0.97	0.91
2	max	0.94	0.98	0.99	0.98	0.98	0.94	0.94	0.99	0.99	0.99	0.98
	min	0.13	0.54	0.96	0.94	0.95	0.87	0.47	0.97	0.98	0.97	0.91
2.2	max	0.89	0.99	0.99	0.99	0.99	0.95	0.94	0.99	0.99	0.99	0.98
	min	0.77	0.30	0.96	0.98	0.95	0.60	0.85	0.97	0.99	0.97	0.83

5.3.2 Impact of considered modes and number of physical sensors

In this subsection, the influence of the number of considered modes, denoted as n_{m}, and the number of physical sensors, represented by k, is examined. To achieve this, a leave-p-out validation was undertaken, as elaborated upon in subsection 4.1.4.

As previously defined in the section detailing the leave-p-out validation, this study utilises the terms *best sensor combination* and *worst sensor combination* to describe configurations that produce the maximum and minimum R^2 values, respectively.

Initially, the influence of the choice of the POD mode set was analysed, independently of sensor combinations, via a leave-one-out validation. Subsequently, a more detailed investigation was carried out using the leave-p-out validation for all four POD mode sets. The outcomes for the best and worst sensor combinations, in terms of strain and accelerations, were plotted for each measurement point (MP). To facilitate a clearer visual representation, the final R^2 values were modified after the mean had been calculated and the maximum and minimum values identified, as follows:

$$R^2_{\mathrm{mod}} = \begin{cases} R^2 & \text{if } R^2 \geq 0 \\ 0 & \text{if } R^2 < 0 \end{cases} \tag{5.1}$$

The modification is introduced to improve the visual representation of the data. Negative R^2 values can vary significantly in magnitude, while positive values are constrained to a maximum of 1. By setting negative R^2 values to zero, the risk of omitting them is avoided when axis limits between 0 and 1 are set for graphical representation.

Illustrative results of this procedure for MP1L can be seen in Figure 5.10. Results pertaining to other measurement points are provided in the appendix figures, ranging from Figure B.1 to Figure B.11.

From Figure 5.10, it was observed that the choice of mode set was of marginal significance, especially for the optimal sensor combination. Results were consistent across mode sets, with POD 1.6 showing a slight advantage. In a departure from the usual trend of nearly identical R^2 values across different POD mode sets, a notable exception was observed for strains when employing ten physical strain sensors. Specifically, sets POD 1.8 and POD 2.0 yielded significantly reduced results.

For other sensor positions evaluated across all mode sets, outcomes were nearly identical for the best sensor combinations. However, for the worst combinations, discernible differences emerged, but no consistent mode superiority was identified, varying from one scenario to another.

Overall, the analysis revealed that to achieve a specific reconstruction quality, fewer physical sensors and considered modes are necessary for strains as compared to accelerations. Additionally, it was observed that when the number of modes, n_m, is fewer than the number of physical sensors, k, the coefficients of determination for the worst sensor combinations tend to rise, converging towards the values for the best combinations, which conversely showed a decrease. This difference, $k - n_{\mathrm{m}}$, represents the degree of over-determination in the system of equations for the modal expansion, as described in Equation 4.2.

Notably, sensors positioned in the mid-span of the bridge yielded better results compared to those situated near the supports. This effect is more pronounced for the acceleration sensors.

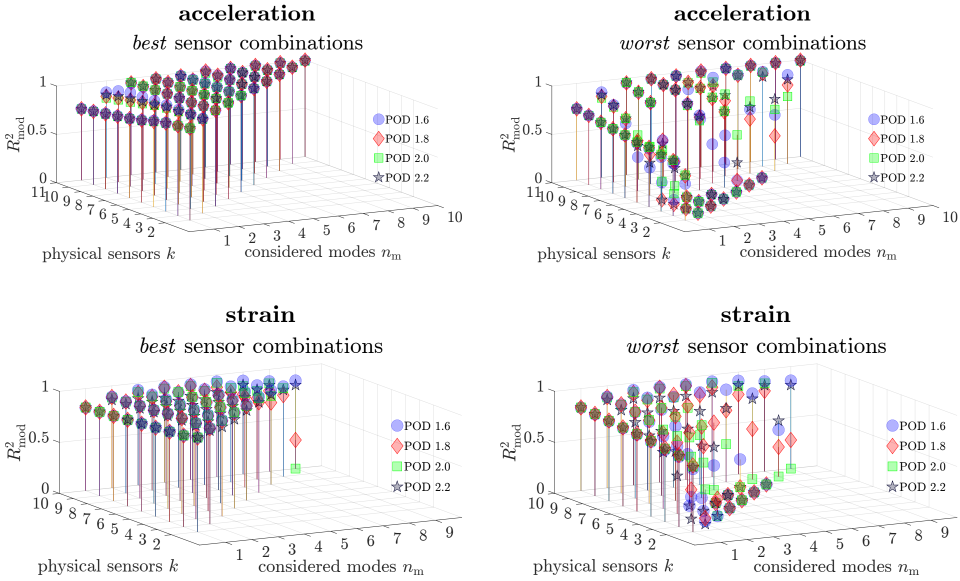

Figure 5.10 Comparison of the maximum and minimum coefficients of determination at **MP 1L** for accelerations and strains for all 4 POD mode sets

The influence of n_{m} and k was also examined for the FE modes. Given that there is only one mode set for the FE modes, the results can be more succinctly represented in a two-dimensional heatmap. The findings pertaining to the acceleration sensors are presented in Figure 5.11, whereas the results for the strain gauges are summarised in Figure 5.12.

A similar behaviour for the POD modes was also evident when employing the FE modes. Sensors located in the mid-span of the bridge consistently yielded superior results in comparison to those positioned near the supports. This effect was particularly pronounced for acceleration measurements.

The observed behaviour aligns with expectations. Vibrations in the centre of the span are predominantly influenced by the lower eigenmodes. Conversely, towards the supports, the contribution of higher eigenmodes increases. This effect is detailed in section 2.9. This discrepancy is further accentuated by the superior signal-to-noise ratio of the accelerometers when compared to strain gauges.

In conclusion, for all mode sets under investigation, encompassing the four POD mode sets and the FE mode set, an accurate approximation of the measured signal at all sensor locations was attainable. If a good sensor combination is ensured, it is advisable to select $n_m = k - 1$ to yield good results while maximizing the information extracted from the sensors. However, it should be noted that this efficiency comes at the expense of the method's stability, here referring to the sensitivity of the results to the choice of sensor combination. Stability can be increased at the cost of reconstruction quality by reducing the number of considered modes relative to the number of deployed sensors.

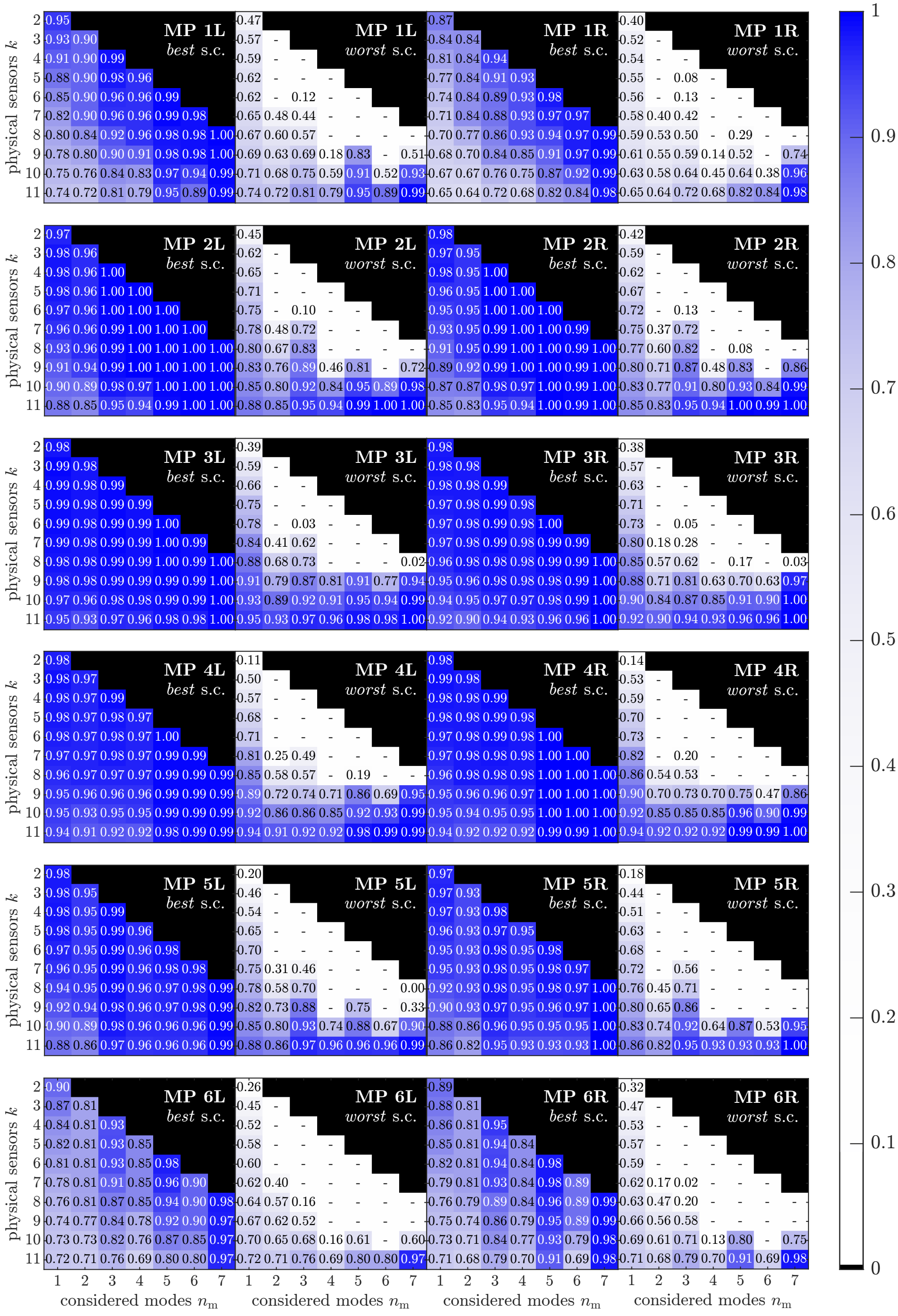

MP 1L *best s.c.*

physical sensors k \ considered modes n_m	1	2	3	4	5	6	7
2	0.95						
3	0.93	0.90					
4	0.91	0.90	0.99				
5	0.88	0.90	0.98	0.96			
6	0.85	0.90	0.96	0.96	0.99		
7	0.82	0.90	0.96	0.96	0.99	0.98	
8	0.80	0.84	0.92	0.96	0.98	0.98	1.00
9	0.78	0.80	0.90	0.91	0.98	0.98	1.00
10	0.75	0.76	0.84	0.83	0.97	0.94	0.99
11	0.74	0.72	0.81	0.79	0.95	0.89	0.99

MP 1L *worst s.c.*

physical sensors k \ considered modes n_m	1	2	3	4	5	6	7
2	0.47						
3	0.57	-					
4	0.59	-	-				
5	0.62	-	-	-			
6	0.62	-	0.12	-	-		
7	0.65	0.48	0.44	-	-	-	
8	0.67	0.60	0.57	-	-	-	-
9	0.69	0.63	0.69	0.18	0.83	-	0.51
10	0.71	0.68	0.75	0.59	0.91	0.52	0.93
11	0.74	0.72	0.81	0.79	0.95	0.89	0.99

MP 1R *best s.c.*

physical sensors k \ considered modes n_m	1	2	3	4	5	6	7
2	0.87						
3	0.84	0.84					
4	0.81	0.84	0.94				
5	0.77	0.84	0.91	0.93			
6	0.74	0.84	0.89	0.93	0.98		
7	0.71	0.84	0.88	0.93	0.97	0.97	
8	0.70	0.77	0.86	0.93	0.94	0.97	0.99
9	0.68	0.70	0.84	0.85	0.91	0.97	0.99
10	0.67	0.67	0.76	0.75	0.87	0.92	0.99
11	0.65	0.64	0.72	0.68	0.82	0.84	0.98

MP 1R *worst s.c.*

physical sensors k \ considered modes n_m	1	2	3	4	5	6	7
2	0.40						
3	0.52	-					
4	0.54	-	-				
5	0.55	-	0.08	-			
6	0.56	-	0.13	-	-		
7	0.58	0.40	0.42	-	-	-	
8	0.59	0.53	0.50	-	0.29	-	-
9	0.61	0.55	0.59	0.14	0.52	-	0.74
10	0.63	0.58	0.64	0.45	0.64	0.38	0.96
11	0.65	0.64	0.72	0.68	0.82	0.84	0.98

MP 2L *best s.c.*

physical sensors k \ considered modes n_m	1	2	3	4	5	6	7
2	0.97						
3	0.98	0.96					
4	0.98	0.96	1.00				
5	0.98	0.96	1.00	1.00			
6	0.97	0.96	1.00	1.00	1.00		
7	0.96	0.96	0.99	1.00	1.00	1.00	
8	0.93	0.96	0.99	1.00	1.00	1.00	1.00
9	0.91	0.94	0.99	1.00	1.00	1.00	1.00
10	0.90	0.89	0.98	0.97	1.00	1.00	1.00
11	0.88	0.85	0.95	0.94	0.99	1.00	1.00

MP 2L *worst s.c.*

physical sensors k \ considered modes n_m	1	2	3	4	5	6	7
2	0.45						
3	0.62	-					
4	0.65	-	-				
5	0.71	-	-	-			
6	0.75	-	0.10	-	-		
7	0.78	0.48	0.72	-	-	-	
8	0.80	0.67	0.83	-	-	-	-
9	0.83	0.76	0.89	0.46	0.81	-	0.72
10	0.85	0.80	0.92	0.84	0.95	0.89	0.98
11	0.88	0.85	0.95	0.94	0.99	1.00	1.00

MP 2R *best s.c.*

physical sensors k \ considered modes n_m	1	2	3	4	5	6	7
2	0.98						
3	0.97	0.95					
4	0.98	0.95	1.00				
5	0.96	0.95	1.00	1.00			
6	0.95	0.95	1.00	1.00	1.00		
7	0.93	0.95	0.99	1.00	1.00	0.99	
8	0.91	0.95	0.99	1.00	1.00	0.99	1.00
9	0.89	0.92	0.99	1.00	1.00	0.99	1.00
10	0.87	0.87	0.98	0.97	1.00	0.99	1.00
11	0.85	0.83	0.95	0.94	1.00	0.99	1.00

MP 2R *worst s.c.*

physical sensors k \ considered modes n_m	1	2	3	4	5	6	7
2	0.42						
3	0.59	-					
4	0.62	-	-				
5	0.67	-	-	-			
6	0.72	-	0.13	-	-		
7	0.75	0.37	0.72	-	-	-	
8	0.77	0.60	0.82	-	0.08	-	-
9	0.80	0.71	0.87	0.48	0.83	-	0.86
10	0.83	0.77	0.91	0.80	0.93	0.84	0.99
11	0.85	0.83	0.95	0.94	1.00	0.99	1.00

MP 3L *best s.c.*

physical sensors k \ considered modes n_m	1	2	3	4	5	6	7
2	0.98						
3	0.99	0.98					
4	0.99	0.98	0.99				
5	0.99	0.98	0.99	0.99			
6	0.99	0.98	0.99	0.99	1.00		
7	0.99	0.98	0.99	0.99	1.00	0.99	
8	0.98	0.98	0.99	0.99	1.00	0.99	1.00
9	0.98	0.98	0.99	0.99	0.99	0.99	1.00
10	0.97	0.96	0.98	0.98	0.99	0.99	1.00
11	0.95	0.93	0.97	0.96	0.98	0.98	1.00

MP 3L *worst s.c.*

physical sensors k \ considered modes n_m	1	2	3	4	5	6	7
2	0.39						
3	0.59	-					
4	0.66	-	-				
5	0.75	-	-	-			
6	0.78	-	0.03	-	-		
7	0.84	0.41	0.62	-	-	-	
8	0.88	0.68	0.73	-	-	-	0.02
9	0.91	0.79	0.87	0.81	0.91	0.77	0.94
10	0.93	0.89	0.92	0.91	0.95	0.94	0.99
11	0.95	0.93	0.97	0.96	0.98	0.98	1.00

MP 3R *best s.c.*

physical sensors k \ considered modes n_m	1	2	3	4	5	6	7
2	0.98						
3	0.98	0.98					
4	0.98	0.98	0.99				
5	0.97	0.98	0.99	0.98			
6	0.97	0.98	0.99	0.98	1.00		
7	0.97	0.98	0.99	0.98	0.99	0.99	
8	0.96	0.98	0.98	0.98	0.99	0.99	1.00
9	0.95	0.96	0.98	0.98	0.98	0.99	1.00
10	0.94	0.95	0.97	0.97	0.98	0.99	1.00
11	0.92	0.90	0.94	0.93	0.96	0.96	1.00

MP 3R *worst s.c.*

physical sensors k \ considered modes n_m	1	2	3	4	5	6	7
2	0.38						
3	0.57	-					
4	0.63	-	-				
5	0.71	-	-	-			
6	0.73	-	0.05	-	-		
7	0.80	0.18	0.28	-	-	-	
8	0.85	0.57	0.62	-	0.17	-	0.03
9	0.88	0.71	0.81	0.63	0.70	0.63	0.97
10	0.90	0.84	0.87	0.85	0.91	0.90	1.00
11	0.92	0.90	0.94	0.93	0.96	0.96	1.00

MP 4L *best s.c.*

physical sensors k \ considered modes n_m	1	2	3	4	5	6	7
2	0.98						
3	0.98	0.97					
4	0.98	0.97	0.99				
5	0.98	0.97	0.98	0.97			
6	0.98	0.97	0.98	0.97	1.00		
7	0.97	0.97	0.98	0.97	0.99	0.99	
8	0.96	0.97	0.97	0.97	0.99	0.99	0.99
9	0.95	0.96	0.96	0.96	0.99	0.99	0.99
10	0.95	0.93	0.95	0.95	0.99	0.99	0.99
11	0.94	0.91	0.92	0.92	0.98	0.99	0.99

MP 4L *worst s.c.*

physical sensors k \ considered modes n_m	1	2	3	4	5	6	7
2	0.11						
3	0.50	-					
4	0.57	-	-				
5	0.68	-	-	-			
6	0.71	-	-	-	-		
7	0.81	0.25	0.49	-	-	-	
8	0.85	0.58	0.57	-	0.19	-	-
9	0.89	0.72	0.74	0.71	0.86	0.69	0.95
10	0.92	0.86	0.86	0.85	0.92	0.93	0.99
11	0.94	0.91	0.92	0.92	0.98	0.99	0.99

MP 4R *best s.c.*

physical sensors k \ considered modes n_m	1	2	3	4	5	6	7
2	0.98						
3	0.99	0.98					
4	0.98	0.98	0.99				
5	0.98	0.98	0.99	0.98			
6	0.97	0.98	0.99	0.98	1.00		
7	0.97	0.98	0.98	0.98	1.00	1.00	
8	0.96	0.98	0.98	0.98	1.00	1.00	1.00
9	0.95	0.96	0.96	0.97	1.00	1.00	1.00
10	0.95	0.94	0.95	0.95	1.00	1.00	1.00
11	0.94	0.92	0.92	0.92	0.99	0.99	1.00

MP 4R *worst s.c.*

physical sensors k \ considered modes n_m	1	2	3	4	5	6	7
2	0.14						
3	0.53	-					
4	0.59	-	-				
5	0.70	-	-	-			
6	0.73	-	-	-	-		
7	0.82	-	0.20	-	-	-	
8	0.86	0.54	0.53	-	-	-	-
9	0.90	0.70	0.73	0.70	0.75	0.47	0.86
10	0.92	0.85	0.85	0.85	0.96	0.90	0.99
11	0.94	0.92	0.92	0.92	0.99	0.99	1.00

MP 5L *best s.c.*

physical sensors k \ considered modes n_m	1	2	3	4	5	6	7
2	0.98						
3	0.98	0.95					
4	0.98	0.95	0.99				
5	0.98	0.95	0.99	0.96			
6	0.97	0.95	0.99	0.96	0.98		
7	0.96	0.95	0.99	0.96	0.98	0.98	
8	0.94	0.95	0.99	0.96	0.97	0.98	0.99
9	0.92	0.94	0.98	0.96	0.97	0.98	0.99
10	0.90	0.89	0.98	0.96	0.96	0.96	0.99
11	0.88	0.86	0.97	0.96	0.96	0.96	0.99

MP 5L *worst s.c.*

physical sensors k \ considered modes n_m	1	2	3	4	5	6	7
2	0.20						
3	0.46	-					
4	0.54	-	-				
5	0.65	-	-	-			
6	0.70	-	-	-	-		
7	0.75	0.31	0.46	-	-	-	
8	0.78	0.58	0.70	-	-	-	0.00
9	0.82	0.73	0.88	-	0.75	-	0.33
10	0.85	0.80	0.93	0.74	0.88	0.67	0.90
11	0.88	0.86	0.97	0.96	0.96	0.96	0.99

MP 5R *best s.c.*

physical sensors k \ considered modes n_m	1	2	3	4	5	6	7
2	0.97						
3	0.97	0.93					
4	0.97	0.93	0.98				
5	0.96	0.93	0.97	0.95			
6	0.95	0.93	0.98	0.95	0.98		
7	0.95	0.93	0.98	0.95	0.98	0.97	
8	0.92	0.93	0.98	0.95	0.98	0.97	1.00
9	0.90	0.93	0.97	0.95	0.96	0.97	1.00
10	0.88	0.86	0.96	0.95	0.95	0.95	1.00
11	0.86	0.82	0.95	0.93	0.93	0.93	1.00

MP 5R *worst s.c.*

physical sensors k \ considered modes n_m	1	2	3	4	5	6	7
2	0.18						
3	0.44	-					
4	0.51	-	-				
5	0.63	-	-	-			
6	0.68	-	-	-	-		
7	0.72	-	0.56	-	-	-	
8	0.76	0.45	0.71	-	-	-	-
9	0.80	0.65	0.86	-	-	-	-
10	0.83	0.74	0.92	0.64	0.87	0.53	0.95
11	0.86	0.82	0.95	0.93	0.93	0.93	1.00

MP 6L *best s.c.*

physical sensors k \ considered modes n_m	1	2	3	4	5	6	7
2	0.90						
3	0.87	0.81					
4	0.84	0.81	0.93				
5	0.82	0.81	0.93	0.85			
6	0.81	0.81	0.93	0.85	0.98		
7	0.78	0.81	0.91	0.85	0.96	0.90	
8	0.76	0.81	0.87	0.85	0.94	0.90	0.98
9	0.74	0.77	0.84	0.78	0.92	0.90	0.97
10	0.73	0.73	0.82	0.76	0.87	0.85	0.97
11	0.72	0.71	0.76	0.69	0.80	0.80	0.97

MP 6L *worst s.c.*

physical sensors k \ considered modes n_m	1	2	3	4	5	6	7
2	0.26						
3	0.45	-					
4	0.52	-	-				
5	0.58	-	-	-			
6	0.60	-	-	-	-		
7	0.62	0.40	-	-	-	-	
8	0.64	0.57	0.16	-	-	-	-
9	0.67	0.62	0.52	-	-	-	-
10	0.70	0.65	0.68	0.16	0.61	-	0.60
11	0.72	0.71	0.76	0.69	0.80	0.80	0.97

MP 6R *best s.c.*

physical sensors k \ considered modes n_m	1	2	3	4	5	6	7
2	0.89						
3	0.88	0.81					
4	0.86	0.81	0.95				
5	0.85	0.81	0.94	0.84			
6	0.82	0.81	0.94	0.84	0.98		
7	0.79	0.81	0.93	0.84	0.98	0.89	
8	0.76	0.79	0.89	0.84	0.96	0.89	0.99
9	0.75	0.74	0.86	0.79	0.95	0.89	0.99
10	0.73	0.71	0.84	0.77	0.93	0.79	0.98
11	0.71	0.68	0.79	0.70	0.91	0.69	0.98

MP 6R *worst s.c.*

physical sensors k \ considered modes n_m	1	2	3	4	5	6	7
2	0.32						
3	0.47	-					
4	0.53	-	-				
5	0.57	-	-	-			
6	0.59	-	-	-	-		
7	0.62	0.17	0.02	-	-	-	
8	0.63	0.47	0.20	-	-	-	-
9	0.66	0.56	0.58	-	-	-	-
10	0.69	0.61	0.71	0.13	0.80	-	0.75
11	0.71	0.68	0.79	0.70	0.91	0.69	0.98

Figure 5.11 Coefficients of determination of the leave-p-out validation, corresponding to the best and worst sensor combinations (s.c.), depending on the number of physical sensors and considered FE modes for each accelerometer. Negative values are marked with -.

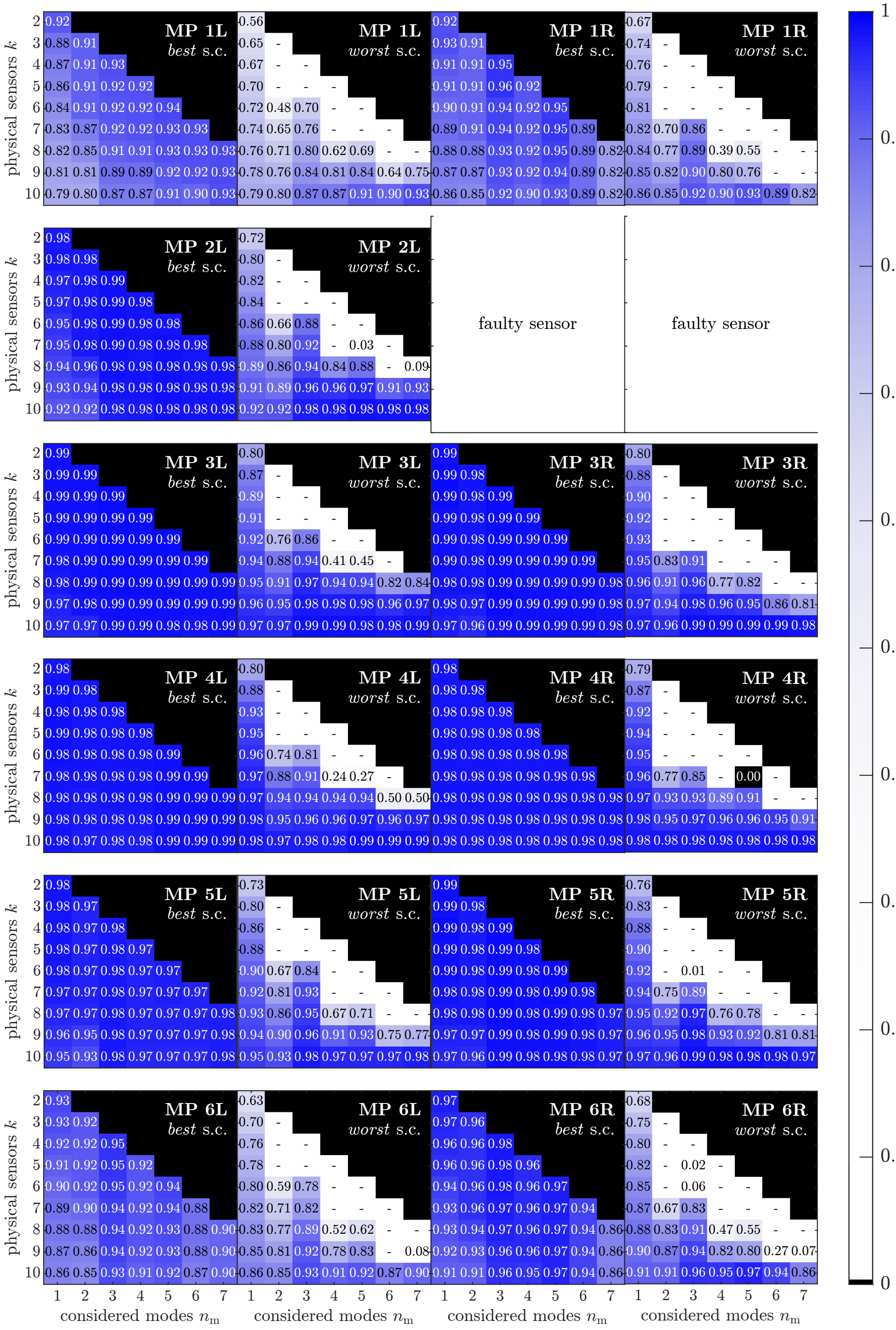

Figure 5.12 Coefficients of determination of the leave-p-out validation, corresponding to the best and worst sensor combinations (s.c.), depending on the number of physical sensors and considered FE modes for each strain gauge. Negative values are marked with -.

5.3.3 Evaluation of different sensor setups

To acquire a comprehensive understanding of optimal sensor placement across a variety of cases, a systematic methodology was employed. For each best sensor combination identified by the leave-p-out validation, using both FE and POD 1.8 modes, the identification numbers for each sensor were extracted. The frequency of each sensor's appearance in the best combinations was tallied, and the relative frequency was calculated. This relative frequency serves as an indicator of the sensor's importance for achieving accurate signal reconstruction at a given measurement point. The procedure was conducted separately for both strain and acceleration signals at each measurement point.

The evaluation results for strain signals are presented in Figure 5.13 for the POD modes. The findings indicate that sensors located either adjacent to the measurement point on the same girder (left/right) or in parallel on the opposite girder usually provide the most effective choice for well selected sensor configurations. An exception is noted at measurement point MP 6R, where the sensor at the opposite end of the same girder, MP 1R, emerges as a highly effective choice. Despite slight variations in results when using FE modes, as depicted in Figure 5.14, the overall trend remains consistent: sensors close to the measurement point on the same girder or in parallel on the opposite girder are generally preferable for effective signal reconstruction at the measurement points.

A similar evaluation for acceleration signals is illustrated in Figure 5.15 for POD modes and in Figure 5.16 for FE modes. While there are some differences, the general trend closely aligns with the observations for strain signals. Specifically, sensors situated either adjacent to the measurement point or in parallel on the opposing girder tend to yield the most advantageous configurations for sensor placement. This observed behaviour is in line with expectations, given that these sensor locations show a high correlation when various mode shapes are superimposed.

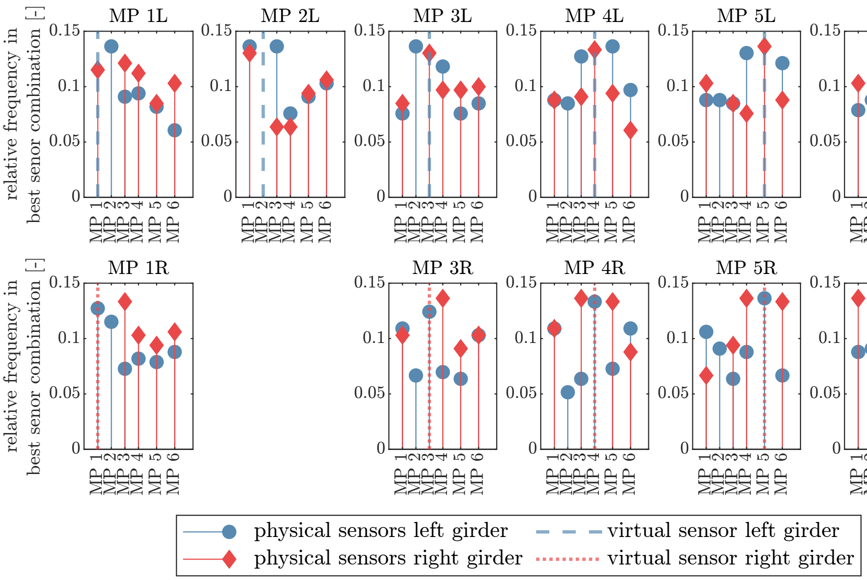

Figure 5.13 Summary of the number of occurrences of each strain gauge in an optimal sensor combination to reconstruct a given measurement point using the POD 1.8 modes. Note that the sensor at MP 2R was defective and is therefore not included in the evaluation.

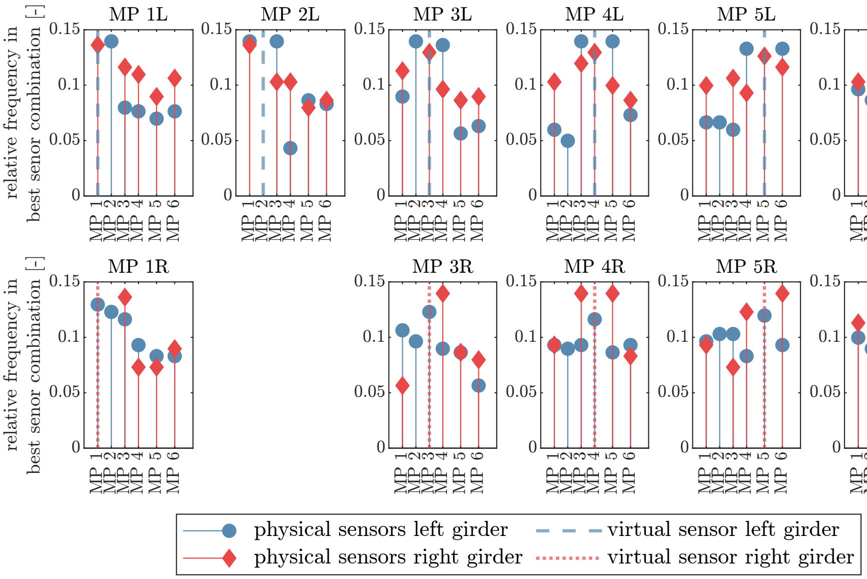

Figure 5.14 Summary of the number of occurrences of each strain gauge in an optimal sensor combination for reconstructing a given measurement point using the FE modes. Note that the sensor at MP 2R was defective and is therefore not included in the evaluation.

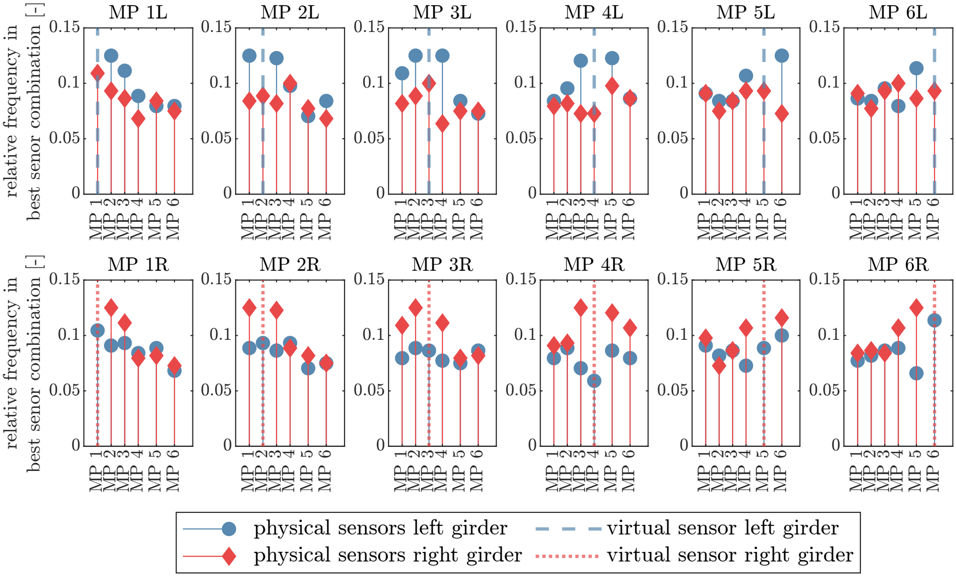

Figure 5.15 Summary of the number of occurrences of each accelerometer in an optimal sensor combination for reconstruction of a given measurement point using the POD 1.8 modes.

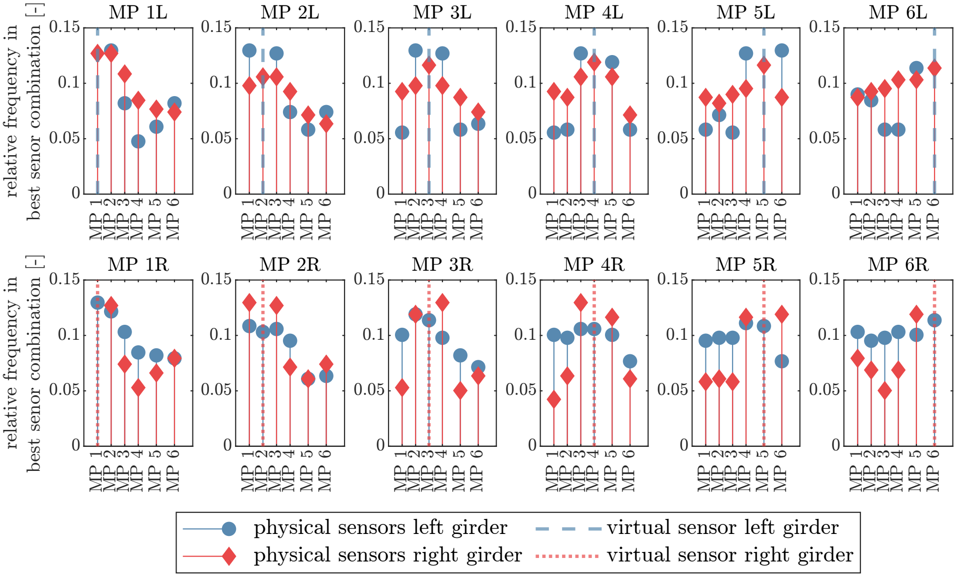

Figure 5.16 Summary of the number of occurrences of each accelerometer in an optimal sensor combination for reconstruction of a given measurement point using the FE modes

5.3.4 Sample comparisons of signals from physical and virtual sensors

To complement the analysis of virtual sensing based on experimental data gathered from the HUMVIB footbridge, selected exemplary virtual sensor signals were compared with their corresponding measured signals at the virtual sensor positions. Additionally, residuals were plotted to provide a more nuanced evaluation. These samples were strategically chosen to correspond to specific values of the coefficient of determination, R^2, thereby augmenting previous results that relied solely on R^2 values. Separate evaluations were conducted for both strain and acceleration signals.

The results for strain signals are summarised in Figure 5.17, and for acceleration signals in Figure 5.18. Notably, the analysis of virtual strain signals revealed the presence of significant outliers. These outliers are attributed to corresponding anomalies in the strain signals utilised for signal reconstruction. This observation exposes both the strengths and weaknesses of the implemented modal expansion approach. Since each time step is analysed independently, there is neither amplification nor temporal propagation of errors, thereby restricting the impact of outliers to their respective samples. However, this also makes the method sensitive to outliers. Such behaviour could potentially be mitigated through advanced pre-processing to clean the data prior to reconstruction or through post-processing to filter outliers in the virtual sensors.

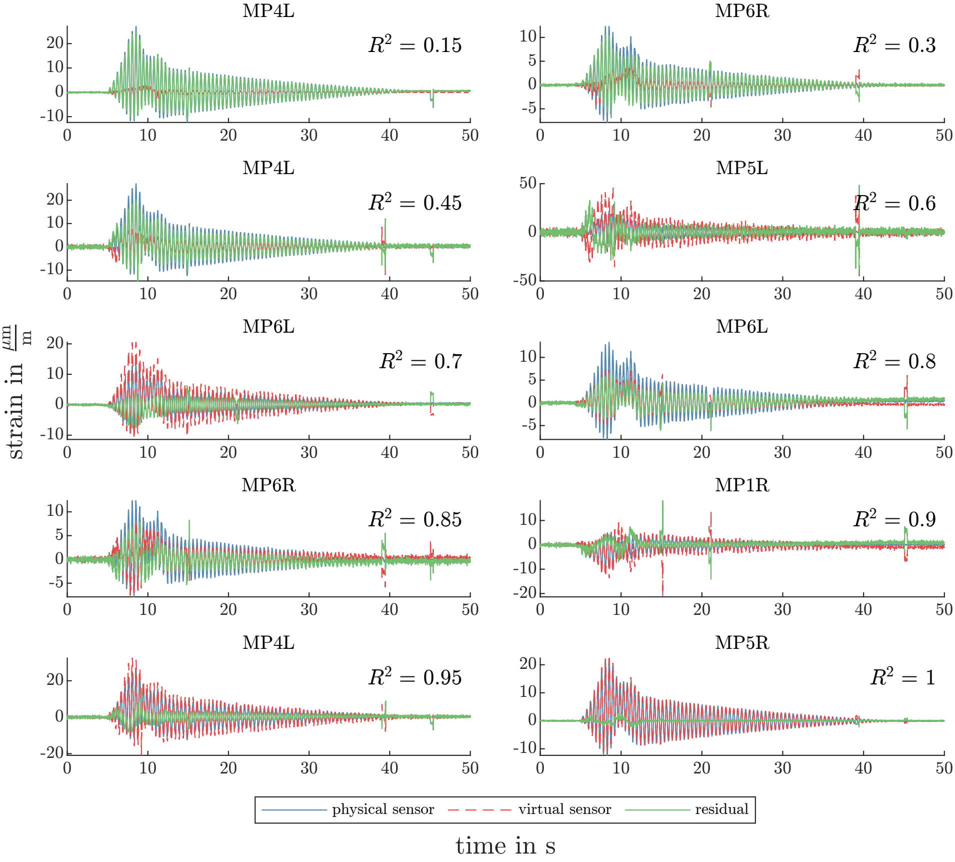

Figure 5.17 Exemplary comparisons of virtual sensor signals for the strains with those of the physical sensors for an arbitrarily chosen crossing to assess the coefficients of determination R^2. The number of FE modes considered and the sensor combination for the physical sensors were chosen to match the respective coefficients of determination.

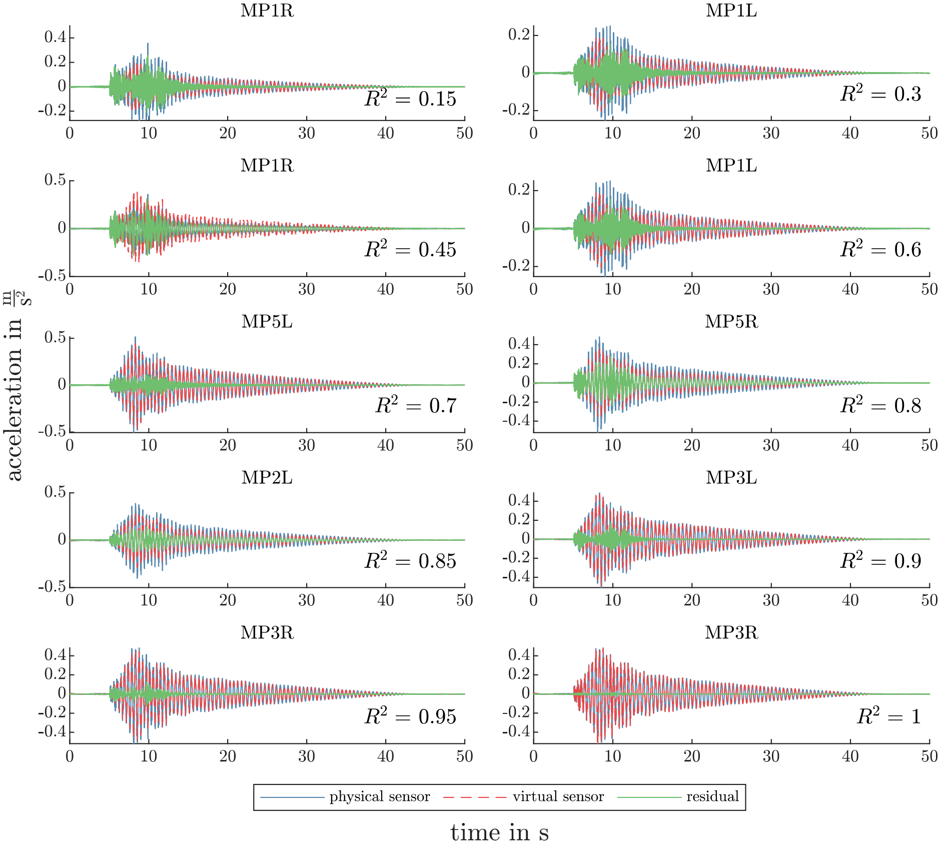

Figure 5.18 Exemplary comparisons of virtual sensor signals for the acceleration with those of the physical sensors for an arbitrarily chosen crossing to assess the coefficients of determination R^2. The number of FE modes considered and the sensor combination for the physical sensors were chosen to match the respective coefficients of determination.

5.4 Conclusion

The primary focus of this chapter was the investigation of the modal expansion as a virtual sensing techniques. Due to its straightforward structure and easy accessibility, the bridge serves as an ideal initial test subject for virtual sensing, despite not being a railway bridge. Both model based FE modes and data-driven POD modes were employed for this purpose, and the following conclusions can be drawn:

(1) The bridge's simplicity enabled easy modelling, as substantiated by the congruence between the FE modes and the beam model modes. These models were found to be interchangeable for the aims of this investigation.

(2) Alongside model-based modes, data-driven POD modes were explored. These modes are load-dependent and were generated from multiple loading scenarios. Despite these distinctions, their influence on signal reconstruction quality was found to be of minor importance.

(3) The study revealed that to achieve a specific reconstruction quality, fewer sensors and modes are required for strains as compared to accelerations. Additionally, suboptimal sensor combinations were found to improve in reconstruction quality as the number of modes considered was reduced relative to the number of deployed sensors.

(4) The coefficients of determination for virtual sensors positioned in the bridge's mid-span were generally higher compared to those situated near the supports. This suggests that signals at these mid-span locations are easier to reconstruct, especially in the case of acceleration measurements.

(5) With respect to sensor positioning, sensors located either adjacent to the measurement point or in parallel on the opposite girder were found to yield the most advantageous configurations, consistent with the high correlation observed at these locations when various mode shapes are superimposed.

(6) The implemented modal expansion approach for virtual sensing exhibited both strengths and weaknesses. While the method is resilient against the temporal propagation of errors, it is sensitive to data outliers. This sensitivity could potentially be mitigated through pre-processing or post-processing techniques.

In summary, an accurate approximation of the measured signal was attainable at all sensor locations, regardless of the mode sets considered. Efficiency in signal reconstruction could be improved, although at the expense of system stability, which refers to the sensitivity of the results to sensor configuration. Stability could be increased by reducing the number of modes considered relative to the number of sensors deployed.

6 Railway bridge Schmutter

This section presents an investigation of a particular bridge – a single-span, double-track, simply supported structure that crosses the River Schmutter in Bavaria, Germany (Figure 6.1). Situated on the route between Augsburg and Ulm, this bridge has a span of 19.5 m, while its cross-section consists of two separate steel box girders. These girders are coupled via the track ballast of the superstructure, a feature that presents complex challenges when attempting to model the dynamic behaviour of the bridge. The coupling causes the system to behave in a non-linear manner and the forces on the joint cause the ballast to degrade, resulting in white ballast being clearly visible (Figure 6.2). The experiment carried out on this structure, described in the following section, involved synchronous measurements on the bridge and on the axle boxes of an ICE 4 train passing over the bridge. Therefore, in this section virtual sensing and drive-by monitoring investigations are carried out.

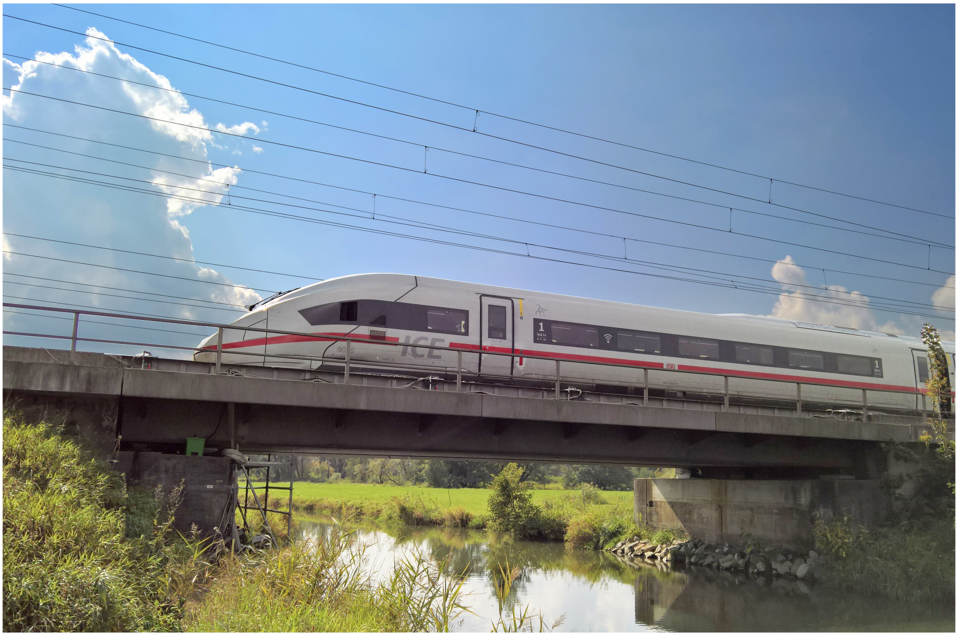

Figure 6.1 Instrumented railway bridge Schmutter with instrumented ICE 4 on it (Photo: Hagen Berthold, Image editing: Robert Akerboom).

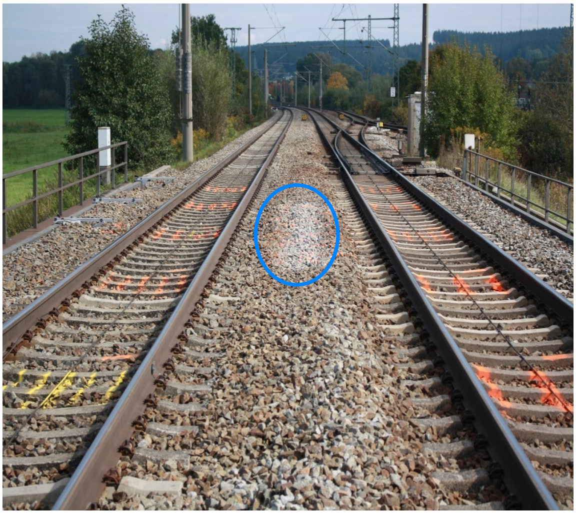

Figure 6.2 White ballast in the coupling joint (photo: Hagen Berthold).

6.1 Experimental set-up and execution

The measurement campaign was conducted due to the introduction of ICE 4 in 2017. Full details of the background to the measurement are provided by FIRUS et al. (2018) and FIRUS (2023). This description focuses on aspects that are essential for understanding the analyses presented in this thesis.

The field measurements were carried out from 23 to 27 September 2017. They took place between 9:00 and 17:00 each day. The weather was consistently sunny, with temperatures between 10 and 20 °C, except for the first seven runs on 27 September 2017, when the sky was overcast. The period was dry with no precipitation.

The bridge contained a dense array of 44 accelerometers, whose specifications are tabulated in Table 6.1. The sensors were placed at 1.95 m intervals along eleven structural axes, each with two parallel sensor lines on the upper flanges of the main girders. Due to the unavailability of some sensors for all crossings, a subset of 37 consistently present sensors was used for analysis (Figure 6.3). The individual sensors are henceforth referred to by their intersection points on the structural axes depicted in Figure 6.3. For instance, the sensor located at the intersection of axis $\boxed{\text{A}}$ and axis $\boxed{6}$ is designated as A6.

Laser vibrometers were used to measure the vertical displacement at two points in the third of the total span. All sensors were connected to HBM MX840B amplifiers, recording data at 1,200 Hz.

In addition to the bridge, the 12-car ICE 4 train used for the test runs was instrumented with eight accelerometers on the axle boxes of cars 8 and 9 (Figure 6.6), whose specifications are tabulated in Table 6.2. The sensors were connected to an HBM 1-ML801B amplifier and the signals were recorded at a sampling rate of 2,400 Hz.

A total of 52 crossings, 26 in each direction, were made during the test period. The axles were detected by photoelectric sensors installed on both sides of the bridge, so that the speed travelled and the position of the axle could be determined at any time of the measurement, assuming a constant speed (Figure 6.5). The assumption of constant speed is supported, as the driver followed set speed instructions and speed variations in the study area were minimal.

To synchronise the bridge and train measurements, coils and magnets were attached to the rails and to the vehicle. This configuration triggered the measurement system when the magnets passed over the coils.

The axle configuration of the ICE 4 is shown in Figure 6.7. The length over buffer required for the frequency identification method described in subsection 4.2.1 is $l_{\mathrm{ob}} = 28.75$ m.

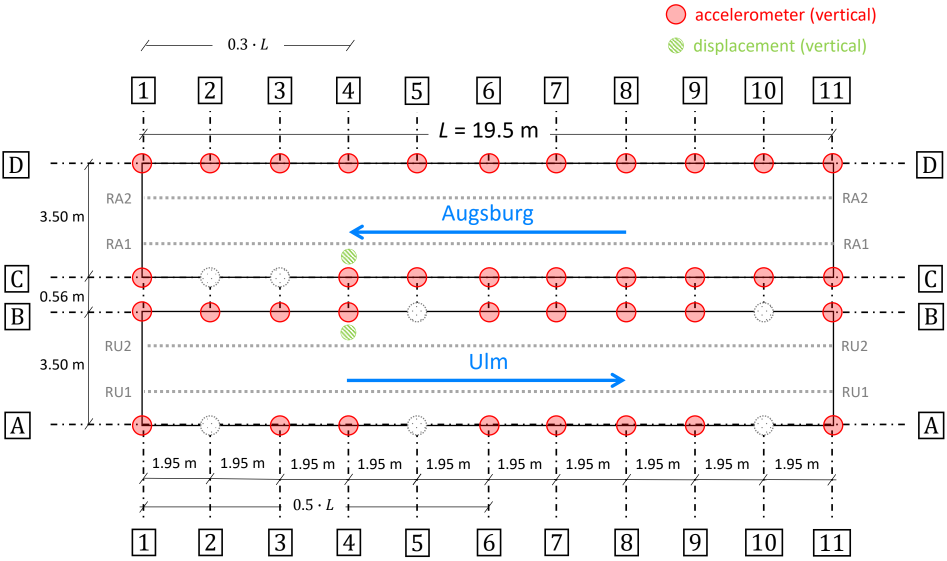
accelerometer (vertical)
displacement (vertical)
0.3 · L
L = 19.5 m
1
2
3
4
5
6
7
8
9
10
11
D
C
B
A
3.50 m
0.56 m
3.50 m
RA2
RA1
RU2
RU1
Augsburg
Ulm
1.95 m
0.5 · L

Figure 6.3 Sensor positions on the Schmutter bridge.

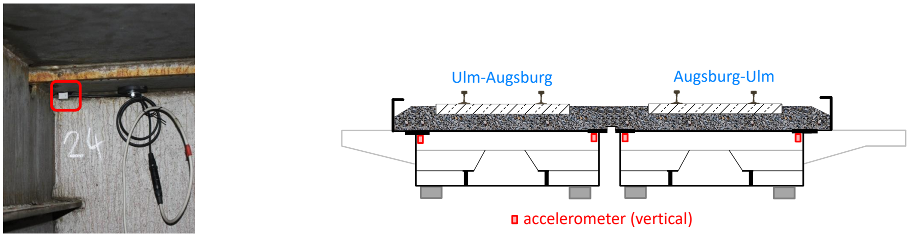
Ulm-Augsburg
Augsburg-Ulm
accelerometer (vertical)

(a) installed sensor (photo: Hagen Berthold)

(b) Cross-section of the Schmutter bridge with indication of sensor position.

Figure 6.4 Illustration of the sensor placement in cross-section.

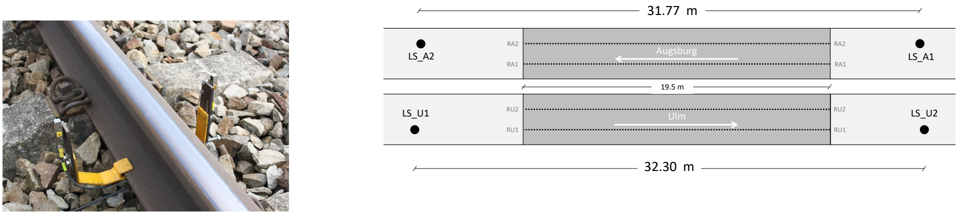
31.77 m
LS_A2
RA2
RA1
Augsburg
RA2
RA1
LS_A1
19.5 m
LS_U1
RU2
RU1
Ulm
RU2
RU1
LS_U2
32.30 m

(a) installed sensor (photo: Hagen Berthold)

(b) Overview of the sensor positions

Figure 6.5 Photoelectric sensors for axle detection and speed measurement.

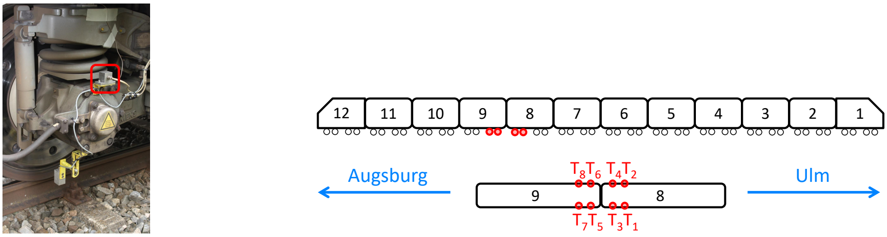
12
11
10
9
8
7
6
5
4
3
2
1
Augsburg
$T_8 T_6$ $T_4 T_2$
Ulm
9
8
$T_7 T_5$ $T_3 T_1$

(a) installed sensor (photo: Hagen Berthold)

(b) Sensor placement on ICE4

Figure 6.6 Instrumentation of the ICE 4 with acceleration sensors on the axle boxes.

Table 6.1 Accelerometers installed on the Schmutter bridge.

position	sensor	measurement range in g	sensitivity in mV/g
A1, A3, A4, A6, A7, A8, A9, A11, B1, B3, B4, B6, B7, B8, B9, B11	PCB-TLD393B04	± 5	1000
D1, D11, C1, C11	PCB-TLD356A17	± 10	500
D2, D3, D4, D5, D6, D7, C4, C5, C6, C7	EGCS-D1SM-5-/V2.5/C	± 5	-
D8, D9, D10, C8, C9, C10	EGCS-D1SM-5-/V05/X	± 5	9697
C2, C3, B5, B10, A2, A5, A10	Dytran 3191A	± 2.5	5000
B2	Dytran 3233A	± 10	1000

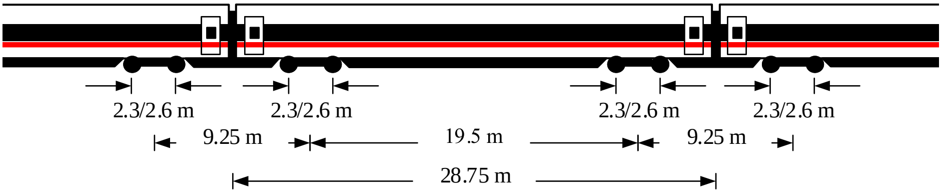

Figure 6.7 Axle configuration of the ICE 4 from (FIRUS, 2023). The axle spacing of a bogie depends on whether it is a powered car (2.6 m) or an unpowered car (2.3 m). The length over the buffers $l_{\mathrm{ob}} = 28.75$ m.

Table 6.2 Accelerometers installed on the ICE 4.

label	sensor	measurement range in g	sensitivity in mV/g
T1	Setra	100	1002.0
T2	Setra	100	992.5
T3	Setra	100	972.5
T4	Setra	100	987.0
T5	FGP	100	506.9
T6	FGP	100	512.6
T7	FGP	100	506.8
T8	FGP	100	500.5

6.2 System identification and structural model

This subsection discusses the system identification through modal analysis, the determination of the bridge's resonance frequency via a resonance curve, and the structural model employed.

6.2.1 Modal analysis

The bridge, with its short span, ballasted superstructure, and coupled main structures, exhibits a pronounced nonlinear system behavior, as evidenced by amplitude-dependent modal frequencies. This nonlinearity contravenes the assumption of a linear time-invariant system, rendering the modal parameters obtained from OMA at small amplitudes inadequate for describing the system at higher amplitudes. Thus, the free decay phases for each run were determined using photoelectric sensors and were subjected to modal analysis through automated SSI .

While automation was largely achieved with an existing code (CHEYNET, 2020), manual intervention was necessary for cases where the first detected mode was not the first bending mode. For these cases, the stabilization diagram was manually evaluated to obtain the modal parameters.

The first bending mode frequency, obtained from the free decay phase signals of each run, is depicted in Figure 6.8, plotted against the maximum deflection at the third point of the main structure during the free decay phase and the speed of travel. Notably, the frequency of the first bending mode decreases as amplitude increases and significantly drops around the resonance speed of 175 $\frac{\text{km}}{\text{h}}$.

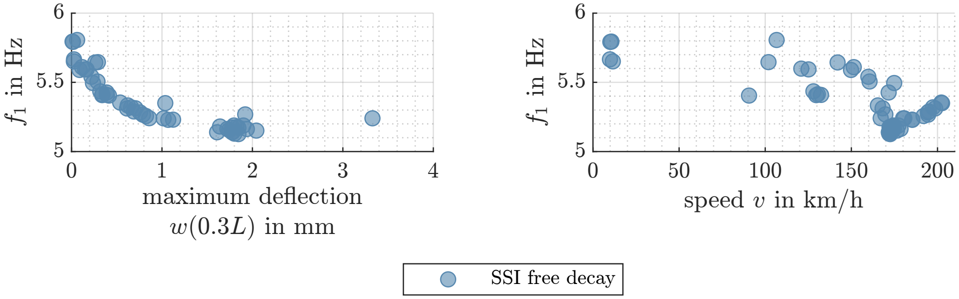

Figure 6.8 Frequency of the first bending mode identified with SSI from the free decay signals of each passage.

For the run towards Ulm with 10 $\frac{\text{km}}{\text{h}}$ the mode shapes and the corresponding frequencies up to 30 Hz are shown in Figure 6.9. The mode shapes clearly show the strong coupling resulting from the common superstructure.

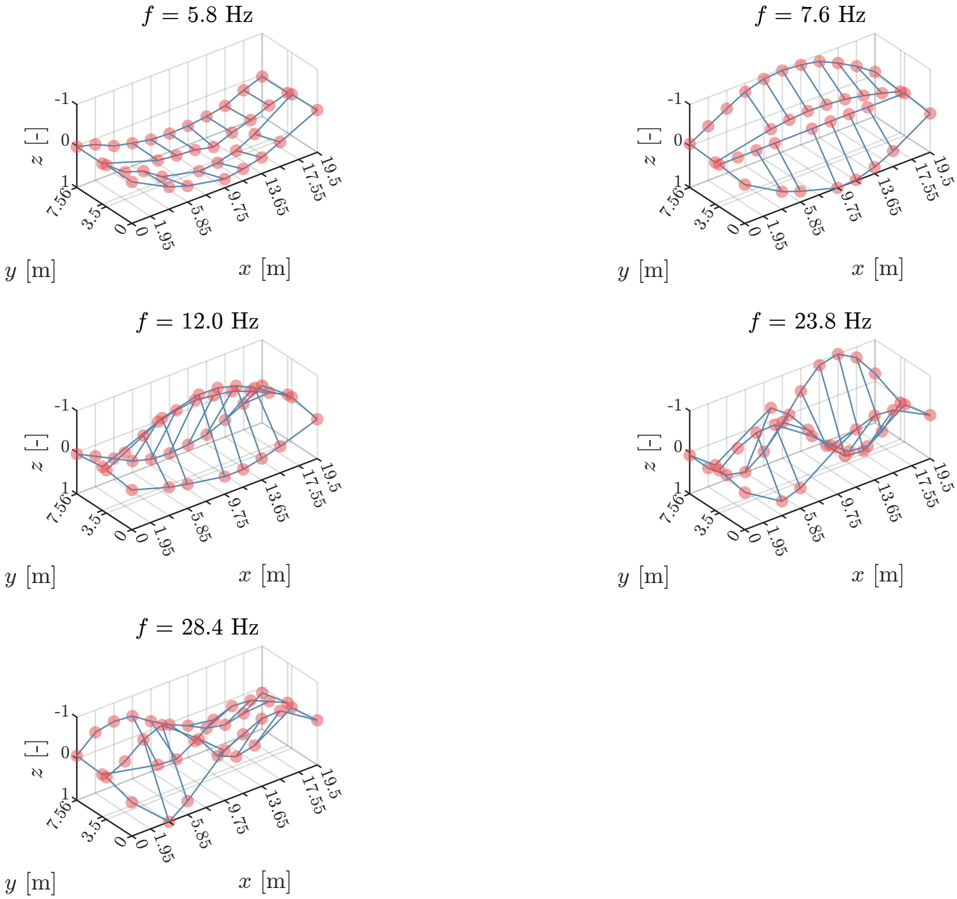

Figure 6.9 Mode shapes identified with the SSI with the free decay signals after a passage in direction of Ulm with $v = 10\ \frac{\text{km}}{\text{h}}$.

6.2.2 Resonance curve

An alternative method of frequency determination involves the use of the resonance speed equation (Equation 2.30) and the resonance curve, obtained using bridge sensors and travel speeds, as previously applied to this measurement campaign (FIRUS et al., 2018; REITERER et al., 2021; FIRUS, 2023). Figure 6.10 shows the maximum absolute acceleration values at the span's midpoint for each main girder, plotted against train speeds. The resulting resonance peaks yield frequencies of 5.11 Hz and 5.00 Hz in the direction of Ulm and Augsburg, respectively. These values align well with the slightly higher frequency values of approximately 5.15 Hz, derived from the corresponding free decay phases through SSI. The higher SSI frequency, compared to the resonance curve evaluation, can be attributed to the influence of the additional train mass contained in the resonance curve and the decrease in amplitude during the free decay, which results in frequency averaging with SSI.

Two outliers can be seen in the resonance curves in Figure 6.10, both in the direction of Ulm and at speeds of 90.6 $\frac{\mathrm{km}}{\mathrm{h}}$ and 171.6 $\frac{\mathrm{km}}{\mathrm{h}}$. The outliers are due to the traffic in the opposite direction on the bridge during the crossing.

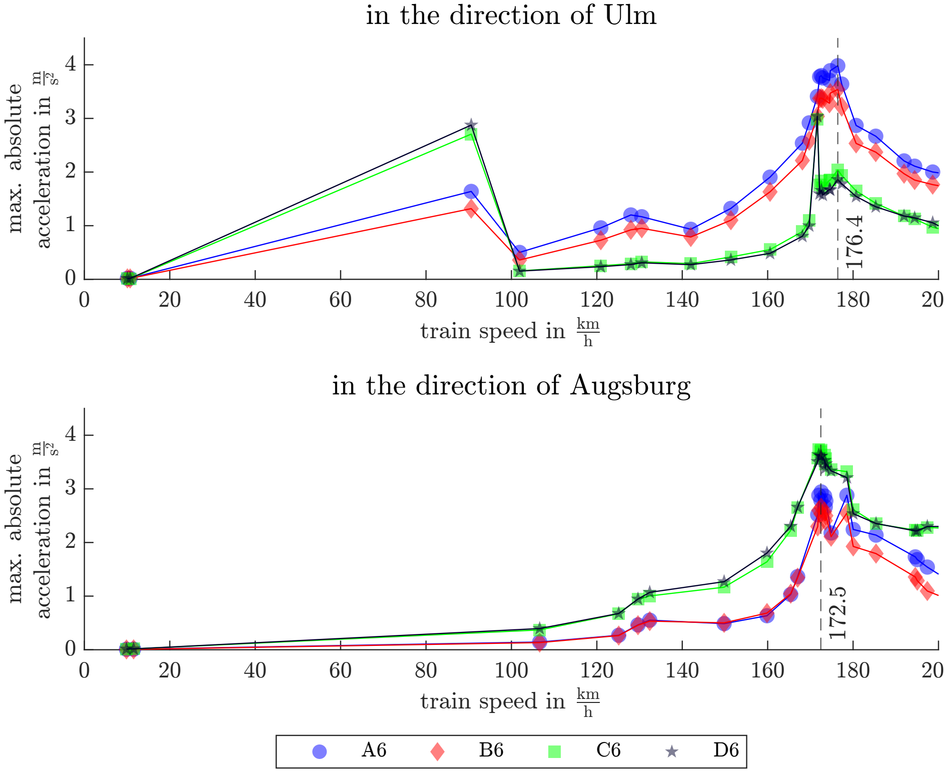

Figure 6.10 Direct resonance curves, maximum absolute acceleration with a low-pass filter with a cut-off frequency of 8 Hz, as a function of train speed for the four mid-span sensors A6 to D6, separately for each direction.

6.2.3 FE model

The structural model of the bridge was developed using a 3D FE model. This model consists of 530,220 degrees of freedom and was created with SOFiSTiK 2020 software, using shell elements(Figure 6.11). The model's design was based on the structure's blueprints. The model and the free parameters for the springs are based on the specifications by FIRUS (2023), which have been shown to yield accurate results for large amplitudes. However, it should be noted that the model is not capable of accurately representing the frequency shift associated with smaller amplitudes, and therefore the free decay phase as indicated by Firus (2023, p. 226). The free parameters were selected such that the model's first bending frequency matched the specified frequency from the resonance curves, and the deflections at the two measured one-third points were in good agreement (Firus, 2023).

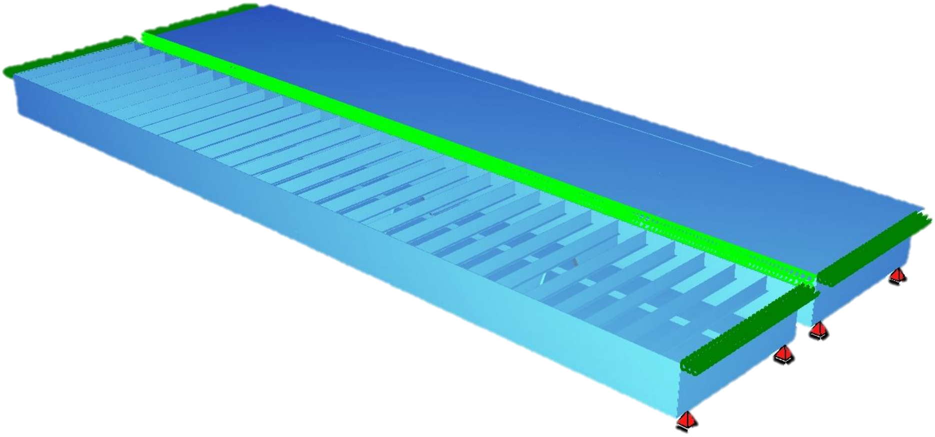

Figure 6.11 Illustration of the FE model of the structure used. The cover plate of a box girder is hidden to illustrate the modelling of the interior

The previously described coupling through the ballast superstructure renders the bridge an ideal subject for testing the substructuring technique discussed in section 3.1. Substructuring refers to the modelling of specific sections of the structure for modal expansion. Consequently, two configurations of the described FE model were employed for modal analysis: one involved the coupled hollow boxes, while the other examined the hollow boxes without interconnection.

For the identification of relevant modes, all bending and torsional modes were manually selected within a frequency range up to 30 Hz. The resultant mode shapes for the coupled model are illustrated in Figure 6.12. The chosen bending and torsional modes corresponding to the hollow box with the track oriented in the direction of Ulm are presented in Figure 6.13. Similarly, the modes resulting from the hollow box with the track oriented towards Augsburg are depicted in Figure 6.14.

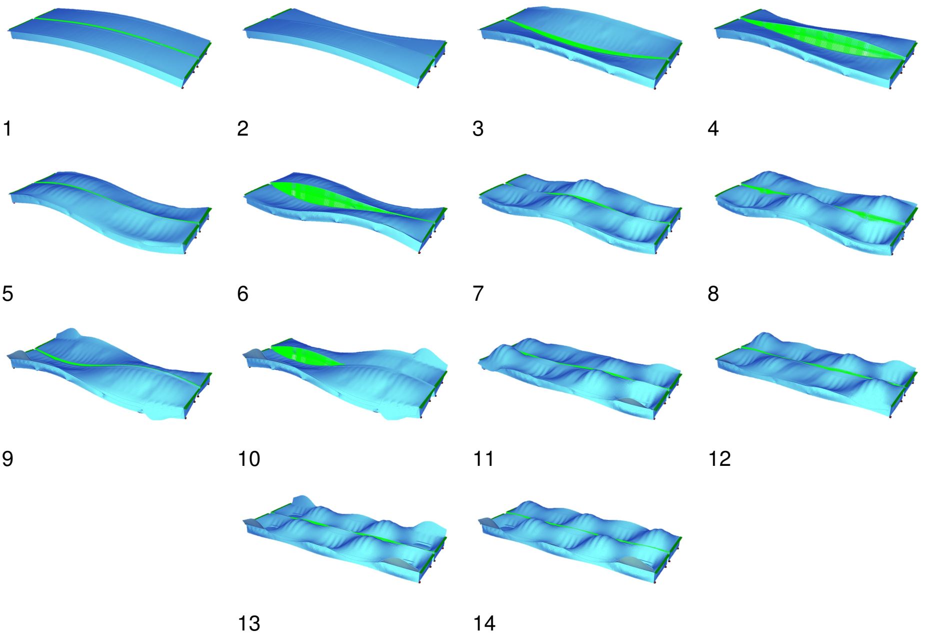
1
2
3
4
5
6
7
8
9
10
11
12
13
14

Figure 6.12 Mode set of the selected bending and torsional modes of the coupled model.

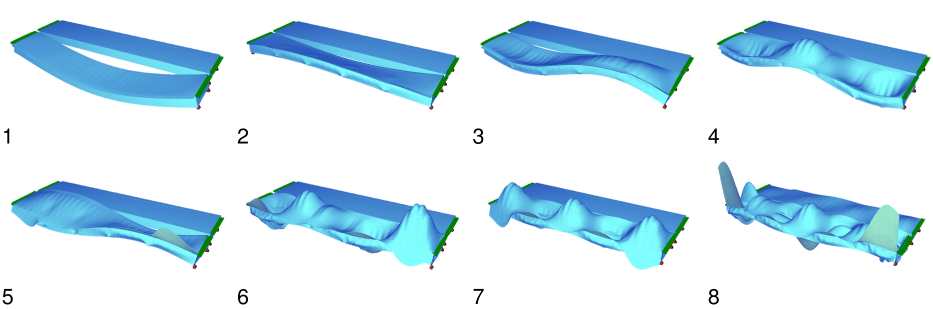

Figure 6.13 Mode set of the selected bending and torsion modes of the uncoupled model towards Ulm.

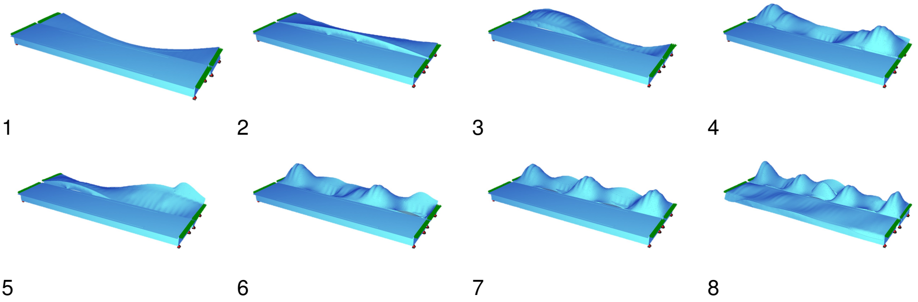

Figure 6.14 Mode set of the selected bending and torsion modes of the uncoupled model towards Augsburg.

6.3 Virtual sensing

Due to the large number of sensors used in this study and the many possible combinations, performing leave-p-out validation becomes impractical. Therefore, the analysis in this chapter is limited to leave-one-out validation, which removes the need to choose specific sensor combinations.

6.3.1 Coupled versus uncoupled model

To assess the performance of the coupled model in comparison to the uncoupled model, a leave-one-out validation was conducted for each sensor using the 52 passages of the ICE 4 train. Two sets of modes were employed, one derived from the coupled model and another from the uncoupled model.

In the leave-one-out validation with the coupled model, all 36 remaining sensors were employed alongside the complete set of modes, as depicted in Figure 6.12. For the validation using the uncoupled model, modes from the hollow box carrying the track in the direction of Ulm were used with sensors on axes $\boxed{\text{A}}$ and $\boxed{\text{B}}$, as shown in Figure 6.13. Conversely, sensors on axes $\boxed{\text{C}}$ and $\boxed{\text{D}}$ were evaluated using modes from the hollow box carrying the track towards Augsburg, as illustrated in Figure 6.14.

Performance comparison between the coupled and uncoupled models for modal expansion was carried out by evaluating the coefficient of determination for each sensor, represented in the form of boxplots[1]. The results for both models and each sensor are compiled in Figure 6.15. The evaluation is organised according to sensor positions on the structure, with corresponding designations of the structural axes provided. Points where no sensor data were available for all passages are indicated in grey, analogous to the representation of the bridge's instrumentation in Figure 6.3.

---

[1] The displayed boxplot indicates the median (inner line within the box), upper and lower quartiles (box edges), and any potential outliers (marked with '.'). Outliers are defined as values that are more than 1.5 times the interquartile range (IQR) away from the box.

Upon examining the box plots depicted in Figure 6.15, it is observed that both models fail to provide accurate signal reconstruction over the supports at axes $\boxed{1}$ and $\boxed{11}$. Due to the chosen y-axis limits of 0 to 1, the majority of the results are not visible as the coefficients of determination R^2 are negative. Generally, it is found that for both models, the results near the supports are slightly inferior to those at the field centre, albeit with some occasional deviations such as at position D6.

In addition to the effect of higher eigenmodes being more relevant for accelerations than for strains, as discussed in the HUMVIB Bridge section chapter 5 and further elaborated in section 2.9, another factor merits consideration. Namely, the modelling of the supports, which are represented as rigid supports, lacks flexibility. Consequently, the load application near the supports is inadequately modelled. Moreover, the springs located at the top of the hollow boxes above the bearings do not provide a realistic representation in terms of local load application. However, this effect diminishes according to the principle of St. Venant[2] and is thus confined to the vicinity of the supports.

When comparing the models to each other, it is noted that the outcomes vary significantly depending on the structural axis. Specifically, the uncoupled model outperforms the coupled model on axes $\boxed{\text{A}}$ and $\boxed{\text{B}}$, which corresponds to the side of the structure carrying the track towards Ulm. Conversely, the coupled model yields slightly better results on axes $\boxed{\text{C}}$ and $\boxed{\text{D}}$, which carry the track in direction of Augsburg.

To quantify and more precisely capture the differences between the coupled and uncoupled models, the difference in the coefficient of determination R^2 was calculated for each sensor position as follows: $R^2_{\text{coupled}} - R^2_{\text{uncoupled}}$. Positive values indicate superior performance by the coupled model, while negative values suggest that the uncoupled model is more effective. However, this interpretation does not hold for axes $\boxed{1}$, $\boxed{2}$, $\boxed{10}$, and $\boxed{11}$, where also negative coefficients of determination were observed. The evaluation is presented in Figure 6.16.

A slight superiority of the uncoupled model's approach is observed. For sensors located on the side carrying the track towards Ulm (axes $\boxed{\text{A}}$ and $\boxed{\text{B}}$), the uncoupled model yields better results. Conversely, for sensors on the side carrying the track in the direction of Augsburg (axes $\boxed{\text{C}}$ and $\boxed{\text{D}}$), better results are predominantly achieved with the coupled model. However, exceptions are noted at positions D7, D8, and C8, where the uncoupled model leads to superior outcomes.

---

[2] *"...states that if the forces acting on a small portion of an elastic body are replaced by a statically equivalent system of forces on the same portion of the surface, this redistribution of loading produces substantial changes in the stresses locally but has a negligible effect on the stresses at distances which are large in comparison with the linear dimensions of the surface on which the forces are changed."* (TIMOSHENKO, 1951, p.33)

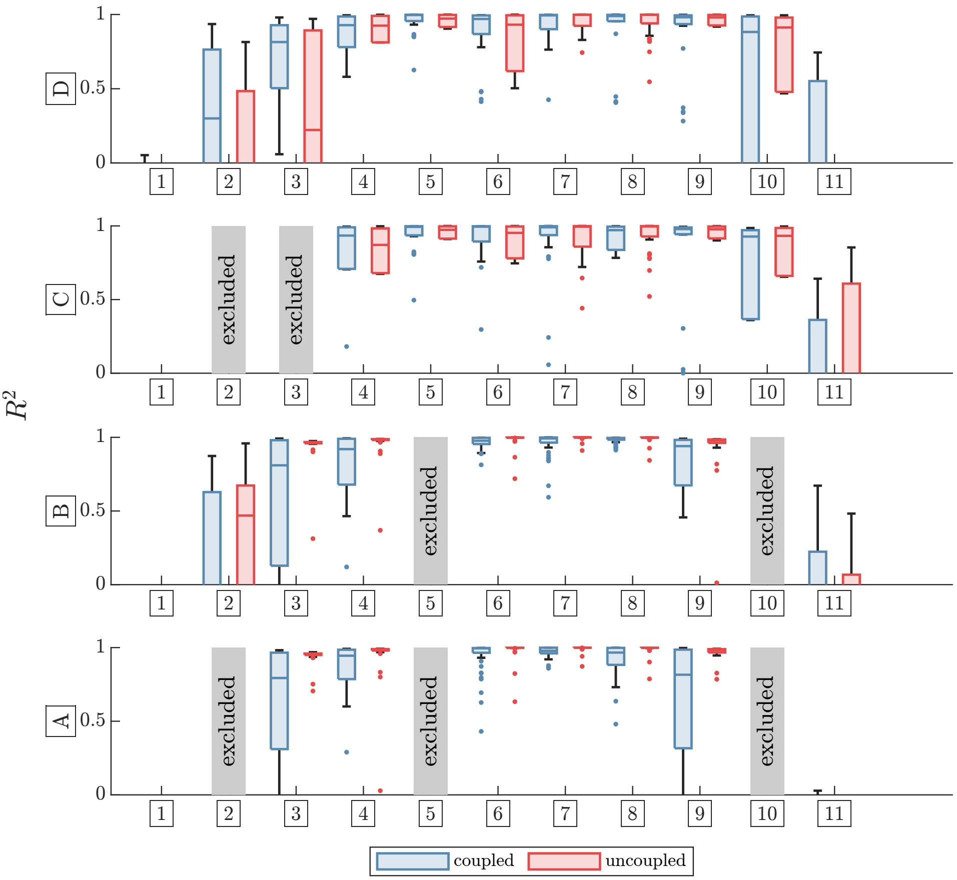

Figure 6.15 Comparison of the coefficients of determination for the coupled and the uncoupled model. For each sensor, the coefficients of determination of the leave-one-out validation are compared for all crossings.

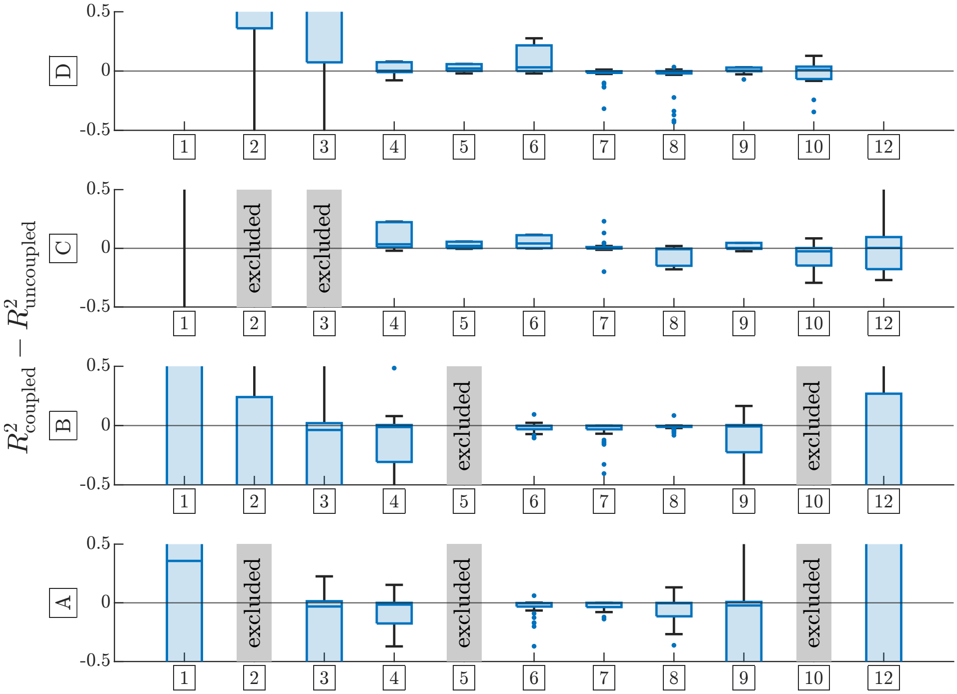

Figure 6.16 Differences in the coefficients of determination R^2 for the coupled and uncoupled model of the leave one out validation for each sensor.

6.3.2 Impact of train speed

To evaluate the influence of train speed on the quality of signal reconstruction by the virtual sensors, the results of the leave-one-out validation were examined for each sensor position, segregated by train speed, direction of travel, and model type (coupled vs. uncoupled). The findings of this analysis are presented in Figure 6.17. It is observed that no clear correlation exists between the coefficients of determination for the virtual sensors and the speed of the ICE 4 train. Interestingly, a significant drop in the coefficients is noted at speeds above approximately 180 $\frac{\mathrm{km}}{\mathrm{h}}$, which are beyond the resonance speeds (172.5 $\frac{\mathrm{km}}{\mathrm{h}}$ towards Ulm / 176.4 $\frac{\mathrm{km}}{\mathrm{h}}$ towards Augsburg). However, at 200 $\frac{\mathrm{km}}{\mathrm{h}}$, the coefficients of determination return to values close to 1.0. A plausible explanation for this behaviour could be the activation of a vibration mode in this speed range, which is not covered by the chosen modes of the model.

From the analysis, no clear functional relationship between the train speed and the coefficients of determination can be discerned. Nevertheless, it is evident that while good results may be achieved across a broad range of speeds, there can be specific speed ranges where the quality of signal reconstruction is substantially reduced.

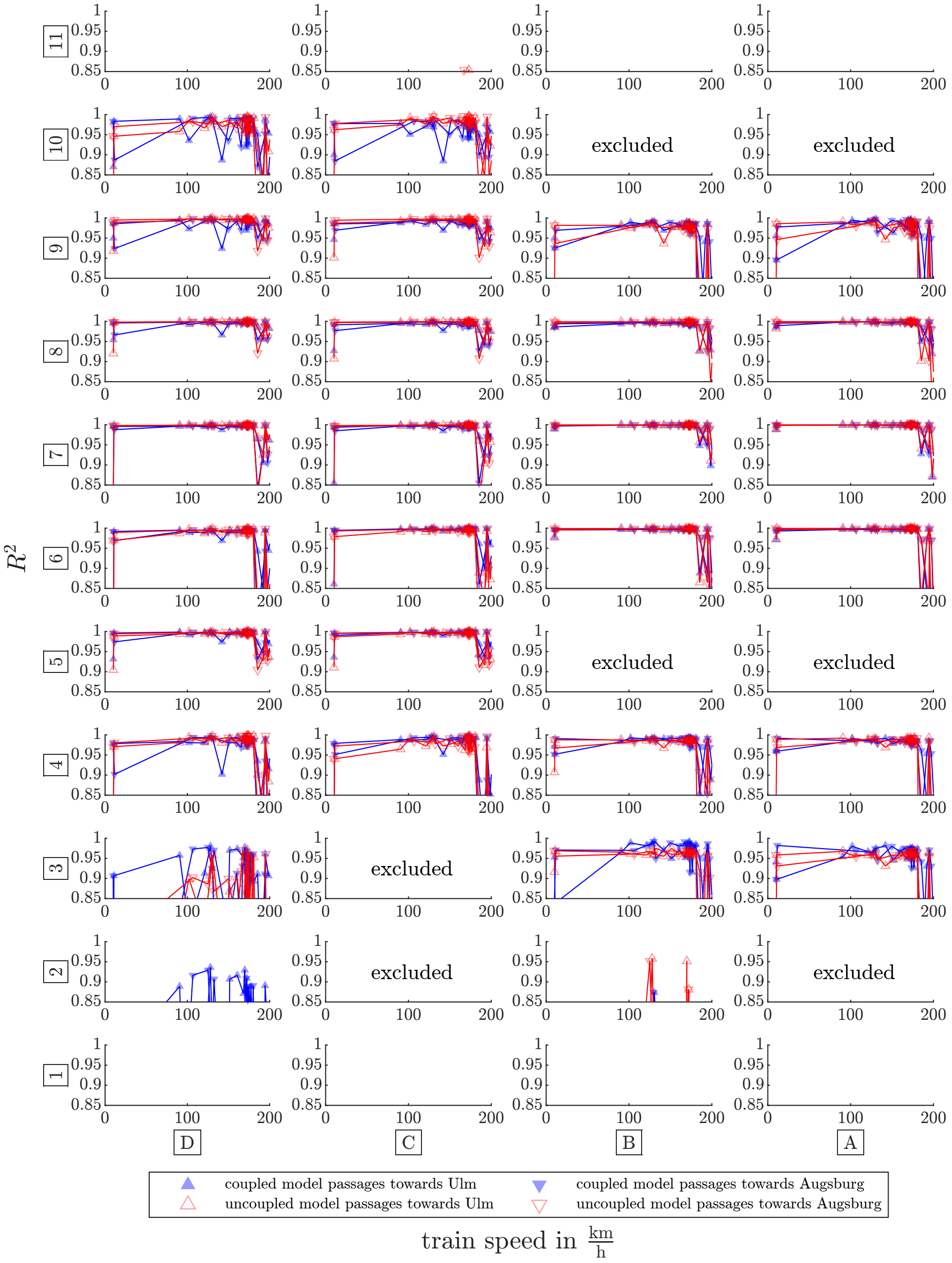

Figure 6.17 Coefficients of determination R^2 of the leave-one-out validation as a function of train speed for each sensor, segregated by direction of travel and model type.

6.3.3 Sample comparisons of signals from physical and virtual sensors

To extend the analysis of virtual sensing based on the experimental data from the Schmutter bridge, selected representative virtual sensor signals were compared with their measured counterparts at the corresponding sensor locations. For a more comprehensive evaluation, the residuals between the measured and virtual signals were also plotted. These sample signals were strategically chosen to correspond to specific values of the coefficient of determination, R^2, thereby enriching the preceding analyses that relied solely on R^2 values.

The results are presented in Figure 6.18, highlighting the effectiveness of modal expansion as a virtual sensing technique. In the last row of the plot, the analysis for position C9 is displayed on the left, with a coefficient of determination $R^2 = 0.95$. It is evident that the model can adequately reconstruct the complex oscillation pattern observed during the slow passage. On the right-hand side of the same row, an analysis for position A7 with a coefficient of determination $R^2 = 1.00$ is shown.

This demonstrates that the same linear model effectively reconstructs signals at both high amplitudes and during the free decay phase without any phase shift. This capability is attributed to the use of only the modes in modal expansion, as opposed to using a full physical model that includes frequencies and damping. Therefore, when using modal expansion, independent frequency adjustments for each mode are possible.

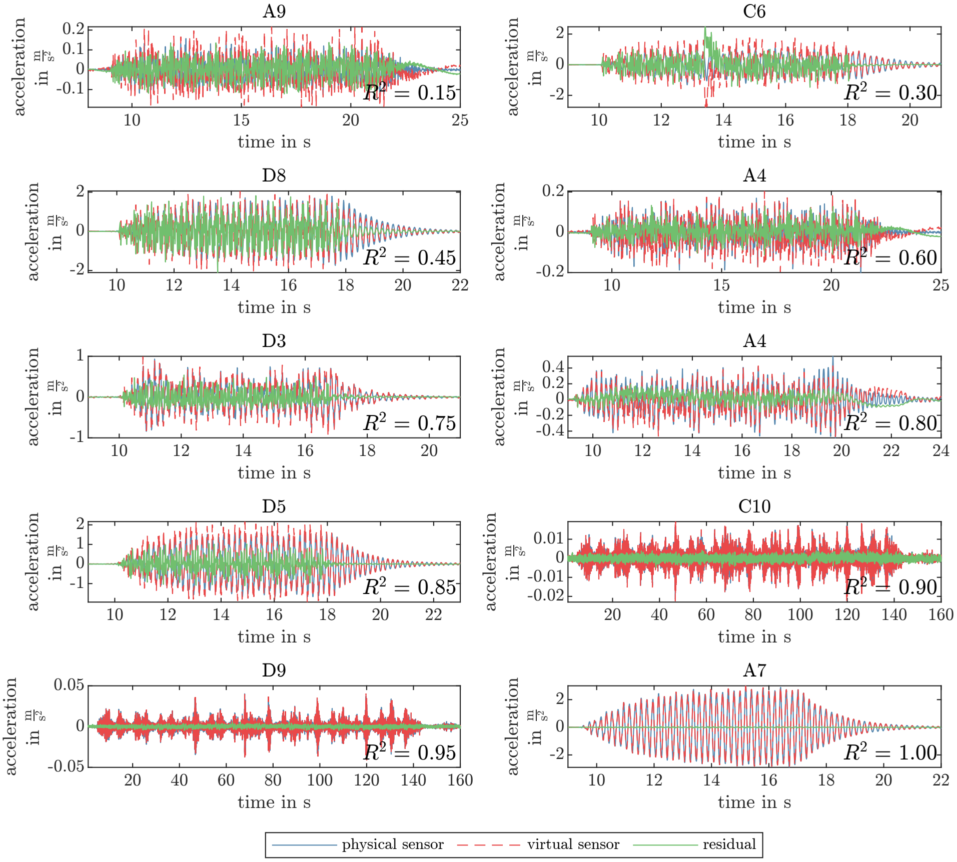

Figure 6.18 Exemplary comparisons of virtual sensor and physical sensor signals to assess the coefficients of determination.

6.4 Drive-by monitoring

The following subsection uses the data from the previous detailed experiment to validate the frequency identification method described in section section 4.2. The acceleration signals recorded at the axle boxes of the ICE 4 are analysed, with 26 crossings available for each direction. These are analysed separately for the directions of Augsburg-Ulm and Ulm-Augsburg. This approach is necessary because of the 48 axles of the 12-car train, only four axles – those of cars 8 and 9 – are instrumented, as shown in Figure 6.6.

This means that in the direction of Ulm, only axles 31 to 34, which cross the bridge, can record acceleration signals. Conversely, in the direction of Augsburg, only the 15th to 18th axles crossing the bridge are instrumented. This means that the bridge is excited differently before the signal is recorded in each direction. The longer excitation in the direction of Ulm makes it more likely that the bridge is already in a steady state.

The contact times of the instrumented axles for resonance passages in both the direction of Ulm and Augsburg are depicted in Figure 6.19 to illuminate these dynamics. The filtered acceleration signals for these runs are presented at points A6 (Ulm) and D6 (Augsburg). A 4th order Butterworth low pass filter with a cut-off frequency of 8 Hz was applied. For the journey towards Ulm, where the instrumented axles are the 31st to 34th axles to cross the bridge, it can be seen that the bridge has already reached a steady state. In contrast, for the journey towards Augsburg, with the instrumented axles as the 15th to 18th to cross, the bridge is not yet in the steady state at this time. For both directions, different approaches to get the indirect resonance curves are investigated in this section. As delineated in subsection 4.2.2, two primary approaches can be utilized. Either the recorded acceleration signal may be utilised to extract extreme values from the signal sequences during each axle's contact time, or a residual signal may be generated by subtracting the signal of one axle from that of a subsequent axle. The residual signal can then be used to extract the extreme values of the resulting acceleration. For both approaches, the influence of the low-pass filter's cut-off frequency is examined.

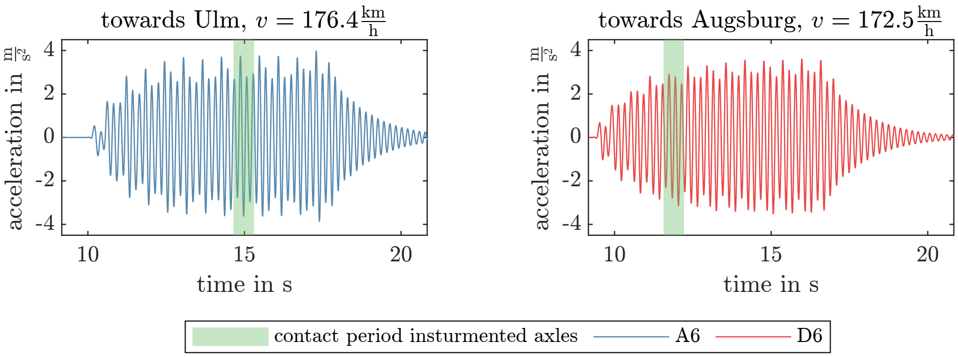

Figure 6.19 Comparison of the contact periods for the resonance crossing in the direction of Ulm and Augsburg.

The generated indirect resonance curves are used to identify the frequency as described in subsection 4.2.1, and are also compared with the direct resonance curves generated with the sensors attached to the bridge.

6.4.1 Influence of the cut-off frequency of the low-pass filter on the indirect resonance curve

As outlined in subsection 4.2.2, it is advised to apply a low-pass filter to the signals. The cut-off frequency of this filter should exceed the anticipated fundamental frequency of the bridge. Hence, the impact of altering the cut-off frequency of the low-pass filter was examined. In this examination, the cut-off frequency was varied between 6 Hz and 30 Hz, which approximately lies 1 Hz above the fundamental bridge frequency, up to the limit defined by DIN EN 1990:2021-10 A2.4.4.2.1 (4) (DIN, 2021)[3]. Under these varied filter settings, indirect resonance curves were computed for all sensors and residual signals in both directions.

Figure 6.20 presents the indirect resonance curves for runs in the Ulm direction. These curves represent the sensor signal T_3 and the residual signal $T_3 - T_1$ under different filter settings.

The comparison reveals that the speed dependence of the accelerations, as described in section 2.10, can be minimized by selective filtering. This allows a resonance peak to be found even when using a single sensor signal. However, this approach is sensitive to the choice of filter settings. Analysis of residual signals reveals that the choice of cut-off frequency affects the amplitudes. Unlike the analysis of the single sensor signal, the shape of the resonance curve and the peak is relatively unaffected by the choice of cut-off frequency. This outcome is anticipated because the subtraction of the signal from the preceding axle largely compensates for the speed-dependent effects.

The results of this evaluation for all sensor and residual signals, in both the Ulm and Augsburg directions, are compiled in Fig. B.12 to B.15. As the comparison indicates, the same observations apply to all signals and both directions. However, no residual signals could be determined for signals T_5, T_7, T_4, and T_6. This is because these signals are too dissimilar, and no corresponding cancellation of accelerations occurs due to phase shift.

---

[3] see section 2.8

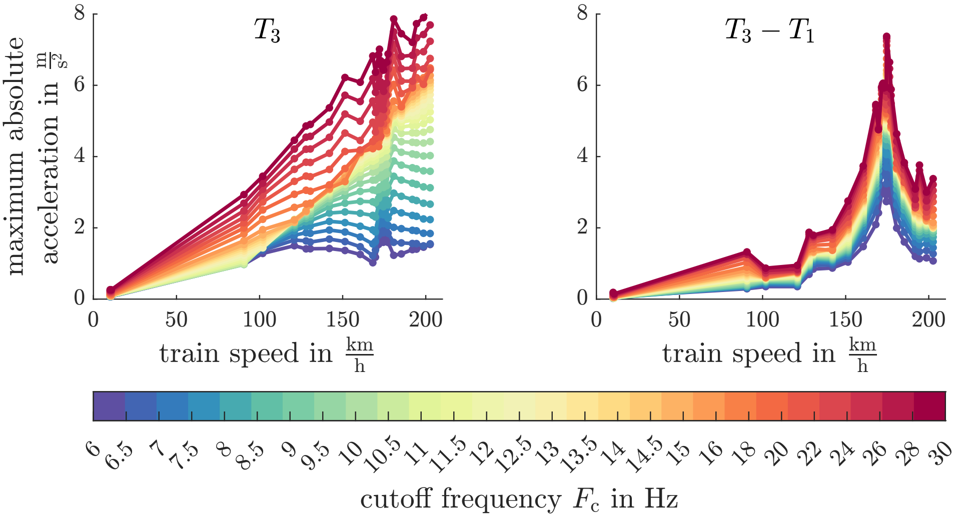

Figure 6.20 Comparison of the influence of the cut-off frequency of the low-pass filter on the indirect resonance curve of the sensor signal T_3 and the residual signal $T_3 - T_1$ for runs in the direction of Ulm.

6.4.2 Frequency identification

The frequency identification at this point is conducted using the indirect resonance curves, as outlined in subsection 4.2.1. This process involves evaluating all resonance curves, including those of the sensor signals and the residual signals, using a 4th-order Butterworth low-pass filter with a cut-off frequency of 8 Hz. Evaluations for the direction of Ulm and Augsburg are shown in Figure 6.21 and Figure 6.22, respectively. For each curve, the maximum value is marked and interpreted as the resonance speed. In 6 out of the 8 evaluations of the residual signals, a second peak is visible, which can be used to determine the value for i in Equation 4.10 based on Equation 4.9. For all cases, $\hat{\imath} = 3$ and $\hat{\jmath} = 4$ are the results. Therefore, by inserting $i = 3$ and $l_{\mathrm{ob}} = 28.75$ m for frequency identification, the frequencies displayed in Table A.9 are obtained. The relative errors refer to the reference frequencies for the resonance speed of the direct resonance curves acquired with the bridge sensors.

An examination of the measured values from the individual sensors reveals a divergence from the bridge measurements in both directions. For the quantitative assessment of the differences, the percentage error was determined. Let $f_{\mathrm{train}}, f_{\mathrm{bridge}} \in \mathbb{R}^+$. The percentage error $E_\%$ is:

$$E_\% = \frac{f_{\mathrm{train}} - f_{\mathrm{bridge}}}{f_{\mathrm{bridge}}} \cdot 100\% \qquad (6.1)$$

In this context, f_{train} represents the frequency determined with the sensors on the train, and f_{bridge} stands for the frequency detected with the sensors on the bridge. Thus, the value of f_{bridge} is considered to be the true value or target value. When calculating the percentage error, the absolute value of the difference was not used in order to preserve the sign. This makes it clear whether the true values are being overestimated or underestimated. Negative values therefore indicate an underestimation of the true value, while positive values represent an overestimation of the true value.

The percentage errors of the individual sensors fluctuate between -3.2 % and 17.2 %. In the direction of Augsburg, the sensors T_3, T_4, T_7, and T_8 exhibit the most substantial deviation at 17.2 %, whilst the sensor T_2 in the same direction presents the most significant negative deviation at -3.2 %. In the direction of Ulm, the discrepancies are generally smaller, ranging between -1.0 % and 2.4 %. This variation can be attributed to the differing states of the bridge during the contact period for the travel directions, as depicted in Figure 6.19 and previously explained.

The residual signals, which embody the combination of two sensors, exhibit a smaller discrepancy compared to the single sensor signals. The relative error here lies between -1.0 % and 0.0 % in both travel directions, indicating a better agreement with the actual bridge measurements.

The outcomes of the comparative analysis are graphically encapsulated in Figure 6.23. The figure lucidly delineates that the residual signals, in both directions, align well with the values recorded by the sensors mounted on the bridge. As for the individual sensor signals, frequency identification, via the resonance curve, proves effective only in the direction of Ulm, where the sensors traverse the bridge in a steady state. Conversely, in the direction of Augsburg, the bridge is not yet in a steady state. This condition results in a reduced level of acceleration, which is presumably the reason why frequency identification fails for half of the sensors.

From the signals of the free decay of the resonance crossings, the frequency of the first bending mode was ascertained to be 5.15 Hz in both cases through the use of SSI. This value is marginally higher than the values determined by means of the resonance curve. Considering the lack of additional mass and the increasing frequency during the free decay phase, there is a strong agreement of the results.

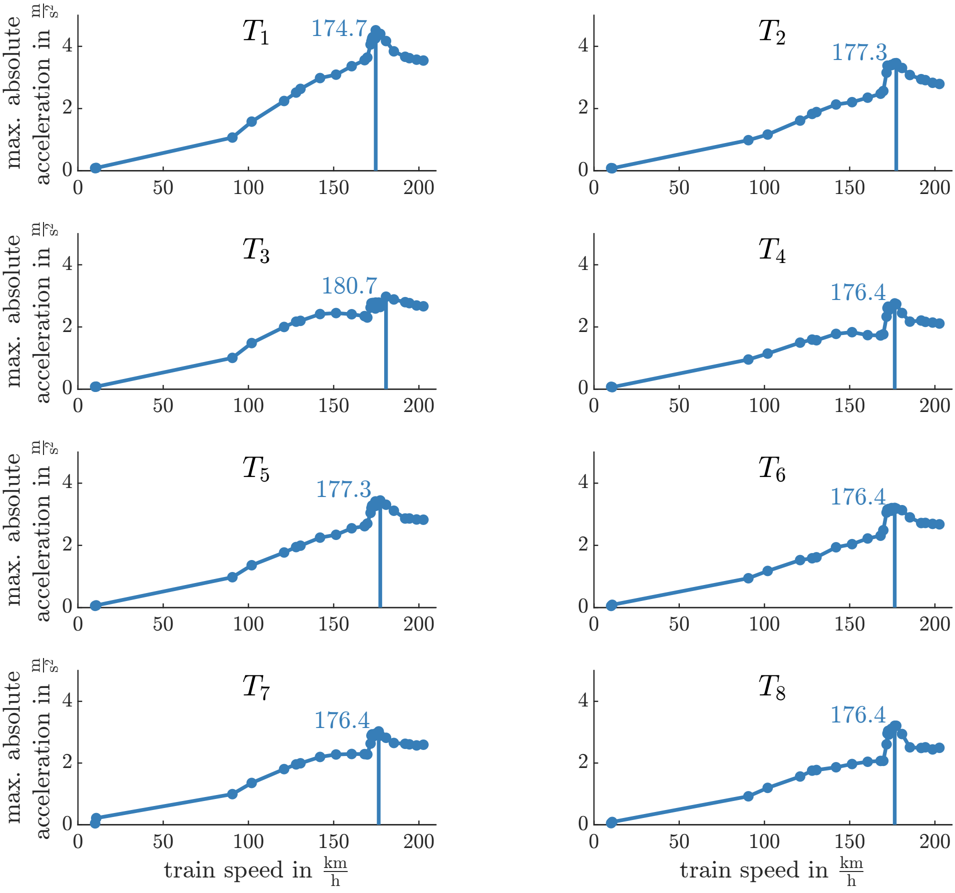

(a) single sensor signals

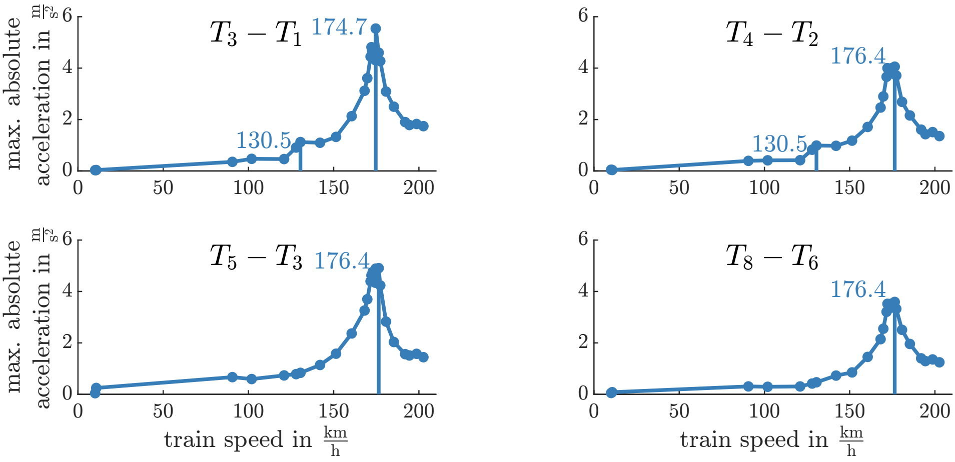

(b) residual signals

Figure 6.21 Indirect resonance curves for the runs towards Ulm with a cut-off frequency of $F_c = 8$ Hz.

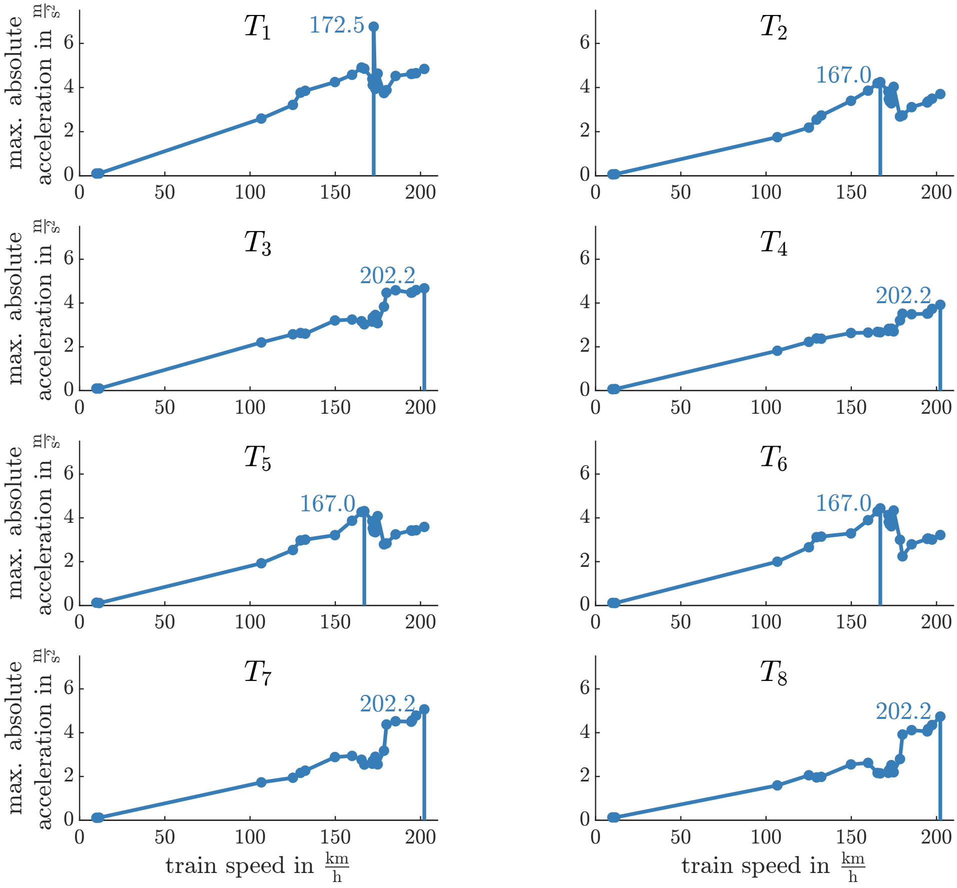

(a) single sensor signals

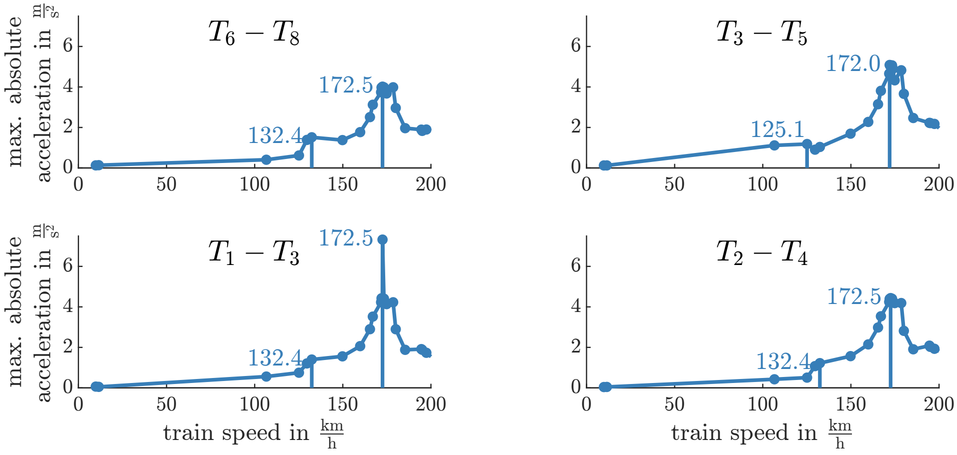

(b) residual signals

Figure 6.22 Indirect resonance curves for the runs towards Augsburg with a cut-off frequency of $F_c = 8$ Hz.

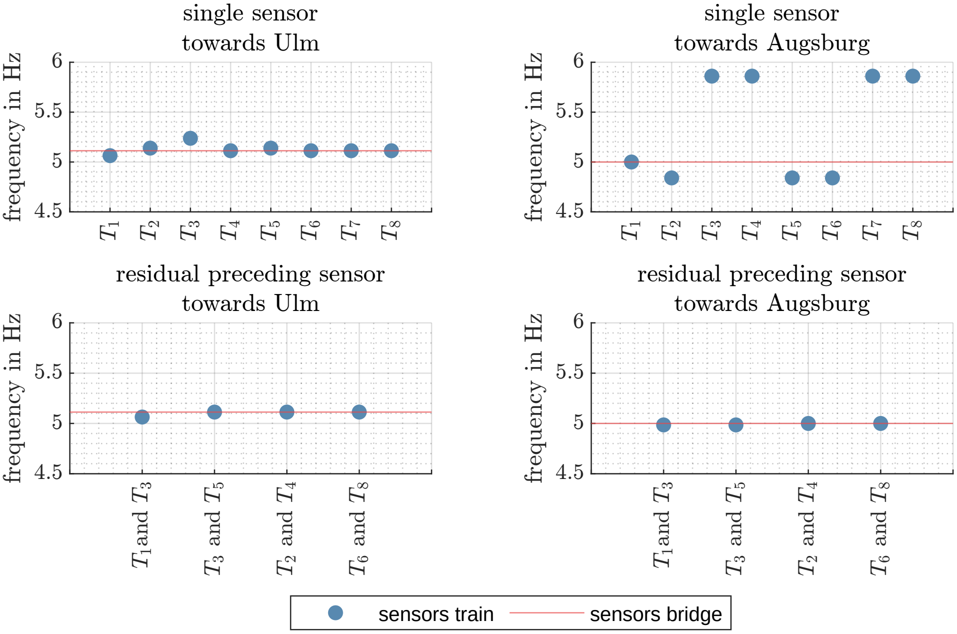

Figure 6.23 Comparison of the identified frequencies for the two approaches: single sensor (top), residual signal with the preceding axle (bottom) separately for the crossings in the direction of Ulm and in the direction of Augsburg. The identified values are compared with the values identified with the bridge mounted sensors.

6.4.3 Comparison of indirect and direct resonance curves

Both the residual signals and the sensors mounted on the bridge were utilised independently to identify the resonance peak, showcasing a considerable concurrence between their findings. However, for the direct resonance curves shown in Figure 6.10, the maximum values gleaned from the entire crossing were utilised, and incorporating moments when the instrumented axles were not positioned on the bridge. As such, a comparison should be conducted here, integrating the residual signals with the bridge sensors located in the centre of the field and closest to the rail, along with the signal times during which the corresponding axle maintained contact with the bridge. Both the train's acceleration measurements and the measurements on the bridge were filtered using a 4th order Butterworth filter with a cut-off frequency of 8 Hz. The results of this comparison are exhibited in Figure 6.24 for the runs towards Ulm, and in Figure 6.25 for the runs towards Augsburg.

For all evaluations, there exists a notable concordance in the curve and the amplitudes are also well correlated. A clear outlier is observed in the resonance run towards Augsburg for the residual signal of the sensors T_1 and T_3. To facilitate a quantitative appraisal, the percentage error of the evaluation of the residual signals from the acceleration measurements on the train was ascertained, in comparison with the evaluation of the acceleration signals on the bridge. Let $\max\left(|a_{\text{train}}|\right), \max\left(|a_{\text{bridge}}|\right) \in \mathbb{R}^{+}$. The percentage error $E_{\%}$ is:

$$E_{\%} = \frac{\max\left(|a_{\text{train}}|\right) - \max\left(|a_{\text{bridge}}|\right)}{\max\left(|a_{\text{bridge}}|\right)} \cdot 100\% \tag{6.2}$$

In this context, $\max\left(|a_{\text{train}}|\right)$ represents the maximum absolute acceleration determined with the sensors on the train, and $\max\left(|a_{\text{bridge}}|\right)$ stands for the maximum absolute acceleration measured with the sensors on the bridge. Thus, the value of $\max\left(|a_{\text{bridge}}|\right)$ is considered to be the true value or target value. In the calculation of the percentage error, as in the determination of the percentage errors of the frequencies (Equation 6.1), the absolute value of the difference was not used in order to preserve the sign. Thus the over- or underestimation of the values is shown.

The results are displayed in Figure 6.26 for both directions as a function of both speed and bridge accelerations. It is evident that the accelerations tend to be overestimated until just prior to the resonance speed and from then on are increasingly underestimated as the speed rises. It is noticeable that the percentage error decreases with increasing bridge acceleration or converges towards a limit. In the direction of Ulm, the values are slightly above -20 %. In the direction of Augsburg, the percentage errors for the high bridge accelerations range between approximately ± 10 %.

The mean values and standard deviations of the calculated percentage errors, as well as their absolute values, have been computed and are tabulated in Table 6.3. A comparison of the absolute values reveals that, on average, the errors in the direction towards Augsburg are marginally lower at 21.7 % compared to 23.8 % in the direction towards Ulm. However, the standard deviation in the direction towards Augsburg is notably higher at 34.6 %, as opposed to 15.1 % in the direction towards Ulm.

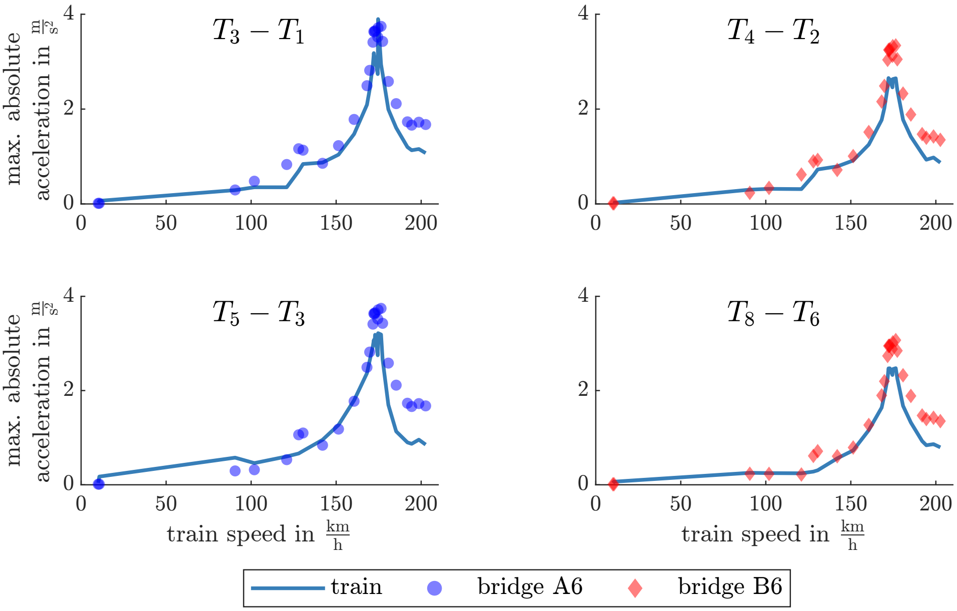

Figure 6.24 Comparison of the direct resonance curves of the signal sections in contact with the axle with which the indirect resonance curve was generated using residual signals in the direction of Ulm

Table 6.3 Summary of the mean and standard deviation for percentage errors: a comparison of the maximum absolute residual signal values derived from axle box accelerations on the ICE 4, with values recorded from sensors installed on the Schmutter bridge.

	Ulm		Augsburg	
	mean in %	std. in %	mean in %	std. in %
percentage error	-18.6	21.2	0.4	40.9
absolut values percentage error	23.8	15.1	21.7	34.6

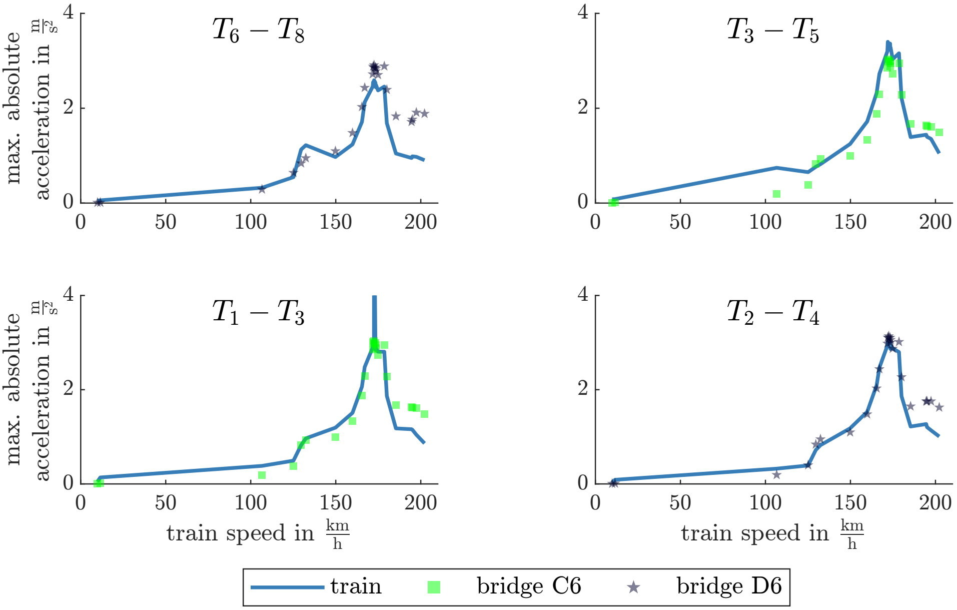

Figure 6.25 Comparison of the direct resonance curves of the signal sections in contact with the axle with which the indirect resonance curve was generated using residual signals in the direction of Augsburg

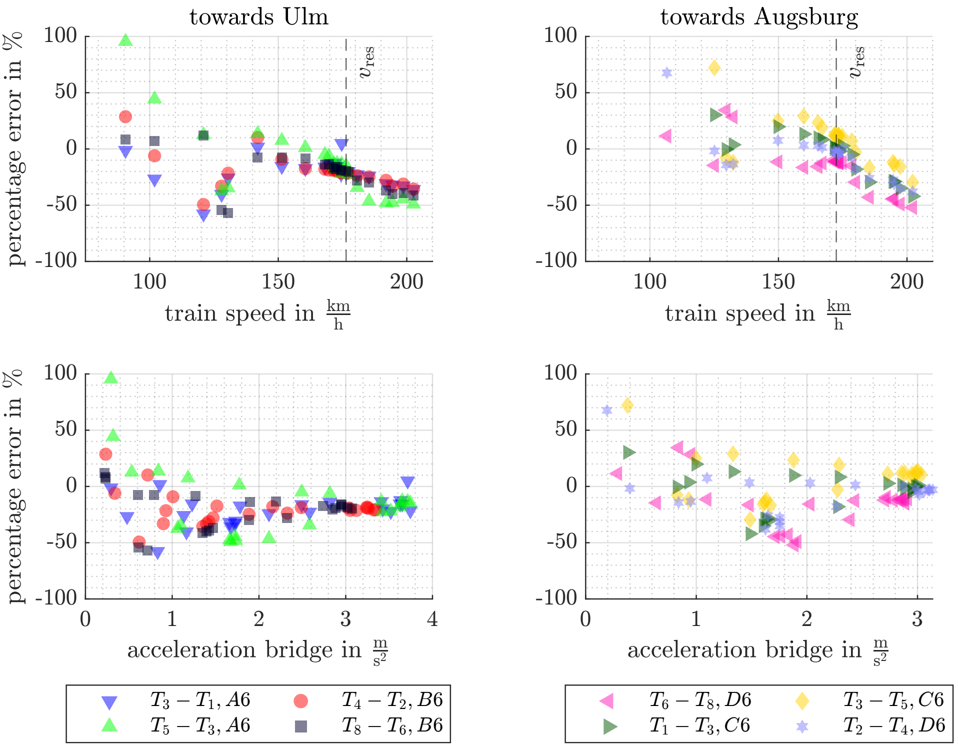

Figure 6.26 Percentage error of the residual signals compared to the measurement at the bridge for both directions of travel as a function of speed and as a function of bridge acceleration.

6.5 Conclusion

6.5.1 Virtual sensing

This section concludes the analysis of virtual sensing on the Schmutter bridge. The structure was shown to display distinct non-linear behaviour, manifested in amplitude-dependent frequencies. The key findings of this analysis are as follows:

(1) Modal expansion is applicable to railway bridges exhibiting non-linear system behaviour, even when relying solely on linear models.

(2) Substructuring, the practice of modelling only parts of the structure, proves sufficient for adequately approximating structural responses within those modelled parts.

(3) The uncoupled model generally outperforms the coupled model for sensors located on axes $\boxed{\text{A}}$ and $\boxed{\text{B}}$, whereas the coupled model yields marginally better results on axes $\boxed{\text{C}}$ and $\boxed{\text{D}}$. Performance was assessed in terms of the coefficient of determination R^2.

(4) Both models encounter limitations in the accurate reconstruction of signals near structural supports. This drawback is attributed to the rigid modelling of these supports and to the springs located at the tops of the hollow boxes, which also inadequately model local effects.

(5) No clear correlation was identified between the train speed and the quality of signal reconstruction. However, specific speed ranges were observed where the quality of signal reconstruction notably declined.

(6) The modal expansion can adequately capture complex vibration patterns during slow passages as well as large amplitudes and their associated frequency shifts.

The analysis herein demonstrates that substructuring allows for modelling only parts of the structure, thereby significantly reducing the modelling effort required. This is especially beneficial when dealing with the coupling through the ballast superstructure, a common challenge in railway bridge modelling. Employing modal expansion for a partial structure is found to be sufficient, although it restricts the conclusions to those modelled parts. Thus, this study provides the inaugural evidence that modal expansion is practically applicable under real conditions on railway bridges with non-linear system behaviour for the implementation of virtual sensing.

6.5.2 Drive by monitoring

The dataset of acceleration signals from the train, acquired during the experiment detailed in section 6.1, enabled the validation of the frequency identification methodology delineated in subsection 4.2.1. This encompassed the scrutiny of two methods, the results of which could subsequently be juxtaposed with those procured from the analysis of the bridge sensor signals. The first method entailed the utilisation of single sensor signals, whereas the second method necessitated the use of signals from two consecutive axles to generate a residual signal. The following conclusions can be drawn:

(1) For both types of signals – the single sensor signal and the residual signal – varying cut-off frequencies of the low-pass filter were examined. The findings imply that the methodology exhibits sensitivity to the chosen filter setting when employing a single signal. Conversely, for the residual signals, the method appears to be only mildly influenced by the selection of cut-off frequency within the explored range. This observation holds particularly true in relation to the shape of the resonance curve or the location of the peak, thereby affecting the identified frequency.

(2) It was discovered that when single sensor signals were deployed, significant discrepancies occurred in the identified frequency, particularly in the direction of Augsburg. As evidenced, this can be most likely attributed to the bridge not being in a steady state at the time of contact with the instrumented axles.

(3) Moreover, the identification of the second resonance peak in the single sensor signals is not clearly distinguishable, necessitating a frequency estimate, or an estimate for i, for the computation of the frequency. Conversely, when utilising residual signals, a second peak could be discerned, facilitating the determination of i for frequency identification without the prerequisite of an estimate.

(4) The application of residual signals led to a highly precise identification of frequencies in both directions, compared to the evaluation of the bridge signals. Consequently, the corresponding indirect resonance curves were juxtaposed with the resonance curves of the bridge sensor signals at the respective contact times. A substantial agreement of the curves was observed and the amplitudes correlated significantly. The relative error decreases with an increase in acceleration.

The study conducted in this section demonstrates that the methodology described in subsection 4.2.1 allows for the identification of the bridge's resonance frequency using sensors on the train under real conditions. Moreover, it was shown that accelerations can also be estimated approximately. Principally, the use of single sensor signals is feasible, meaning the methodology could be realised even with a single instrumented axle. However, it has been found that instrumenting multiple axles provides significant benefits, as the use of residual signals can partially compensate for speed-dependent effects. This approach results in significantly less scatter in the results and reduces dependency on the choice of filter settings.

7 Railway bridge Garather Bach

This chapter contains the experimental investigations carried out on a single span steel trough bridge with a span of 16.4 m over a rivulet in Düsseldorf (Figure 7.1). The bridge is a single track bridge and has a ballasted track. A long-term monitoring system was installed in the bridge, which is described in the following section. In addition to the long-term monitoring system, crossings with an instrumented ICE TD were made over the instrumented bridge. Using the experimental data obtained, several investigations have been conducted. These investigations focus on virtual sensing under different operational and environmental conditions. Additionally, the proposed method for frequency identification, based on resonance curves drive-by monitoring, has been evaluated.

7.1 Experimental set-up and execution

7.1.1 Bridge instrumentation

The installation of the long-term monitoring system was carried out as part of the research project ZEKISS, funded by the Federal Ministry for Digital and Transport. The monitoring system comprises ten acceleration sensors, eight uniaxial strain gauges, eight rosette strain gauges for four axle load measurement points[1], and four type K thermocouples. Due to the failure of one acceleration sensor, only nine sensors were utilised in this thesis. The position of each sensor and their designation is illustrated in Figure 7.2.

On the 11th and 12th of August 2021, the eight measuring points on the tracks (G1 to G8) were installed. The installation was carried out under sunny conditions, with temperatures ranging from approximately 15 °C to 18 °C; thus, no issues with moisture were encountered during the installation. For the measuring points, 1-VY41-3/350 rosette strain gauges from the company HBK (Hottinger Brüel & Kjaer GmbH, 64293 Darmstadt, Germany) were used. The neutral axis of the rail profiles was treated with sandpaper at four points on both sides to prepare the site. Care was taken to ensure that the removal was as flat as possible, to prevent any depressions or unevenness. The neutral axis was marked with adhesive tape Figure 7.3a; it lies about 50 mm above the rounding radius at the transition from the rail base to the web. The sanded surfaces were subsequently cleaned with acetone. Z70 adhesive from HBK was used for bonding. The DMS were pressed with thumb pressure using a Teflon paper for 2 minutes each. To ensure that no delamination of

---

[1] Due to a fault in the soldering of the circuit, these are only used as axle detectors.

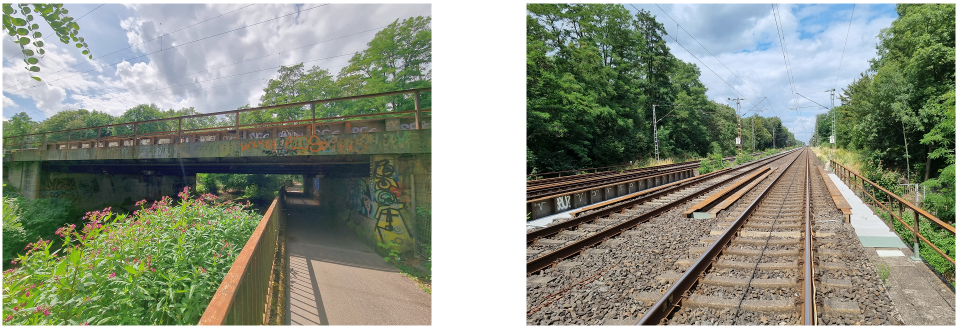

(a) Side view of the bridge

(b) View from above in the direction of travel

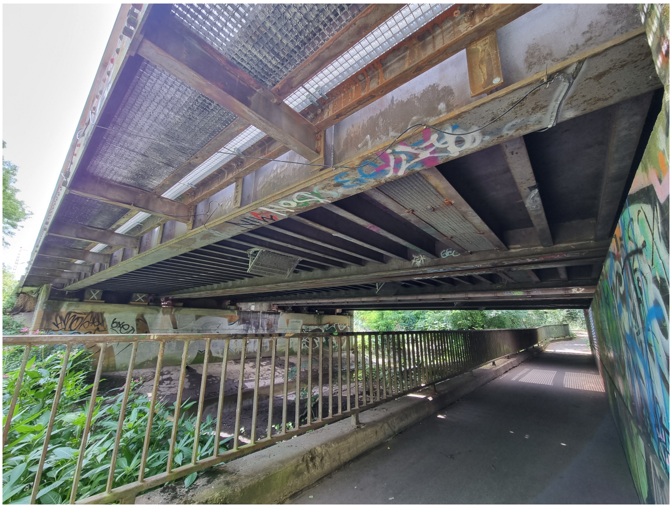

(c) View of the load-bearing structure from below

Figure 7.1 Garather Bach bridge

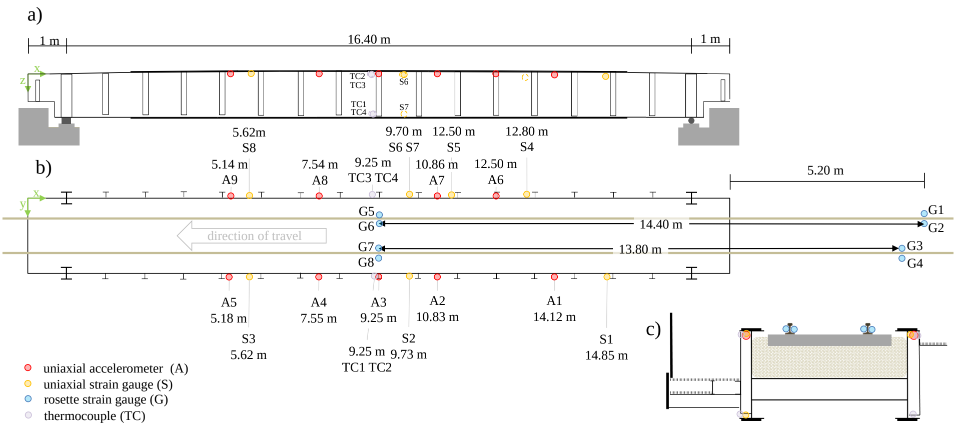
a)
1 m
16.40 m
1 m
x
z
TC2
TC3
TC1
TC4
S6
S7
5.62m
S8
9.70 m
S6 S7
12.50 m
S5
12.80 m
S4
b)
5.14 m
A9
7.54 m
A8
9.25 m
TC3 TC4
10.86 m
A7
12.50 m
A6
5.20 m
x
y
G5
G6
G7
G8
direction of travel
14.40 m
13.80 m
G1
G2
G3
G4
A5
5.18 m
A4
7.55 m
A3
9.25 m
A2
10.83 m
A1
14.12 m
S3
5.62 m
9.25 m
TC1 TC2
S2
9.73 m
S1
14.85 m
c)
uniaxial accelerometer (A)
uniaxial strain gauge (S)
rosette strain gauge (G)
thermocouple (TC)

Figure 7.2 Sensor positions on the Garather Bach bridge a) side view b) top view c) cross-section.

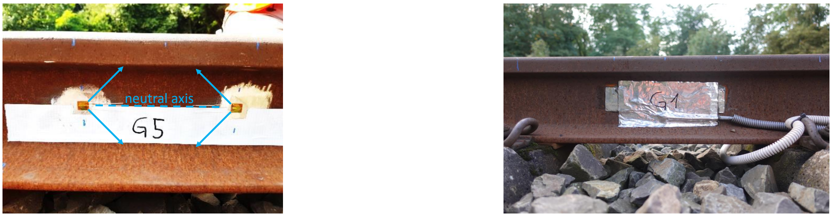
neutral axis
G5
G1

(a) Axle load measuring point G5 after gluing and before soldering.

(b) Axle load measuring point G1 with cover.

Figure 7.3 Installation of the axle load measuring points.

the strain gauges occurred, the cables were soldered at temperatures of less than 350 °C and with contact times of less than one second. Subsequently, the measuring points were protected from environmental influences with Silicone Rubber SG250 and 1-ABM75 (both from HBK) putty with aluminium foil as a cover (Figure 7.3b). The arrangement of the strain gauges allows for the determination of the lateral force jump, and thus the axle load, when it is on the rail between the rosettes. Details about this methodology for axle load determination is given by KOUROUSSIS et al. (2015). Since two measuring points with a known distance from each other are arranged on each rail, the average driving speed for each axle can also be determined.

The installation of the power supply, the acceleration sensors, and the control cabinet took place from 12th to 14th of October, 2021. To ensure an uninterrupted, continuous power supply with a 230 V earthed plug, more than 400 m of power cable was laid from the nearest stopping point to the bridge. To compensate short-term failures, a QuantumX uninterruptible power supply from HBK was installed in the control cabinet. Piezoelectric seismic sensors PCB 393 B04 (PCB Synotech GmbH, 41836 Hückelhoven, Germany) were used as acceleration sensors. These were attached to the bottom of the top flanges (Figure 7.4a) with magnets and positioned as close as possible to the transition radius leading to the web, without making contact. To relieve the cable connection on the sensors, the connecting cables near the sensors were fixed with a magnetic holder and cable ties.

The installation of the strain gauges and the thermocouples on the main girders of the bridge took place on October 20th; temperatures ranged between approximately 13 °C and 18 °C. The humidity was relatively high that day ranging between 76 % and 86 %. There were several light rain showers with a total rainfall of 0.71 mm. Due to the weather conditions, protective measures were taken to prepare the measuring points. A pavilion was set up over the work area to protect it from precipitation. Before the application, the spots were dried with towels and subsequently freed from moisture using a hot air gun. The spots for the strain gauges were freed from the protective varnish with sandpaper, taking care again for an even removal. Before gluing the strain gauge, the area was dried again with the hot air gun and cleaned with acetone. The uniaxial strain gauge 1-LY61-10/350 was then mounted centrally between the web and the outer edge of the flanges using the Z70 adhesive (both from HBK). As a cover agent, Silicone Rubber SG250 was used again. A magnet was attached to each strain gauge on the main girders; this contained a screw to install a sample of construction steel with a strain gauge (also 1-LY61-10/350) stress-free on the girder for temperature compensation of the strain measurements. Soldering took place, as previously described, at <350 °C and under one second of contact time. The measuring point was then protected from environmental influences with the kneadable putty AK22 from HBK (Figure 7.4c).

For the type K thermocouples, holders made of aluminium were manufactured to facilitate their attachment to the structure. The holders had a blind hole into which the thermocouple can be inserted. To prevent the element from sliding out, it is secured with a screw. On the underside of the holders, four magnets are embedded in the corners to attach the holders to the structure (Figure 7.4d). The thermocouples were mounted on the outer tops of the bottom flanges and the undersides of the top flanges (Figure 7.4e). Thermal paste was applied at the contact point to improve heat conduction.

All sensors were connected to two HBK measuring amplifiers MX1601B. Throughout the measurements, different sampling rates were used for various purposes; these are tabulated in the appendix (Table A.10). To ensure a uniform data basis for this work, the sampling rates of the bridge's acceleration and strain sensors were downsampled to match the first setting used ($F_s = 600$ Hz).

At all times, the installation was able to be carried out as the track remained closed. The system was commissioned on 28th of October, 2021, and has been in operation since then.

The measurement signals are recorded upon being triggered by the signal from sensor G1 located on the rails. Whenever an axle crosses the designated point, signals are captured for a duration of 10 seconds preceding the trigger and 50 seconds following it, resulting in

(a) Installed accelerometer A7 **(b)** The strain gauge S7 before covering **(c)** The strain gauge S7 after covering

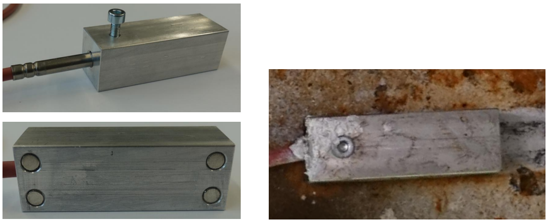

(d) The manufactured holder for the thermocouples **(e)** The installed thermocouple TC4

Figure 7.4 Sensors installed on the main girders.

a total recording time of 60 seconds for each crossing. The recorded acceleration and strain signals have been adjusted to zero.

For the investigations in this thesis, data up to March 23rd, 2023, were evaluated. Due to failures of the facility and one hard drive, data for crossings were available for 330 out of 511 days during this period. On these days, a total of 38,133 crossings were recorded.In the following, these crossings are evaluated.

To approximately capture the environmental influences in addition to the temperature measurements on the structure, data from the two nearby weather stations IDSSEL60 and IDSSEL168 were used. The locations of the weather stations and their distance to the bridge and to each other are shown in Figure 7.5. The weather data was recorded with a sampling rate of $\frac{1}{300}$ Hz, meaning one value per measurement size every 5 minutes. To compare the data from the weather stations, the Pearson correlation coefficient was determined for all sizes. The values are tabulated in Table 7.1. The wind speed and the precipitation rate show a strong correlation, while all other measurement sizes show a very strong correlation. As data for the entire measurement period is only available for the IDSSEL60 station. In the following, only data from this weather station will be used. his approach is justified by the high correlation of the data from the weather stations and the short distance of the station to the bridge.

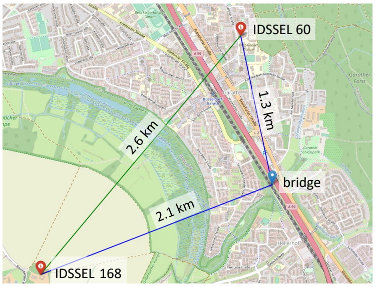

Figure 7.5 Location of IDSSEL 60 and IDSSEL168 weather stations with distances to each other and to the bridge

Table 7.1 Pearson's correlation coefficient between the data from the IDSSEL 60 weather station and the IDSSEL168 weather station

measured quantity	temperature	dew point	Humidity	Wind Speed	Wind Gust	Pressure	Precip Rate	Precipitation Accumulation
Pearson corelation coefficient	0.99	0.99	0.98	0.78	0.8	0.99	0.73	0.99

The measurement data from the IDSSEL60 weather station for the entire investigated period is shown in Figure 7.6. In the figure, the periods for which measurement data from the monitoring facility on the bridge are available are marked.

7.1.2 Train instrumentation

In addition to the bridge instrumentation, the 4-car ICE TD train was equipped with 32 PCB-(M)622B01 accelerometers (PCB Synotech GmbH, 41836 Hückelhoven, Germany) on the axle boxes, as illustrated in Figure 7.8. To facilitate the mounting of these sensors, steel brackets were fabricated which could be affixed to the caps of the axle boxes. The sensors were then mounted onto a threaded section atop these brackets. These accelerometers were linked to an HBK QuantumX MX1601B and three QuantumX MX840B amplifiers, and signals were recorded at a sampling rate of 5,000 Hz. Due to voltage fluctuations within the train's power supply, which led to distortions in the measurement results, a continuous power supply unit, APC-Back-UPS Pro (Schneider Electric GmbH, 40880 Ratingen, Germany), was connected to ensure a consistent voltage supply for the measuring devices.

To capture the train's position, two 1-GPS-USB-18Hz (HBK) Multi-GNSS receivers were connected to the measurement computer aboard the train. A GPS module was also installed on the bridge setup. Using the satellite timing of the GPS receivers, measurements from both systems were synchronised.

The measurement campaign was conducted in the period from 26th to 28th July 2022. On the first day, there was 0.2 mm of precipitation before the first run, and the temperature was 20.5 °C. The second day was dry with temperatures between 15.7 °C and 20.1 °C. The third day was also dry with temperatures between 15.7 °C and 23 °C. During the campaign, 13 crossings were available, during which the resonance peak needed to be hit. To detect the peak even with a limited number of passings, a methodology using Bayesian optimisation was published by RUPP et al. (2023). This was employed to provide the next speed recommendation for the driver based on the previous measurements.

To determine the frequency from the peak of the indirect resonance curves, as detailed in subsection 4.2.1, the axle configuration of the ICE TD, depicted in Figure 7.9, was required. The length over buffer of the ICE TD is $l_{\mathrm{ob}} = 25.90$ m.

Speeds of individual passings were gauged from the train's GPS readings during the experiment. For the analysis presented in this work, the speeds were determined using sensors G1 to G8 of the monitoring system on the bridge.

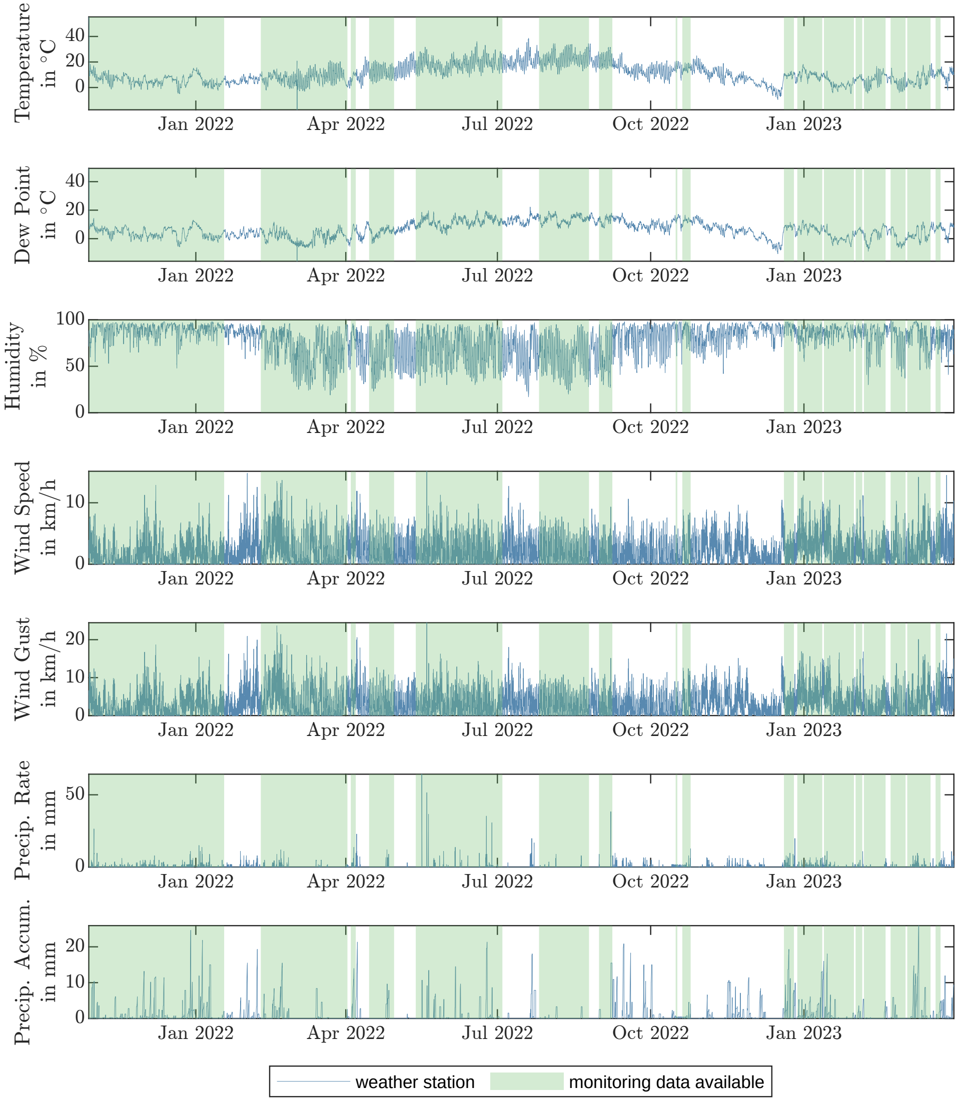

Figure 7.6 Weather data from the IDSSEL60 weather station, with an indication of the time periods for which the monitoring data is available.

advanced TrainLab

Figure 7.7 instrumented ICE TD passing the bridge of the track in the opposite direction (photo: Hagen Berthold). It should be noted that the investigations were carried out on the right bridge (directional track).

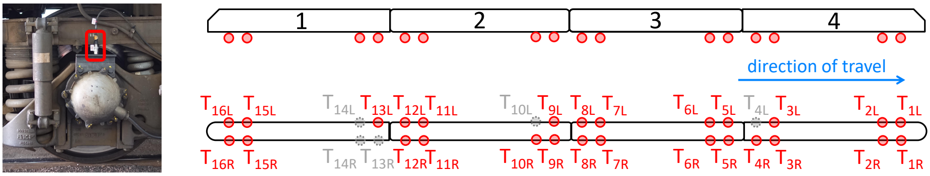
1
2
3
4
direction of travel
T_{16L} T_{15L} T_{14L} T_{13L} T_{12L} T_{11L} T_{10L} T_{9L} T_{8L} T_{7L} T_{6L} T_{5L} T_{4L} T_{3L} T_{2L} T_{1L}
T_{16R} T_{15R} T_{14R} T_{13R} T_{12R} T_{11R} T_{10R} T_{9R} T_{8R} T_{7R} T_{6R} T_{5R} T_{4R} T_{3R} T_{2R} T_{1R}

(a) Installed sensor **(b)** Sensor placement on ICE TD

Figure 7.8 Instrumentation of the ICE TD with acceleration sensors on the axle boxes.

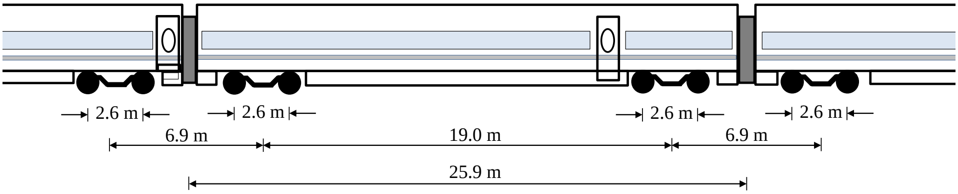
2.6 m
2.6 m
2.6 m
2.6 m
6.9 m
19.0 m
6.9 m
25.9 m

Figure 7.9 Axle configuration of the ICE TD. The length over the buffers is $l_{\mathrm{ob}} = 25.90\ \mathrm{m}$.

7.2 System identification and structural model

7.2.1 Modal analysis

A modal analysis was performed based on ambient measurement data collected on the 3rd of March 2022, using the Macec software as referenced in (REYNDERS et al., 2021). In the initial step of signal pre-processing, the signal offset was removed by employing the Matlab function *detrend()*. Subsequently, the Matlab function *decimate()* was utilised to reduce the signal's sampling rate to 120 Hz. The processed signals were then subjected to a 4th-order Butterworth bandpass filter within the frequency range of 0.5 Hz to 50 Hz. From the entirety of the processed signal, a central segment of 200 seconds was extracted for analysis with the Data-Driven-SSI method. The two free parameters were selected as $i = 10$ and $n = 200$. The identified modes in the relevant frequency range up to 30 Hz are summarised in Table 7.2.

In addition to the modal analysis based on ambient measurements, as described in subsection 6.2.1, the free decay phases of the crossings were used for a modal analysis. The starting points of the free decay phase were determined using sensors G1 to G8. The acceleration signals were downsampled to a sampling rate of 50 Hz for the modal analysis. The first 20 seconds of the decay phase were then used to conduct an automated SSI using the existing code (CHEYNET, 2020). It was observed that the bridge exhibits pronounced amplitude-dependent behaviour. The frequencies also showed temperature dependency, although this was found to be minor compared to the amplitude dependence. The identified frequencies of the first bending mode are presented as a function of the maximum absolute acceleration in the decay phase, temperature, and measurement date in Figure 7.10.

In the analysis, two periods were identified during which there was a sudden change compared to the adjacent measurements. This was attributed to a speed reduction to 150 $\frac{\mathrm{km}}{\mathrm{h}}$ and the associated lower amplitudes of bridge vibration. In the second period, however, the

Table 7.2 Modes identified by analysing ambient measurements

no.	type	frequency f in Hz	damping ξ in %	modal phase collinearity (MPC)
1	1st bending	6.73	1.40	0.98
2	1st torsion	8.99	0.90	0.98
3	2nd bending	16.14	3.60	0.84
4	2nd torsion	18.68	3.00	0.93
5	undefined	24.13	3.20	0.54

frequencies were somewhat higher and the temperatures were around the freezing point, suggesting that frozen ballast had likely contributed to stiffer system behaviour.

With the exception of the small area where the ballast on the bridge was presumably frozen, an increase in frequencies with rising temperature was observed. Thermal expansion could increase the clamping effects of the superstructure, thereby increasing the stiffness.

7.2.2 POD modes

As elucidated in chapter 5 regarding the HUMVIB Bridge, investigations into different POD methods revealed that while the resulting POD modes differ, they lead to approximately equivalent reconstruction accuracies. Consequently, the transit on July 5, 2022, at 07:38 AM was arbitrarily selected for generating the POD modes for this bridge. These derived modes are depicted in Figure 7.11.

In the case of acceleration modes, a marked resemblance to the eigenmodes is observable, particularly for the first four modes. Conversely, the strain modes do not manifest a clear correlation with the strains anticipated from the eigenmodes.

The generated POD modes serve as data-driven counterparts to the model-based eigenmodes in the subsequent analysis.

7.2.3 FE model

The FE model was created using the Sofistik software in accordance with the design plan of the structure, comprising 585,084 degrees of freedom. The main load-bearing structure was modelled using shell elements, whilst the attached walkway and handrail were modelled by beam elements (Figure 7.12). The ballast was treated as an additional mass, with its stiffness contribution being neglected. However, the partial clamping effects from the ballast superstructure and rails were approximated using springs at the ends of the top flanges of the main girders. The material parameters for the steel are the same as in Table 5.1. The springs on the upper flanges have a modulus of subgrade reaction of 700,000 $\frac{\mathrm{kN}}{\mathrm{m}^3}$. This value was arrived at through iterative adjustments to align the modal shapes of the model closely with those observed in measurements, a comparison of which is provided in the subsequent section.

Using this model, a modal analysis was conducted. From the modes identified, all bending and torsional modes of the structure up to approximately 30 Hz were selected. In this range, there are four bending modes and two torsional modes as shown in Figure 7.13.

7.2.4 Comparison of mode shapes

The comparison of the modes obtained with the FE model and those of the SSI with the signals from the ambient measurements reveals a good agreement of the four assignable mode shapes (Figure 7.14).

The mode shapes determined from free decay agree less well with the FE modes. The first bending mode no longer corresponds at all, while the first torsional mode and the second bending mode still relatively correspond (Figure 7.15).

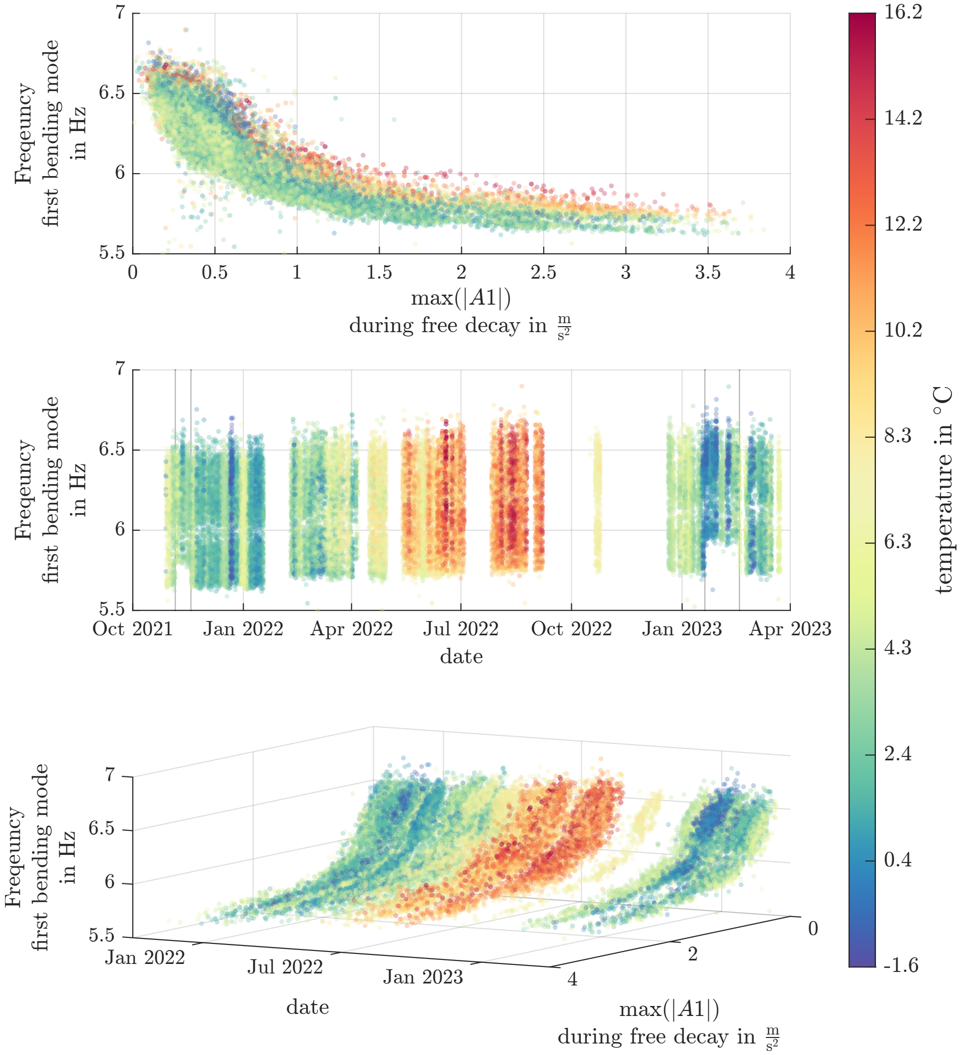

Figure 7.10 The graph illustrates the first bending frequency, identified through SSI analysis of the free decay signals. This is plotted at three different views as a function of the maximum amplitude during the free decay phase and is further categorized by date and temperature. Within the middle section of the graph, two specific periods are highlighted with vertical lines: November 5 to 18, 2021, and January 19 to February 17, 2023. During these intervals, the maximum speed was restricted to 150 $\frac{\mathrm{km}}{\mathrm{h}}$.

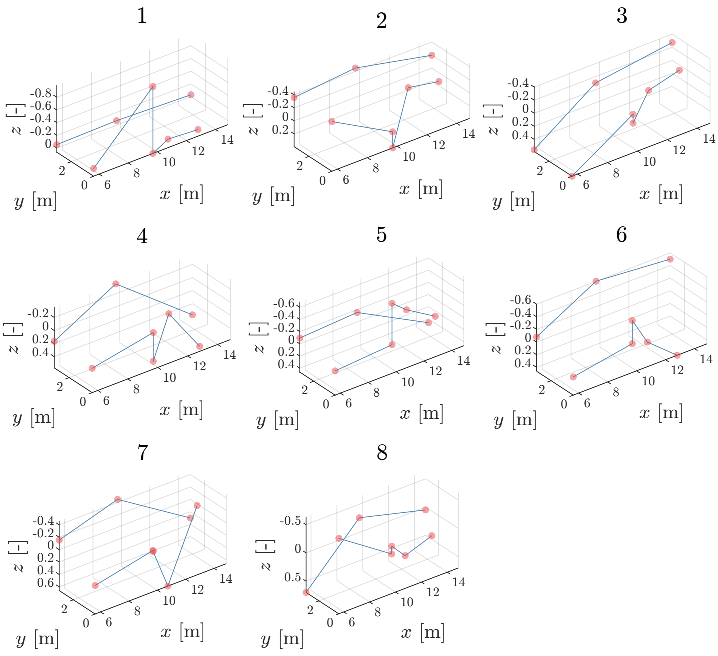

(a) Strain modes

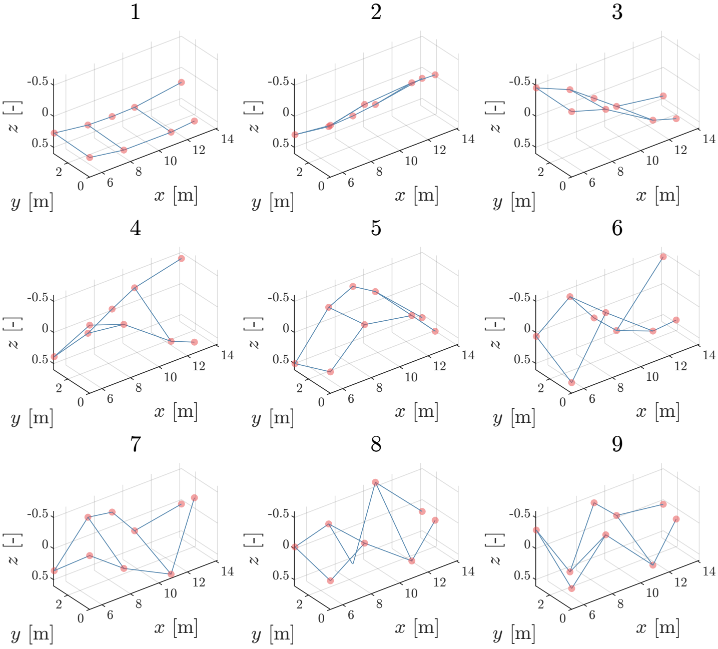

(b) Acceleration modes

Figure 7.11 POD modes for the Garather Bach bridge.

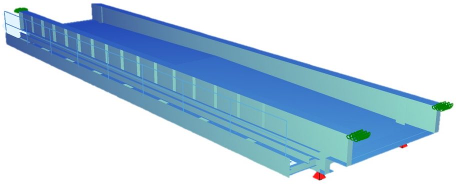

Figure 7.12 FE model of the bridge

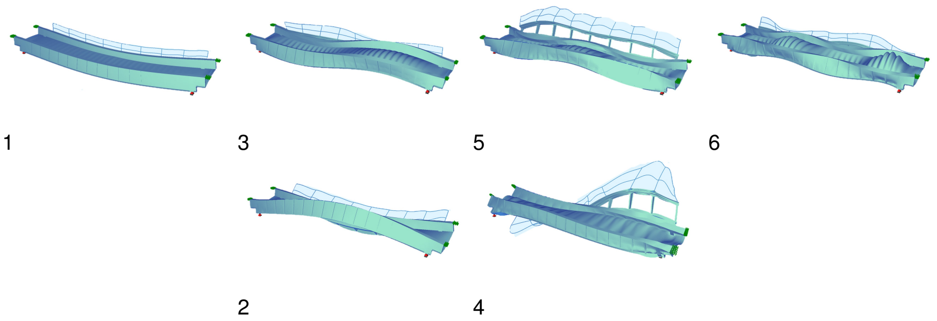

1 3 5 6

2 4

Figure 7.13 The six considered modes of the FE model, four bending modes and two torsional modes.

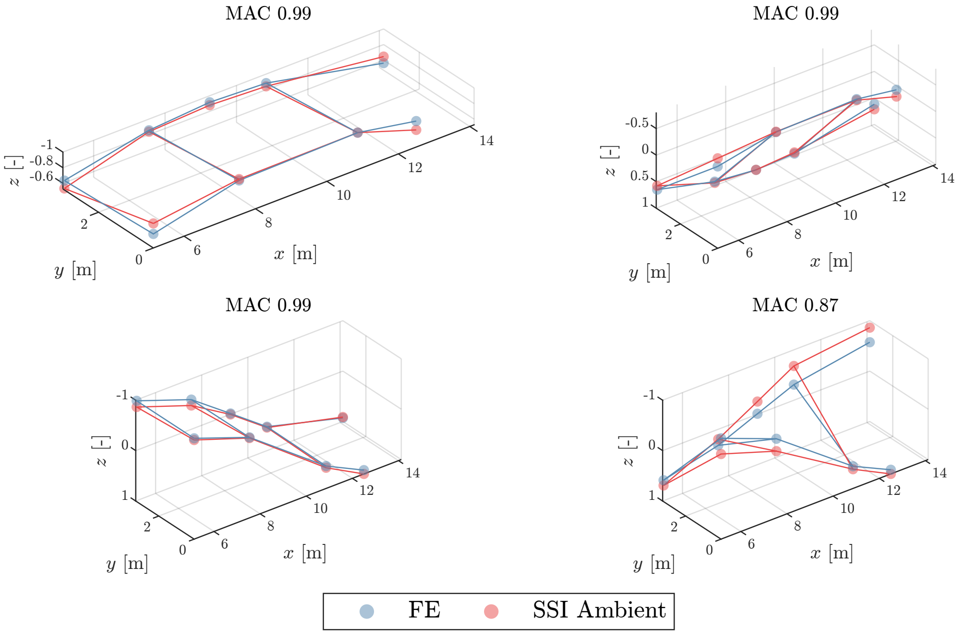

Figure 7.14 Comparison of four assigned FE modes with those of a SSI with ambient measurements and corresponding MAC values.

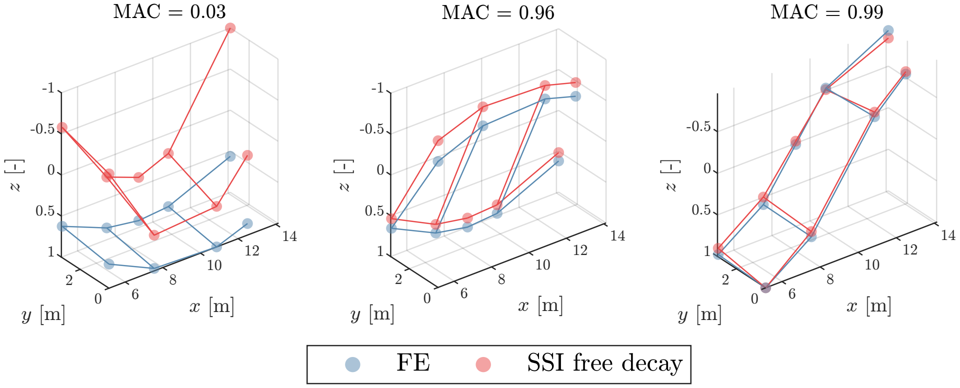

Figure 7.15 Comparison of three assigned FE modes with those of a SSI with free decay signals and corresponding MAC values.

7.2.5 Resonance curve

Understanding the dynamic interaction between various types of trains and the monitored bridge is central to this research. The analysis begins with the identification of train types based on their axle configurations. The axle distances were determined and the trains classified using sensors G1 to G8. For the research conducted in this thesis, the five most frequently identified vehicle types were analysed. One of the vehicle types was represented twice, once with a configuration of 32 axles and once with 64 axles. The summary of frequencies for each vehicle is presented in Figure 7.18. The experimental probability associated with the speeds driven by the vehicles is shown in Figure 7.17.

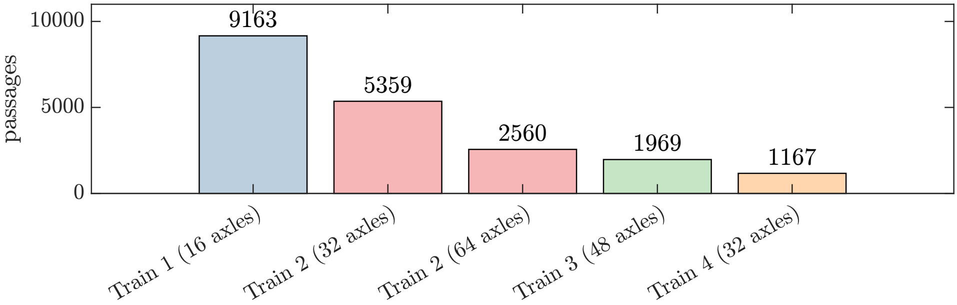

Figure 7.16 Number of crossings for the five most frequent train types passing the bridge.

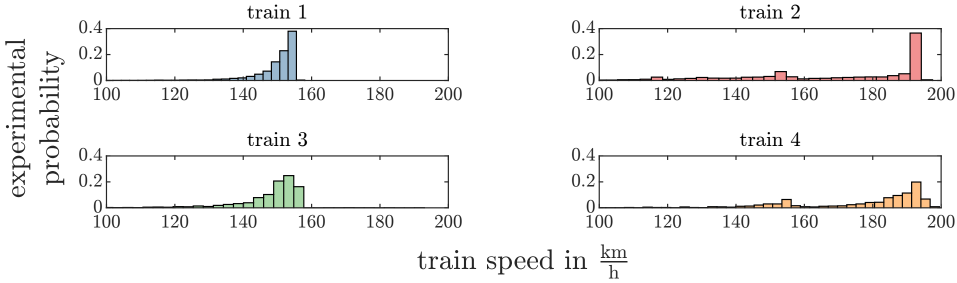

Figure 7.17 Experimental probability of the speeds of the trains for the four different types of train.

With the filtered vehicles, resonance curves were created. The evaluation was conducted for all crossings, with the maximum absolute values of the accelerations being determined in relation to the driven speed. The mean value was calculated in increments of 2 km/h. The resulting mean value curves are depicted in Figure 7.18. A distinctly different behaviour for the various train types is evident.

In addition to the five most common vehicles, the resonance curve was also created for the passages of the previously described instrumented ICE TD using the sensors on the bridge. The result is shown in Figure 7.19. From the illustration, it can be seen that, in the

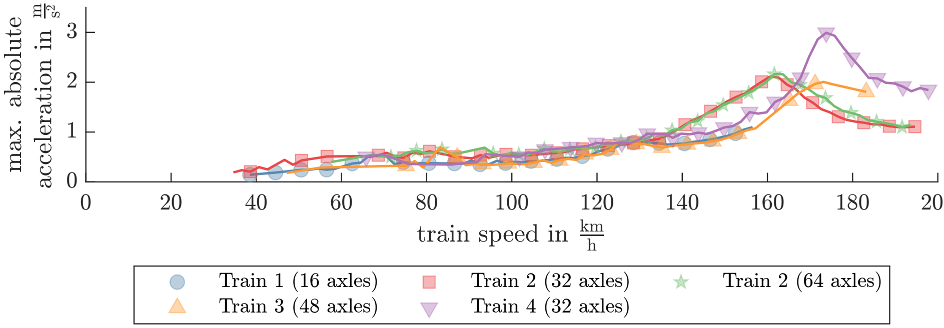

Figure 7.18 Resonance curve from the acceleration signals of sensor A1 for the crossings of the five most frequent train types. The train type "Train 2" is included as 32 axle and 64 axle configuration.

resonance case, the accelerations on the side of the footpath are greater than those on the other girder. This corresponds well with the mode shape determined from the decay phase, as shown in Figure 7.15.

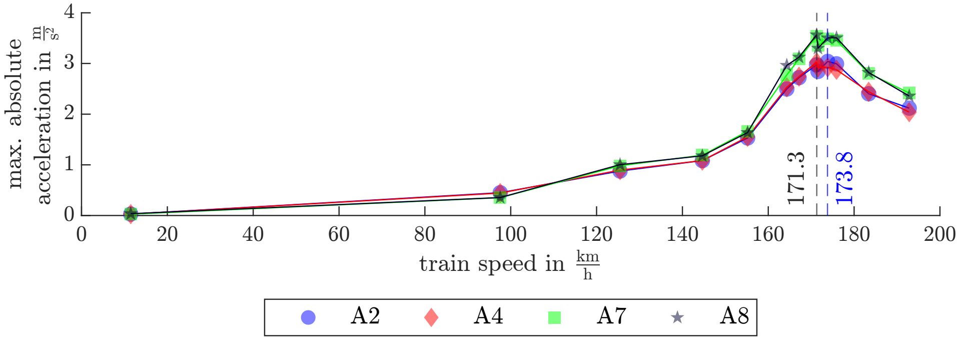

Figure 7.19 Resonance curve from the acceleration signals of sensors A2, A4, A7 and A8 for the crossings of the ICE TD.

7.3 Virtual sensing

7.3.1 Impact of considered modes and number of physical sensors

To assess the influence of the number of considered modes n_m and the quantity of physical sensors k, a leave-p-out validation approach was utilised, as elaborated in **??**. This methodology was also previously implemented for the HUMVIB Bridge, as discussed in subsection 5.3.2.

The mean values of all 38,133 passages were calculated for every conceivable sensor combination. Subsequently, the best and worst sensor combinations were identified by locating those with the maximum and minimum coefficients of determination, respectively, for each possible pair of n_m and k.

This procedure was executed for the signals from strain gauges S1 to S8, as well as for accelerometers A1 to A9. The analysis utilised FE modes, as depicted in Figure 7.13, and POD modes, as illustrated in Figure 7.11. A comprehensive summary of the results can be found in the appendix, from Figure B.16 to B.19.

In the analysis of strain modes, particularly in the FE strain modes as seen in Figure B.16, two main trends were discerned with respect to the coefficient of determination R^2. First, when the number of modes n_m remained constant, R^2 exhibited opposing trends for the best and worst sensor combinations. Specifically, an increase in the number of physical sensors k led to a decrease in R^2 for the best sensor combinations, while it led to an increase for the worst combinations. This phenomenon was also observed in the POD strain modes (Figure B.17), reinforcing its generality. Second, when the number of physical sensors k was held constant, R^2 varied in an oscillatory fashion as the number of considered modes changed. This oscillatory behaviour was especially noticeable for edge sensors such as S1, S3, and S8.

The analysis also showed that for a good sensor combination, the best result is obtained when $n_m = k - 1$. In contrast, if the sensor combination was less optimal, a reduction in the number of modes was advisable, albeit at the expense of reconstruction quality, to achieve a lower sensitivity in relation to the choice of sensor combination.

Distinctive trends were also observed in the POD strain modes. For instance, a significant decline in R^2 was noted when using one mode with seven sensors as compared to six sensors. This decline was attributed to the inadequate correlation between strains on the upper and lower flanges offered by the POD modes. In fact, such a poor correlation made signal reconstruction for sensor S7 impossible for all combinations of n_m and k.

Turning to the acceleration modes, both the FE and POD modes generally showed behaviours similar to those observed in the strain modes, although the results for sensors near the supports were slightly less accurate with POD modes than with FE modes. Unlike the oscillatory behaviour seen in the strain modes, R^2 tended to increase consistently as the number of considered modes n_m increased, provided that k was held constant.

Across all modes and sensor types, it was consistently observed that the results were generally poorer near the supports and improved towards the centre of the field.

7.3.2 Impact of train type and speed

This subsection explores the impact of train type and speed on the coefficient of determination, R^2. The evaluation focuses on the five most frequent train types traversing the bridge, as shown in Figure 7.16.

To eliminate the influence of sensor combinations, a leave-one-out validation approach was employed. In this context, the number of considered modes, n_{m}, remained as the sole variable parameter. This number was separately determined for each set of modes (FE and POD) and for both accelerations and strains. The selection was made by identifying the most frequent n_{m} that led to the highest R^2 for each set of modes. Consequently, three modes were considered for strains and six for accelerations in the FE modes, while four modes were used for both in the POD modes.

The obtained R^2 values were then associated with train speeds, discretised at 1 $\frac{\mathrm{m}}{\mathrm{s}}$ intervals. For each train type and speed group, the interquartile range of the R^2 values was selected and plotted against the speed. The choice of the interquartile range aimed to eliminate distortions that could be caused by outliers. This is particularly significant here as good results are limited to 1.0, while poor results have no negative limit.

In summary, it was indicated that superior performance was achieved using POD modes compared to FE modes in the results for strain measurements. However, a notable exception exists in the case of sensor S7, for which, as previously stated, no signal reconstruction was possible using the POD modes.

No discernible relationship was found between the train speeds and the coefficients of determination, R^2. Nonetheless, sporadic outliers were observed with lower R^2 values, and the locations of these outliers varied depending on the train type. This phenomenon is similar to the one observed for the Schmutter Bridge, as discussed in subsection 6.3.2, where a significant drop in R^2 was recorded just above the resonance speed.

Regarding the acceleration signals, a similar pattern was observed, and no significant differences in R^2 were detected when the FE and POD approaches were compared.

7.3.3 Impact of signal amplitudes

In this subsection, the impact of signal amplitudes on the coefficients of determination (R^2) is investigated. The analysis builds upon the established leave-one-out validation approach used in the previous section. The rationale for focusing on signal amplitudes stems from the intuitive expectation that higher amplitudes should yield better results, a hypothesis supported by observations from physical sensors. To ensure uniformity across sensors, the amplitudes were normalized to a maximum value of 1.0. This was accomplished by dividing each sensor's maximum amplitude by the highest amplitude recorded for all passages. The normalized amplitudes were then discretised in increments of 0.01, and for each level, the interquartile range and median were calculated for both POD and FE modes.

The findings, compiled in Figure B.24 for strain sensors and in Figure B.25 for acceleration sensors, corroborate the superior performance of POD modes over FE modes in reconstructing strain data. The sole exception to this trend is sensor S7.

An intriguing variation appears between POD and FE modes when examining their correlation with normalized amplitudes. POD modes exhibit a generally negative correlation, whereas FE modes lean towards a positive trend. Of particular note, sensors S1, S2, S3, and S8 manifest a marked decrease in R^2 values at around 0.3 of the normalized amplitude.

The strain sensor dataset stands out for its significant outliers, particularly at higher amplitudes. This issue is notably absent in the acceleration sensors, where the data representation extends fully up to 1.0 of the normalized amplitude.

In contrast, acceleration signals display a clearer relationship between R^2 and normalised amplitudes, with R^2 values sharply rising before converging towards 1.0. Moreover, FE modes yield superior results, especially for edge sensors like A1, A5, A6, and A9, which also demonstrate greater R^2 variance at lower amplitudes when POD modes are utilized.

7.3.4 Impact of environmental conditions

The effect of fluctuating environmental conditions, such as temperature, on structural properties is well-documented. Therefore, this subsection aims to investigate the influence of varying environmental factors on modal expansion. To this end, data from four thermocouples (TC1 to TC4) and the IDSSEL60 weather station has been employed.

To explore these correlations, the same leave-one-out validation approach used in the previous sections was applied. The coefficients of determination R^2 for all passages were gathered for each sensor, and their interquartile range was calculated. As in earlier analyses, this methodology minimises the distortion caused by outliers.

Separate Pearson correlation coefficients were computed for the interquartile ranges of each sensor with respect to the weather station data, for both POD modes and FE modes. A significance level of $\alpha = 0.001$ was chosen for these calculations. The results for the strain sensors are tabulated in Table 7.3, and those for the acceleration sensors can be found in Table 7.4.

A marked contrast is observed between the correlation of the coefficients of determination R^2 with environmental factors for acceleration and strain sensors. While acceleration sensors display minimal or no correlation with weather data, strain sensors exhibit pronounced correlations, particularly with temperature and humidity. It is noteworthy that these correlations are sensor-specific, varying in both magnitude and direction.

Interestingly, the direction of the correlation for a given sensor can also differ depending on whether FE or POD modes are employed. For instance, sensor S5 shows a strong positive correlation with temperature when using FE modes, but a negative correlation when POD modes are applied. It is observed that correlations with temperature generally outweigh those with humidity.

In terms of wind speed and wind gust speed, minimal correlations are found for strain sensors. However, a slight correlation is discerned for all acceleration sensors. The R^2 values for accelerations are consistently negatively correlated, while those for strains display varying directions.

Table 7.3 Pearson correlation coefficients between the coefficients of determination R^2 of the leave one out validation and the environmental data of the IDSSEL 60 weather station for each starin gauge (S1 to S8). 3 FE modes and 4 POD modes are considered with a significance level of $\alpha = 0.001$. Insignificant results are indicated by n.s.

sensor	temperature		humidity		wind speed		wind gust		precipitation rate		precipitation accumulation	
	FE	POD	FE	POD	FE	POD	FE	POD	FE	POD	FE	POD
S1	0.18	0.06	0.07	-0.14	0.07	0.12	0.08	0.12	n.s.	n.s.	n.s.	n.s.
S2	-0.13	-0.46	n.s.	0.28	n.s.	0.07	n.s.	0.09	n.s.	0.04	n.s.	0.11
S3	-0.48	-0.29	-0.02	0.26	-0.14	-0.05	-0.13	-0.04	0.03	0.02	0.04	0.04
S4	0.13	-0.60	-0.13	0.43	0.09	-0.04	0.10	-0.02	n.s.	n.s.	n.s.	0.09
S5	0.54	-0.41	-0.44	0.24	0.12	n.s.	0.12	n.s.	n.s.	n.s.	-0.02	0.05
S6	0.11	-0.60	-0.03	0.39	-0.04	0.02	-0.03	0.04	n.s.	0.04	n.s.	0.11
S7	-0.39	-0.25	0.34	0.08	-0.11	0.10	-0.10	0.11	n.s.	n.s.	0.03	0.06
S8	0.07	-0.25	-0.08	0.20	0.00	n.s.	n.s.	n.s.	n.s.	n.s.	n.s.	0.04

Lastly, both precipitation rate and accumulation are found to have negligible correlations with the coefficients of determination for both types of sensors.

In addition to the data from the weather station, temperature measurements from thermocouples TC1 to TC4, located directly on the structure, were also employed. The mean temperature for each passage was calculated and then discretised in increments of 0.2 °C. Subsequently, the interquartile range and median were computed for these grouped data, differentiated by type of sensor signal (acceleration or strain) and the type of modes used (FE or POD). The results are presented in figures Figure B.26 to B.29 in the appendix. As there was negligible difference between the results for TC1 and TC2 compared to TC3 and TC4, only the evaluations for TC1 and TC2 are displayed.

The findings align with the previously observed correlations with weather station data. A notable change in R^2 values is evident at lower temperatures, especially for sensors S6, A5, and A9. This might be attributed to the potentially frozen ballast, as suggested by Figure 7.10. However, it must be emphasized that the data sample size in this temperature range is insufficient to draw definitive conclusions on this matter.

Table 7.4 Pearson correlation coefficients between the coefficients of determination R^2 of the leave one out validation and the environmental data of the IDSSEL 60 weather station for each accelerometer (A1 to A9). 6 FE modes and 4 POD modes are considered with a significance level of $\alpha = 0.001$. Insignificant results are indicated by n.s.

sensor	temperature		humidity		wind speed		wind gust		precipitation rate		precipitation accumulation	
	FE	POD	FE	POD	FE	POD	FE	POD	FE	POD	FE	POD
A1	0.03	-0.09	0.07	0.13	-0.07	-0.07	-0.07	-0.07	0.02	n.s.	0.03	n.s.
A2	n.s.	-0.04	0.08	0.10	-0.07	-0.06	-0.07	-0.06	n.s.	n.s.	n.s.	0.03
A3	-0.08	-0.03	0.14	0.09	-0.09	-0.07	-0.09	-0.07	n.s.	n.s.	n.s.	n.s.
A4	n.s.	-0.07	0.05	0.09	-0.04	-0.06	-0.04	-0.06	n.s.	n.s.	n.s.	0.02
A5	-0.04	-0.07	0.09	0.11	-0.05	-0.06	-0.05	-0.06	n.s.	n.s.	0.04	n.s.
A6	n.s.	-0.14	0.08	0.17	-0.06	-0.07	-0.06	-0.07	0.03	0.02	0.05	0.04
A7	0.04	-0.15	0.05	0.18	-0.05	-0.08	-0.05	-0.08	0.02	0.02	0.05	0.05
A8	-0.02	-0.08	0.05	0.09	-0.03	-0.03	-0.02	-0.03	n.s.	n.s.	0.04	0.03
A9	-0.05	-0.10	0.09	0.11	-0.05	-0.04	-0.05	-0.03	0.02	n.s.	0.05	0.03

7.3.5 Evaluation of different sensor setups

To investigate the most suitable sensor positioning for signal reconstruction at a given measurement point, the methodology employed in the HUMVIB bridge analysis was utilised, as detailed in subsection 5.3.3. The results for strains are depicted in Figure 7.20 and Figure 7.21. Results concerning accelerations for the FE modes are presented in Figure 7.22, and for the POD modes in Figure 7.23.

The outcomes of this evaluation are in accordance with the findings from the HUMVIB bridge investigation. Distinct variations in the distribution of relative frequencies were observed, depending on whether POD modes or FE modes were applied. Generally, it was found that for both strains and accelerations, sensors adjacent on the same girder and the sensor opposite to it on the other girder constitute good choices for signal reconstruction at the given point. This result is consistent with expectations based on the modal shapes, as previously noted in the HUMVIB analysis.

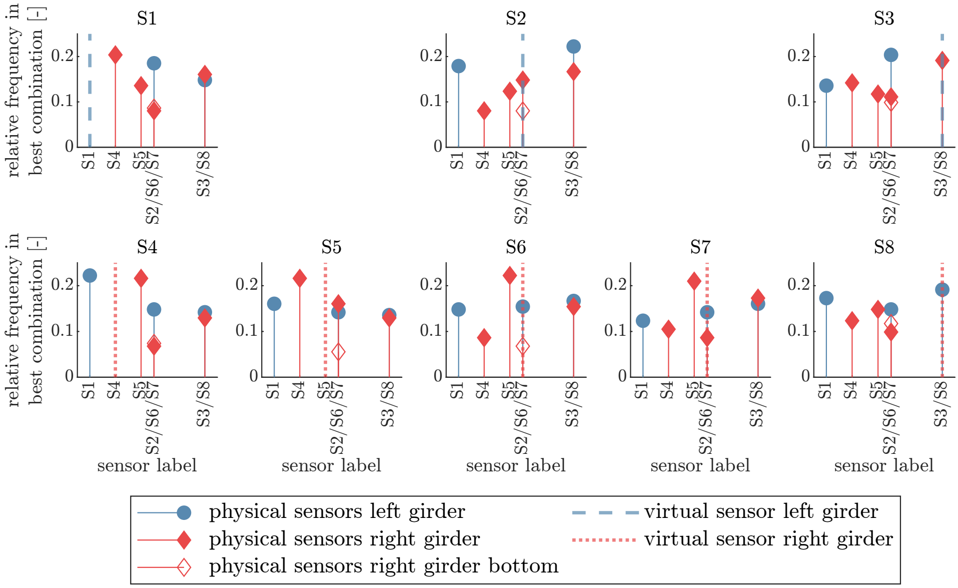

Figure 7.20 Summary of the number of occurrences of each strain gauge in an optimal sensor combination for reconstruction of a given measurement point using the FE modes.

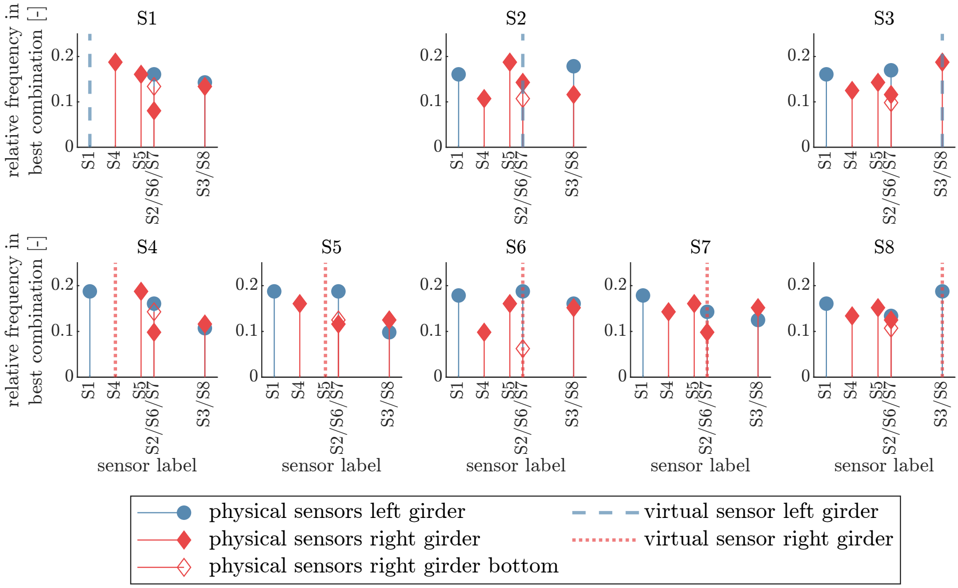

Figure 7.21 Summary of the number of occurrences of each strain gauge in an optimal sensor combination for reconstruction of a given measurement point using the POD modes.

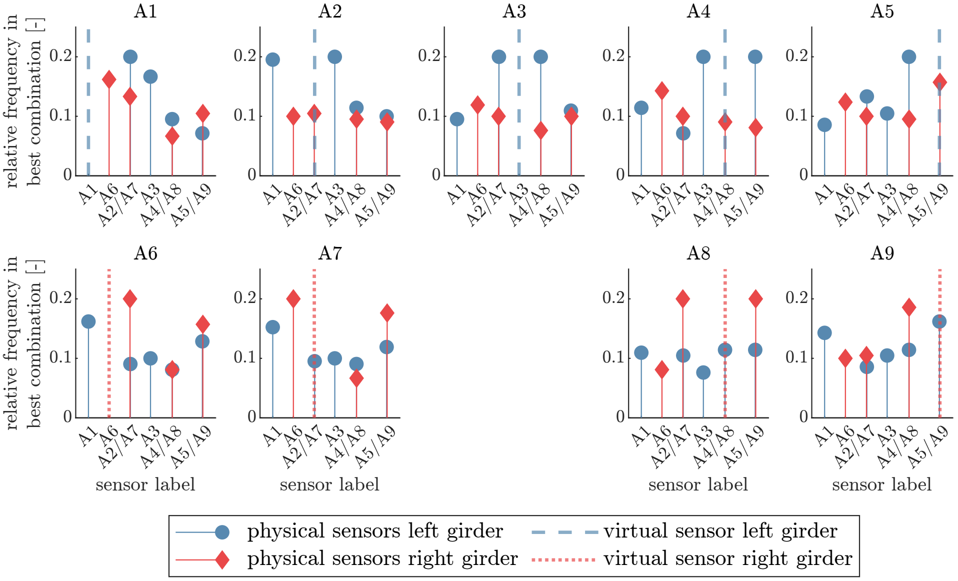

Figure 7.22 Summary of the number of occurrences of each accelerometer in an optimal sensor combination for reconstruction of a given measurement point using the FE modes.

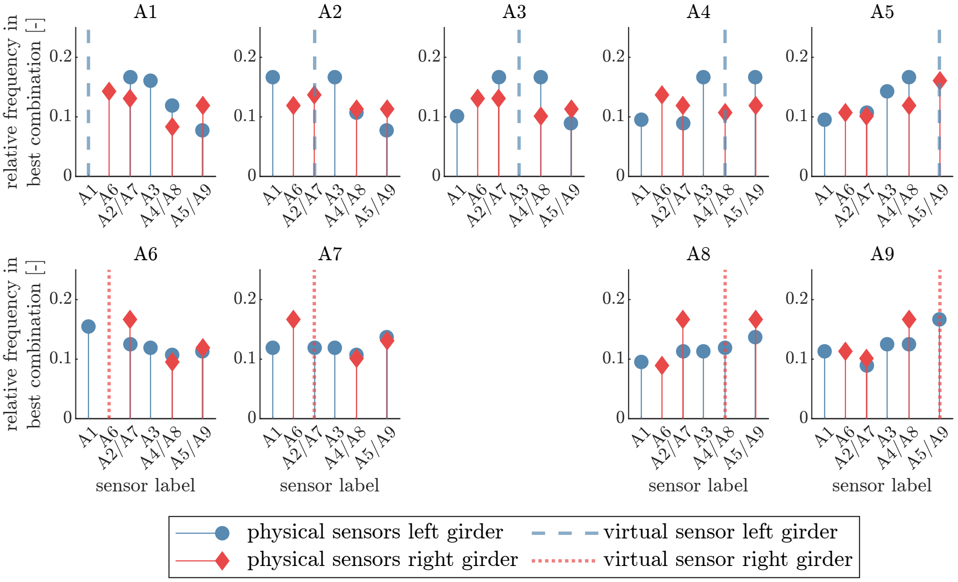

Figure 7.23 Summary of the number of occurrences of each accelerometer in an optimal sensor combination for reconstruction of a given measurement point using the POD modes.

7.3.6 Sample comparisons of signals from physical and virtual sensors

To further substantiate the findings on virtual sensing for this bridge, exemplary plots comparing signals from virtual and physical sensors are presented, along with the residual signals. The compilation of plots for strain signals can be found in Figure 7.24, while those for acceleration signals are available in Figure 7.25.

An arbitrarily selected passage was used for this analysis. Locations for the virtual sensors and sensor combinations were chosen in accordance with the predetermined coefficients of determination (R^2). The aim of this strategy is to offer a more nuanced understanding of the previously discussed coefficients of determination.

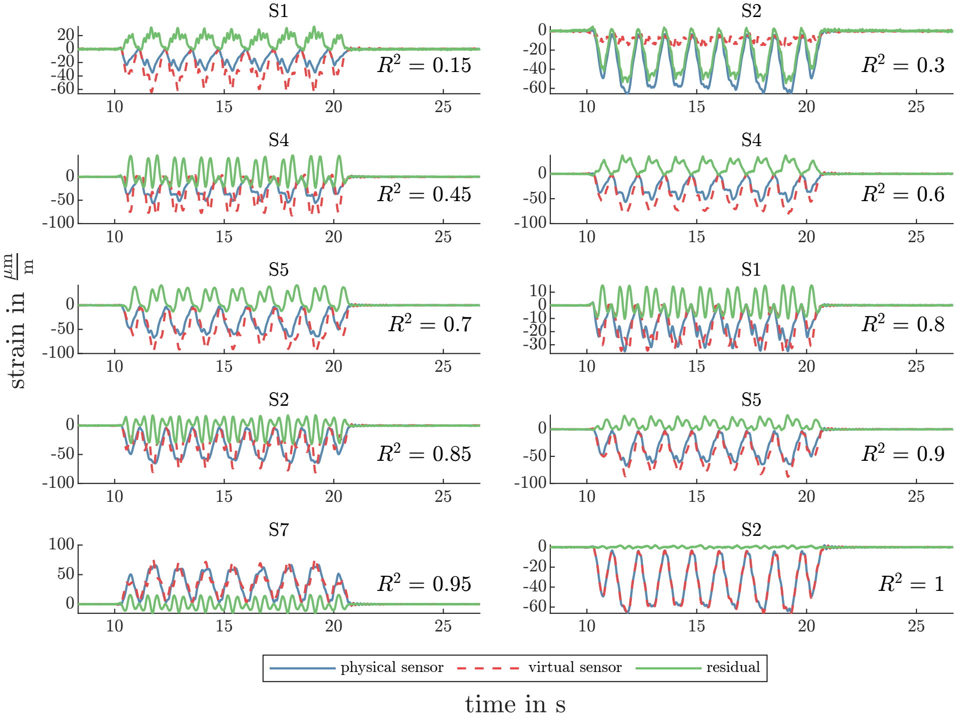

Figure 7.24 Exemplary comparisons of virtual sensor signals for the strains with those of the physical sensors for an arbitrarily chosen crossing to assess the coefficients of determination. The number of FE modes considered and the sensor combination for the physical sensors were chosen to match the respective coefficients of determination.

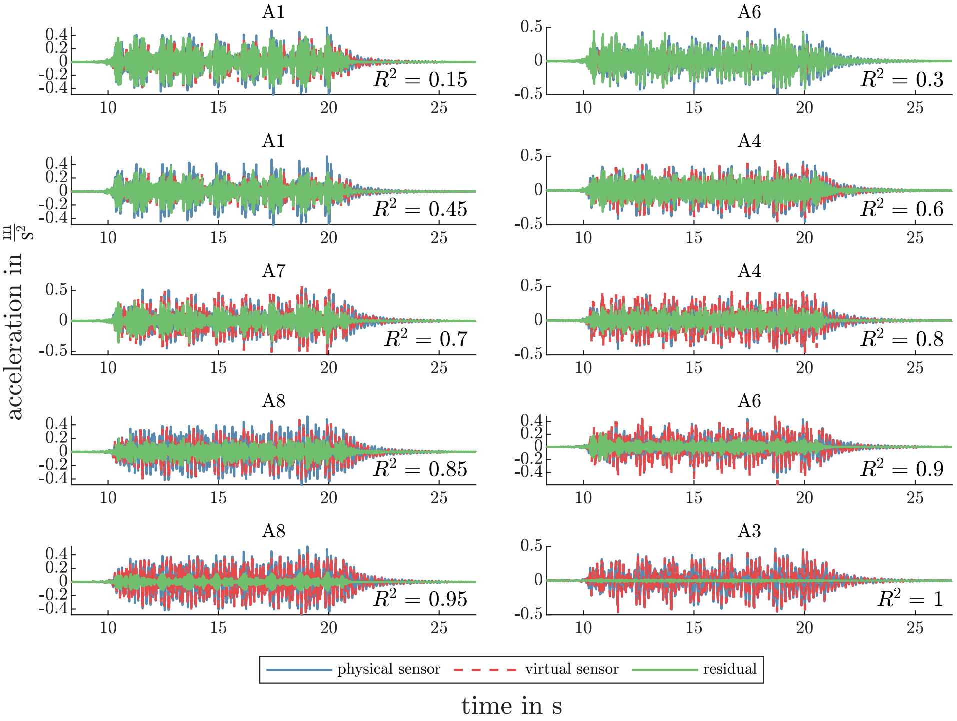

Figure 7.25 Exemplary comparisons of virtual sensor signals for the accelerations with those of the physical sensors for an arbitrarily chosen crossing to assess the coefficients of determination. The number of FE modes considered and the sensor combination for the physical sensors were chosen to match the respective coefficients of determination.

7.4 Drive-by monitoring

In this subsection, the data collected from the ICE TD crossings over the instrumented bridge, as detailed in section 6.1, are analysed. In comparison to the experiment in chapter 6, the vehicle with four cars is only one-third as long as the twelve car variant. Since all axles were instrumented on the ICE TD, in addition to the approaches used in section 6.4 of single sensor signals and residual signals to the preceding instrumented axle, the approach of the residual signal to the first axle can be examined. The expectation is that the residual signals to the first axle should provide the best results, as the bridge oscillation is minimal during the crossing of the first axle. In Figure 7.26, for the speeds of $v = 175.9\ \frac{\mathrm{km}}{\mathrm{h}}$ within the resonance range, and for a run at $v = 97.5\ \frac{\mathrm{km}}{\mathrm{h}}$ significantly outside of the resonance range, the times from each instrumented axle on the bridge are marked[2]. It turns out that the assumption is well-founded, particularly for crossings in the resonant range. In the case of non-resonant crossing, at the time of the first bogie crossing (axle 1 and axle 2), the amplitudes are already approximately corresponding to those of the rest of the crossing. For all three approaches, the impact of the filter setting is examined. This is followed by the identification of frequencies for all three approaches, in order to compare these with the values from the analysis of the bridge sensors. The final step is to compare the maximum absolute values of the measurements on the train with the maximum absolute values of the measurements on the structure.

---

[2] The contact times of the axles were determined utilising sensors G1 to G8.

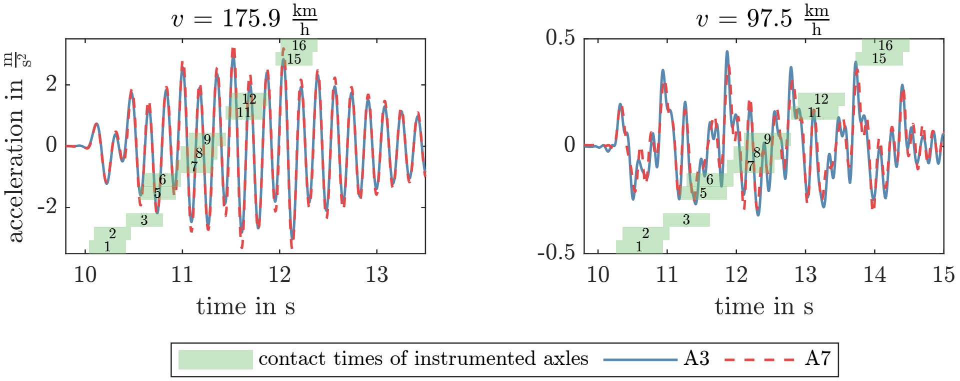

Figure 7.26 Contact periods of the instrumented axles of the ICE TD during resonance passage.

7.4.1 Influence of the cut-off frequency of the low-pass filter on the indirect resonance curve

In this analysis, the influence of cut-off frequency selection on the low-pass filter was scrutinised by considering three different approaches: 'single sensor signal', 'residual signal to preceding instrumented axle', and 'residual signal to the first axle'. The cut-off frequency of the 4th-order Butterworth low-pass filter was varied between 6.5 and 30 Hz in order to construct the indirect resonance curve. The examined range lies approximately 1 Hz above the bridge frequency, extending to the limit as prescribed by the Eurocode (DIN, 2021)[3]. The results for all three approaches and each sensor position have been compiled in the appendix, within figures Fig. B.30 to B.35. At this point, Figure 7.27 exemplarily only presents the evaluations for the left and right sides of the last axle.

The investigation reveals, as previously determined in section 6.4, that the use of 'single sensor signals' yields a strong dependency of the outcomes on the selection of the cut-off frequency. However, utilising the residual signals – both those related to the preceding axle and the first axle – significantly reduces this dependency. Notably, in contrast to the findings in section 6.4, there is a larger scattering. For instance, the sensors on T_{11L} and

---

[3] see section 2.8

T_{11R} exhibit stability for the residual signal to the first axle. The sensors T_{13L} and T_{10R} display a stable shape and peak position of the indirect resonance curve across the entire range of selected cutoff frequencies for the residual signal to the preceding axle. However, it becomes apparent with sensors like T_{5L} for both approaches that the curve shapes are no longer stable from around approximately 15 Hz cut-off frequency.

For the residual signals, a similar curve is produced for both the left and right sides. However, a significant difference arises between the left and right sides when using 'single sensor signals'. This difference will be further discussed in the context of frequency identification via indirect resonance curves.

From the comparison of sensitivity towards filter settings, it is not immediately apparent that either of the residual approaches is superior to the other in terms of resonance curve form stability.

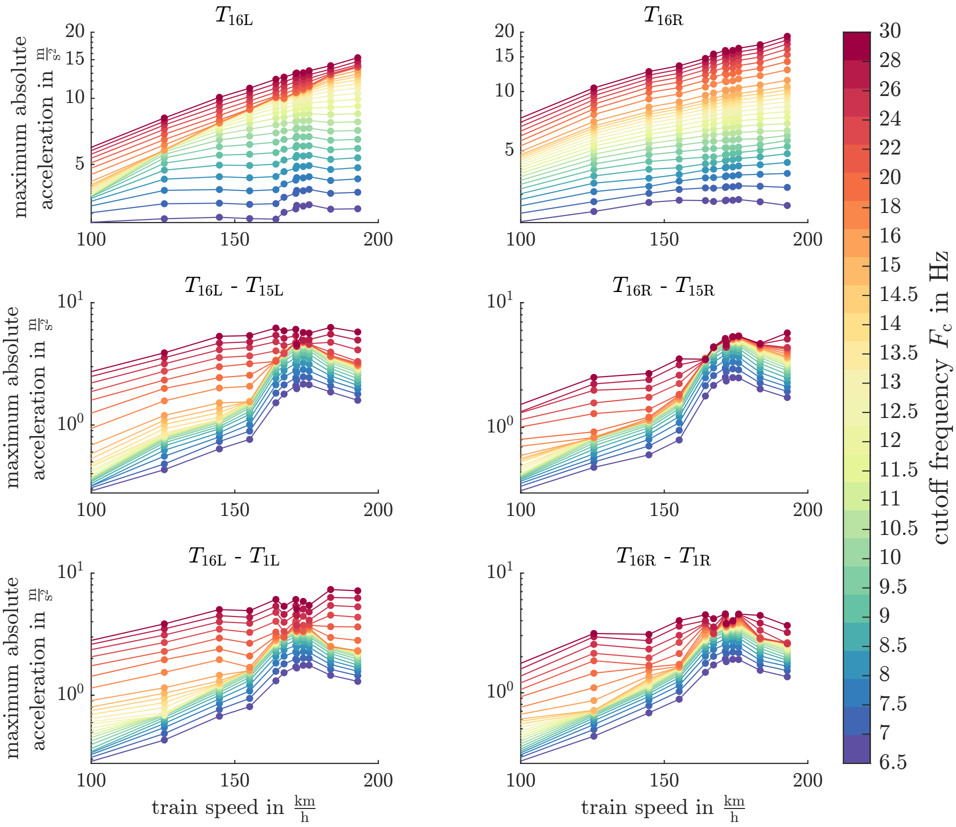

Figure 7.27 Exemplary compilation of the filter comparison for the last axle for the three approaches of a single sensor (top), the residual signal to the previous axle (middle) and the residual signal to the first axle (bottom).

7.4.2 Frequency identification

To validate the method for identifying the resonance frequency through the indirect resonance curve, as described in subsection 4.2.1, the cut-off frequency of the low-pass filter was set to approximately 3 Hz above the expected bridge frequency for all three approaches, mirroring the investigation in section 6.4. A 4th-order Butterworth filter was also employed as the low-pass filter.

The results of the ’single sensor signals’ approach are compiled in Figure 7.28. As previously observed during the examination of filter settings, there is a distinct difference between the results for the left and right sides of the instrumented axles. On the left side, the location of the resonance peak can be identified for 9 of the 14 sensors. In contrast, the resonance velocity cannot be identified for any of the 13 instrumented axles on the right side. This could be attributed to the higher acceleration values observed on the left side. These increased values of measured accelerations are somewhat surprising, as Figure 7.26 indicates that the accelerations on the right main girder are larger during resonance than those on the bridge’s left main girder.

The compilation of indirect resonance curves using the ’signal to preceding instrumented axle’ approach, presented in Figure 7.30, shows that for all bidirectionally instrumented axles, barring axles 3,5, and 11, the identified peak is at the same speed. The preceding axles for 5 and 11 vary due to sensor failures. Contrasting with the ’single sensor signals’ approach, there is congruence between the acceleration levels on the left and right sides of the train and those on the bridge’s left and right main girders. Consequently, the determined maximum absolute values on the right side are slightly higher than those on the left, corroborating the results from the bridge measurements. For axles 5, 11, and 15, different preceding instrumented axles are due to failed sensors, leading to a significant discrepancy in amplitudes.

Analysing the signals using the ’residual signal to the first axle’ approach leads to the same resonance peak location for all axles on both sides, except for the third. Also, in contrast to the ’single sensor signals’ approach, it shows that the right side, corresponding to the accelerations on the main carriers, has larger amplitudes.

Due to the small number of crossings, only one resonance peak can be idetified for this experiment, therefore an estimate for i in Equation 4.10 is necessary for the calculation of the frequencies. With the known frequency from the bridge measurements, it could be determined that $i = 3$.The results of the identified frequencies for all three approaches, comparing each sensor with the values determined by the bridge sensors, are compiled in Figure 7.31. The graph clearly indicates that, as expected, the ’residual signal to the first axle’ approach yields the best results. The precise values and the percentage error Equation 6.1 compared to the mean value of the frequencies identified by the bridge sensors are tabulated in the appendix in Tab. A.11 to A.14.

The ’residual signal to the first axle’ approach yields an average absolute percentage error of 1.9 % across all axles. The second axle has proven to be the only one unsuitable for generating the resonance curve in this approach. Excluding this as an outlier from the calculation reduces the average absolute percentage error to 0.9 %.

The ’residual signal to preceding instrumented axle’ approach, which exhibits the second-best performance, has an average absolute percentage error of 3.1 %. As the evaluation for the second axle is the same as the ’residual signal to the first axle’ approach, the signal here is also unsuitable for creating a resonance curve. Excluding the second axle from this mean calculation reduces the average absolute percentage error to 2.1 %.

The ’single sensor signal’ approach, which displays the poorest performance, has an average absolute percentage error of 4.4 % for the functioning left side and 12.2 % for the non-functioning side. Across all sensors, this approach results in an average error of 8.5 %. It’s important to note, while interpreting the error for the non-functioning side, that the error is limited only by the maximum speed driven in the experiment; higher speeds would yield a larger error. As no peak was detected in these curves, the maximum lies merely at the maximum speed achieved.

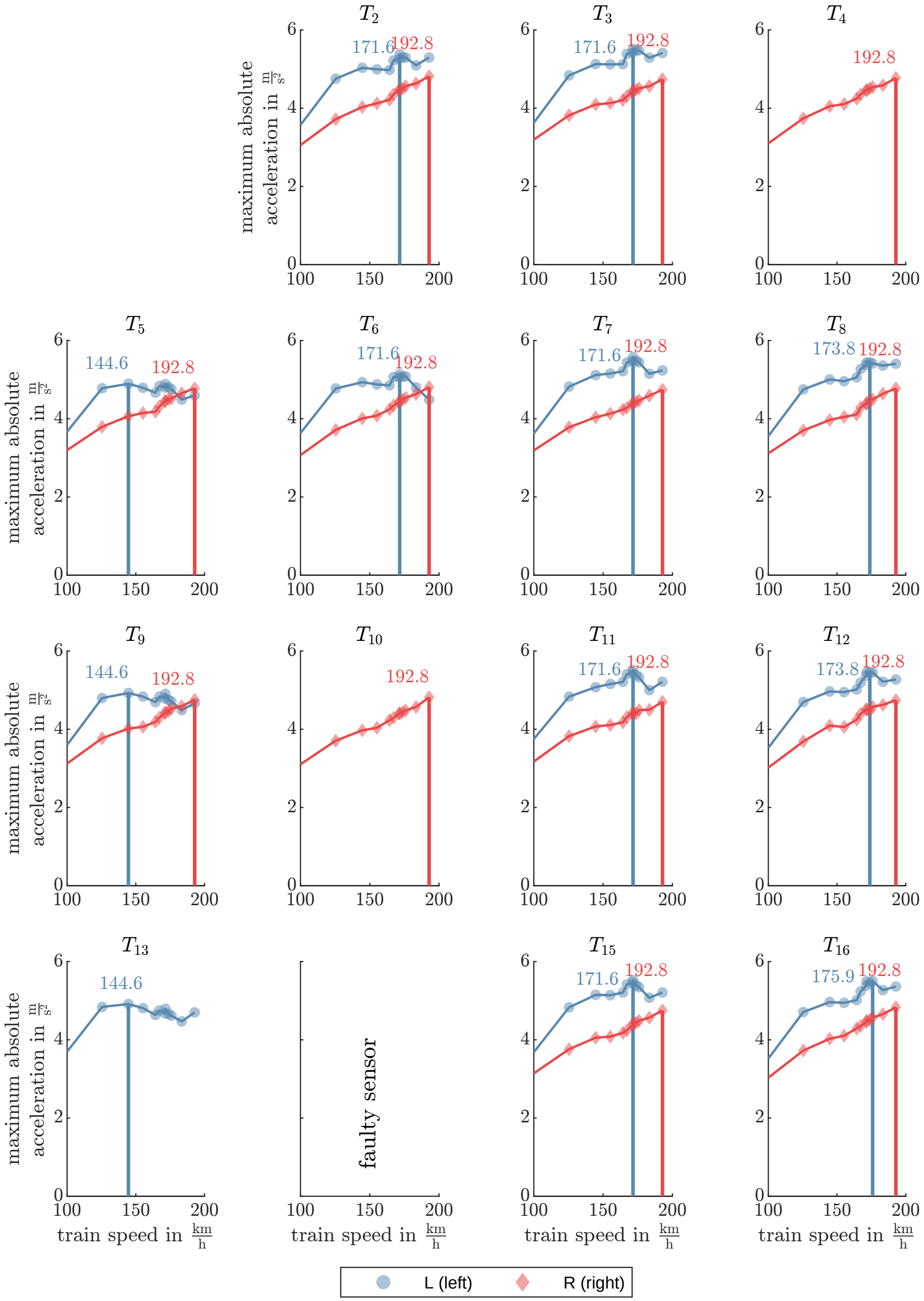

Figure 7.28 Compilation of the indirect resonance curves and their maxima for the 'single-sensor' approach for the cut-off frequency of the low-pass filter of $F_c = 8.5\ Hz$.

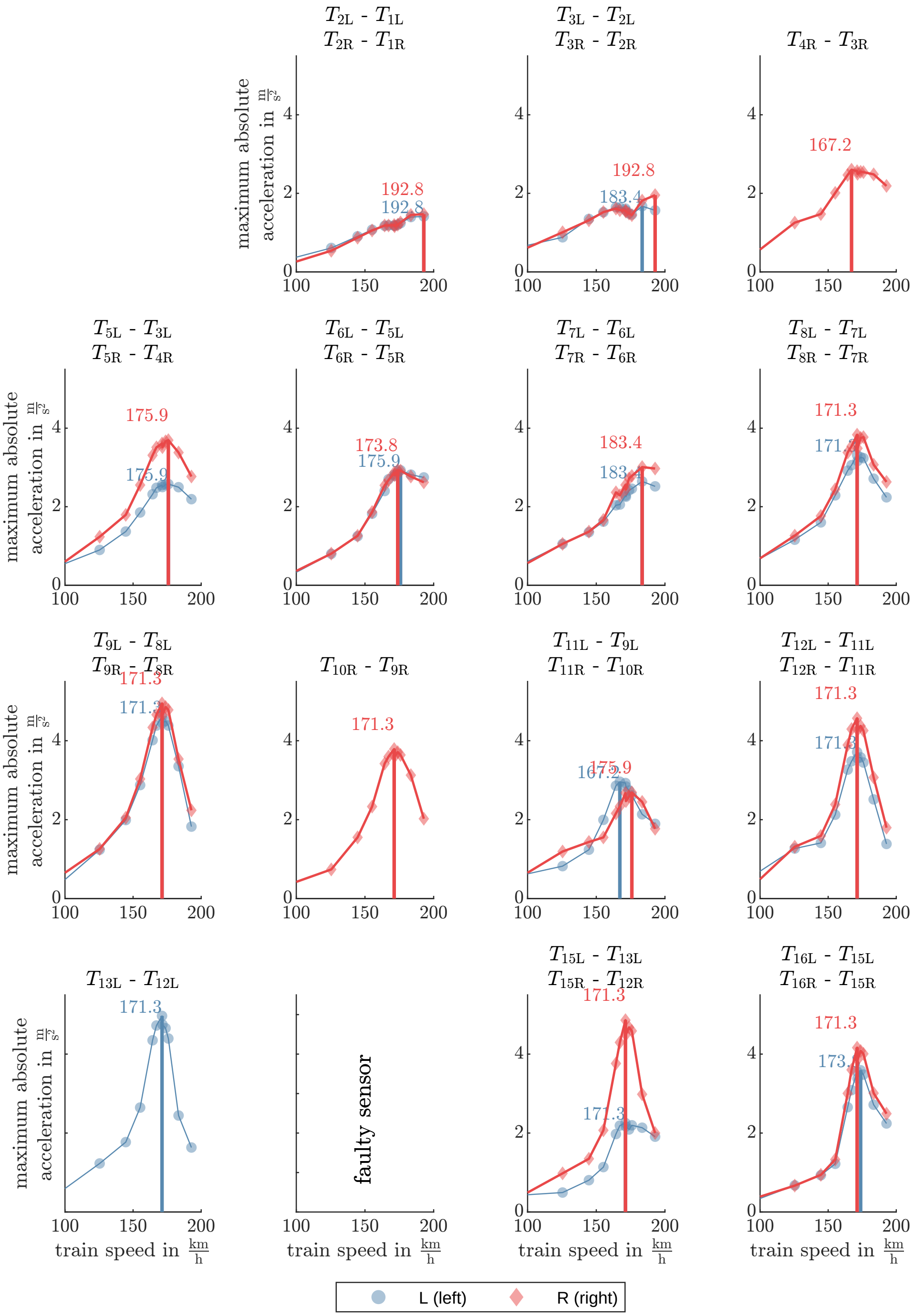

Figure 7.29 Compilation of the indirect resonance curves and their maxima for the 'residual signal to preceding instrumented axle' approch for the cut-off frequency of the low-pass filter of $F_c = 8.5\ Hz$.

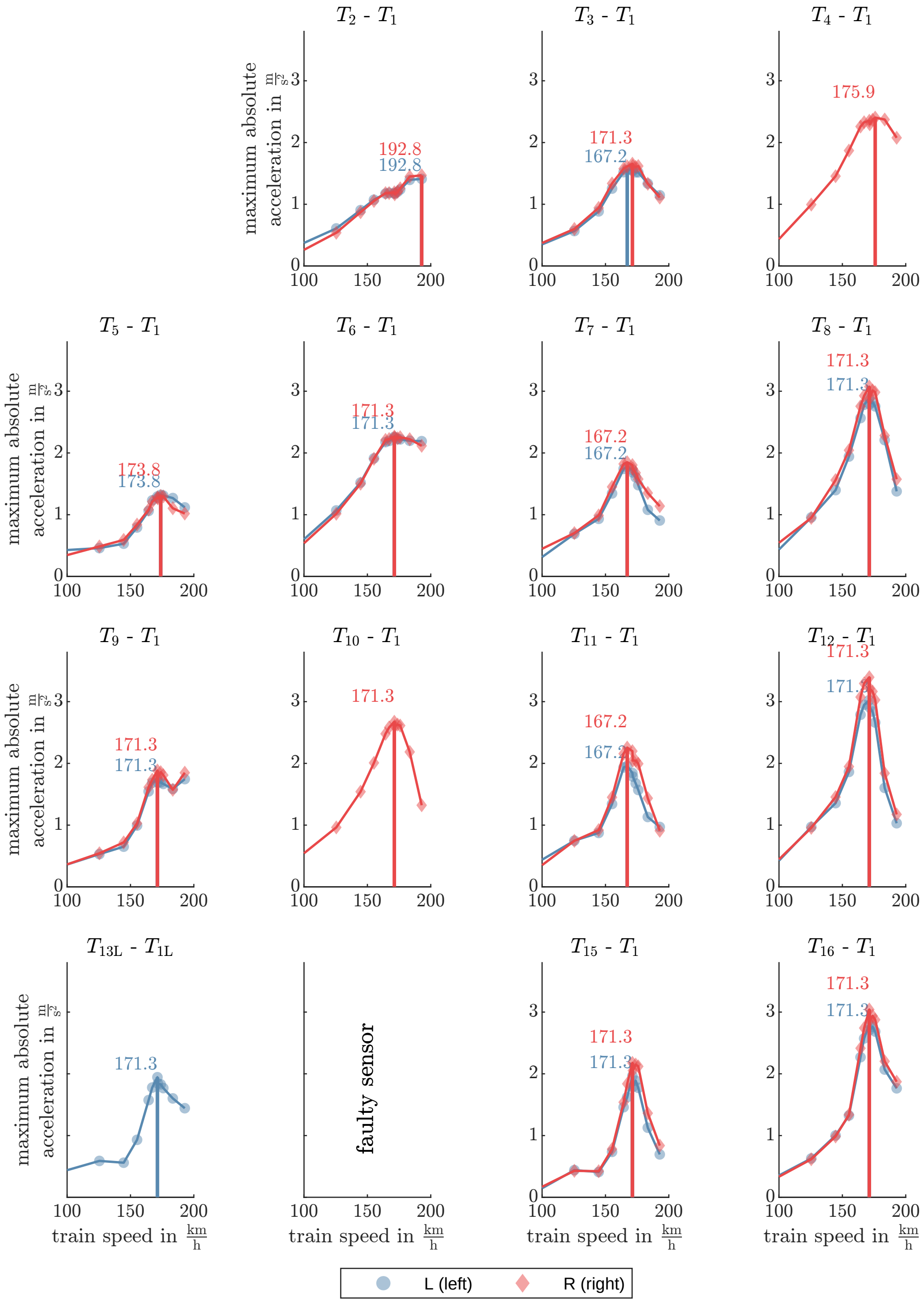

Figure 7.30 Compilation of the indirect resonance curves and their maxima for the 'residual signal to the first axle' approach for the cut-off frequency of the low-pass filter of $F_c = 8.5\ Hz$.

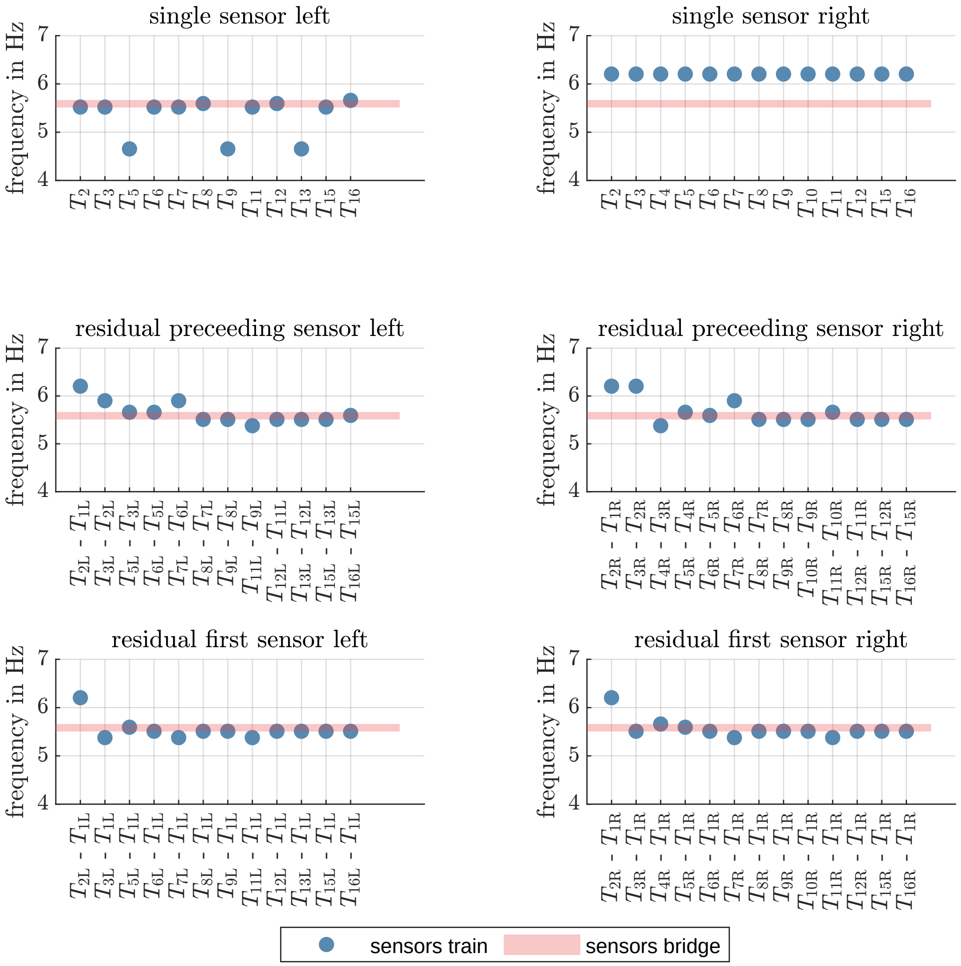

Figure 7.31 Comparison of the frequencies identified for the three approaches: single sensor (top), residual signal with the previous axle (middle) and residual signal with the first axle (bottom) for each of the sensors in comparison with the range identified with the bridge-mounted sensors

7.4.3 Comparison of indirect and direct resonance curves

Following the same approach as in the investigation detailed in section 6.4, the entire passage was utilised to determine the resonance peaks for frequency identification via bridge sensors. Therefore, in order to draw comparisons between the accelerations measured at the axles and those at the bridge, the maximum absolute values were recorded from the acceleration sensors at the bridge during the contact periods of the 16 axles. These resonance curves were then compared with the resonance curves created using the residual signals. A 4th-order Butterworth low-pass filter with a cut-off frequency of 8.5 Hz was also selected for all signals.

The results are shown in Figure 7.32 for the ’residual signal to the first axle’ approach. It is evident that there is a strong correlation between the amplitudes for all resonance curves, indicating a high level of consistency in the shape of the curves.

For the first axle of the cars (axles 5, 9, and 13), the amplitudes are underestimated by the indirect resonance curves. The second axle (axes 2 and 10) shows a concordance to the direct resonance curve. The third axle of the cars (axles 3, 7, 11, and 15) also underestimates the amplitudes. The last axle of the cars (axles 4, 8, 12, and 16) again shows a concordance with the amplitudes of the direct resonance curve, with the first three cars showing a slight overestimation while the last axle of the last car shows a slight underestimation of the amplitudes. For all comparisons, as previously in frequency identification, there is a match between the acceleration levels of the right and left train axle with the accelerations of the left and right main girders of the bridge.

In principle, the ’residual signal to the first axle’ approach, as illustrated in Figure 7.33, demonstrates a strong correlation between the amplitudes of the direct and indirect resonance curves. The approach exhibits a slightly poorer amplitude match, whereby, unlike the ’residual signal to the first axle’, the amplitudes are not underestimated but rather overestimated.

To obtain a quantitative comparison, the percentage error for all values of the comparison was determined according to Equation 6.2. The results are displayed for both approaches, separated by the left and right vehicle side in Figure 7.34[4], depending on the bridge acceleration as a comparative value. It is clear here that the values of the ’residual signal to preceding instrumented axle’ approach lie above the ’residual signal to the first axle’ approach, reflecting the over- and underestimation of the amplitudes for both approaches.

For the ’residual signal to the first axle’ approach, the mean and standard deviations of the percentage error for both the left and right sides are tabulated in Table 7.5. Similarly, the mean and standard deviation for the absolute values of the percentage error for the left and right sides are detailed in Table 7.6.

---

[4] It should be noted that for axle 2, the ’residual signal to the first axle’ approach is identical to the ’residual signal to the preceding instrumented axle’ approach.

Table 7.5 Summary of mean and standard deviation for percentage errors: This compares the maximum absolute values derived from the residual signals to the first axle box accelerations on the ICE TD, with the values recorded from sensors on the Garather Bach bridge.

	left		right	
	mean in %	std. in %	mean in %	std. in %
percantage error	-15	24.2	-15	25.5
absolut values percantage error	24.2	15	24.3	15.4

Table 7.6 Summary of mean and standard deviation for percentage errors: This involves comparing the maximum absolute values derived from the residual signals related to the preceding axle box accelerations on the ICE TD, with the values recorded from sensors on the Garather Bach bridge.

	left		right	
	mean in %	std. in %	mean in %	std. in %
percantage error	22.9	34.7	24	32.1
absolut values percantage error	31.8	26.7	32.3	23.7

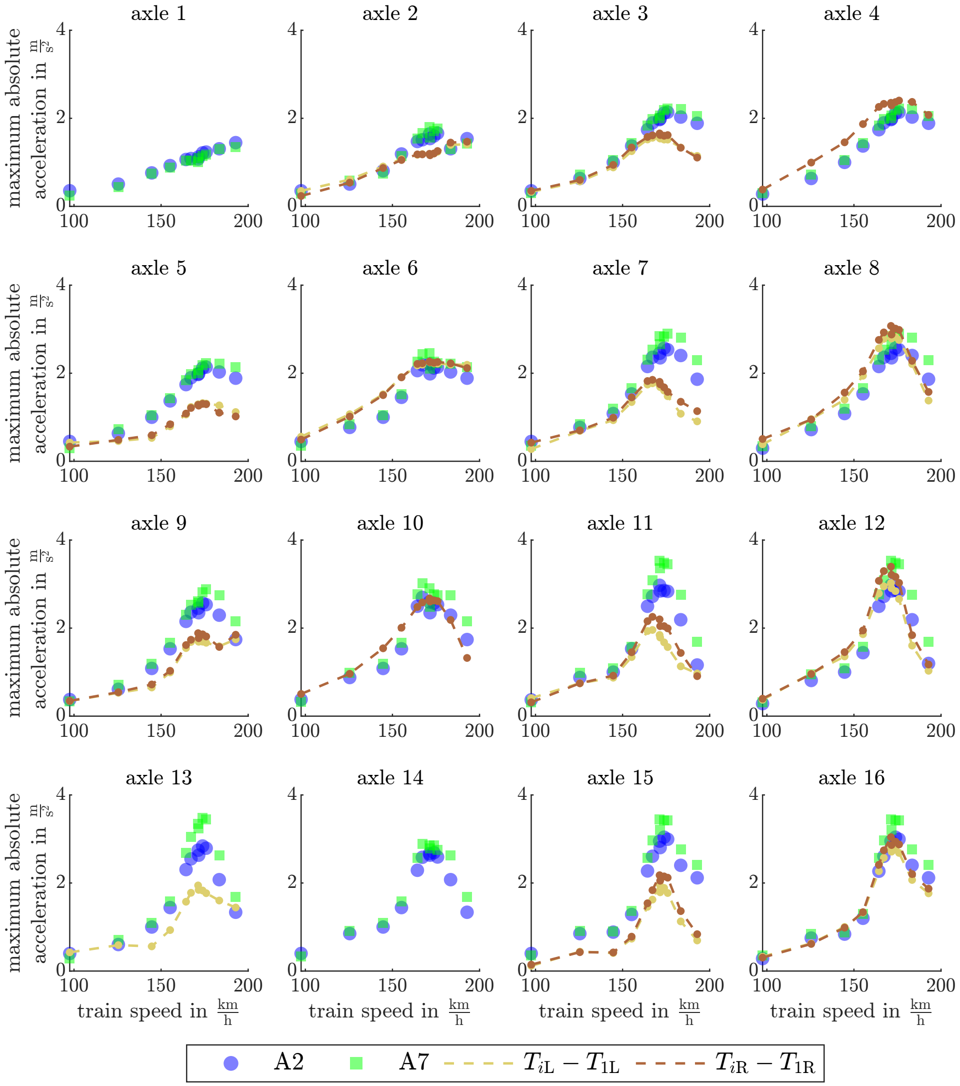

Figure 7.32 Comparison of the direct and indirect resonance curves for the contact periods of axle 1 to 16. For the indirect resonance curves, the residual signals to the first axle were used. All sigals were low-pass filtered with a cut-off frequency of 8.5 Hz.

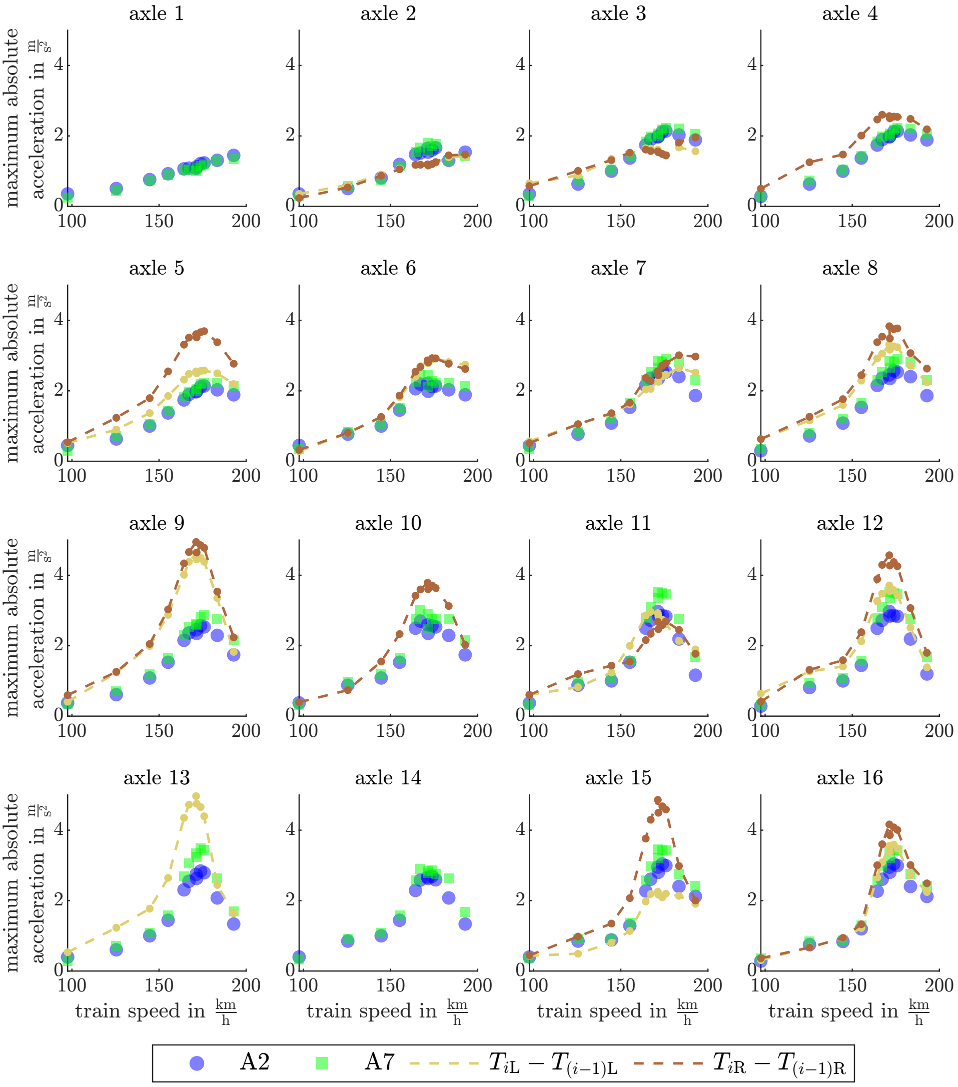

Figure 7.33 Comparison of the direct and indirect resonance curves for the contact periods of axle 1 to 16. For the indirect resonance curves, the residual signals to the preceding axle were used. All sigals were low-pass filtered with a cut-off frequency of 8.5 Hz.

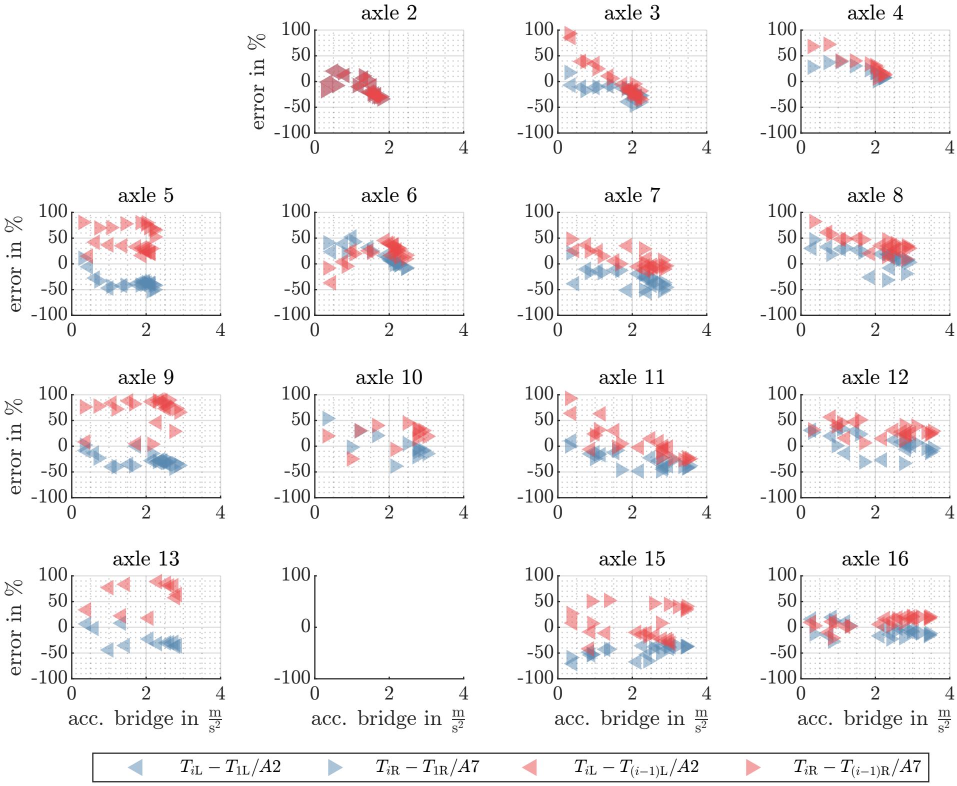

Figure 7.34 Percentage error of the maximum absolute values of the accelerations from the residual signals with the first axle $T_i - T_1$ and the residual signals with the preceding axle $T_i - T_{(i-1)}$ compared to the maximum absolute values of the sensors at bridge A2 and A7.

7.5 Conclusion

7.5.1 Virtual sensing

The primary focus of the investigations of virtual sensing in this chapter centered on the long-term validation of the modal expansion. An examination was conducted on the influence of varying operational and environmental conditions on the outcomes of the virtual sensors, comparing them to the readings of a physical sensor. The key findings from this analysis are as follows:

(1) The bridge exhibits nonlinear behavior similar to the Schmutter Bridge, characterized by amplitude-dependent frequencies. Despite this nonlinear behavior, the reconstruction of structural responses is still feasible using linear combinations of either FE modes or POD modes

(2) For an optimally chosen sensor combination, the best results are derived when the number of modes considered is $n_m = k - 1$. However, for less ideal sensor combinations, reducing the number of modes is recommended to attain reduced sensitivity to sensor choice, even though this might compromise reconstruction quality.

(3) Sensors located adjacently on the same girder or opposite on the other girder are especially apt for signal reconstruction, corroborating findings from the HUMVIB bridge study.

(4) Results for measurement points closer to the bridge supports are typically not as good as those at the center of the span, aligning with observations from preceding bridge analyses.

(5) Train speeds exhibited no clear association with the coefficients of determination R^2. However, occasional outliers with reduced R^2 values were identified whose positions fluctuated depending on the type of train, in line with the behaviour observed for the Schmutter bridge.

(6) The effectiveness of virtual sensor reconstructions was shown to increase with increasing signal amplitude. The notable exception is the reconstruction of the strain signals using the POD modes, which show a negative correlation with amplitude.

(7) In the context of the investigation, the POD modes outperform the FE modes in signal reconstruction of strains. A significant outlier was sensor S7, where signal reconstruction using POD modes was not feasible. For signal reconstruction of accelerations, FE modes outperform the POD modes, especially for sensors close to the supports (A1, A5, A6 and A9).

(8) There was a strong contrast between the correlations of R^2 values with weather data for strain and acceleration sensors. Strain sensors presented pronounced correlations, especially with temperature and humidity, whereas acceleration sensors showed negligible or zero correlation.
The correlation direction for specific sensors was contingent upon the mode type employed. For instance, sensor S5 registered a strong positive correlation with temperature using FE modes but a negative one with POD modes.

(9) No significant correlations were discerned between wind, rain, and the coefficients of determination for virtual sensors.

(10) A noticeable shift in coefficients of determination was observed at lower temperatures, particularly affecting sensors S6, A5, and A9. While this trend could potentially be attributed to frozen ballast, as indicated in Figure 7.10, it's important to emphasize that the sample size for this temperature range is too limited to draw conclusive findings.

In summary, environmental factors exerted a minimal influence on the quality of signal reconstruction across all sensors. This holds true even in instances where a correlation was observed between weather data and the coefficients of determination. More significant dependencies were noted with respect to train type and speed. A noticeable decline in reconstruction quality was observed at specific speeds, depending on the train type. It is plausible that these speeds activate vibration modes whose structural responses are not captured by the selected modes.

7.5.2 Drive by monitoring

The method for frequency identification using the indirect resonance curve, as described in subsection 4.2.1, was validated in section 7.4. For this, the data from the crossings of the instrumented ICE TD over the instrumented bridge described in section 7.1 were analysed. All axles of the vehicle were instrumented in this experiment, despite the failure of some sensors. Therefore, besides the two approaches 'single sensor signal' and 'residual signal preceding instrumented axle', which were already examined in section 6.4, the 'residual signal first axle' approach was also tested. The results of these three approaches were compared with the analysis of the bridge sensor signals, thus enabling the performance of the three approaches to be compared. The following conclusions can be drawn from the analysis:

(1) For all three approaches, the sensitivity to the choice of cut-off frequency of the low-pass filter was examined. The analysis shows that, as also in the investigations in section 6.4, the 'single sensor signals' approach has a strong dependence on the choice of cut-off frequency. In this approach, both the amplitudes and the shape

of the curves depend on the choice of cut-off frequency. For the two approaches ’residual signal preceding instrumented axle’ and ’residual signal first axle’, there is a greatly reduced dependence of the indirect resonance curves on the choice of cut-off frequency. Here, the shapes of the curves and the position of the peaks are stable; essentially, only the amplitudes of the curve change. Unlike the investigations in section 6.4, some resonance curves created with residual signals diverge in form from a cut-off frequency of about 15 Hz. In section 6.4, the shapes were stable up to the upper cut-off frequency of 30 Hz.

(2) The ’single sensor signals’ approach proved to be only partially suitable for frequency identification; although the resonance peak could be detected with the left axle in 9 out of 14 sensors, no peak could be found for the sensors on the right side of the train.

(3) With the approaches ’residual signal first axle’ and ’residual signal preceding instrumented axle’, the frequency can be identified very accurately compared to the values determined with the sensors on the bridge. However, it is shown that the second axle is not suitable for creating an indirect resonance curve using a residual signal. If we exclude this as an outlier, the mean of the absolute percentage error for the ’residual signal first axle’ approach is 0.9 %, and for the ’residual signal preceding instrumented axle’ approach it is 2.1 %. Thus, the ’residual signal first axle’ approach shows the best performance for frequency identification.

(4) The two residual signal approaches are also suitable for estimating the accelerations of the bridge structure. Here again, the ’residual signal first axle’ approach shows better performance. In this experiment, the accelerations for this approach tend to be underestimated; the mean of the absolute values of the percentage error is approximately 24 % with a standard deviation of about 15 %. The ’residual signal preceding instrumented axle’ approach, on the other hand, tends to overestimate the accelerations. The mean of the absolute values of the percentage error is approximately 32 % for both sides, with a standard deviation of about 27 % for the left side and 24 % for the right side.

Although the method for frequency identification was also possible for some sensors using the ’single sensor signal’ approach, the fact that it only worked for sensors on the left side suggests that this approach is not reliable. Therefore, multiple axles of the vehicle should be instrumented to determine the indirect resonance curves. In the comparison of the three approaches, the ’residual signal first axle’ method is demonstrated to have superior performance. This is observed both in the identification of frequency and in the estimation of accelerations on the structure. Consequently, it is recommended that instrumentation be applied to the first axle, along with at least one other, for the effective determination of the indirect resonance curves.

8 Conclusion and future research directions

8.1 Virtual sensing

8.1.1 Primary contributions and findings

As described in section 3.1, which summarises the state of the art in virtual sensing of railway bridges, two specific research gaps have been identified that are addressed in this thesis. The first gap refers to the limited investigations conducted on short-span, particularly ballasted, bridges that are prevalent in Germany. The second gap involves the lack of long-term studies that examine the influence of operational and environmental variations.

To address these gaps, two datasets recorded during field measurements were analysed.

The first dataset includes recordings from 52 passages of an ICE 4 train traversing the double-track railway bridge Schmutter at various speeds. This bridge consists of two parallel steel hollow boxes with a span of 19.5 meters, interconnected by a ballasted superstructure.

The second dataset comes from a long-term monitoring system attached to the single-track steel trough bridge Garather Bach, which has a ballasted superstructure and a 16.4-meter span. The dataset analysed encompasses a total of 38,133 passages.

Prior to the railway bridge investigations, data recorded on the HUMVIB footbridge were used to establish the basic properties of modal expansion on an easily accessible structure that allows comparatively simple modelling.

The primary contributions to the field of virtual sensing of railway bridges, made within the scope of this thesis, are summarised as follows:

(1) The applicability of modal expansion to railway bridges with nonlinear system behaviour was demonstrated. This was validated using both FE and POD modes, and included measurements of both accelerations and strains.

(2) Execution of the first long-term validation was carried out, which encompassed investigations under various operational and environmental conditions.

(3) The very first validation specific to short-span bridges (less than 20 m) with ballasted superstructure was conducted.

(4) The feasibility of using substructuring was shown, allowing for the modelling of only specific parts of the observed structure for virtual sensing. This approach eliminates the need for the challenging modelling of the coupling through the ballast superstructure.

The key findings from the research are as follows:

(1) The influence of environmental conditions on strains and accelerations was found to be markedly different; negligible correlations were found for accelerations, whereas significant correlations were observed for strains with respect to humidity and temperature. These effects were sensor-dependent and also varied depending on whether POD or FE modes were used.

(2) It was revealed that a clear relation between train speeds and the quality of signal reconstruction does not exist. Nevertheless, declines in the quality of virtual sensor signals within specific small speed ranges were observed, these declines being dependent on the type of train. Compared to these observed declines, the influence of environmental conditions on reconstruction quality was determined to be minimal.

(3) It was demonstrated that for optimally selected sensor combinations, the best results are achieved when the number of considered modes is equal to the number of physical sensors minus one ($n_m = k - 1$). However, in case of suboptimal sensor combinations, there is a risk of obtaining unusable signal reconstructions. Therefore, using fewer modes can be advantageous for ensuring usable reconstructions.

(4) POD modes were demonstrated to be load-dependent, yet still capable of reconstructing structural responses under varying load conditions. A notable exception was observed for a strain sensor on a bridge equipped with long-term monitoring. This deviation was attributed to the chosen POD modes' insufficient representation of the correlation between strains at the top and bottom flanges.

(5) Regarding sensor positioning, it was shown that adjacent sensor positions on the same girder and opposite positions on the neighbouring girder are particularly suitable for signal reconstruction at a point of interest.

(6) The quality of signal reconstruction was found to be lower near the supports compared to the centre of the span.

8.1.2 Limitations

Several limitations inherent to the studies presented in this thesis need to be acknowledged as they have implications for the interpretation of the findings.

(1) Sensors were solely installed on the main girders of the bridges, restricting the generalisability of the findings to the entire structure. This limitation is particularly important considering that the aim of virtual sensing is to extrapolate measurements to, ideally, all unmeasured parts of the structure. The poorer results near the supports indicate that further refinement of the methodology is required for such applications.

(2) The focus was maintained on observing changes attributable to environmental and operational conditions; therefore, comparisons between multiple physical and data-driven structural models – specifically, multiple sets of FE and POD modes – were not conducted. As a result, a definitive assessment regarding the dependence of the results on the choice of model could not be made.

(3) For the investigations concerning environmental influences, individual train passages were compared with their corresponding weather data. In relation to a larger time scale, this approach resulted in a dense sampling of data points, thereby producing noisy signals. Although the interquartile ranges of the coefficients of determination were utilised for evaluation, no further refinement, such as averaging daily temperatures, was undertaken on the weather data.

(4) Frozen ballast significantly alters the dynamic properties of railway bridges. However, insufficient amounts of data were collected on the frozen state to demonstrate that the same modes could be used to reconstruct structural responses under both frozen and unfrozen conditions.

(5) The long-term evaluation dataset has several gaps. While the dataset largely covers all environmental states, these gaps could introduce bias. Specifically, the bias could affect the correlation between weather data and the quality of virtual sensor reconstructions, in comparison to a complete dataset.

(6) A significant impact on the results was observed due to the choice of sensor positioning. Nevertheless, the sensor positions in the monitoring systems were not optimised specifically for virtual sensing. This limitation restricts the interpretation of the findings. However, the quality of the results, even without explicit optimisation, underscores the robustness and practical applicability of the methodology.

(7) No variations in the combinations of modes were investigated. Only the initial modes up to the number of considered modes were selected, meaning that no modes were omitted. It is plausible that by selectively choosing modes, the results could be further improved.

8.1.3 Recommendations for future research

Based on the findings of the study and its previously mentioned limitations, some recommendations for future research can be enumerated as follows:

(1) To further investigate the methodology of modal expansion and draw generalizable conclusions, additional measurements on real structures are urgently needed. A variety of bridge types, including multi-span beams, arch bridges, and different materials like steel-concrete composites, should be considered. However, the focus should be on bridges that are representative of the network, rather than on prestigious projects. During these measurements, attention should be paid to capturing both global structural responses on the main girders and local details. This is necessary to assess the suitability of virtual sensing for fatigue safety verification.

(2) For the practical application of virtual sensing results, a quantification of uncertainties is essential. A methodology should be developed to quantify the uncertainties associated with reconstructed signals, taking into account both model and measurement uncertainties.

(3) Another critical aspect regarding uncertainties arises from the choice of sensor positioning. It has been observed that the results from virtual sensors can significantly vary depending on the positioning of the physical sensors. Therefore, a methodology is needed to ensure appropriate sensor placement.

(4) An automated selection of modes should be implemented, initially for the entire set of modes and subsequently a subset of this set. Methods such as L1-Regression could be considered for this purpose.

(5) An investigation should be conducted to determine how improved results for structural responses near the supports can be achieved. For instance, weighting the structural responses in the regression could be considered. Alternatively or additionally, the use of local models may be explored. Successful determination of structural responses near the supports is crucial, as variations in cross-section height frequently occur in this area, leading to fatigue-prone details.

8.2 Drive-by monitoring

8.2.1 Primary contributions and findings

In section 3.2, the state of the art for drive-by monitoring of railway bridges was reviewed. The nascent stage of the field and the paucity of field tests were highlighted. A need was identified for a robust frequency identification methodology that can operate at regular train speeds and does not require detailed knowledge of the vehicle's dynamic characteristics.

To address this need, a methodology for the identification of resonance frequencies of railway bridges was developed. Validation was achieved through field tests conducted under real-world conditions, using accelerometers mounted on the train's axle boxes. The following key contributions were made:

(1) Introduction of a novel approach: A new technique, termed 'Resonance Curve-based Drive-by Monitoring', was introduced. This approach utilises multiple bridge crossings at varying speeds to form what is commonly referred to as the resonance curve, in which maximum accelerations are described as a function of speed.

(2) Resonance frequency identification: Based on the new approach, a methodology was developed for the identification of resonance frequencies from these curves. This addresses the problem of poor frequency resolution commonly encountered in frequency analyses, which are limited by the short contact times between the train and bridge.

(3) Real-world validation: The methodology was validated through two field tests. The bridges used for these tests were the same bridges utilised for validating virtual sensing techniques. For the 19.5-meter span bridge, an ICE 4 train was employed, featuring 48 axles, and accelerometers were mounted on both sides of four of these axles. For the 16.4-meter span bridge, an ICE TD train was employed, featuring 16 axles, and each axle was equipped with accelerometers on both sides.

The main findings of the research on the proposed methodology are:

(1) Though the methodology could be applied using signals from a single sensor for some axles, it is recommended that residual signals from two axles be utilised for reliable frequency identification. The utilisation of residual signals from two axles effectively eliminates the influence of speed-dependent effects that affect the acceleration measurements.

(2) Two different approaches for forming residual signals were investigated: 'residual signal to the first axle' and 'residual signal to preceding instrumented axle'. While both approaches were found to be reliable, the method involving the first axle outperformed the one involving the preceding axle, with a lower error rate of 0.9 % compared to 2.1 %.

(3) In addition to frequency identification, the methodology allows for the approximate determination of maximum bridge accelerations. This is particularly crucial at high amplitudes, where compliance with technical standards regarding maximum structural accelerations is essential for ensuring ballast stability.

8.2.2 Limitations

Several limitations inherent to the presented methodology and experimental investigations must be considered when interpreting the results:

(1) The methodology does not account for vehicle bridge interaction effects such as added mass and additional damping. As a result, the identified parameters are properties of the coupled system. While the effect is minor for the investigated train-bridge combinations, it will increase with decreasing bridge span.

(2) The methodology is dependent on the instrumented train's capability to resonantly excite the bridge. While the dynamic parameters may be less critical for non-resonant bridges, the possibility remains that trains with different axle configurations could induce resonance. Therefore, for practical implementation, it would be advisable to equip a fleet of trains that is representative in terms of axle configurations and operating speeds with instrumentation.

(3) Due to the limited number of bridge crossings conducted, particularly for the railway bridge Garther Bach, the resonance curves obtained were sparsely sampled. This sparse sampling precluded the identification of multiple peaks in the resonance curves for both structures. Multiple peaks are required for determining the resonance frequency without requiring a priori frequency estimates. Consequently, the sparse data hindered a comprehensive assessment of the methodology's capability in resonance frequency identification without estimates.

(4) When comparing the structural accelerations with the measurements on the axle boxes of the train, the values were compared over the entire contact time of the individual axles. For a more detailed comparison, zones of influence should be established, meaning, for example, that comparisons should always be made with the nearest sensor.

8.2.3 Recommendations for future research

Based on the investigations of the proposed new methodology and the description of its limitations, the following research tasks can be derived:

(1) Further detailed studies are required to ensure reliable evaluations with a minimal deployment of sensors. This is particularly necessary because, according to current technology, wireless instrumentation is not yet market-ready. Given the limited space available for measurement technology in existing regularly operating trains, only a few axles can be instrumented.

(2) The integration of vehicle-structure interaction effects should be considered in future studies. This would enable the methodology to be applied effectively to structures where these effects are significant.

(3) A method should be developed to determine the frequency with partial resonance curves, even without explicit peaks. One possible approach could involve formulating an optimisation problem for a beam model, which would significantly broaden the methodology's applicability and possibly obviate the need for instrumenting a representative fleet.

(4) An investigation should be conducted into the extent to which the performance can be enhanced by combining different approaches for forming residual signals. In this context, it would also be interesting to explore what additional information about the bridge vibrations can be extracted from the difference between the left and right sides of an axle.

(5) Additional parameters that can be derived from the resonance curves, potentially using another model like a mass-spring-damper system, should be examined. For example, the identification of damping could be considered.

(6) A more detailed comparison of the relationship between the measured accelerations and bridge accelerations should be carried out, along with an estimation of maximum bridge accelerations even outside of contact times.

(7) Further field measurements would provide significant added value, especially densely sampled resonance curves, which would benefit ongoing research and development in resonance curve-based drive-by monitoring.

8.3 Final remarks

The primary motivation for this work was to contribute to the cost-effective monitoring of deteriorating railway bridge infrastructure. To fulfil this primary aim, two specific objectives were established. The first objective was to identify a suitable methodology for the virtual sensing of railway bridges and validate its effectiveness through long-term studies, taking into account varying operational and environmental conditions. The second objective focused on the development and validation of a methodology for frequency identification through drive-by monitoring.

This work takes initial steps to address existing research gaps in both virtual sensing and drive-by monitoring, specifically the lack of field tests on short-span bridges with ballasted superstructures.

In terms of virtual sensing, long-term validation has demonstrated the applicability of modal expansion under changing operational and environmental conditions. Effective implementation requires the use of a sufficient number of well-positioned physical sensors. Additionally, an appropriate selection of modes is needed. Together, these factors can minimize the need for sensors in hard-to-reach locations on the main load-bearing structure. Thus, This approach not only enhances safety but also reduces both instrumentation costs and track closure times.

The development and validation of the resonance curve-based drive-by monitoring methodology were carried out, introducing a robust technique for identifying resonance frequencies. This methodology holds the potential to monitor an entire network of bridges. Information about the resonance frequency obtained can be utilised for model calibration. Furthermore, integrating the information about resonance speed into a networked system that can relay resonance speeds to individual trains could prevent resonant crossings, thereby extending the service life of the bridges. Minimal adjustments to train speeds, either faster or slower, can significantly reduce structural responses. Thus, the method not only enables more accurate engineering calculations but also optimises the use of the bridges, thereby contributing to their extended service life.

Bibliography

Literature

ALESSIO, S. M. (2016): *Digital Signal Processing and Spectral Analysis for Scientists*, Springer, pp. 153–182.

ANASTASOPOULOS, D., MORETTI, P., GEERNAERT, T., DE PAUW, B., NAWROT, U., DE ROECK, G., BERGHMANS, F. and REYNDERS, E. (2017): Identification of modal strains using sub-microstrain FBG data and a novel wavelength-shift detection algorithm, in: *Mechanical Systems and Signal Processing* vol. 86, pp. 58–74.

AZAM, S. E., DIDYK, M. M., LINZELL, D. and RAGEH, A. (2022): Experimental validation and numerical investigation of virtual strain sensing methods for steel railway bridges, in: *Journal of Sound and Vibration* vol. 537, p. 117207.

BARTHORPE, R. J. and WORDEN, K. (2020): Emerging trends in optimal structural health monitoring system design: From sensor placement to system evaluation, in: *Journal of Sensor and Actuator Networks* vol. 9.31.

BERCIN, A. N. and TANAKA, M. (1997): Coupled flexural-torsional vibrations of Timoshenko beams, in: *Journal of Sound and Vibration* vol. 207.1, pp. 47–59.

BRUNTON, S. L. and KUTZ, J. N. (2019): *Data-Driven Science and Engineering*, Cambridge: Cambridge University Press.

CHEYNET, E. (2020): Operational modal analysis with automated SSI-COV algorithm, Available online: `https://zenodo.org/record/3774061#.YdM0OlkxlhE`. DOI: 10.5281/ZENODO.3774061.

DE ROECK, G., REYNDERS, E. and ANASTASOPOULOS, D. (2018): Assessment of small damage by direct modal strain measurements, in: *Experimental Vibration Analysis for Civil Structures, Lecture Notes in Civil Engineering*, ed. by J. P. CONTE, R. ASTROZA, G. BENZONI, G. FELTRIN, K. J. LOH and B. MOAVENI, vol. 5, Springer International Publishing, pp. 3–16.

EFTEKHAR AZAM, S. and MARIANI, S. (2013): Investigation of computational and accuracy issues in POD-based reduced order modeling of dynamic structural systems, in: *Engineering Structures* vol. 54, pp. 150–167.

ERCAN, T. and PAPADIMITRIOU, C. (2021): Optimal sensor placement for reliable virtual sensing using modal expansion and information theory, in: *Sensors* vol. 21, p. 3400.

ERDURAN, E., PETTERSEN, F. M., GONEN, S. and LAU, A. (2023): Identification of vibration frequencies of railway bridges from train-mounted sensors using wavelet transformation, in: *Sensors* vol. 23, p. 1191.

FIRUS, A., BERTHOLD, H., SCHNEIDER, J. and GRUNERT, G. (2018): Untersuchungen zum dynamischen Verhalten einer Eisenbahnbrücke bei Anregung durch den neuen ICE 4, in: *VDI-Berichte* vol. 2321, pp. 233–248.

FIRUS, A. (2023): *A contribution to moving force identification in bridge dynamics*, vol. 65, Springer Nature.

FIRUS, A., KEMMLER, R., BERTHOLD, H. and LORENZEN, S. (2022): A time domain method for reconstruction of pedestrian induced loads on vibrating structures, in: *Mechanical Systems and Signal Processing* vol. 171, p. 108887.

FRÝBA, L. (1976): *Vibration of Solids and Structures Under Moving Loads*, Groningen, Netherlands: Noordhoff International Publishing.

FRÝBA, L. (1996): *Dynamica of Railway Bridges*, London, United Kingdom: Thomas Telford Publishing.

GATTULLI, V. (2016): Implementation of Identification Methodologies on Large-Scale Structures, in: *Identification Methods for Structural Health Monitoring*, ed. by E. CHATZI and C. PAPADIMITRIOU, Cham, Switzerland: Springer International Publishing, pp. 1–34.

GEISSLER, K. (2014): *Handbuch Brückenbau: Entwurf, Konstruktion, Berechnung, Bewertung und Ertüchtigung*, Berlin, Germany: John Wiley & Sons.

GEISSLER, K., STEFFENS, N. and STEIN, R. (2019): Grundlagen der sicherheitsäquivalenten Bewertung von Brücken mit Bauwerksmonitoring, in: *Stahlbau* vol. 88.4, pp. 338–353.

GRAUGAARD-JENSEN, J., BRINCKER, R., HJELM, H. P. and MUNCH, K. (2005): “Modal based fatigue monitoring of steel structures”, in: *Structural Dynamics EURODYN 2005: Proceedings of 6th International Conference on Structural Dynamics, Paris, France, 4-7 september 2005*, Millpress, pp. 305–310.

GROSS, D., HAUGER, W., WALL, J. and SCHRÖDER, W. A. (2021): *Technische Mechanik 2*, 14th ed., Berlin, Germany: Springer Vieweg.

GULGEC, N. S., TAKÁČ, M. and PAKZAD, S. N. (2020): Structural sensing with deep learning: Strain estimation from acceleration data for fatigue assessment, in: *Computer-Aided Civil and Infrastructure Engineering* vol. 35.12, pp. 1349–1364.

HE, J. and FU, Z.-F. (2001): *Modal Analysis*, Oxford, United Kingdom: Butterworth-Heinemann.

HENKEL, M., HÄFELE, J., WEIJTJENS, W., DEVRIENDT, C., GEBHARDT, C. and ROLFES, R. (2020): Strain estimation for offshore wind turbines with jacket substructures using dual-band modal expansion, in: *Marine Structures* vol. 71, p. 102731.

HOELZL, C., DERTIMANIS, V., LANDGRAF, M., ANCU, L., ZURKIRCHEN, M. and CHATZI, E. (2022): On-board monitoring for smart assessment of railway infrastructure: A systematic review, in: *The Rise of Smart Cities*, pp. 223–259.

JUNG, B. K. and JEONG, W. B. (2015): Mode selection of modal expansion method estimating vibration field of washing machine, in: *Journal of Sound and Vibration* vol. 340, pp. 343–353.

KAMMER, D. (1987): Test-Analysis-Model Development Using an Exact Modal Reduction, in: *The International Journal of Analytical and Experimental Modal Analysis* vol. 2, pp. 174–179.

KARIMI, F., AKBARI, R. and MAALEK, S. (2022): A Simple Conceptual Model for Estimating the First Bending Natural Frequency of Bridge Superstructures, in: *Shock and Vibration* vol. 2022, pp. 1–8.

KARIMI, S. (2020): Experimentelle und numerische Untersuchung der Wechselwirkung zwischen Tragwerk und Gleis, PhD thesis, Universität für Bodenkultur Wien.

KERSCHEN, G., GOLINVAL, J. C., VAKAKIS, A. F. and BERGMAN, L. A. (2005): The method of proper orthogonal decomposition for dynamical characterization and order reduction of mechanical systems: An overview, in: *Nonlinear Dyn.* vol. 41, p. 147.

KNAPP, N. (2019): Brücken bei der Deutschen Bahn, Available online: `https://www.deutschebahn.com/resource/blob/6860076/452fa9432001be62ac986886a2e60dd2/MP-Bruecken-Faktenblatt-875-Bruecken-data.pdf`. Accessed: 28.06.2022.

KOHL, A. M., CLEMENT, K. D., SCHNEIDER, J., FIRUS, A. and LOMBAERT, G. (2023): An investigation of dynamic vehicle-bridge interaction effects based on a comprehensive set of trains and bridges, in: *Engineering Structures* vol. 279, p. 115555.

KOUROUSSIS, G., CAUCHETEUR, C., KINET, D., ALEXANDROU, G., VERLINDEN, O. and MOEYAERT, V. (2015): Review of trackside monitoring solutions: From strain gages to optical fibre sensors, in: *Sensors* vol. 15.8, pp. 20115–20139.

KULLAA, J. (2019): Bayesian virtual sensing in structural dynamics, in: *Mechanical Systems and Signal Processing* vol. 115, pp. 497–513.

KULLAA, J. (2016): Virtual sensing of structural vibrations using dynamic substructuring, in: *Mechanical Systems and Signal Processing* vol. 79, pp. 203–224.

LI, J., ZHU, X., LAW, S.-S. and SAMALI, B. (2019): Indirect bridge modal parameters identification with one stationary and one moving sensors and stochastic subspace identification, in: *Journal of Sound and Vibration* vol. 446, pp. 1–21.

LI, W. M., JIANG, Z. H., WANG, T. L. and ZHU, H. P. (2014): Optimization method based on Generalized Pattern Search Algorithm to identify bridge parameters indirectly by a passing vehicle, in: *Journal of Sound and Vibration* vol. 333.2, pp. 364–380.

LIN, C. and YANG, Y. (2005): Use of a passing vehicle to scan the fundamental bridge frequencies: An experimental verification, in: *Engineering Structures* vol. 27.13, pp. 1865–1878.

LIU, L., KUO, S. M. and ZHOU, M. (2009): “Virtual sensing techniques and their applications”, in: *2009 International Conference on Networking, Sensing and Control*, IEEE, pp. 31–36.

LOCKE, W., REDMOND, L. and SCHMID, M. (2022): Evaluating OMA System Identification Techniques for Drive-by Health Monitoring on Short Span Bridges, in: *Journal of Bridge Engineering* vol. 27.9, pp. 1–14.

LORENZEN, S. R., BERTHOLD, H., RUPP, M., SCHMEISER, L., SCHNEIDER, J., THIELE, C.-D., BRÖTZMANN, J. and RÜPPEL, U. (2022a): “Künstliche Intelligenz, Digitale Zwillinge und die Zukunft des Brückenmanagements”, in: *Baudynamik 2022*, VDI Verlag, pp. 109–124.

LORENZEN, S., BERTHOLD, H., RUPP, M., SCHMEISER, L., APOSTOLIDI, E., SCHNEIDER, J., BRÖTZMANN, J., THIELE, C.-D. and RÜPPEL, U. (2022b): Deep learning based indirect monitoring to identify bridge natural frequencies using sensors on a passing train, in: *Bridge Safety, Maintenance, Management, Life-Cycle, Resilience and Sustainability*, CRC Press, pp. 401–409.

LUBER, B. (2011): Methoden zur Bewertung von Gleislageabweichungen auf Basis von Fahrzeugreaktionen, PhD thesis, Universität Graz.

LUNDMAN, S. and PARNÉUS, P. (2018): Virtual sensing for fatigue assessment of the Rautasjokk Bridge, MA thesis, Stockholm, Sweden: KTH Royal Institute of Technology School of Architecture and the Built Environment.

LURIE, A. I. and BELYAEV, A. (2005): *Theory of Elasticity*, pp. 755–878.

MAES, K., DE ROECK, G., LOMBAERT, G., CUNHA, A, CAETANO, E., RIBEIRO, P and MÜLLER, G (2014): “Response estimation in structural dynamics”, in: *Proceedings of the 9th International Conference on Structural Dynamics, EURODYN 2014*, vol. 2014, EUROPEAN ASSOC STRUCTURAL DYNAMICS.

MAES, K., ILIOPOULOS, A., WEIJTJENS, W., DEVRIENDT, C. and LOMBAERT, G. (2016): Dynamic strain estimation for fatigue assessment of an offshore monopile wind turbine using filtering and modal expansion algorithms, in: *Mechanical Systems and Signal Processing* vol. 76, pp. 592–611.

MAES, K. and LOMBAERT, G. (2021): “Validation of virtual sensing for the fatigue assessment of steel railway bridges”, in: *Life-Cycle Civil Engineering: Innovation, Theory and Practice: Proceedings of the 7th International Symposium on Life-Cycle Civil Engineering (IALCCE 2020), October 27-30, 2020, Shanghai, China*, CRC Press, pp. 29–3047.

MALEKJAFARIAN, A. and OBRIEN, E. J. (2014): Identification of bridge mode shapes using Short Time Frequency Domain Decomposition of the responses measured in a passing vehicle, in: *Engineering Structures* vol. 81, pp. 386–397.

MALEKJAFARIAN, A., CORBALLY, R. and GONG, W. (2022): A review of mobile sensing of bridges using moving vehicles: Progress to date, challenges and future trends, in: *Structures* vol. 44.August, pp. 1466–1489.

MALEKJAFARIAN, A., MCGETRICK, P. J., OBRIEN, E. J. et al. (2015): A review of indirect bridge monitoring using passing vehicles, in: *Shock and vibration* vol. 2015.

MATSUOKA, K. and TANAKA, H. (2023): Drive-by deflection estimation method for simple support bridges based on track irregularities measured on a traveling train, in: *Mechanical Systems And Signal Processing* vol. 182, p. 109549.

MATSUOKA, K., TANAKA, H., KAWASAKI, K., SOMASCHINI, C. and COLLINA, A. (2021): Drive-by methodology to identify resonant bridges using track irregularity measured by high-speed trains, in: *Mechanical Systems and Signal Processing* vol. 158, p. 107667.

OBRIEN, E. J., MCGETRICK, P. J. and GONZÁLEZ, A. (2014): A drive-by inspection system via vehicle moving force identification, in: *Smart Structures and Systems* vol. 13.5, pp. 821–848.

PAPADIMITRIOU, C., FRITZEN, C.-P., KRAEMER, P. and NTOTSIOS, E. (2011): Fatigue predictions in entire body of metallic structures from a limited number of vibration sensors using Kalman filtering, in: *Structural Control and Health Monitoring* vol. 18.5, pp. 554–573.

PENG, Z., DONG, K. and YIN, H. (2019): A modal-based kalman filter approach and OSP method for structural response reconstruction, in: *Shock and Vibration* vol. 2019.

PETERSEN, C. and WERKLE, H. (2018): *Dynamik der Baukonstruktionen*, Wiesbaden, Germany: Springer Vieweg.

REITERER, M., BETTINELLI, L., STOLLWITZER, A., SCHELLANDER, J. and FINK, J. (2022): “Vehicle-Based Indirect SHM of an Austrian Railway Bridge: Simulation and In-Situ Test”, in: *European Workshop on Structural Health Monitoring*, Springer, pp. 721–731.

REITERER, M. and FIRUS, A. (2021): Dynamische Analyse der Zugüberfahrt bei Eisenbahnbrücken unter Berücksichtigung von nichtlinearen Effekten, in: *Beton- und Stahlbetonbau* vol. 117.

REN, P. and ZHOU, Z. (2017): Strain estimation of truss structures based on augmented Kalman filtering and modal expansion, in: *Advances in Mechanical Engineering* vol. 9.11, pp. 1–10.

REYNDERS, E. (2012): System Identification Methods for (Operational) Modal Analysis: Review and Comparison, in: *Archives of Computational Methods in Engineering* vol. 19.1, pp. 51–124.

REYNDERS, E., SCHEVENELS, M. and DE ROECK, G. (2021): MACEC 3.4 The Matlab Toolbox for Experimental and Operational Modal Analysis.

RUPP, M. M. (2019): Schwingungsmessung zur inversen Lastberechnung mittels Dehnungsmessstreifen an einer Fußgängerbrücke, bachelor thesis, Darmstadt, Germany: Technische Universität Darmstadt.

RUPP, M. M., LORENZEN, S. R., FRITZSCHE, M. A., RIEDEL, H., KOHL, A., APOSTOLIDI, E. and SCHNEIDER, J. (2023): “High-speed drive-by monitoring: field testing with an intercity express train (ICE)”, in: *2nd Conference of the European Association on*

Quality Control of Bridges and Structures - EUROSTRUCT2023, Accepted, not yet published.

SARWAR, M. Z. and PARK, J.-W. (2020): Bridge displacement estimation using a co-located acceleration and strain, in: *Sensors* vol. 20.4, p. 1109.

SENJANOVIĆ, I., ĆATIPOVIĆ, I. and TOMAŠEVIĆ, S. (2007): Coupled flexural and torsional vibrations of ship-like girders, in: *Thin-Walled Structures* vol. 45.12, pp. 1002–1021.

SESTIERI, A. (2000): Structural dynamic modification, in: *Sadhana - Academy Proceedings in Engineering Sciences* vol. 25.3, pp. 247–259.

SIRINGORINGO, D. M. and FUJINO, Y. (2012): Estimating bridge fundamental frequency from vibration response of instrumented passing vehicle: analytical and experimental study, in: *Advances in Structural Engineering* vol. 15.3, pp. 417–433.

SOGABE, M., MATSUMOTO, N., KANAMORI, M., SATO, T. and WAKUI, H. (2005): Impact Factors of Concrete Girders Coping with Train Speed-up, in: vol. 46.1, pp. 0–6.

STRANG, G (2006): *Linear Algebra and Its Applications*, Cengage Learning India Private Limited.

STRANG, G (2007): *Computational Science and Engineering*, Wellesley-Cambridge Press.

STRANG, G. (2012): *Wissenschaftliches Rechnen*, vol. T-6, Springer, Berlin, Heidelberg.

TAN, C., ELHATTAB, A. and UDDIN, N. (2017): "Drive-by" bridge frequency-based monitoring utilizing wavelet transform, in: *Journal of Civil Structural Health Monitoring* vol. 7, pp. 615–625.

TARPØ, M., FRIIS, T., GEORGAKIS, C. and BRINCKER, R. (2021): Full-field strain estimation of subsystems within time-varying and nonlinear systems using modal expansion, in: *Mechanical Systems and Signal Processing* vol. 153, p. 107505.

TARPØ, M., NABUCO, B., GEORGAKIS, C. and BRINCKER, R. (2020): Expansion of experimental mode shape from operational modal analysis and virtual sensing for fatigue analysis using the modal expansion method, in: *International journal of fatigue* vol. 130, p. 105280.

THOMSEN, J. J. (2021): *Vibrations and Stability*, Cham, Switzerland.

TIMOSHENKO, S. (1951): *Theory of elasticity*, Oxford.

TSAI, H.-C., WANG, C.-Y., HUANG, N. E., KUO, T.-W. and CHIENG, W.-H. (2015): Railway track inspection based on the vibration response to a scheduled train and the Hilbert–Huang transform, in: *Proceedings of the Institution of Mechanical Engineers, Part F: Journal of Rail and Rapid Transit* vol. 229.7, pp. 815–829.

VAGNOLI, M., REMENYTE-PRESCOTT, R. and ANDREWS, J. (2018): Railway bridge structural health monitoring and fault detection: State-of-the-art methods and future challenges, in: *Structural Health Monitoring* vol. 17.4, pp. 971–1007.

VAN OVERSCHEE, P. and DE MOOR, B. (1996): *Subspace Identification for Linear Systems*, Springer Science.

XIA, H., ZHANG, N. and GUO, W. (2018): *Dynamic interaction of train-bridge systems in high-speed railways : theory and applications*, Springer Berlin, Heidelberg.

YANG, Y. B. and CHEN, W.-F. (2016): Extraction of Bridge Frequencies from a Moving Test Vehicle by Stochastic Subspace Identification, in: *Journal of Bridge Engineering* vol. 21.3, pp. 1–13.

YANG, Y.-B., LIN, C. and YAU, J. (2004): Extracting bridge frequencies from the dynamic response of a passing vehicle, in: *Journal of Sound and Vibration* vol. 272.3-5, pp. 471–493.

YANG, Y. B., SHI, K., WANG, Z. L., XU, H. and WU, Y. T. (2021): Theoretical study on a dual-beam model for detection of track/bridge frequencies and track modulus by a moving vehicle, in: *Engineering Structures* vol. 244.

YANG, Y. B., WANG, Z. L., SHI, K., XU, H. and WU, Y. T. (2020): State-of-the-Art of Vehicle-Based Methods for Detecting Various Properties of Highway Bridges and Railway Tracks, in: *International Journal of Structural Stability and Dynamics* vol. 20.13.

YANG, Y. B., XU, H., WANG, Z. L. and SHI, K. (2022): Using vehicle–bridge contact spectra and residue to scan bridge's modal properties with vehicle frequencies and road roughness eliminated, in: *Structural Control and Health Monitoring* vol. 29.8, pp. 1–25.

YANG, Y. B., ZHANG, B., QIAN, Y. and WU, Y. (2017): Contact-Point Response for Modal Identification of Bridges by a Moving Test Vehicle, in: *International Journal of Structural Stability and Dynamics* vol. 18.5, pp. 1–24.

YANG, Y. and YANG, J. P. (2018): State-of-the-art review on modal identification and damage detection of bridges by moving test vehicles, in: *International Journal of Structural Stability and Dynamics* vol. 18.02, p. 1850025.

YAO, H., GAO, Y. and LIU, Y. (2020): FEA-Net: A physics-guided data-driven model for efficient mechanical response prediction, in: *Computer Methods in Applied Mechanics and Engineering* vol. 363, p. 112892.

ZABEL, V. (2019): Operational modal analysis - Theory and aspects of application in civil engineering, ed. by C. KÖNKE, T. LAHMER and T. RABCZUK, habilitation, Institut für Strukturmechanik (ISM).

ZAHID, F. B., ONG, Z. C. and KHOO, S. Y. (2020): A review of operational modal analysis techniques for in-service modal identification, in: *Journal of the Brazilian Society of Mechanical Sciences and Engineering* vol. 42.8, pp. 1–18.

ZAYERI BAGHLANI NEJAD, A. and MAHMOUDI SAHEBI, M. (2021): An investigation on the capability of proper orthogonal modes in determining the natural frequencies and damping ratios of linear structural systems, in: *Engineering Structures* vol. 243.June.

ZHAN, J., YOU, J., KONG, X. and ZHANG, N. (2021a): An indirect bridge frequency identification method using dynamic responses of high-speed railway vehicles, in: *Engineering structures* vol. 243.

ZHAN, Y., AU, F. T. and ZHANG, J. (2021b): Bridge identification and damage detection using contact point response difference of moving vehicle, in: *Structural Control and Health Monitoring* vol. 28.12.

ZHU, X., LAW, S.-S. and SAMALI, B. (2014): “Indirect structural health monitoring of bridge structures using moving sensors”, in: *Proceedings of the 23rd Australasian Conference on the Mechanics of Structures and Materials (ACMSM23), Byron Bay, Australia, 9-12 December 2014*, pp. 1097–1102.

Standards and technical guidelines

DIN (2021): *Eurocode: Grundlagen der Tragwerksplanung: Deutsche Fassung EN 1990:2002 + A1:2005 + A1:2005/AC:2010.*

Table of appendices

A Tables **163**
A.1 Footbridge HUMVIB ... 163
A.2 Railway bridge Schmutter ... 166
A.3 Railway bridge Garather Bach ... 166

B Figures **171**
B.1 Footbridge HUMVIB ... 171
B.2 Railway bridge Schmutter ... 177
B.3 Railway bridge Garather Bach ... 182

A Tables

A.1 Footbridge HUMVIB

Table A.1 Maximum and minimum coefficients of determination R^2 and the corresponding number of considered modes n_m for the *leave-one-out validation* for each accelerometer and 4 different sets of POD modes at a **step frequency of 1.6 Hz**.

POD		**MP1 L**		**MP2 L**		**MP3 L**		**MP4 L**		**MP5 L**		**MP6 L**		**MP1 R**		**MP2 R**		**MP3 R**		**MP4 R**		**MP5 R**		**MP6 R**	
		R²	n_m	R²	n_m	R²	n_m	R²	n_m	R²	n_m	R²	n_m	R²	n_m	R²	n_m	R²	n_m	R²	n_m	R²	n_m	R²	n_m
1.6	max	0.99	9	1.00	9	1.00	10	0.99	9	1.00	8	0.99	8	1.00	7	1.00	7	1.00	7	1.00	8	1.00	10	0.99	7
	min	0.43	1	0.69	1	0.88	1	0.85	1	n.v.	10	0.24	2	n.v.	10	0.61	1	0.80	2	0.84	1	0.60	1	0.18	2
1.8	max	1.00	10	1.00	10	1.00	10	0.99	7	1.00	8	0.99	8	1.00	8	1.00	10	1.00	8	1.00	9	1.00	9	0.99	7
	min	0.42	1	0.67	1	0.87	1	0.86	1	0.66	1	0.34	1	0.30	1	0.59	1	0.79	1	0.84	1	0.61	1	0.32	1
2.0	max	0.99	9	1.00	9	1.00	7	0.99	7	1.00	10	0.99	8	1.00	7	1.00	7	1.00	7	1.00	8	1.00	9	0.99	7
	min	0.42	1	0.67	1	0.87	1	0.86	1	0.66	1	0.34	1	0.30	1	0.59	1	0.79	1	0.84	1	0.61	1	0.32	1
2.2	max	0.99	10	1.00	10	1.00	8	0.99	7	1.00	8	0.99	7	1.00	8	1.00	8	1.00	7	1.00	7	1.00	10	0.99	10
	min	0.42	1	0.67	1	0.87	1	0.86	1	0.66	1	0.34	1	0.30	1	0.59	1	0.79	1	0.84	1	0.61	1	0.32	1

Table A.2 Maximum and minimum coefficients of determination R^2 and the corresponding number of considered modes n_m for the *leave-one-out validation* for each accelerometer and 4 different sets of POD modes at a **step frequency of 1.8 Hz**.

POD		**MP1 L**		**MP2 L**		**MP3 L**		**MP4 L**		**MP5 L**		**MP6 L**		**MP1 R**		**MP2 R**		**MP3 R**		**MP4 R**		**MP5 R**		**MP6 R**	
		R²	n_m	R²	n_m	R²	n_m	R²	n_m	R²	n_m	R²	n_m	R²	n_m	R²	n_m	R²	n_m	R²	n_m	R²	n_m	R²	n_m
1.6	max	1.00	10	1.00	10	1.00	10	1.00	10	1.00	8	0.99	8	0.99	8	1.00	8	1.00	9	1.00	10	1.00	10	0.99	10
	min	0.69	1	0.89	1	0.96	1	0.94	1	0.17	10	0.69	1	0.39	10	0.86	1	0.93	1	0.93	1	0.89	1	0.69	1
1.8	max	1.00	10	1.00	8	1.00	8	1.00	8	1.00	8	0.99	8	1.00	10	1.00	10	1.00	9	1.00	8	1.00	9	0.99	7
	min	0.69	1	0.89	1	0.96	1	0.94	1	0.91	1	0.70	1	0.57	1	0.86	1	0.93	1	0.93	1	0.89	1	0.69	1
2.0	max	0.99	9	1.00	9	1.00	7	1.00	7	1.00	10	0.99	10	0.99	7	1.00	10	1.00	10	1.00	8	1.00	9	0.99	7
	min	0.69	1	0.89	1	0.96	1	0.94	1	0.91	1	0.70	1	0.57	1	0.86	1	0.93	1	0.93	1	0.89	1	0.69	1
2.2	max	1.00	8	1.00	8	1.00	9	1.00	8	1.00	9	0.99	10	0.99	10	1.00	10	1.00	9	1.00	10	1.00	10	0.99	10
	min	0.69	1	0.89	1	0.96	1	0.94	1	0.91	1	0.70	1	0.57	1	0.86	1	0.93	1	0.93	1	0.89	1	0.69	1

Table A.3 Maximum and minimum coefficients of determination R^2 and the corresponding number of considered modes n_m for the *leave-one-out validation* for each accelerometer and 4 different sets of POD modes at a **step frequency of 2.0 Hz**.

POD		MP1 L		MP2 L		MP3 L		MP4 L		MP5 L		MP6 L		MP1 R		MP2 R		MP3 R		MP4 R		MP5 R		MP6 R	
		R^2	n_m	R^2	n_m	R^2	n_m	R^2	n_m	R^2	n_m	R^2	n_m	R^2	n_m	R^2	n_m	R^2	n_m	R^2	n_m	R^2	n_m	R^2	n_m
1.6	max	1.00	9	1.00	9	1.00	10	1.00	7	1.00	7	1.00	7	1.00	7	1.00	7	1.00	9	1.00	10	1.00	10	1.00	10
	min	0.98	1	0.99	2	1.00	2	1.00	1	0.87	10	0.97	2	0.98	2	0.99	2	0.99	2	1.00	1	0.99	1	0.96	2
1.8	max	1.00	9	1.00	10	1.00	10	1.00	7	1.00	7	1.00	7	1.00	10	1.00	10	1.00	9	1.00	7	1.00	8	1.00	9
	min	0.99	1	0.99	1	1.00	1	1.00	1	0.99	1	0.98	1	0.98	1	0.99	1	1.00	1	1.00	1	0.99	1	0.98	1
2.0	max	1.00	10	1.00	9	1.00	9	1.00	7	1.00	10	1.00	10	1.00	9	1.00	10	1.00	10	1.00	10	1.00	9	1.00	10
	min	0.99	1	0.99	1	1.00	1	1.00	1	0.99	1	0.98	1	0.98	1	0.99	1	1.00	1	1.00	1	0.99	1	0.98	1
2.2	max	1.00	10	1.00	10	1.00	10	1.00	6	1.00	7	1.00	8	1.00	10	1.00	10	1.00	8	1.00	9	1.00	10	1.00	10
	min	0.99	1	0.99	1	1.00	1	1.00	2	0.99	1	0.98	1	0.98	1	0.99	1	1.00	1	1.00	2	0.99	1	0.98	1

Table A.4 Maximum and minimum coefficients of determination R^2 and the corresponding number of considered modes n_m for the *leave-one-out validation* for each accelerometer and 4 different sets of POD modes at a **step frequency of 2.2 Hz**.

POD		MP1 L		MP2 L		MP3 L		MP4 L		MP5 L		MP6 L		MP1 R		MP2 R		MP3 R		MP4 R		MP5 R		MP6 R	
		R^2	n_m	R^2	n_m	R^2	n_m	R^2	n_m	R^2	n_m	R^2	n_m	R^2	n_m	R^2	n_m	R^2	n_m	R^2	n_m	R^2	n_m	R^2	n_m
1.6	max	1.00	9	1.00	8	1.00	10	1.00	8	1.00	8	1.00	8	1.00	7	1.00	7	1.00	9	1.00	10	1.00	8	1.00	8
	min	0.85	1	0.95	1	0.98	1	0.97	1	n.v.	10	0.85	1	0.61	10	0.95	1	0.96	1	0.97	1	0.95	2	0.85	1
1.8	max	1.00	10	1.00	10	1.00	10	1.00	8	1.00	8	1.00	7	1.00	10	1.00	10	1.00	9	1.00	7	1.00	8	1.00	8
	min	0.85	1	0.96	1	0.98	1	0.97	1	0.96	1	0.85	2	0.75	1	0.95	1	0.96	1	0.97	1	0.95	1	0.86	2
2.0	max	1.00	9	1.00	9	1.00	9	1.00	7	1.00	10	1.00	10	1.00	8	1.00	9	1.00	10	1.00	10	1.00	9	1.00	10
	min	0.85	1	0.96	1	0.98	1	0.97	1	0.96	1	0.85	2	0.75	2	0.95	1	0.96	1	0.97	1	0.95	1	0.86	2
2.2	max	1.00	8	1.00	10	1.00	10	1.00	8	1.00	9	1.00	9	1.00	9	1.00	9	1.00	10	1.00	9	1.00	8	1.00	8
	min	0.85	1	0.96	1	0.98	1	0.97	1	0.96	1	0.85	2	0.75	1	0.95	1	0.96	1	0.97	1	0.95	1	0.85	2

Table A.5 Maximum and minimum coefficients of determination R^2 and the corresponding number of considered modes n_m for the *leave-one-out validation* for each strain gauge and 4 different sets of POD modes at a **step frequency of 1.6 Hz**.

POD		MP1 L		MP2 L		MP3 L		MP4 L		MP5 L		MP6 L		MP1 R		MP3 R		MP4 R		MP5 R		MP6 R	
		R^2	n_m	R^2	n_m	R^2	n_m	R^2	n_m	R^2	n_m	R^2	n_m	R^2	n_m	R^2	n_m	R^2	n_m	R^2	n_m	R^2	n_m
1.6	max	0.93	7	0.98	6	0.99	5	0.98	3	0.98	7	0.91	6	0.88	9	0.99	6	0.99	5	0.99	7	0.96	3
	min	0.65	1	n.v.	9	0.93	1	0.96	6	0.89	1	0.03	9	0.71	1	0.94	1	0.97	1	0.93	1	n.v.	9
1.8	max	0.89	4	0.98	4	0.97	5	0.98	5	0.98	8	0.90	7	0.90	6	0.98	6	0.99	5	0.98	6	0.96	5
	min	0.15	9	0.71	9	0.89	9	0.96	9	0.89	1	0.70	1	n.v.	9	0.84	9	0.97	8	0.93	1	0.80	1
2.0	max	0.91	6	0.97	5	0.97	3	0.97	1	0.95	2	0.87	8	0.87	4	0.98	5	0.98	5	0.99	9	0.96	7
	min	n.v.	9	0.04	9	0.93	1	0.87	8	0.89	1	0.70	1	n.v.	9	0.94	1	0.96	7	0.93	1	0.80	1
2.2	max	0.85	7	0.98	7	0.98	7	0.98	9	0.98	9	0.88	7	0.85	9	0.99	5	0.98	9	0.99	8	0.97	5
	min	0.65	1	n.v.	9	0.93	1	0.97	1	0.89	1	0.55	9	0.71	1	0.94	1	0.97	3	0.93	1	0.78	9

Table A.6 Maximum and minimum coefficients of determination R^2 and the corresponding number of considered modes n_m for the *leave-one-out validation* for each strain gauge and 4 different sets of POD modes at a **step frequency of 1.8 Hz**.

POD		MP1 L		MP2 L		MP3 L		MP4 L		MP5 L		MP6 L		MP1 R		MP3 R		MP4 R		MP5 R		MP6 R	
		R²	n_m	R²	n_m	R²	n_m	R²	n_m	R²	n_m	R²	n_m	R²	n_m	R²	n_m	R²	n_m	R²	n_m	R²	n_m
1.6	max	0.89	4	0.98	5	0.99	5	0.98	3	0.98	2	0.97	5	0.93	3	0.98	6	0.99	6	0.99	5	0.98	7
	min	0.67	9	n.v.	9	0.96	9	0.95	6	0.95	9	n.v.	9	0.78	8	0.97	1	0.98	9	0.96	1	n.v.	9
1.8	max	0.89	5	0.98	7	0.99	3	0.98	3	0.98	2	0.97	4	0.94	7	0.98	2	0.99	4	0.99	2	0.98	8
	min	n.v.	9	0.59	9	0.84	9	0.96	7	0.95	1	0.86	1	n.v.	9	0.83	9	0.97	9	0.96	1	0.89	1
2.0	max	0.90	4	0.97	2	0.99	6	0.98	4	0.98	8	0.96	6	0.94	4	0.99	5	0.99	9	0.99	8	0.98	8
	min	n.v.	9	0.65	9	0.96	1	0.97	8	0.95	1	0.86	1	0.63	9	0.97	1	0.98	1	0.96	1	0.89	1
2.2	max	0.78	1	0.98	7	0.99	7	0.98	4	0.98	2	0.96	4	0.93	5	0.98	6	0.99	9	0.99	2	0.97	7
	min	0.63	5	n.v.	9	0.93	9	0.95	6	0.95	1	0.15	9	0.81	9	0.97	1	0.98	5	0.96	1	0.69	9

Table A.7 Maximum and minimum coefficients of determination R^2 and the corresponding number of considered modes n_m for the *leave-one-out validation* for each strain gauge and 4 different sets of POD modes at a **step frequency of 2.0 Hz**.

POD		MP1 L		MP2 L		MP3 L		MP4 L		MP5 L		MP6 L		MP1 R		MP3 R		MP4 R		MP5 R		MP6 R	
		R²	n_m	R²	n_m	R²	n_m	R²	n_m	R²	n_m	R²	n_m	R²	n_m	R²	n_m	R²	n_m	R²	n_m	R²	n_m
1.6	max	1.00	3	1.00	7	1.00	3	1.00	5	1.00	6	1.00	3	1.00	1	1.00	8	1.00	2	1.00	5	1.00	2
	min	0.98	9	0.53	9	1.00	4	1.00	8	0.99	9	0.87	9	0.99	4	1.00	4	1.00	3	1.00	9	0.89	9
1.8	max	1.00	4	1.00	5	1.00	3	1.00	4	1.00	2	1.00	3	1.00	3	1.00	6	1.00	3	1.00	5	1.00	2
	min	0.80	9	0.95	9	0.98	9	0.99	9	1.00	9	0.99	9	0.59	9	0.98	9	1.00	9	1.00	1	1.00	9
2.0	max	1.00	5	1.00	6	1.00	4	1.00	4	1.00	2	1.00	3	1.00	7	1.00	7	1.00	1	1.00	4	1.00	2
	min	0.50	9	0.92	9	1.00	9	0.99	9	1.00	6	0.99	8	0.93	9	1.00	9	1.00	9	1.00	1	1.00	6
2.2	max	0.99	2	1.00	3	1.00	4	1.00	3	1.00	4	1.00	4	1.00	4	1.00	6	1.00	3	1.00	5	1.00	3
	min	0.97	9	0.69	9	1.00	9	1.00	8	1.00	8	0.91	9	0.99	9	1.00	1	1.00	7	1.00	9	0.96	9

Table A.8 Maximum and minimum coefficients of determination R^2 and the corresponding number of considered modes n_m for the *leave-one-out validation* for each strain gauge and 4 different sets of POD modes at a **step frequency of 2.2 Hz**.

POD		MP1 L		MP2 L		MP3 L		MP4 L		MP5 L		MP6 L		MP1 R		MP3 R		MP4 R		MP5 R		MP6 R	
		R²	n_m	R²	n_m	R²	n_m	R²	n_m	R²	n_m	R²	n_m	R²	n_m	R²	n_m	R²	n_m	R²	n_m	R²	n_m
1.6	max	0.97	6	0.99	5	1.00	7	0.99	6	0.99	7	0.96	6	0.96	7	1.00	8	1.00	9	1.00	7	0.98	3
	min	0.83	1	n.v.	9	0.98	1	0.98	1	0.97	1	0.56	9	0.89	4	0.98	1	0.99	1	0.98	1	0.58	9
1.8	max	0.96	4	0.99	5	0.99	2	0.99	5	0.99	8	0.95	4	0.96	8	0.99	6	1.00	5	0.99	6	0.98	4
	min	0.59	9	0.89	9	0.96	9	0.98	2	0.97	1	0.91	1	n.v.	9	0.93	9	0.99	2	0.98	1	0.95	1
2.0	max	0.96	6	0.99	5	0.99	3	0.98	1	0.98	2	0.94	3	0.95	7	0.99	5	0.99	5	0.99	7	0.98	7
	min	n.v.	9	0.56	9	0.97	9	0.94	5	0.96	4	0.91	1	0.32	9	0.98	9	0.99	9	0.98	1	0.95	1
2.2	max	0.93	7	0.99	7	0.99	7	0.99	7	0.99	7	0.96	3	0.97	7	1.00	9	1.00	9	0.99	9	0.99	5
	min	0.83	1	0.20	9	0.98	1	0.98	1	0.97	1	0.79	9	0.91	1	0.98	1	0.99	4	0.98	1	0.91	9

A.2 Railway bridge Schmutter

Table A.9 Identified frequencies from the peaks of the indirect resonance curves compared to the value of the bridge measurements

	in direction of:	**Ulm**			**Augsburg**		
	signal	v_{res}	f_{res}	relative error	v_{res}	f_{res}	relative error
	bridge	176.4	5.11		172.5	5.00	
single sensor signal	T_1	174.7	5.06	-1.0%	172.5	5.00	0.0%
	T_2	177.3	5.14	0.5%	167.0	4.84	-3.2%
	T_3	180.7	5.24	2.4%	202.2	5.86	17.2%
	T_4	176.4	5.11	0.0%	202.2	5.86	17.2%
	T_5	177.3	5.14	0.5%	167.0	4.84	-3.2%
	T_6	176.4	5.11	0.0%	167.0	4.84	-3.2%
	T_7	176.4	5.11	0.0%	202.2	5.86	17.2%
	T_8	176.4	5.11	0.0%	202.2	5.86	17.2%
residual signal	T_1 and T_3	174.7	5.06	-1.0%	172.0	4.99	-0.3%
	T_3 and T_5	176.4	5.11	0.0%	172.0	4.99	-0.3%
	T_2 and T_4	176.4	5.11	0.0%	172.5	5.00	0.0%
	T_6 and T_8	176.4	5.11	0.0%	172.5	5.00	0.0%

A.3 Railway bridge Garather Bach

Table A.10 Sampling rates of the sensors in the different setups

name	start	end	$F_{\mathrm{s,bridge}}$ in Hz	$F_{\mathrm{s,rail}}$ in Hz	$F_{\mathrm{s,temperature}}$ in Hz
setup 1	10/28/2021	01/05/2022	600	600	600
setup 2	02/09/2022	03/03/2022	600	2400	10
setup 3	03/03/2022	04/06/2022	600	4800	600
setup 4	04/15/2022	04/29/2022	1000	5000	100
setup 5	07/04/2022	03/23/2023	1000	5000	100

Table A.11 List of the identified resonance peaks and the corresponding calculated frequencies for the accelerometers on the bridge

type of signal	side of the sensors	label	v_{res} in $\frac{\mathrm{km}}{\mathrm{h}}$	f_{red} in Hz
bridge sensors	left	A1	173.8	5.59
		A2	173.8	5.59
		A3	171.3	5.51
		A4	171.3	5.51
		A5	171.3	5.51
	right	A6	171.3	5.51
		A7	171.3	5.51
		A8	171.3	5.51
		A9	171.3	5.51
		mean	171.8	5.53
		standard deviation	1.1	0.0

Table A.12 List of identified resonance peaks and corresponding calculated frequencies for the 'single sensor signal' approach compared to the mean value obtained with the sensors on the bridge.

type of signal	side of the sensors	label	v_{res} in $\frac{\mathrm{km}}{\mathrm{h}}$	f_{red} in Hz	percantage error
single senor	left	$T_{2\mathrm{L}}$	171.6	5.52	-0.1%
		$T_{3\mathrm{L}}$	171.6	5.52	-0.1%
		$T_{5\mathrm{L}}$	144.6	4.65	-15.8%
		$T_{6\mathrm{L}}$	171.6	5.52	-0.1%
		$T_{7\mathrm{L}}$	171.6	5.52	-0.1%
		$T_{8\mathrm{L}}$	173.8	5.59	1.2%
		$T_{9\mathrm{L}}$	144.6	4.65	-15.8%
		$T_{11\mathrm{L}}$	171.6	5.52	-0.1%
		$T_{12\mathrm{L}}$	173.8	5.59	1.2%
		$T_{13\mathrm{L}}$	144.6	4.65	-15.8%
		$T_{15\mathrm{L}}$	171.6	5.52	-0.1%
		$T_{16\mathrm{L}}$	175.9	5.66	2.4%
		mean	165.6	5.3	-3.6%
		standard deviation	12.2	0.4	7.1%
	right	$T_{2\mathrm{R}}$	192.8	6.20	12.2%
		$T_{3\mathrm{R}}$	192.8	6.20	12.2%
		$T_{4\mathrm{R}}$	192.8	6.20	12.2%
		$T_{5\mathrm{R}}$	192.8	6.20	12.2%
		$T_{6\mathrm{R}}$	192.8	6.20	12.2%
		$T_{7\mathrm{R}}$	192.8	6.20	12.2%
		$T_{8\mathrm{R}}$	192.8	6.20	12.2%
		$T_{9\mathrm{R}}$	192.8	6.20	12.2%
		$T_{10\mathrm{R}}$	192.8	6.20	12.2%
		$T_{11\mathrm{R}}$	192.8	6.20	12.2%
		$T_{12\mathrm{R}}$	192.8	6.20	12.2%
		$T_{15\mathrm{R}}$	192.8	6.20	12.2%
		$T_{16\mathrm{R}}$	192.8	6.20	12.2%
		mean	192.8	6.2	12.2%
		standard deviation	0.0	0.0	0.0%

Table A.13 List of identified resonance peaks and corresponding calculated frequencies for the ’residual preceding sensor’ approach compared to the mean value obtained with the sensors on the bridge.

type of signal	side of the sensors	label	v_{res} in $\frac{\mathrm{km}}{\mathrm{h}}$	f_{red} in Hz	percantage error
residual preceding sensor	left	$T_{2\mathrm{L}}$ - $T_{1\mathrm{L}}$	192.8	6.20	12.2%
		$T_{3\mathrm{L}}$ - $T_{2\mathrm{L}}$	183.4	5.90	6.7%
		$T_{5\mathrm{L}}$ - $T_{3\mathrm{L}}$	175.9	5.66	2.4%
		$T_{6\mathrm{L}}$ - $T_{5\mathrm{L}}$	175.9	5.66	2.4%
		$T_{7\mathrm{L}}$ - $T_{6\mathrm{L}}$	183.4	5.90	6.7%
		$T_{8\mathrm{L}}$ - $T_{7\mathrm{L}}$	171.3	5.51	-0.3%
		$T_{9\mathrm{L}}$ - $T_{8\mathrm{L}}$	171.3	5.51	-0.3%
		$T_{11\mathrm{L}}$ - $T_{9\mathrm{L}}$	167.2	5.38	-2.7%
		$T_{12\mathrm{L}}$ - $T_{11\mathrm{L}}$	171.3	5.51	-0.3%
		$T_{13\mathrm{L}}$ - $T_{12\mathrm{L}}$	171.3	5.51	-0.3%
		$T_{15\mathrm{L}}$ - $T_{13\mathrm{L}}$	171.3	5.51	-0.3%
		$T_{16\mathrm{L}}$ - $T_{15\mathrm{L}}$	173.8	5.59	1.2%
		mean	175.7	5.7	2.3%
		standard deviation	7.0	0.2	4.1%
	right	$T_{2\mathrm{R}}$ - $T_{1\mathrm{R}}$	192.8	6.20	12.2%
		$T_{3\mathrm{R}}$ - $T_{2\mathrm{R}}$	192.8	6.20	12.2%
		$T_{4\mathrm{R}}$ - $T_{3\mathrm{R}}$	167.2	5.38	-2.7%
		$T_{5\mathrm{R}}$ - $T_{4\mathrm{R}}$	175.9	5.66	2.4%
		$T_{6\mathrm{R}}$ - $T_{5\mathrm{R}}$	173.8	5.59	1.2%
		$T_{7\mathrm{R}}$ - $T_{6\mathrm{R}}$	183.4	5.90	6.7%
		$T_{8\mathrm{R}}$ - $T_{7\mathrm{R}}$	171.3	5.51	-0.3%
		$T_{9\mathrm{R}}$ - $T_{8\mathrm{R}}$	171.3	5.51	-0.3%
		$T_{10\mathrm{R}}$ - $T_{9\mathrm{R}}$	171.3	5.51	-0.3%
		$T_{11\mathrm{R}}$ - $T_{10\mathrm{R}}$	175.9	5.66	2.4%
		$T_{12\mathrm{R}}$ - $T_{11\mathrm{R}}$	171.3	5.51	-0.3%
		$T_{15\mathrm{R}}$ - $T_{12\mathrm{R}}$	171.3	5.51	-0.3%
		$T_{16\mathrm{R}}$ - $T_{15\mathrm{R}}$	171.3	5.51	-0.3%
		mean	171.3	5.7	2.5%
		standard deviation	8.0	0.3	4.7%

Table A.14 List of identified resonance peaks and corresponding calculated frequencies for the 'residual first sensor' approach compared to the mean value obtained with the sensors on the bridge.

type of signal	side of the sensors	label	v_{res} in $\frac{\mathrm{km}}{\mathrm{h}}$	f_{red} in Hz	percantage error
residual first sensor	left	$T_{2\mathrm{L}}$ - $T_{1\mathrm{L}}$	192.8	6.20	12.2%
		$T_{3\mathrm{L}}$ - $T_{1\mathrm{L}}$	167.2	5.38	-2.7%
		$T_{5\mathrm{L}}$ - $T_{1\mathrm{L}}$	173.8	5.59	1.2%
		$T_{6\mathrm{L}}$ - $T_{1\mathrm{L}}$	171.3	5.51	-0.3%
		$T_{7\mathrm{L}}$ - $T_{1\mathrm{L}}$	167.2	5.38	-2.7%
		$T_{8\mathrm{L}}$ - $T_{1\mathrm{L}}$	171.3	5.51	-0.3%
		$T_{9\mathrm{L}}$ - $T_{1\mathrm{L}}$	171.3	5.51	-0.3%
		$T_{11\mathrm{L}}$ - $T_{1\mathrm{L}}$	167.2	5.38	-2.7%
		$T_{12\mathrm{L}}$ - $T_{1\mathrm{L}}$	171.3	5.51	-0.3%
		$T_{13\mathrm{L}}$ - $T_{1\mathrm{L}}$	171.3	5.51	-0.3%
		$T_{15\mathrm{L}}$ - $T_{1\mathrm{L}}$	171.3	5.51	-0.3%
		$T_{16\mathrm{L}}$ - $T_{1\mathrm{L}}$	171.3	5.51	-0.3%
		mean	172.2	5.5	0.2%
		standard deviation	6.5	0.2	3.8%
	right	$T_{2\mathrm{R}}$ - $T_{1\mathrm{R}}$	192.8	6.20	12.2%
		$T_{3\mathrm{R}}$ - $T_{1\mathrm{R}}$	171.3	5.51	-0.3%
		$T_{4\mathrm{R}}$ - $T_{1\mathrm{R}}$	175.9	5.66	2.4%
		$T_{5\mathrm{R}}$ - $T_{1\mathrm{R}}$	173.8	5.59	1.2%
		$T_{6\mathrm{R}}$ - $T_{1\mathrm{R}}$	171.3	5.51	-0.3%
		$T_{7\mathrm{R}}$ - $T_{1\mathrm{R}}$	167.2	5.38	-2.7%
		$T_{8\mathrm{R}}$ - $T_{1\mathrm{R}}$	171.3	5.51	-0.3%
		$T_{9\mathrm{R}}$ - $T_{1\mathrm{R}}$	171.3	5.51	-0.3%
		$T_{10\mathrm{R}}$ - $T_{1\mathrm{R}}$	171.3	5.51	-0.3%
		$T_{11\mathrm{R}}$ - $T_{1\mathrm{R}}$	167.2	5.38	-2.7%
		$T_{12\mathrm{R}}$ - $T_{1\mathrm{R}}$	171.3	5.51	-0.3%
		$T_{15\mathrm{R}}$ - $T_{1\mathrm{R}}$	171.3	5.51	-0.3%
		$T_{16\mathrm{R}}$ - $T_{1\mathrm{R}}$	171.3	5.51	-0.3%
		mean	172.8	5.6	0.6%
		standard deviation	6.2	0.2	3.6%

B Figures

B.1 Footbridge HUMVIB

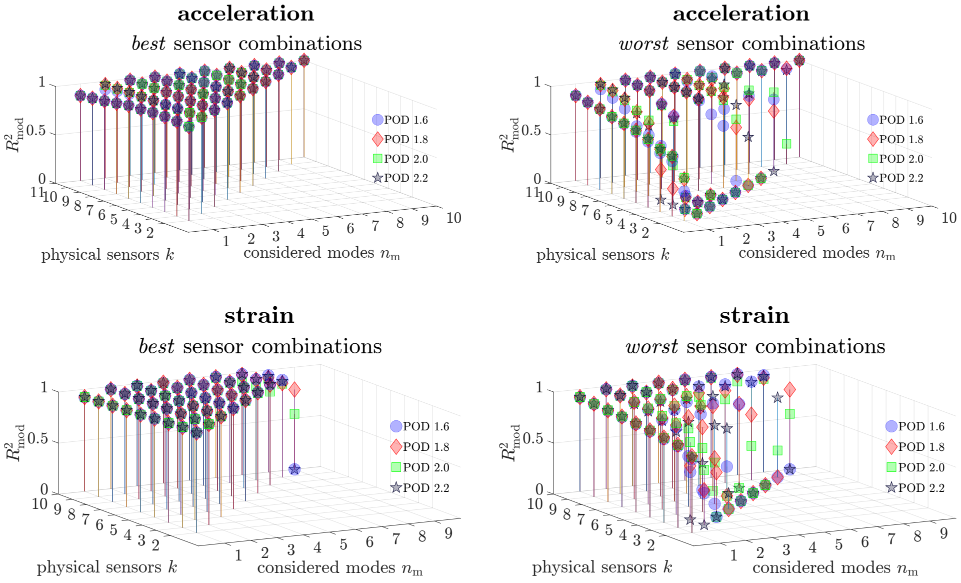

Figure B.1 Comparison of the maximum and minimum coefficients of determination at **MP 2L** for accelerations and strains for all 4 POD mode sets.

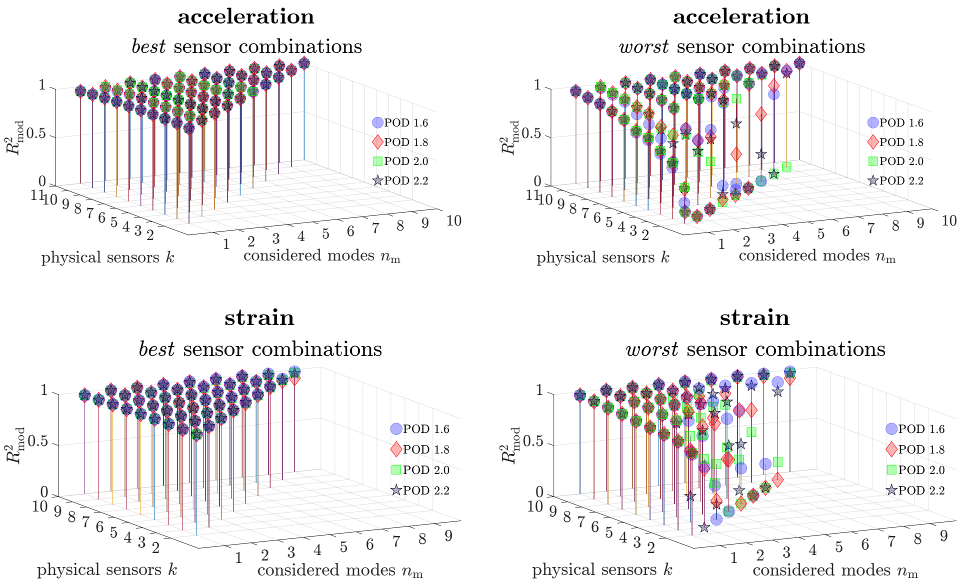

Figure B.2 Comparison of the maximum and minimum coefficients of determination at **MP 3L** for accelerations and strains for all 4 POD mode sets.

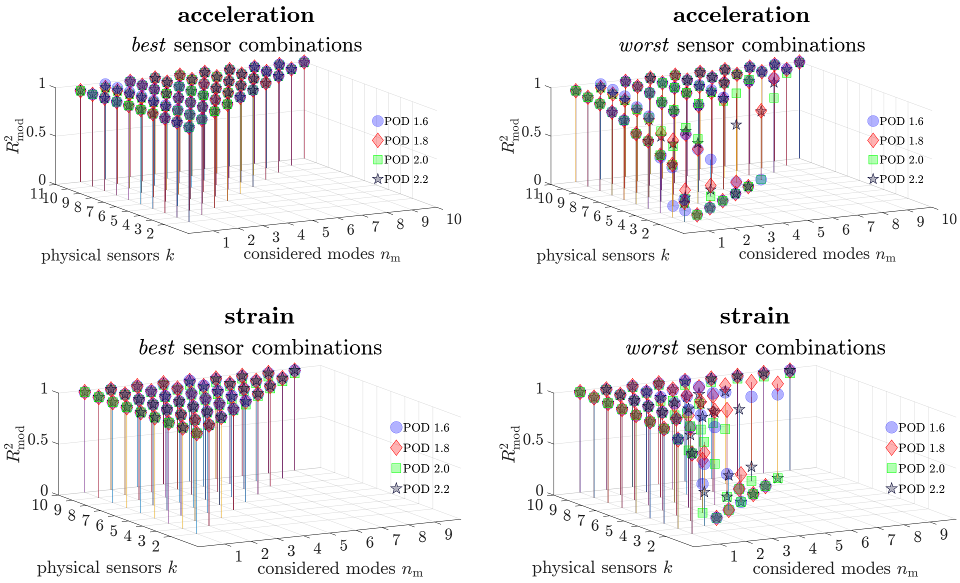

Figure B.3 Comparison of the maximum and minimum coefficients of determination at **MP 4L** for accelerations and strains for all 4 POD mode sets.

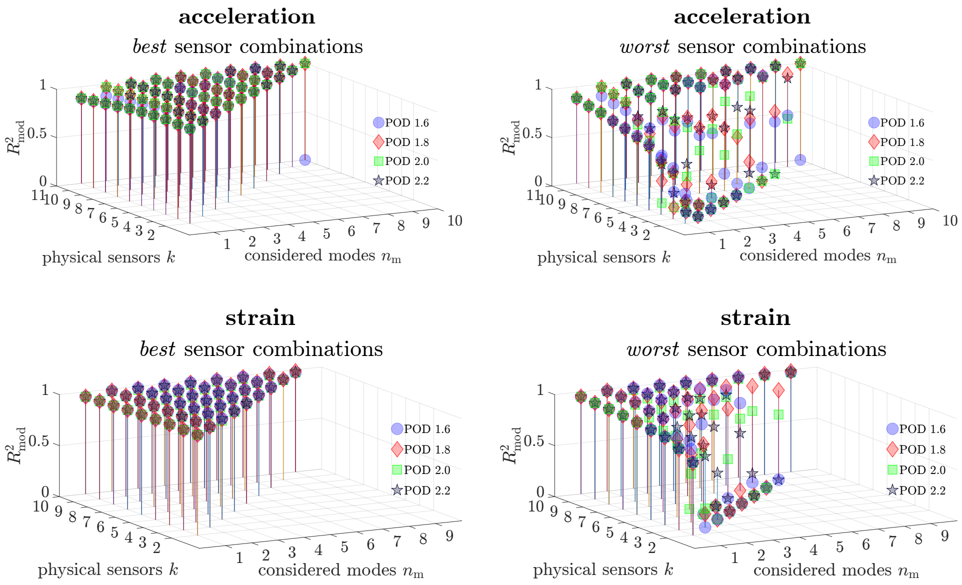

Figure B.4 Comparison of the maximum and minimum coefficients of determination at **MP 5L** for accelerations and strains for all 4 POD mode sets.

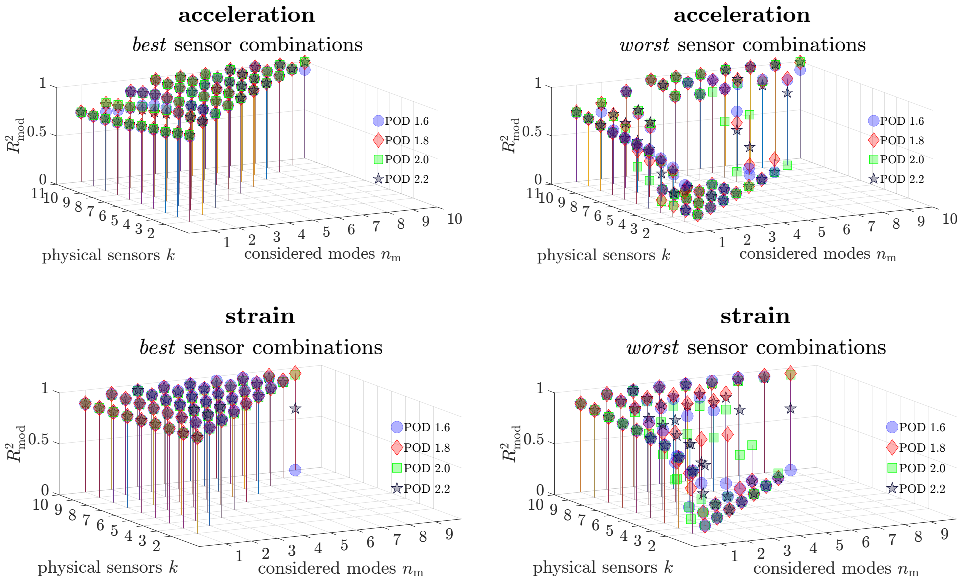

Figure B.5 Comparison of the maximum and minimum coefficients of determination at **MP 6L** for accelerations and strains for all 4 POD mode sets.

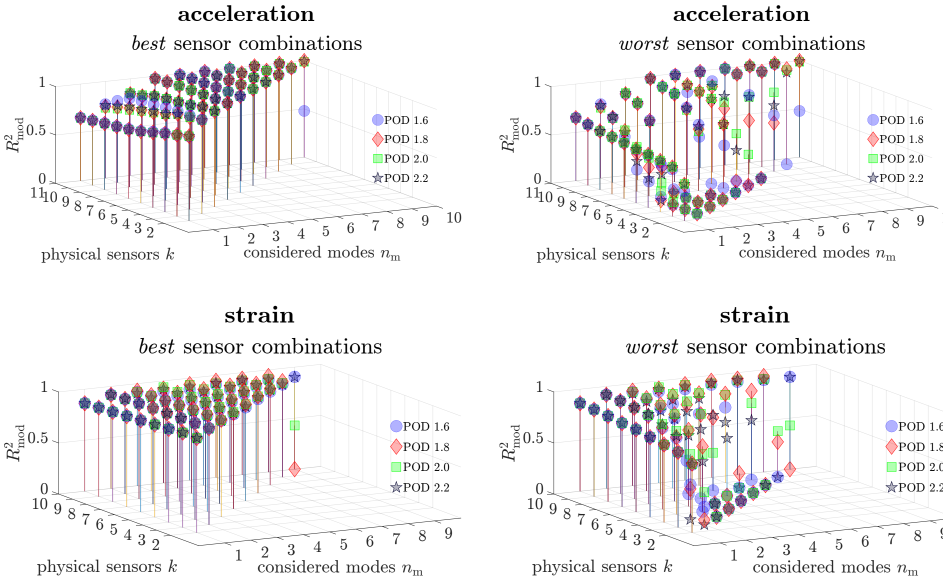

Figure B.6 Comparison of the maximum and minimum coefficients of determination at **MP 1R** for accelerations and strains for all 4 POD mode sets.

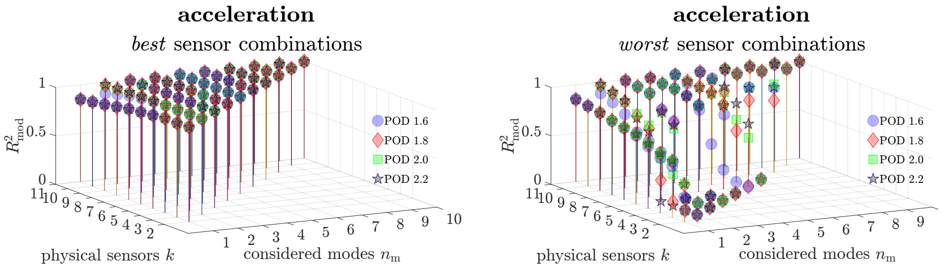

Figure B.7 Comparison of the maximum and minimum coefficients of determination at **MP 2R** for accelerations and strains for all 4 POD mode sets. The strain gauge at the point was defective.

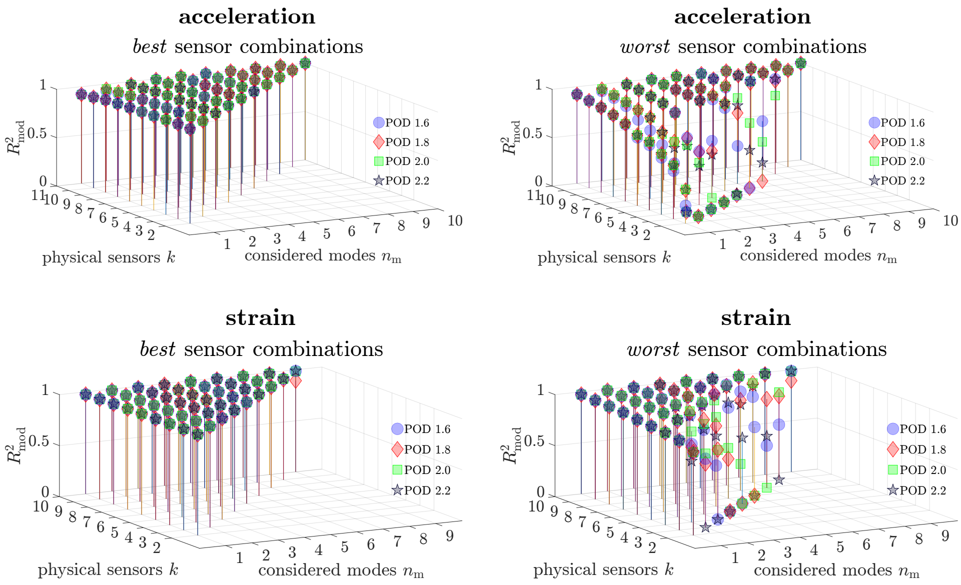

Figure B.8 Comparison of the maximum and minimum coefficients of determination at **MP 3R** for accelerations and strains for all 4 POD mode sets.

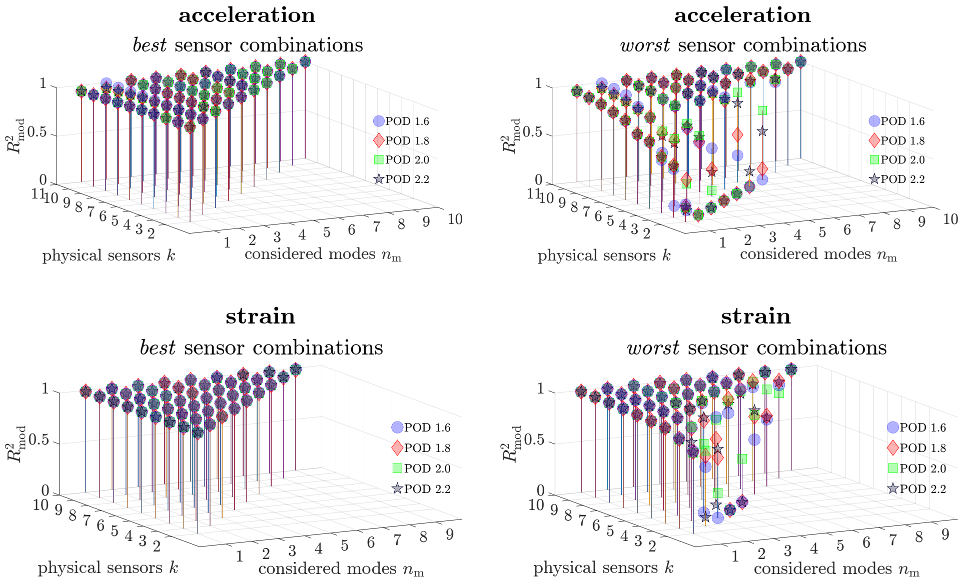

Figure B.9 Comparison of the maximum and minimum coefficients of determination at **MP 4R** for accelerations and strains for all 4 POD mode sets.

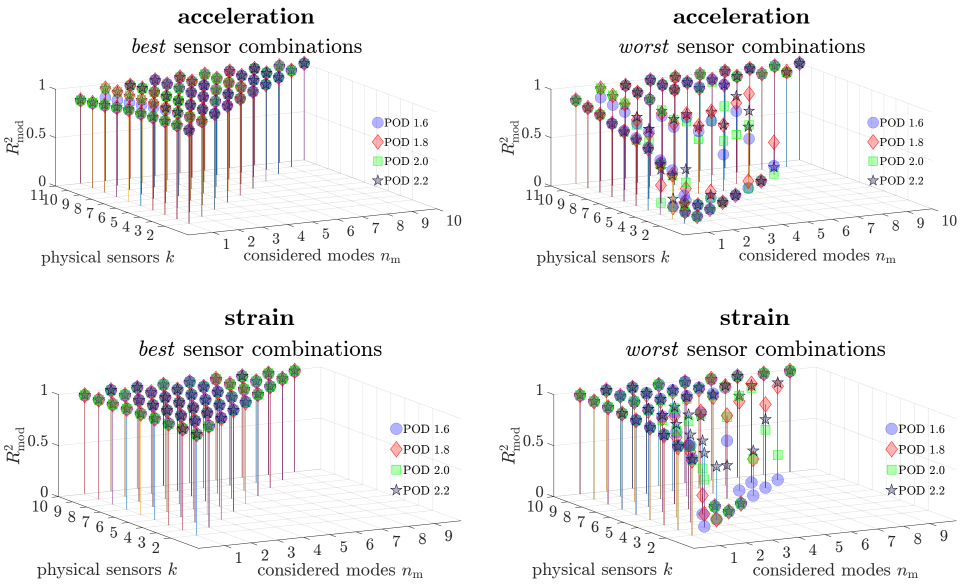

Figure B.10 Comparison of the maximum and minimum coefficients of determination at **MP 5R** for accelerations and strains for all 4 POD mode sets.

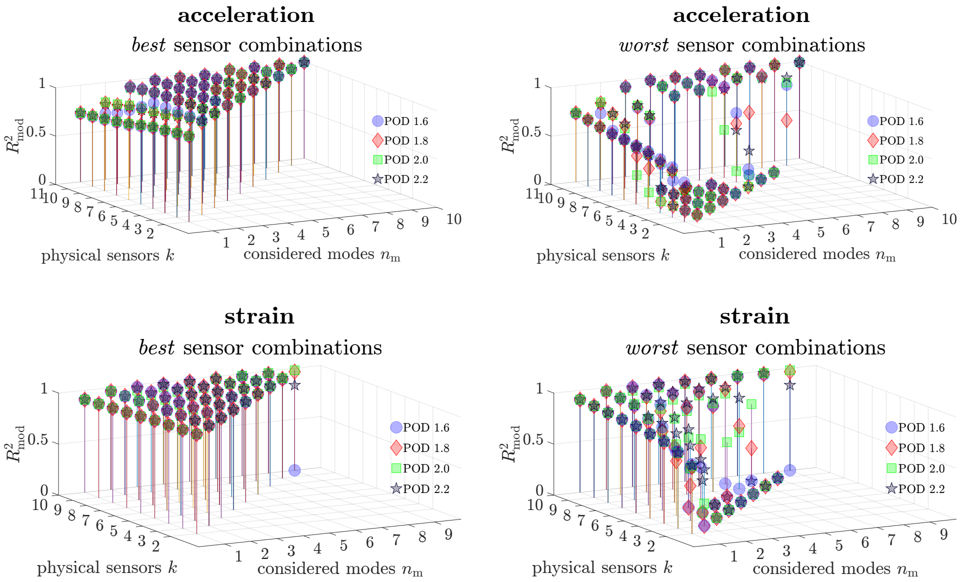

Figure B.11 Comparison of the maximum and minimum coefficients of determination at **MP 6R** for accelerations and strains for all 4 POD mode sets.

B.2 Railway bridge Schmutter

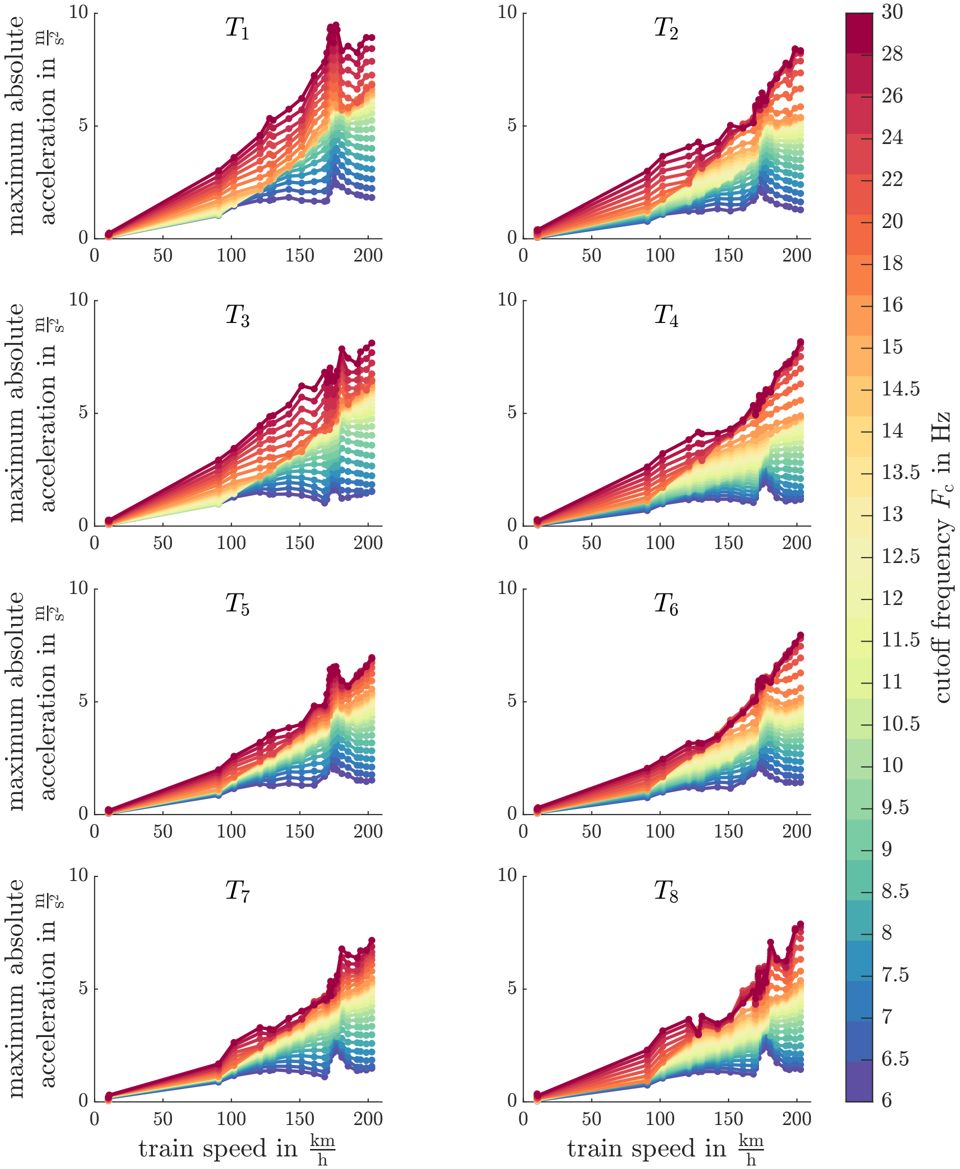

Figure B.12 Influence of the cut-off frequency F_c on the resonance curve with the maximum absolute values of the accelerations for sensors T_1 to T_8 for runs in the direction of Ulm

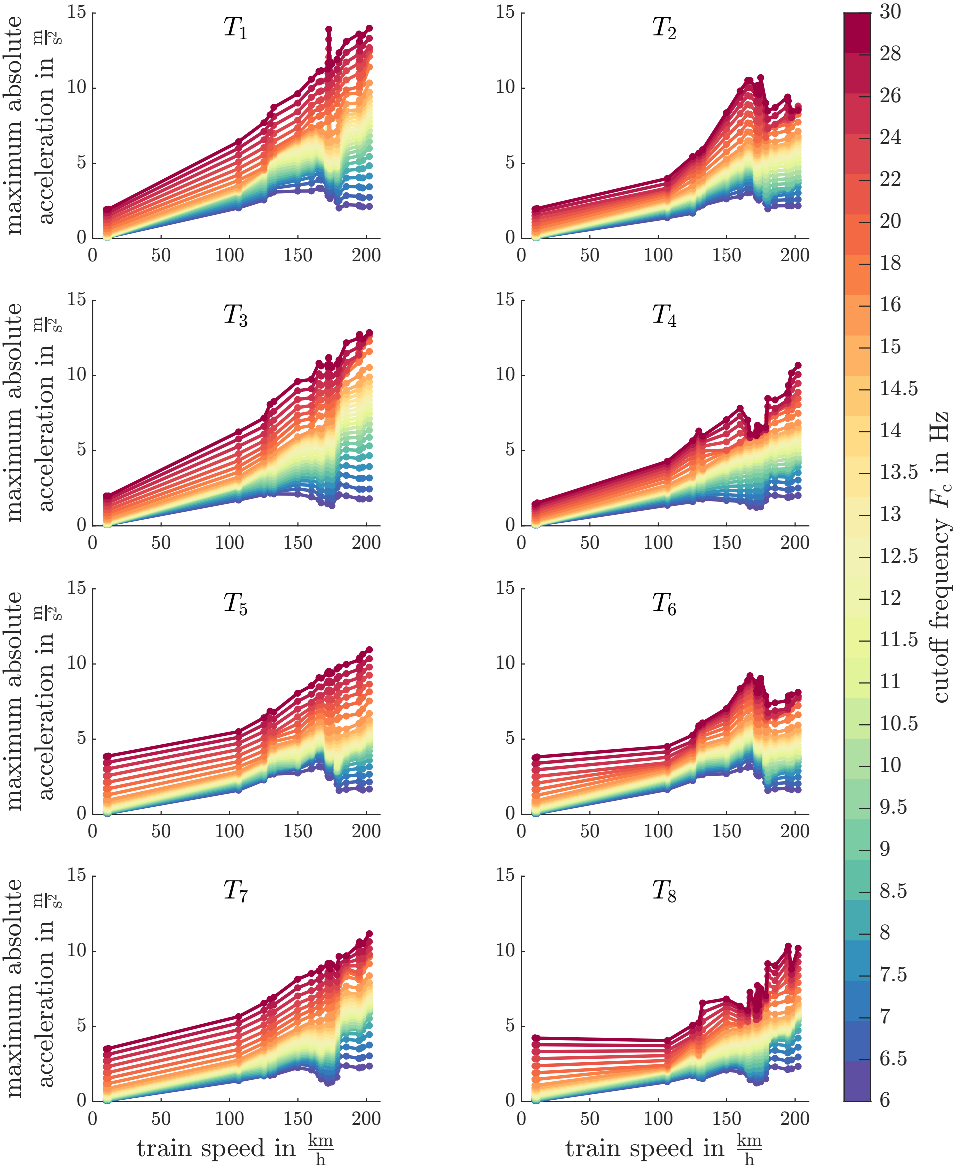

Figure B.13 Influence of the cut-off frequency F_c on the resonance curve with the maximum absolute values of the accelerations for sensors T_1 to T_8 for runs in the direction of Augsburg

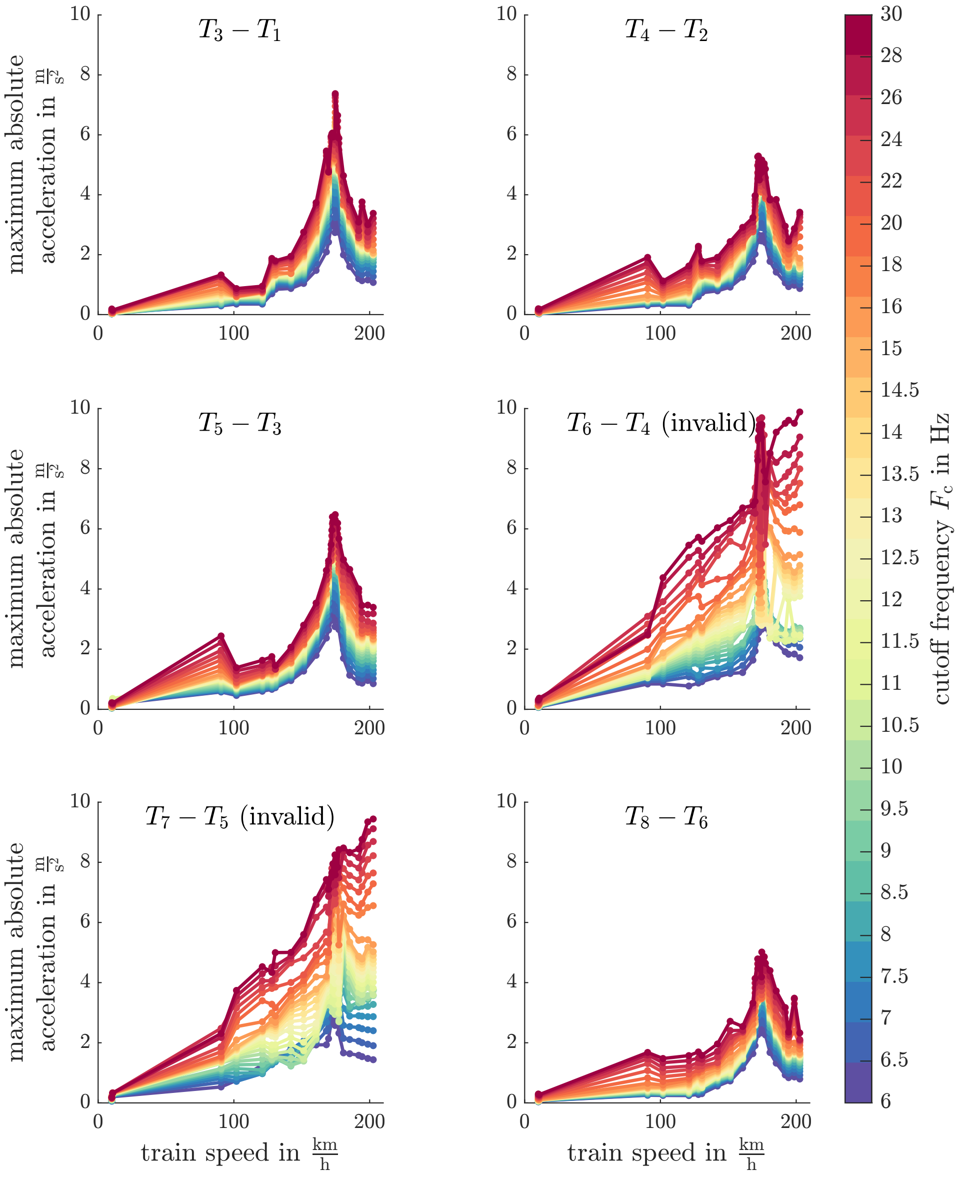

Figure B.14 Influence of the cut-off frequency F_c on the resonance curve with the maximum absolute values of the acceleration for the residual signals for runs in the direction of Ulm

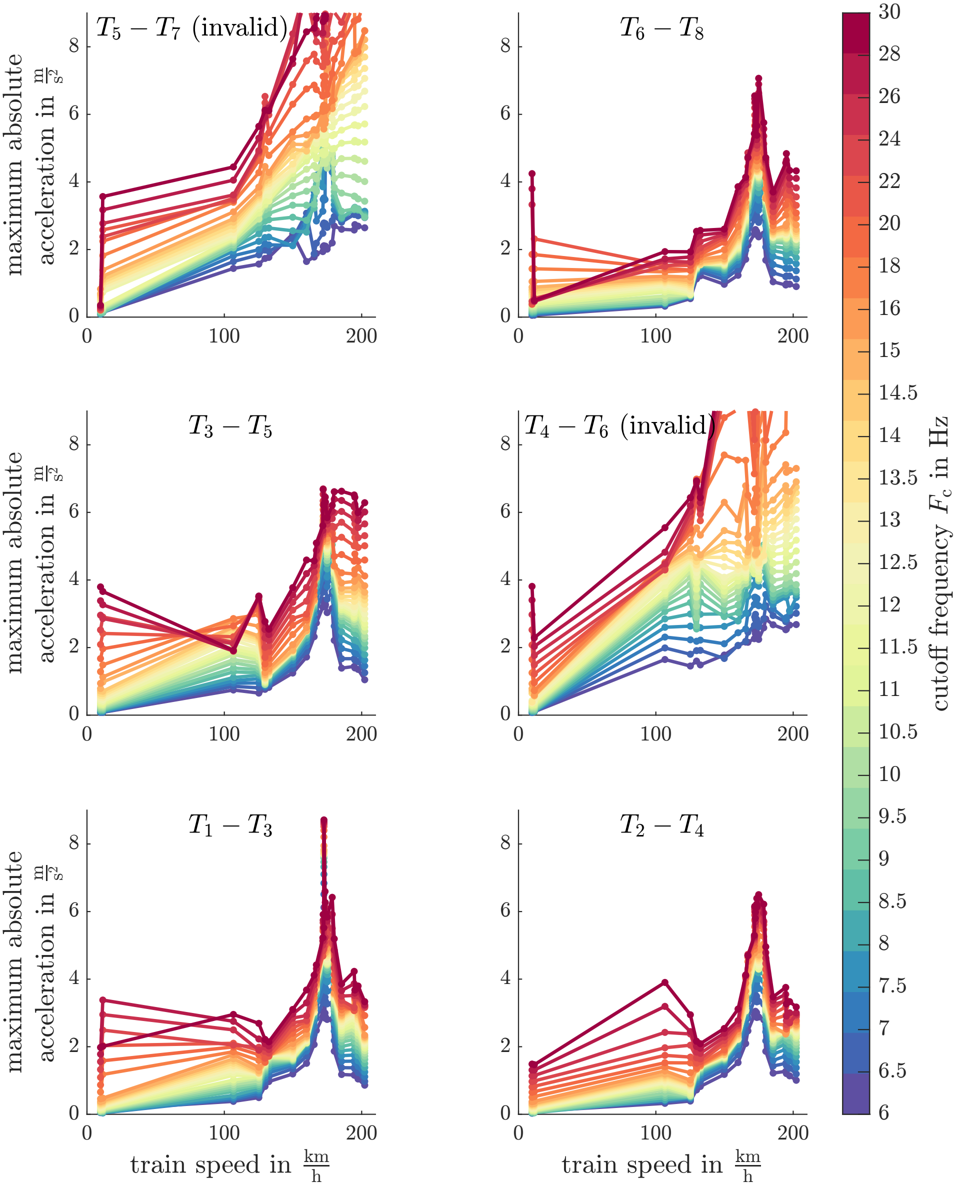

Figure B.15 Influence of the cut-off frequency F_c on the resonance curve with the maximum absolute values of the acceleration for the residual signals for runs in the direction of Augsburg

B.3 Railway bridge Garather Bach

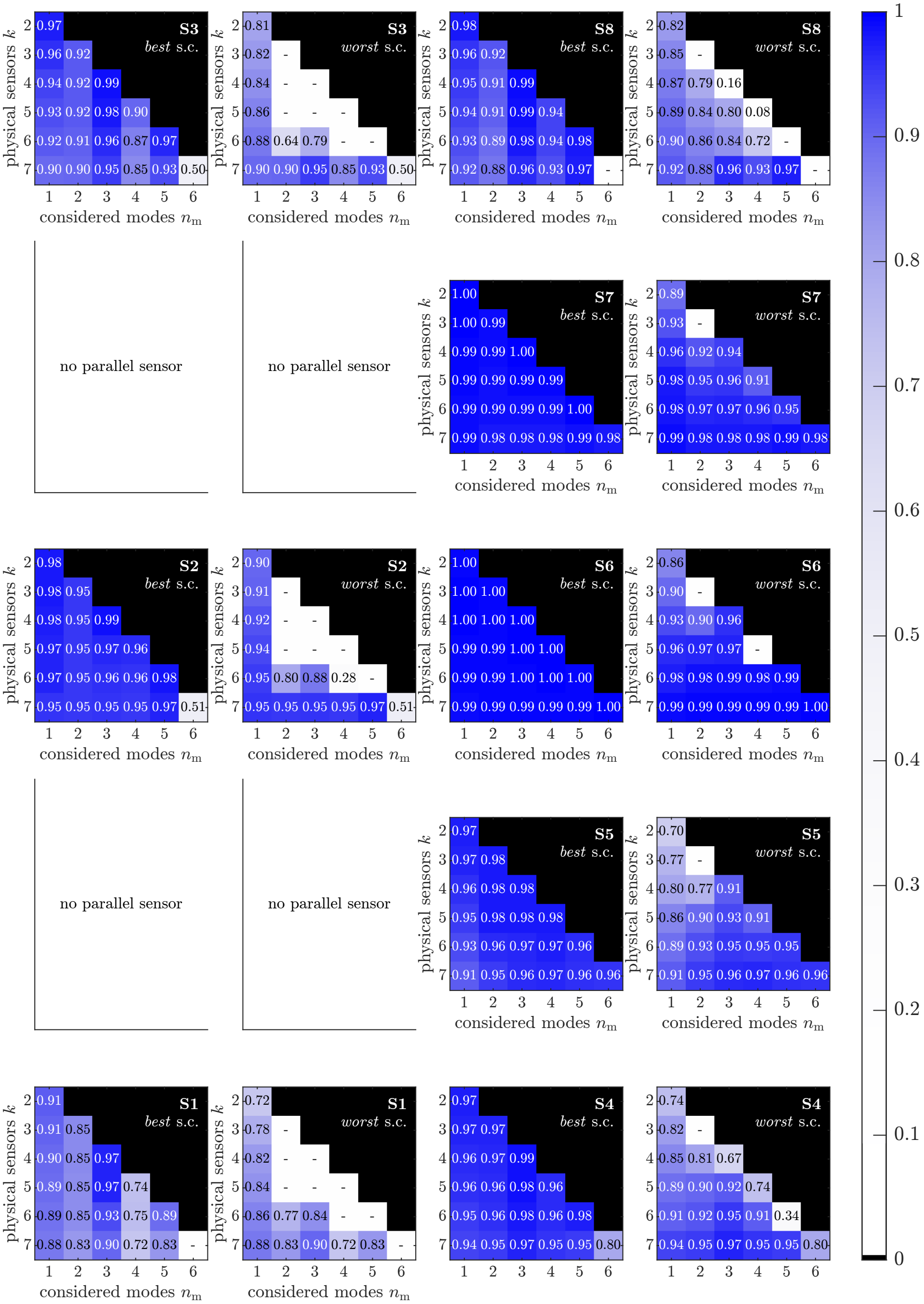

Figure B.16 Coefficients of determination of the leave-p-out validation for the best and worst sensor combination (s.c.) depending on the number of physical sensors and considered FE modes for each strain gauge.

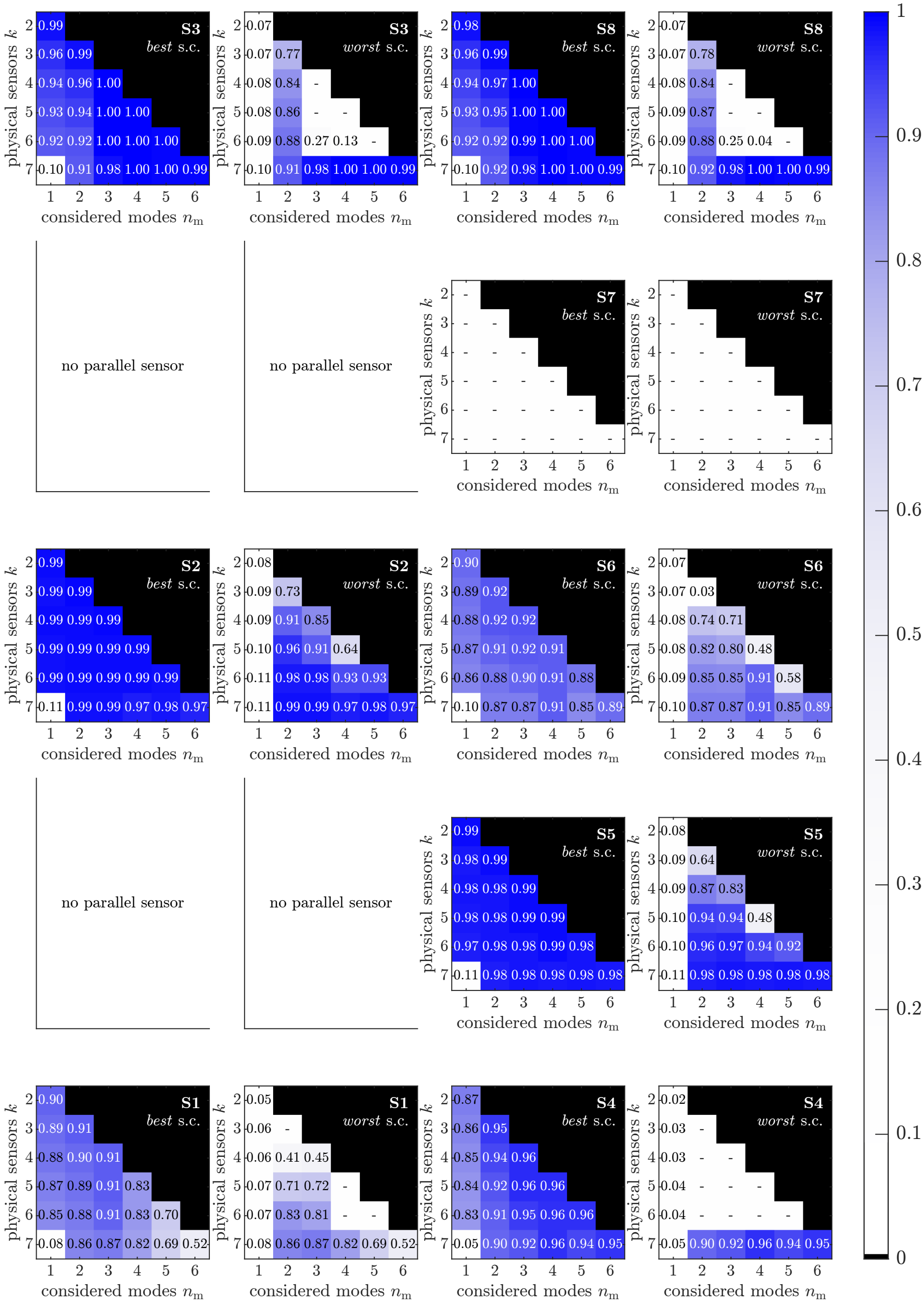

Figure B.17 Coefficients of determination of the leave-p-out validation for the best and worst sensor combination (s.c.) depending on the number of physical sensors and considered POD modes for each strain gauge.

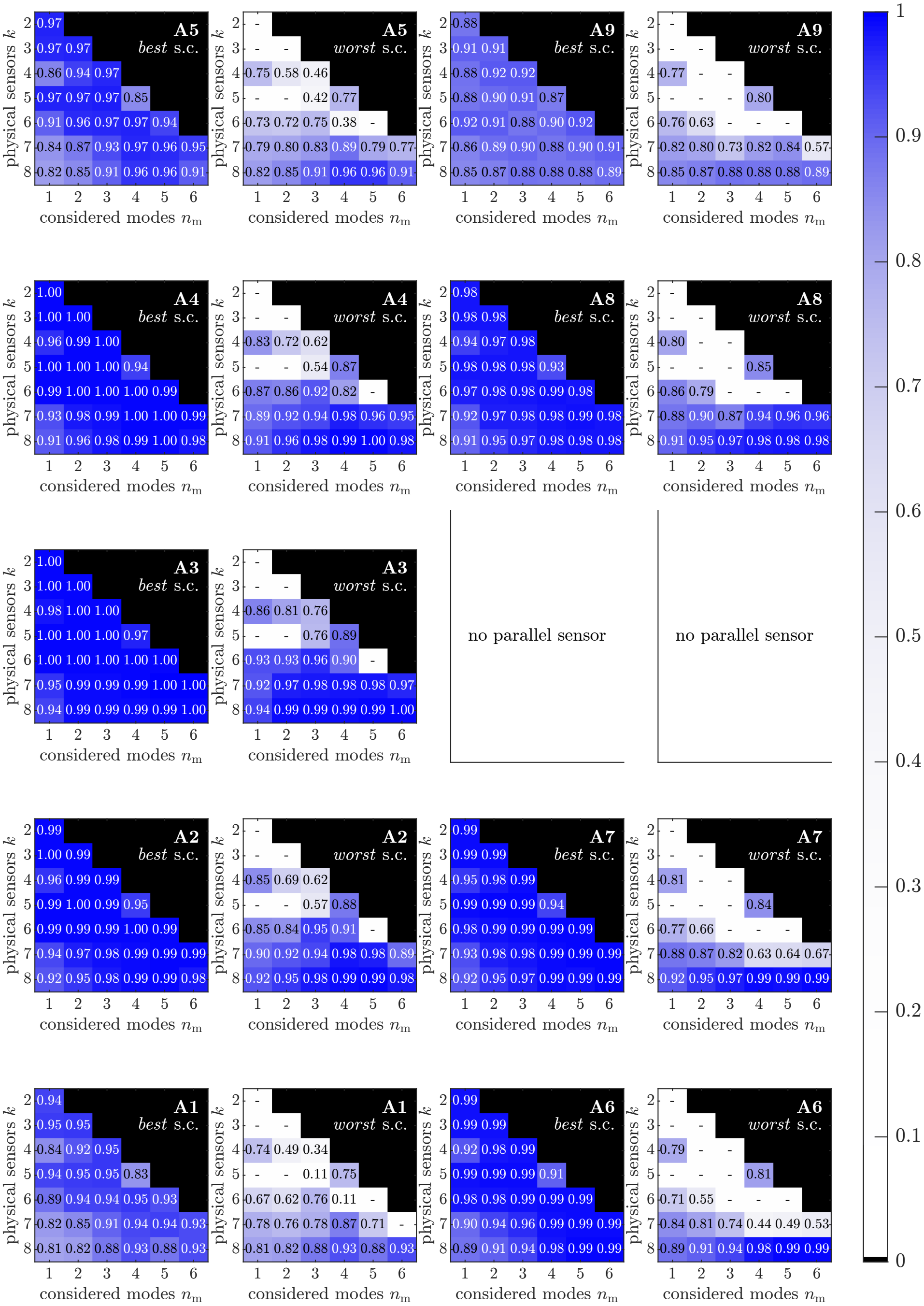

A5 *best* s.c.

physical sensors k	1	2	3	4	5	6
2	0.97					
3	0.97	0.97				
4	0.86	0.94	0.97			
5	0.97	0.97	0.97	0.85		
6	0.91	0.96	0.97	0.97	0.94	
7	0.84	0.87	0.93	0.97	0.96	0.95
8	0.82	0.85	0.91	0.96	0.96	0.91

A5 *worst* s.c.

physical sensors k	1	2	3	4	5	6
2	-					
3	-	-				
4	0.75	0.58	0.46			
5	-	-	0.42	0.77		
6	0.73	0.72	0.75	0.38	-	
7	0.79	0.80	0.83	0.89	0.79	0.77
8	0.82	0.85	0.91	0.96	0.96	0.91

A9 *best* s.c.

physical sensors k	1	2	3	4	5	6
2	0.88					
3	0.91	0.91				
4	0.88	0.92	0.92			
5	0.88	0.90	0.91	0.87		
6	0.92	0.91	0.88	0.90	0.92	
7	0.86	0.89	0.90	0.88	0.90	0.91
8	0.85	0.87	0.88	0.88	0.88	0.89

A9 *worst* s.c.

physical sensors k	1	2	3	4	5	6
2	-					
3	-	-				
4	0.77	-	-			
5	-	-	-	0.80		
6	0.76	0.63	-	-	-	
7	0.82	0.80	0.73	0.82	0.84	0.57
8	0.85	0.87	0.88	0.88	0.88	0.89

A4 *best* s.c.

physical sensors k	1	2	3	4	5	6
2	1.00					
3	1.00	1.00				
4	0.96	0.99	1.00			
5	1.00	1.00	1.00	0.94		
6	0.99	1.00	1.00	1.00	0.99	
7	0.93	0.98	0.99	1.00	1.00	0.99
8	0.91	0.96	0.98	0.99	1.00	0.98

A4 *worst* s.c.

physical sensors k	1	2	3	4	5	6
2	-					
3	-	-				
4	0.83	0.72	0.62			
5	-	-	0.54	0.87		
6	0.87	0.86	0.92	0.82	-	
7	0.89	0.92	0.94	0.98	0.96	0.95
8	0.91	0.96	0.98	0.99	1.00	0.98

A8 *best* s.c.

physical sensors k	1	2	3	4	5	6
2	0.98					
3	0.98	0.98				
4	0.94	0.97	0.98			
5	0.98	0.98	0.98	0.93		
6	0.97	0.98	0.98	0.99	0.98	
7	0.92	0.97	0.98	0.98	0.99	0.98
8	0.91	0.95	0.97	0.98	0.98	0.98

A8 *worst* s.c.

physical sensors k	1	2	3	4	5	6
2	-					
3	-	-				
4	0.80	-	-			
5	-	-	-	0.85		
6	0.86	0.79	-	-	-	
7	0.88	0.90	0.87	0.94	0.96	0.96
8	0.91	0.95	0.97	0.98	0.98	0.98

A3 *best* s.c.

physical sensors k	1	2	3	4	5	6
2	1.00					
3	1.00	1.00				
4	0.98	1.00	1.00			
5	1.00	1.00	1.00	0.97		
6	1.00	1.00	1.00	1.00	1.00	
7	0.95	0.99	0.99	0.99	1.00	1.00
8	0.94	0.99	0.99	0.99	0.99	1.00

A3 *worst* s.c.

physical sensors k	1	2	3	4	5	6
2	-					
3	-	-				
4	0.86	0.81	0.76			
5	-	-	0.76	0.89		
6	0.93	0.93	0.96	0.90	-	
7	0.92	0.97	0.98	0.98	0.98	0.97
8	0.94	0.99	0.99	0.99	0.99	1.00

A2 *best* s.c.

physical sensors k	1	2	3	4	5	6
2	0.99					
3	1.00	0.99				
4	0.96	0.99	0.99			
5	0.99	1.00	0.99	0.95		
6	0.99	0.99	0.99	1.00	0.99	
7	0.94	0.97	0.98	0.99	0.99	0.99
8	0.92	0.95	0.98	0.99	0.99	0.98

A2 *worst* s.c.

physical sensors k	1	2	3	4	5	6
2	-					
3	-	-				
4	0.85	0.69	0.62			
5	-	-	0.57	0.88		
6	0.85	0.84	0.95	0.91	-	
7	0.90	0.92	0.94	0.98	0.98	0.89
8	0.92	0.95	0.98	0.99	0.99	0.98

A7 *best* s.c.

physical sensors k	1	2	3	4	5	6
2	0.99					
3	0.99	0.99				
4	0.95	0.98	0.99			
5	0.99	0.99	0.99	0.94		
6	0.98	0.99	0.99	0.99	0.99	
7	0.93	0.98	0.98	0.99	0.99	0.99
8	0.92	0.95	0.97	0.99	0.99	0.99

A7 *worst* s.c.

physical sensors k	1	2	3	4	5	6
2	-					
3	-	-				
4	0.81	-	-			
5	-	-	-	0.84		
6	0.77	0.66	-	-	-	
7	0.88	0.87	0.82	0.63	0.64	0.67
8	0.92	0.95	0.97	0.99	0.99	0.99

A1 *best* s.c.

physical sensors k	1	2	3	4	5	6
2	0.94					
3	0.95	0.95				
4	0.84	0.92	0.95			
5	0.94	0.95	0.95	0.83		
6	0.89	0.94	0.94	0.95	0.93	
7	0.82	0.85	0.91	0.94	0.94	0.93
8	0.81	0.82	0.88	0.93	0.88	0.93

A1 *worst* s.c.

physical sensors k	1	2	3	4	5	6
2	-					
3	-	-				
4	0.74	0.49	0.34			
5	-	-	0.11	0.75		
6	0.67	0.62	0.76	0.11	-	
7	0.78	0.76	0.78	0.87	0.71	-
8	0.81	0.82	0.88	0.93	0.88	0.93

A6 *best* s.c.

physical sensors k	1	2	3	4	5	6
2	0.99					
3	0.99	0.99				
4	0.92	0.98	0.99			
5	0.99	0.99	0.99	0.91		
6	0.98	0.98	0.99	0.99	0.99	
7	0.90	0.94	0.96	0.99	0.99	0.99
8	0.89	0.91	0.94	0.98	0.99	0.99

A6 *worst* s.c.

physical sensors k	1	2	3	4	5	6
2	-					
3	-	-				
4	0.79	-	-			
5	-	-	-	0.81		
6	0.71	0.55	-	-	-	
7	0.84	0.81	0.74	0.44	0.49	0.53
8	0.89	0.91	0.94	0.98	0.99	0.99

Figure B.18 Coefficients of determination of the leave-p-out validation for the best and worst sensor combination (s.c.) depending on the number of physical sensors and considered FE modes for each accelerometer.

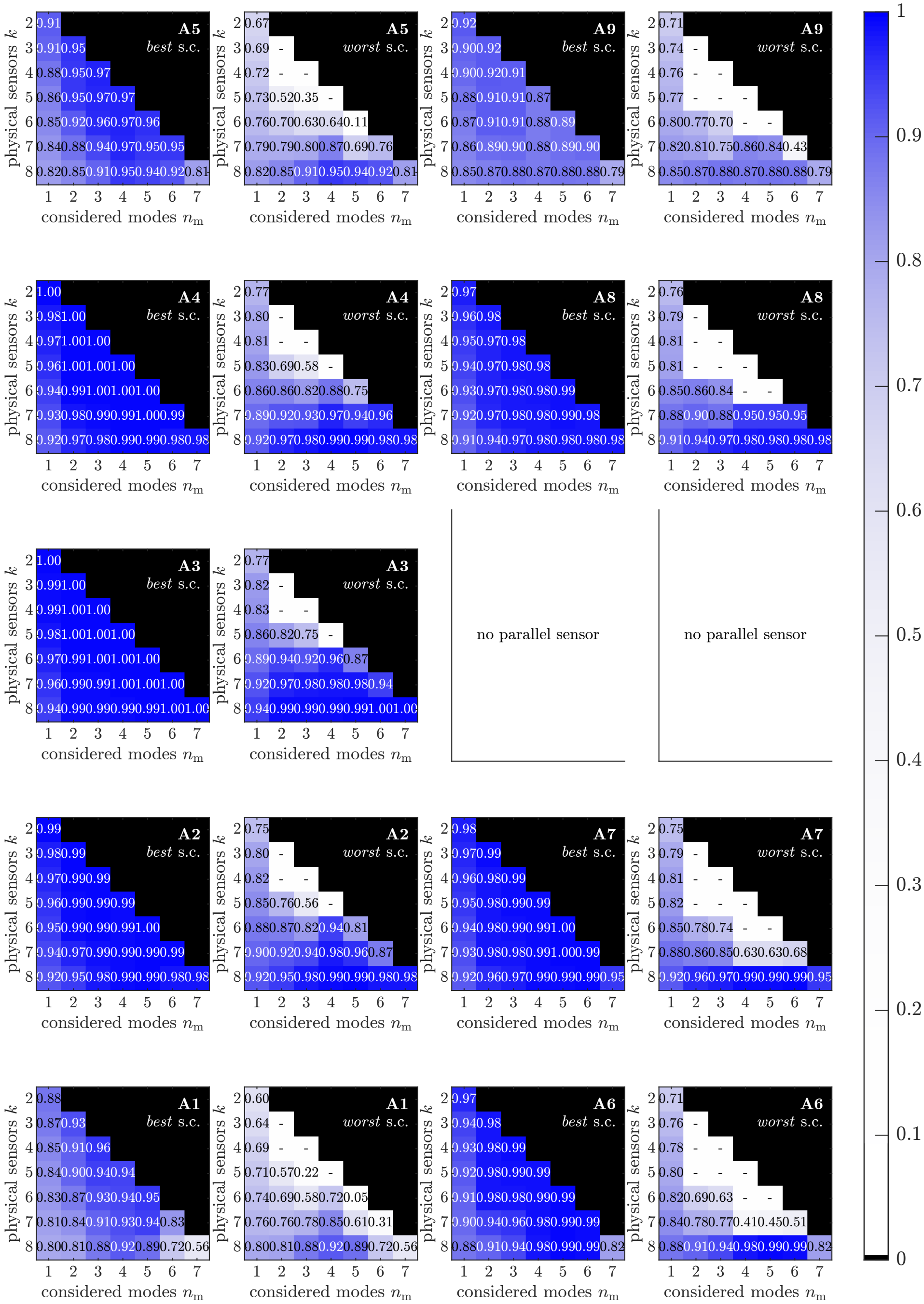

Figure B.19 Coefficients of determination of the leave-p-out validation for the best and worst sensor combination (s.c.) depending on the number of physical sensors and considered POD modes for each accelerometer.

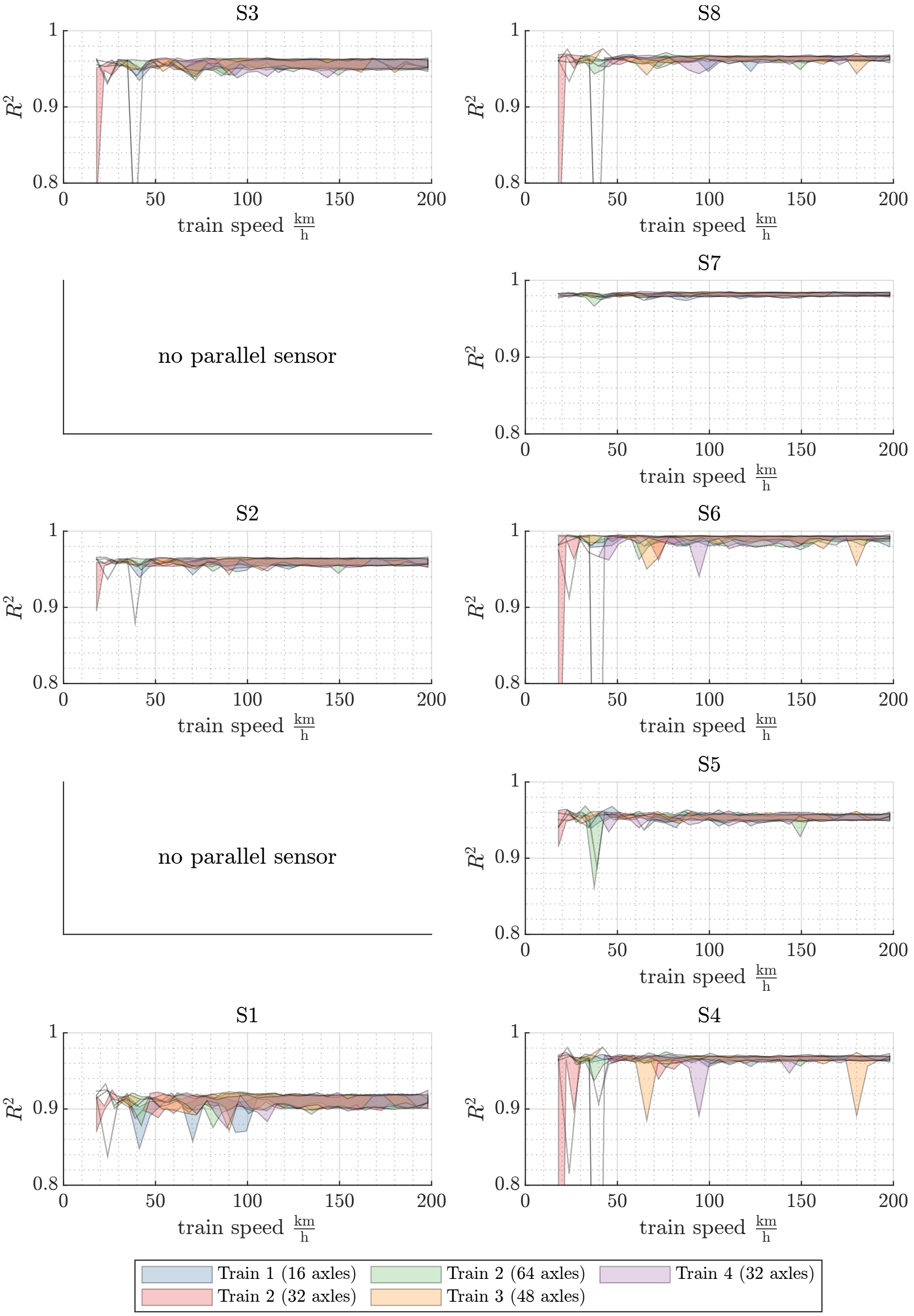

Figure B.20 Inerquartile range of the coefficients of determination for the 5 most frequent train types and as a function of train speed, obtained by leave-one-out validation for each strain gauge using 3 FE modes.

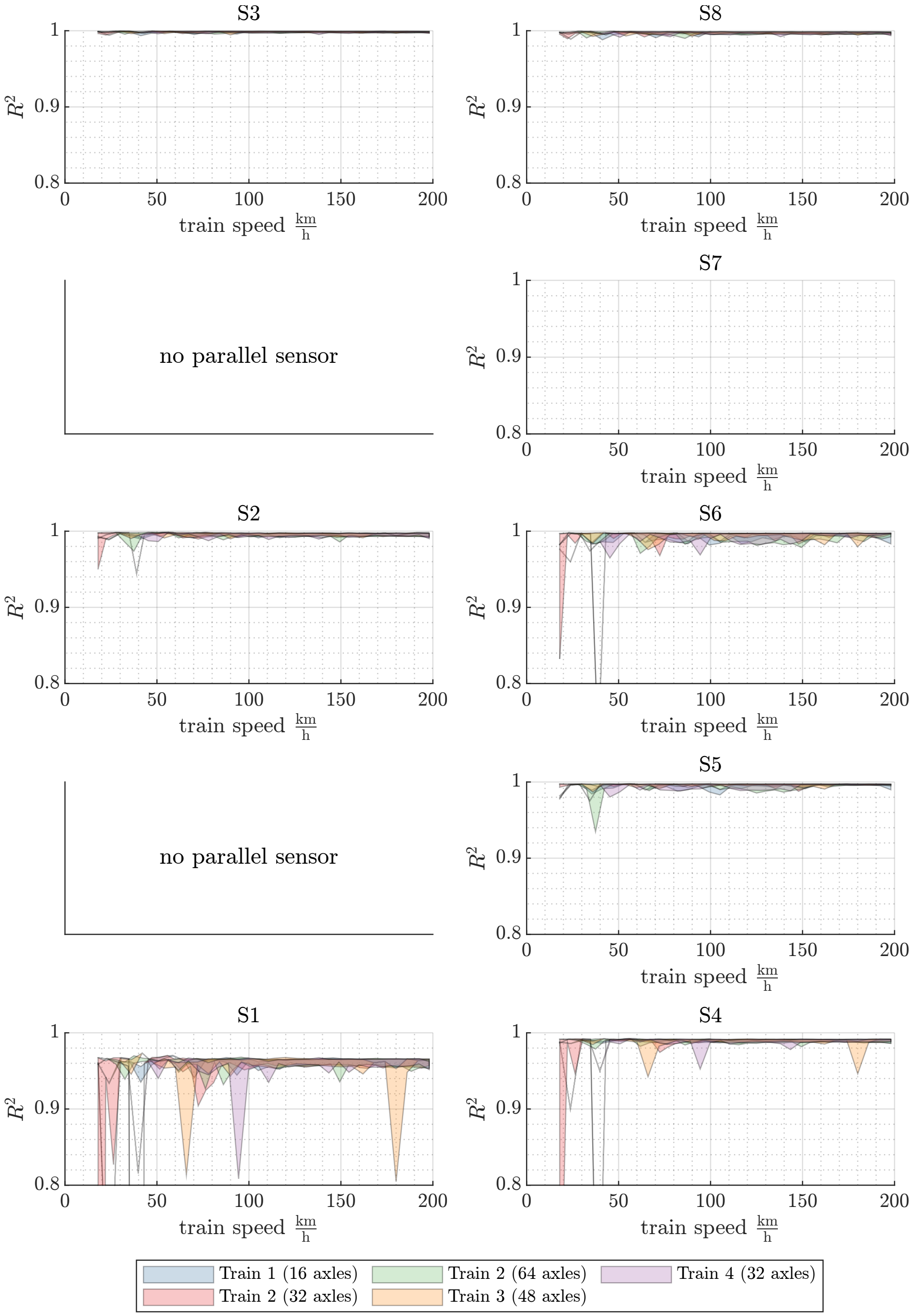

Figure B.21 Inerquartile range of the coefficients of determination for the 5 most frequent train types and as a function of train speed, obtained by leave-one-out validation for each strain gauge using 4 POD modes.

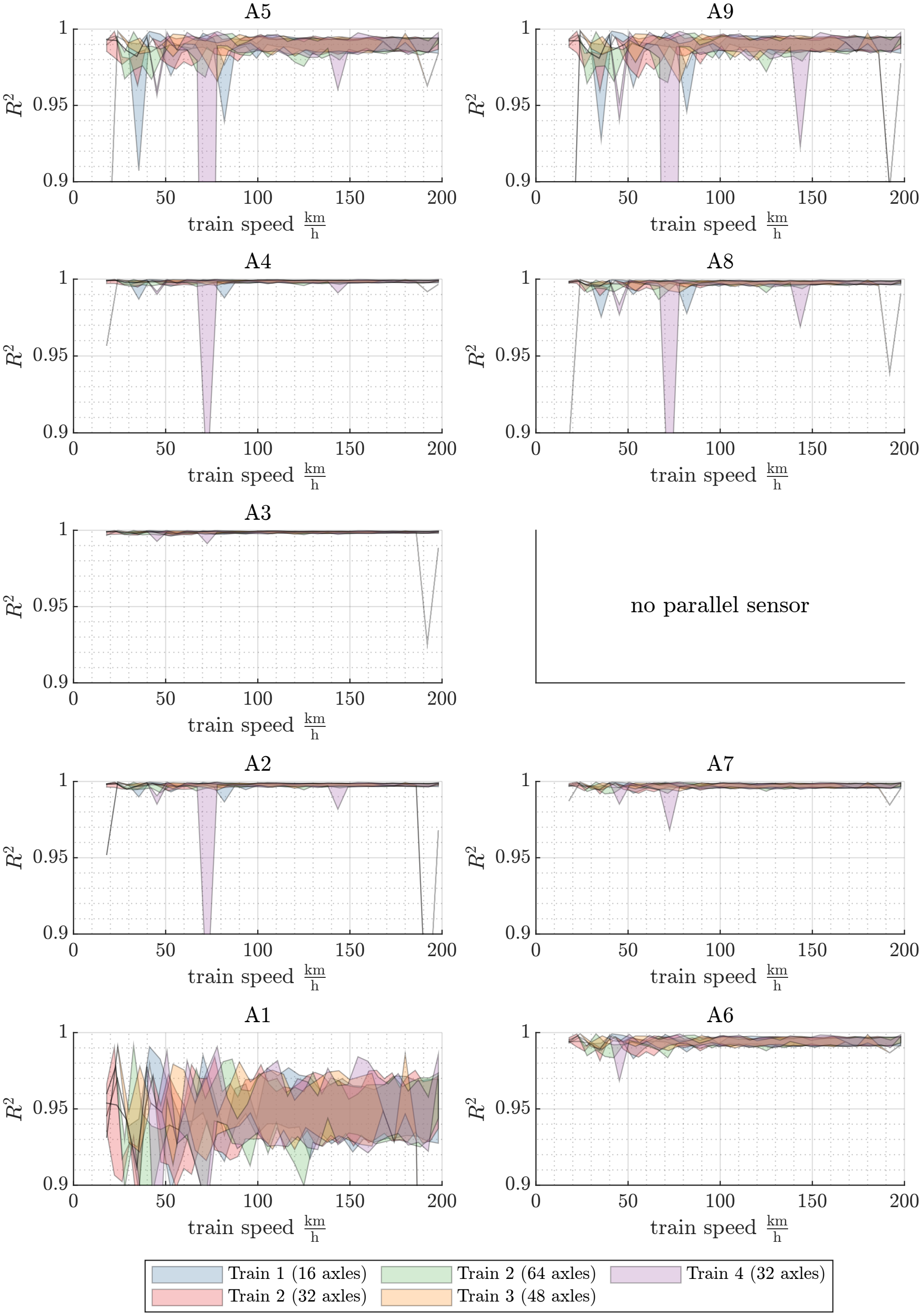

Figure B.22 Inerquartile range of the coefficients of determination for the 5 most frequent train types and as a function of train speed, obtained by leave-one-out validation for each accelerometer using 6 FE modes.

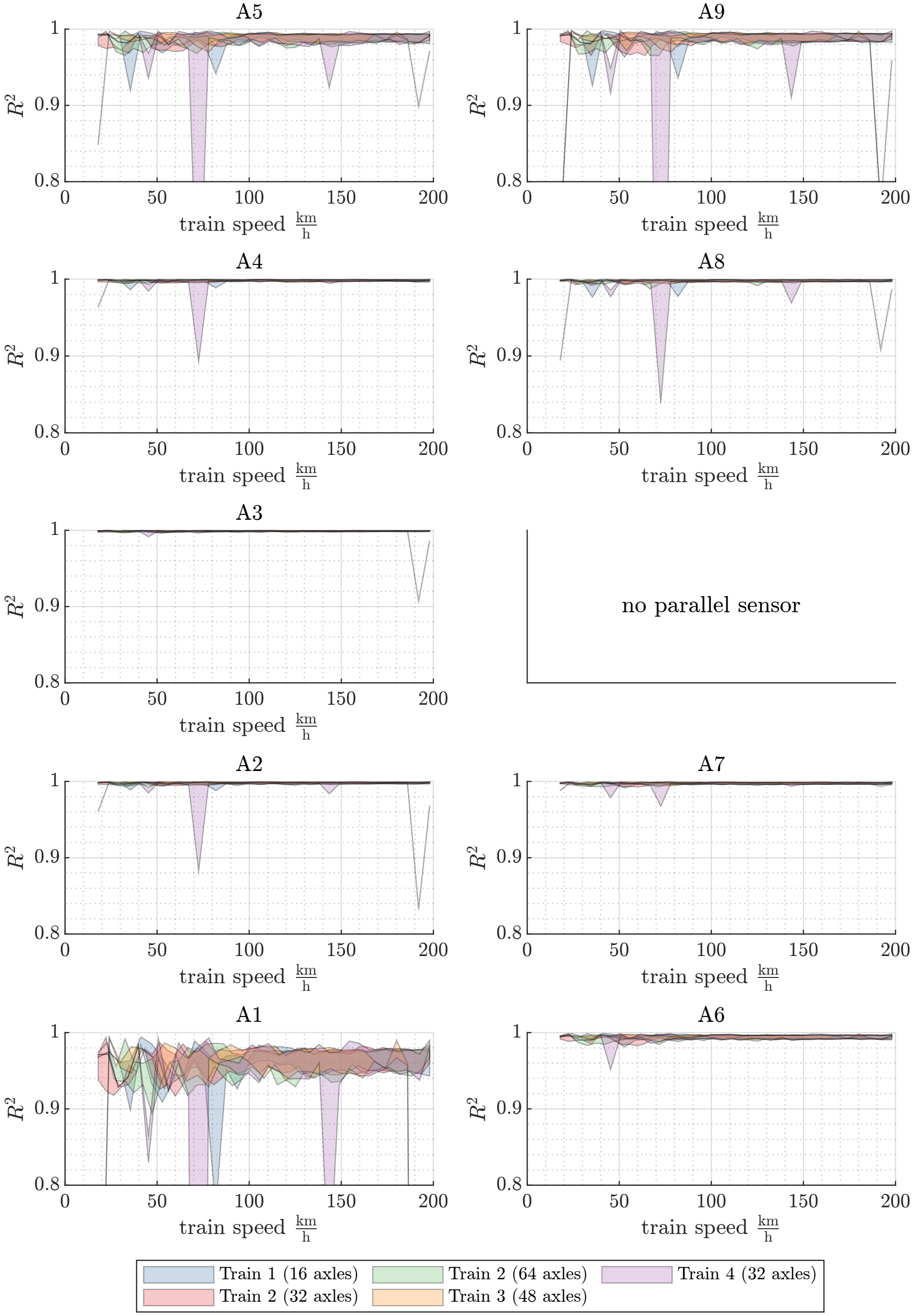

Figure B.23 Inerquartile range of the coefficients of determination for the 5 most frequent train types and as a function of train speed, obtained by leave-one-out validation for each accelerometer using 4 POD modes.

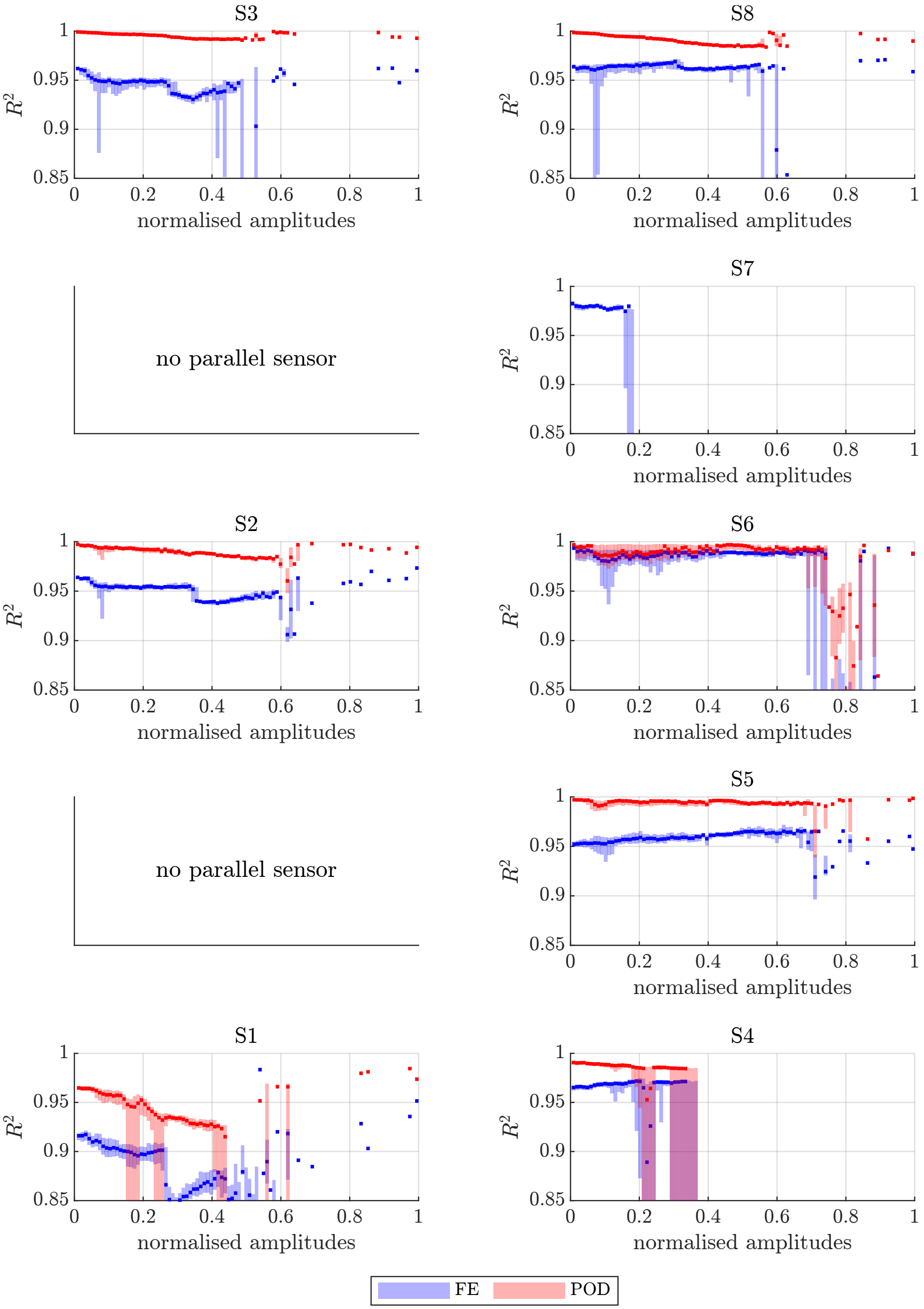

Figure B.24 Inerquartile range and median of the coefficients of determination R^2 against the normalised amplitudes, obtained by leave-one-out validation for each strain gauge (S1 to S8) using 3 FE modes / 4 POD modes.

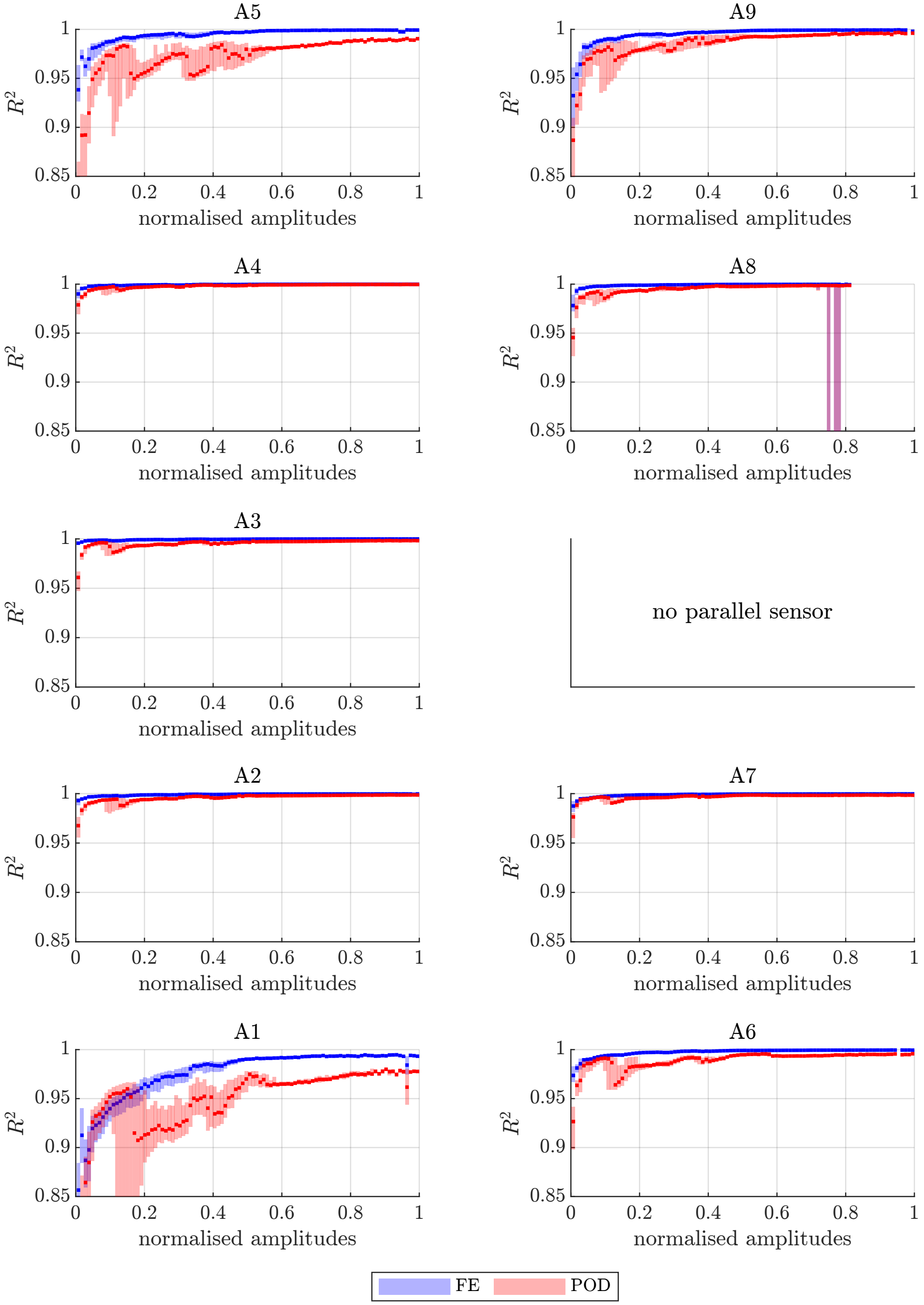

Figure B.25 Inerquartile range and median of the coefficients of determination R^2 against the normalised amplitudes, obtained by leave-one-out validation for each strain gauge (S1 to S8) using 6 FE modes / 4 POD modes.

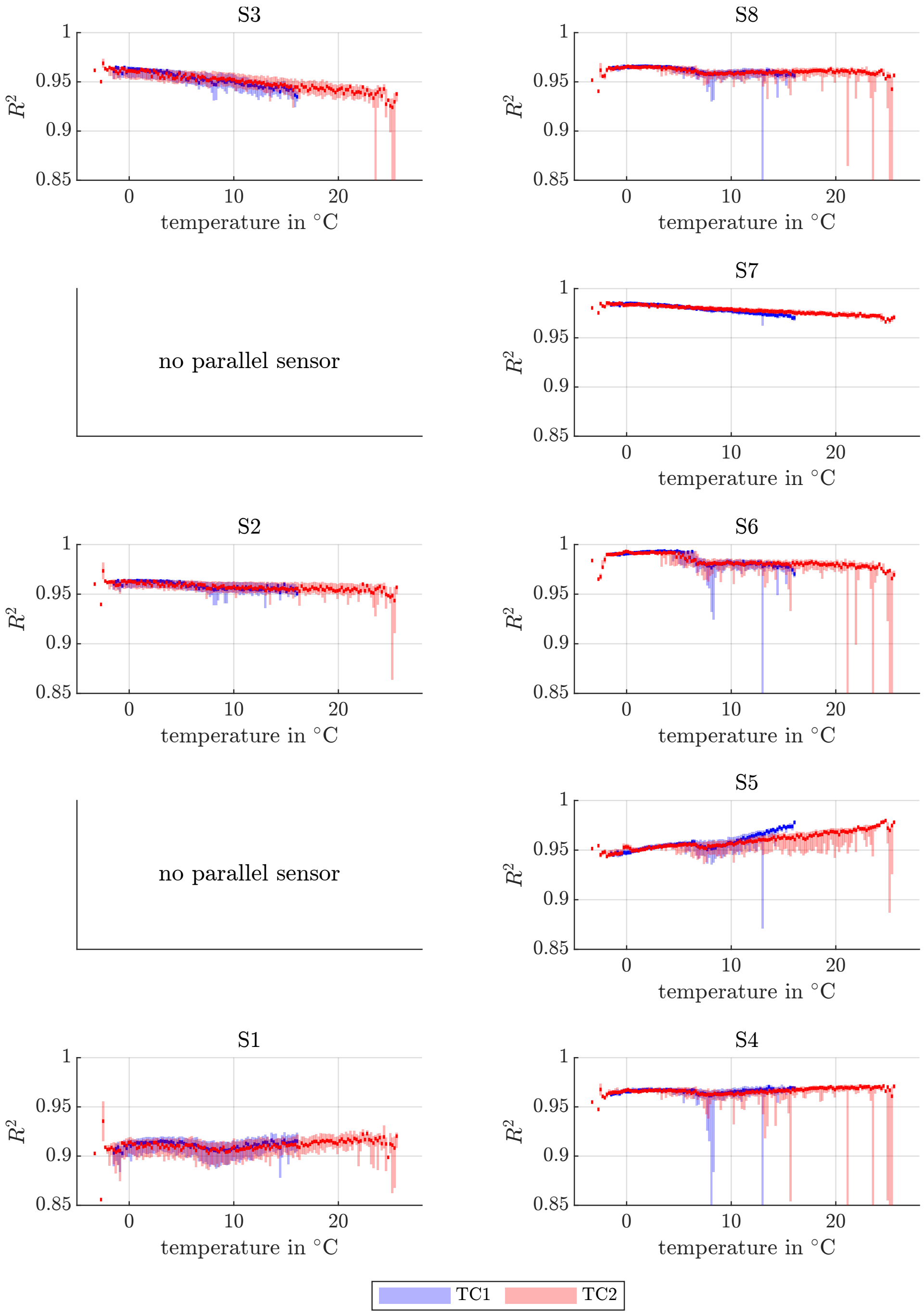

Figure B.26 Interquartile ranges and median of the determination coefficients (R^2) for each strain sensor (S1 to S8), derived from Leave-One-Out validation results, are compared to the mean value recorded during the associated train passage using temperature sensors TC1 and TC2. Three FE modes were considered.

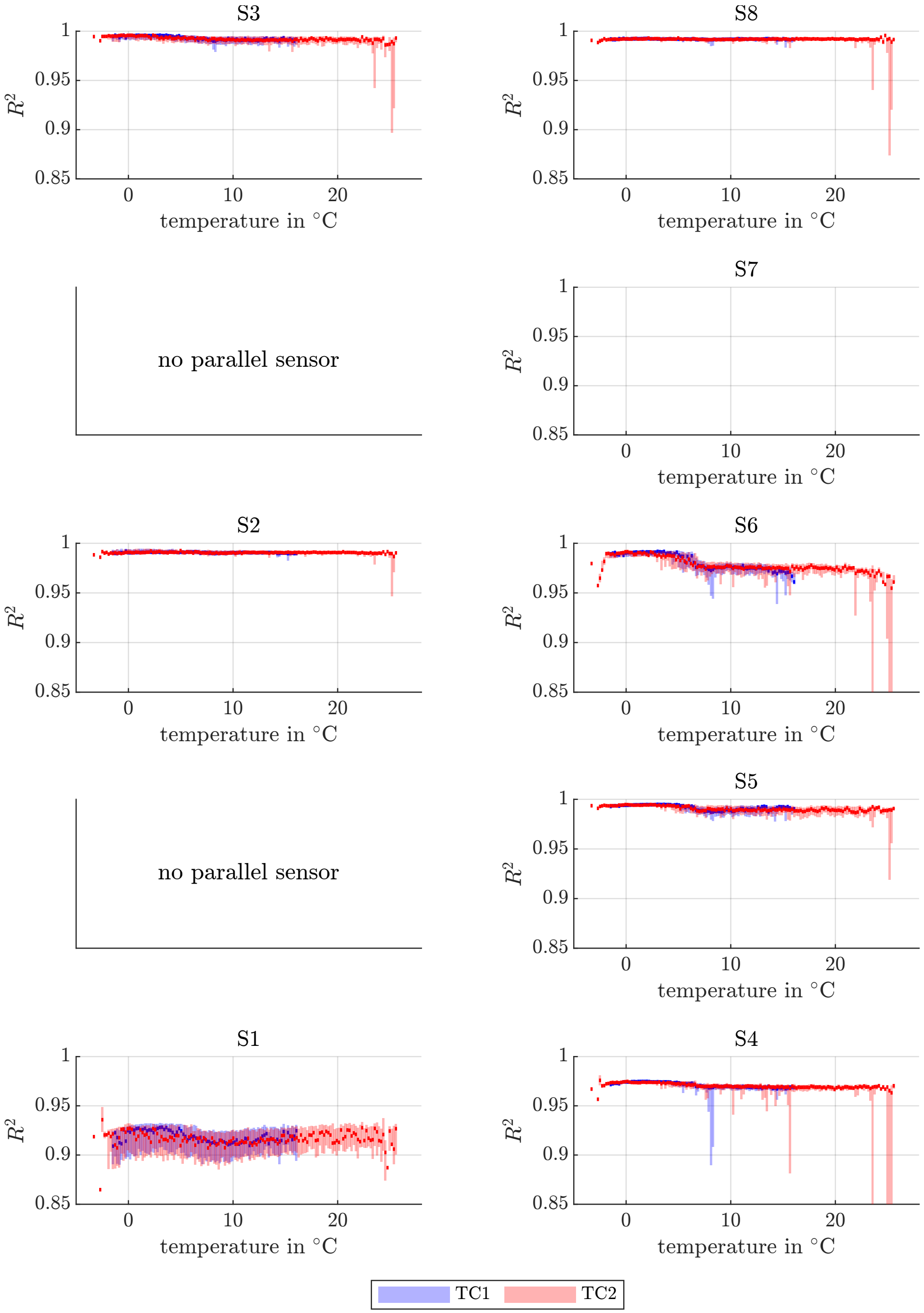

Figure B.27 Interquartile ranges and median of the determination coefficients (R^2) for each strain sensor (S1 to S8), derived from Leave-One-Out validation results, are compared to the mean value recorded during the associated train passage using temperature sensors TC1 and TC2. Four POD modes were considered.

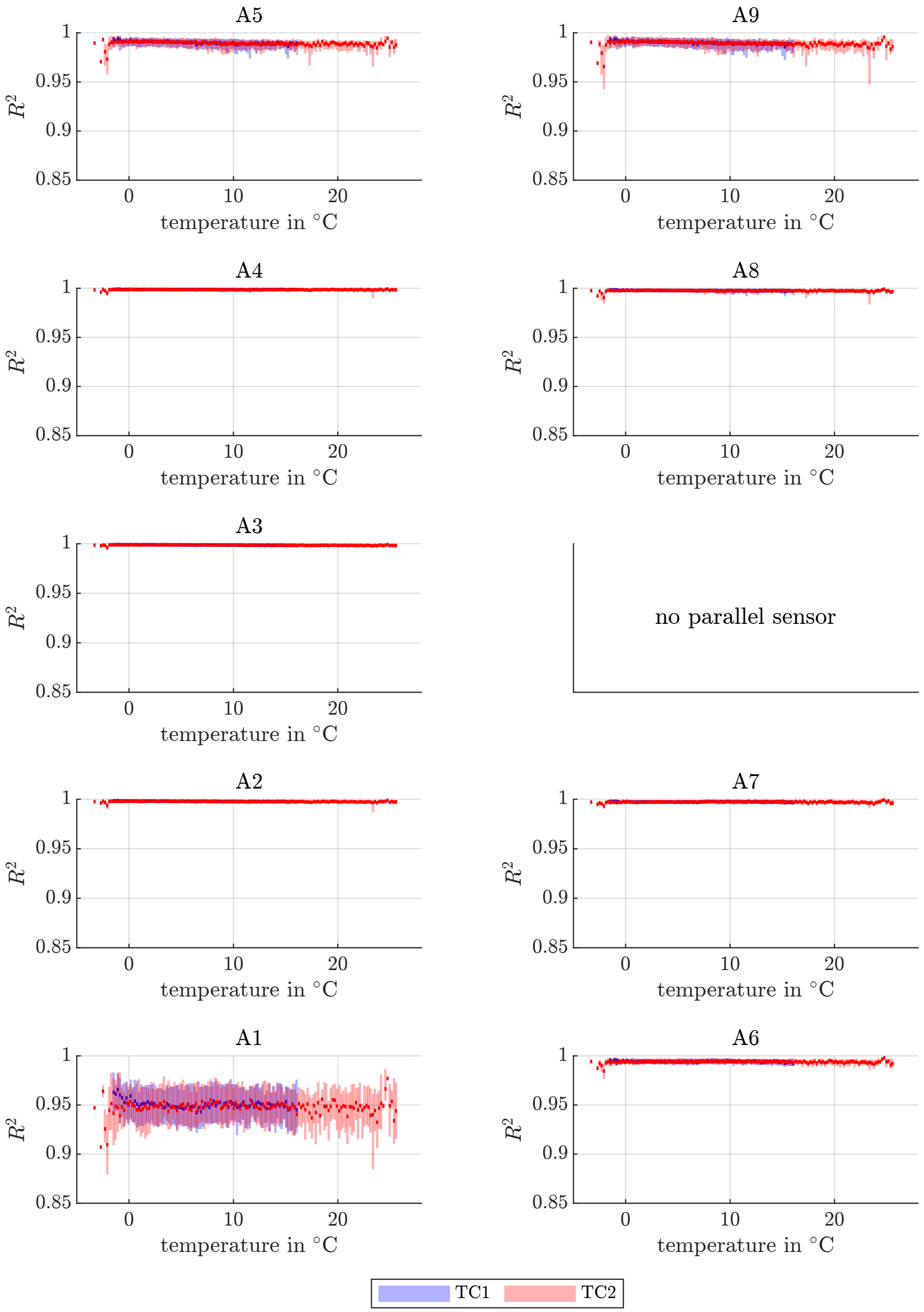

Figure B.28 Interquartile ranges and median of the determination coefficients (R^2) for each accelerometer (A1 to A9), derived from Leave-One-Out validation results, are compared to the mean value recorded during the associated train passage using temperature sensors TC1 and TC2. Six FE modes were considered.

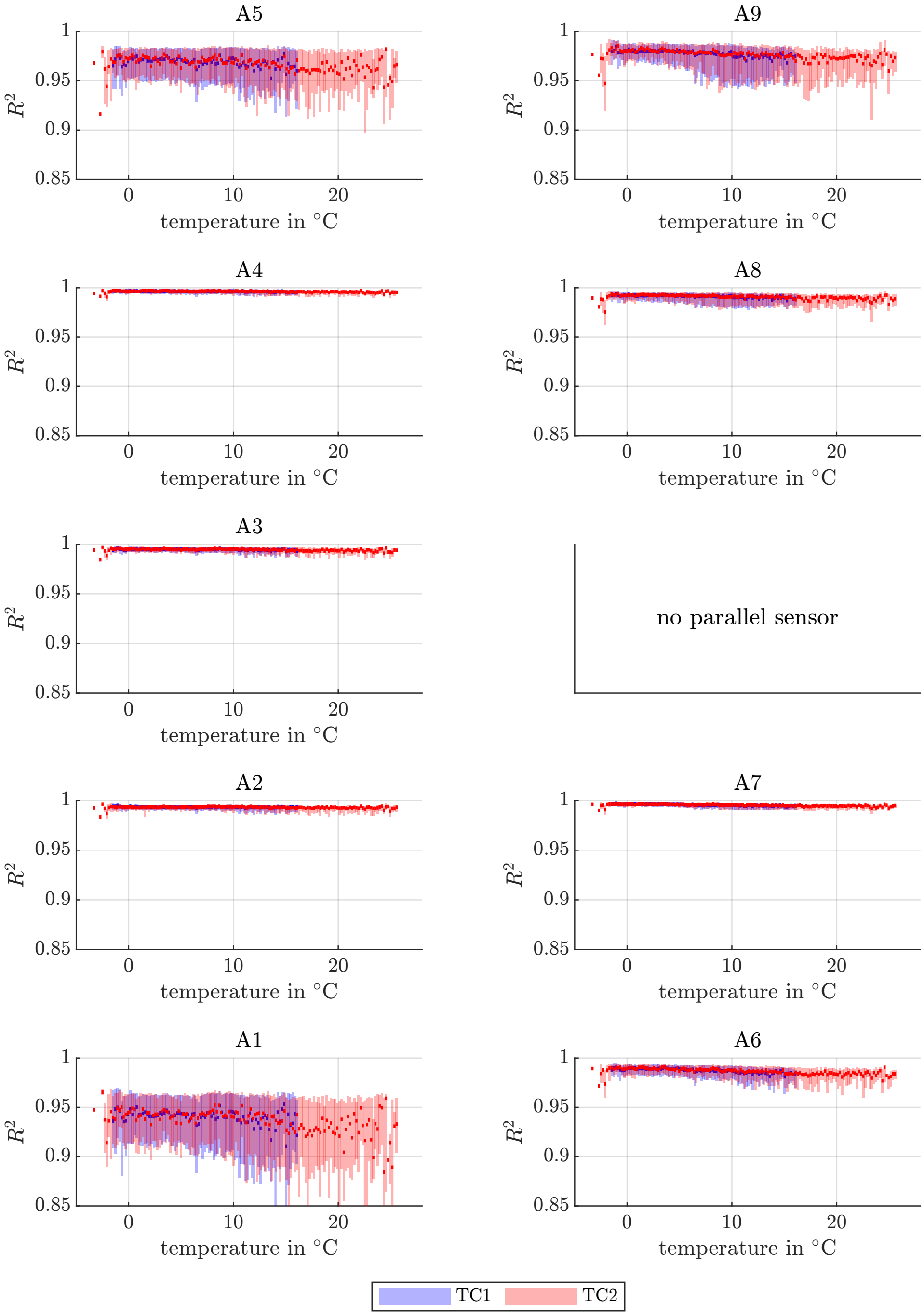

Figure B.29 Interquartile ranges and median of the determination coefficients (R^2) for each accelerometer (A1 to A9), derived from Leave-One-Out validation results, are compared to the mean value recorded during the associated train passage using temperature sensors TC1 and TC2. Four POD modes were considered.

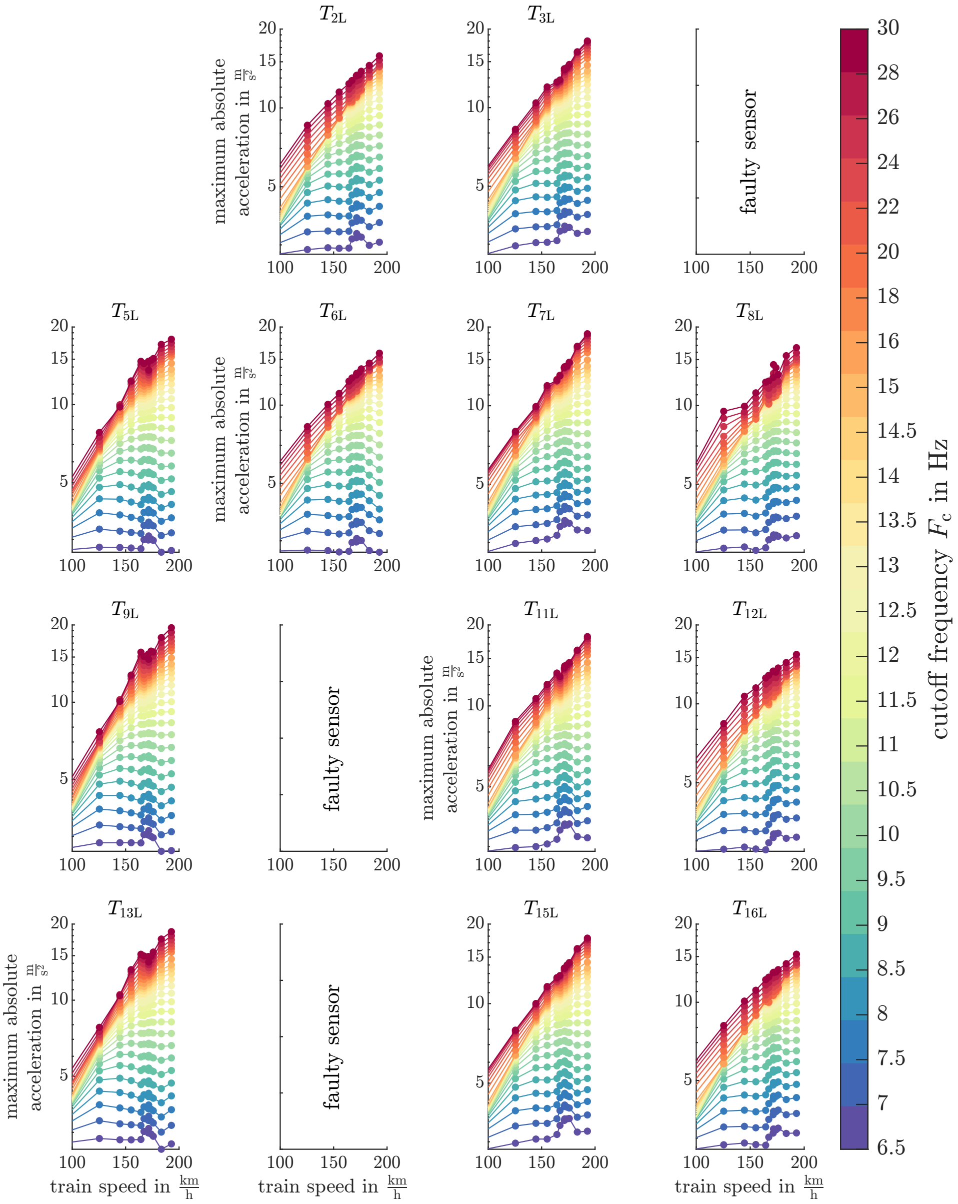

Figure B.30 Influence of the cut-off frequency F_c on the resonance curve with the maximum absolute values of the accelerations of the singel senor signals 100

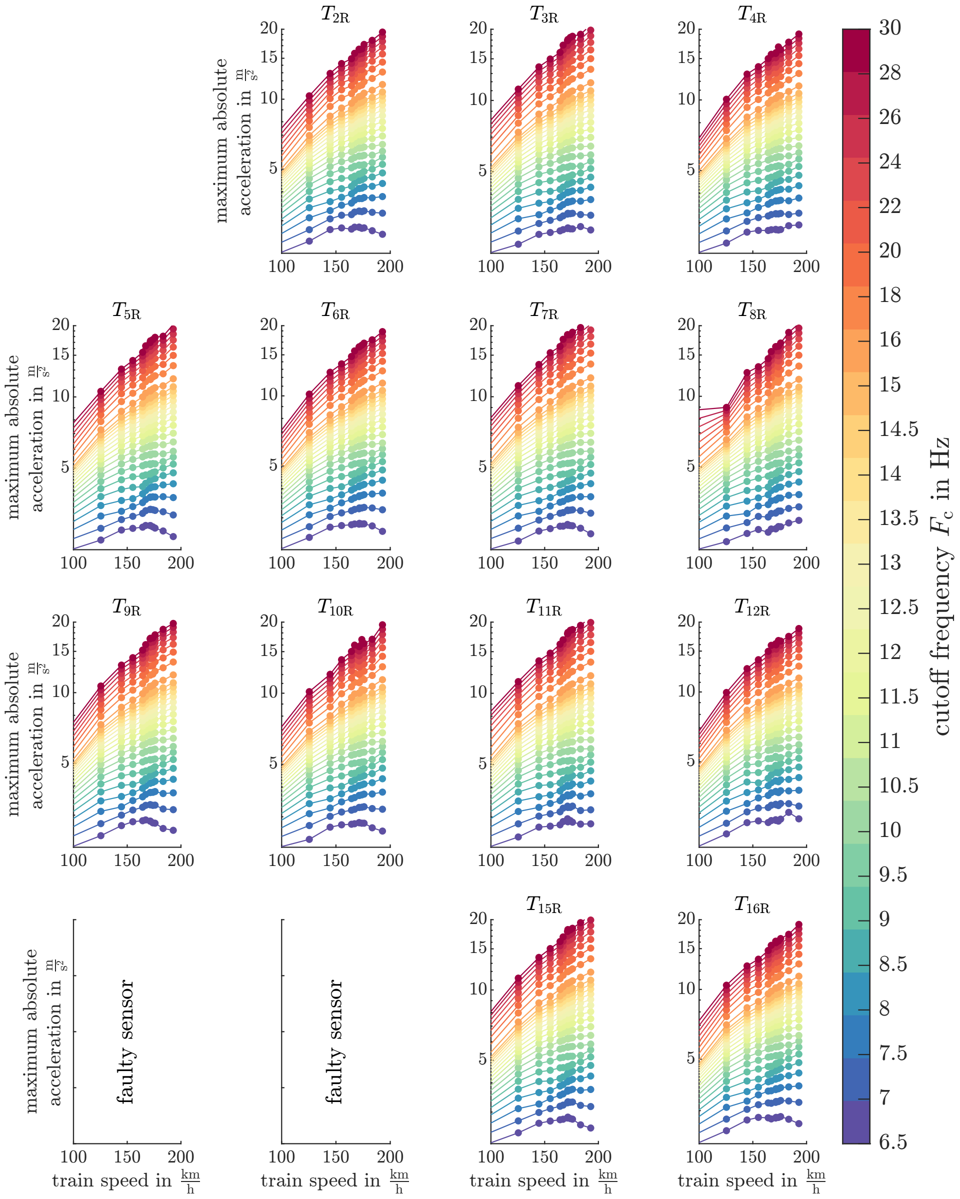

Figure B.31 Influence of the cut-off frequency F_c on the resonance curve with the maximum absolute values of the accelerations of the singel senor signals 200

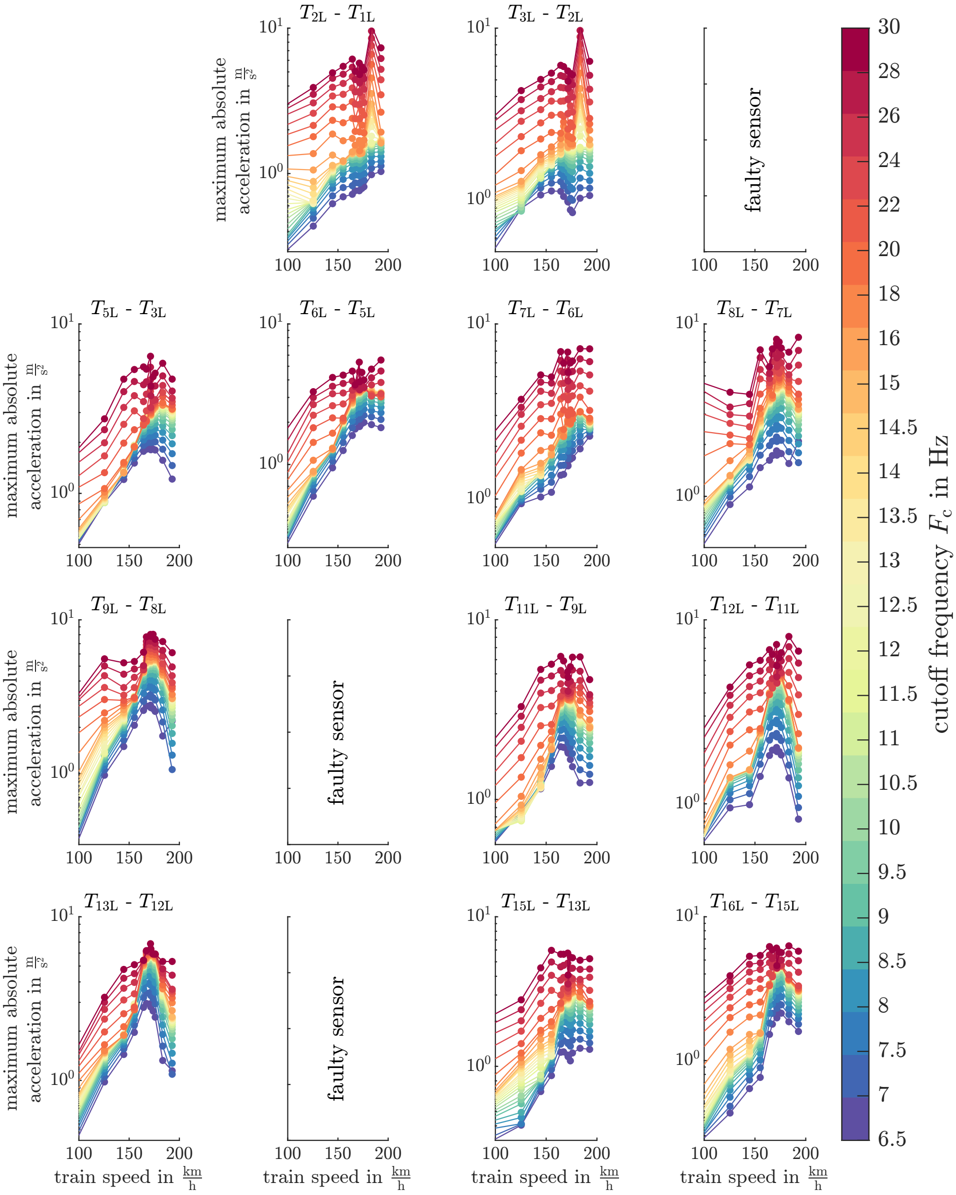

Figure B.32 Influence of the cut-off frequency F_c on the resonance curve with the maximum absolute values of the accelerations of the residual signals to the preceding axle 100

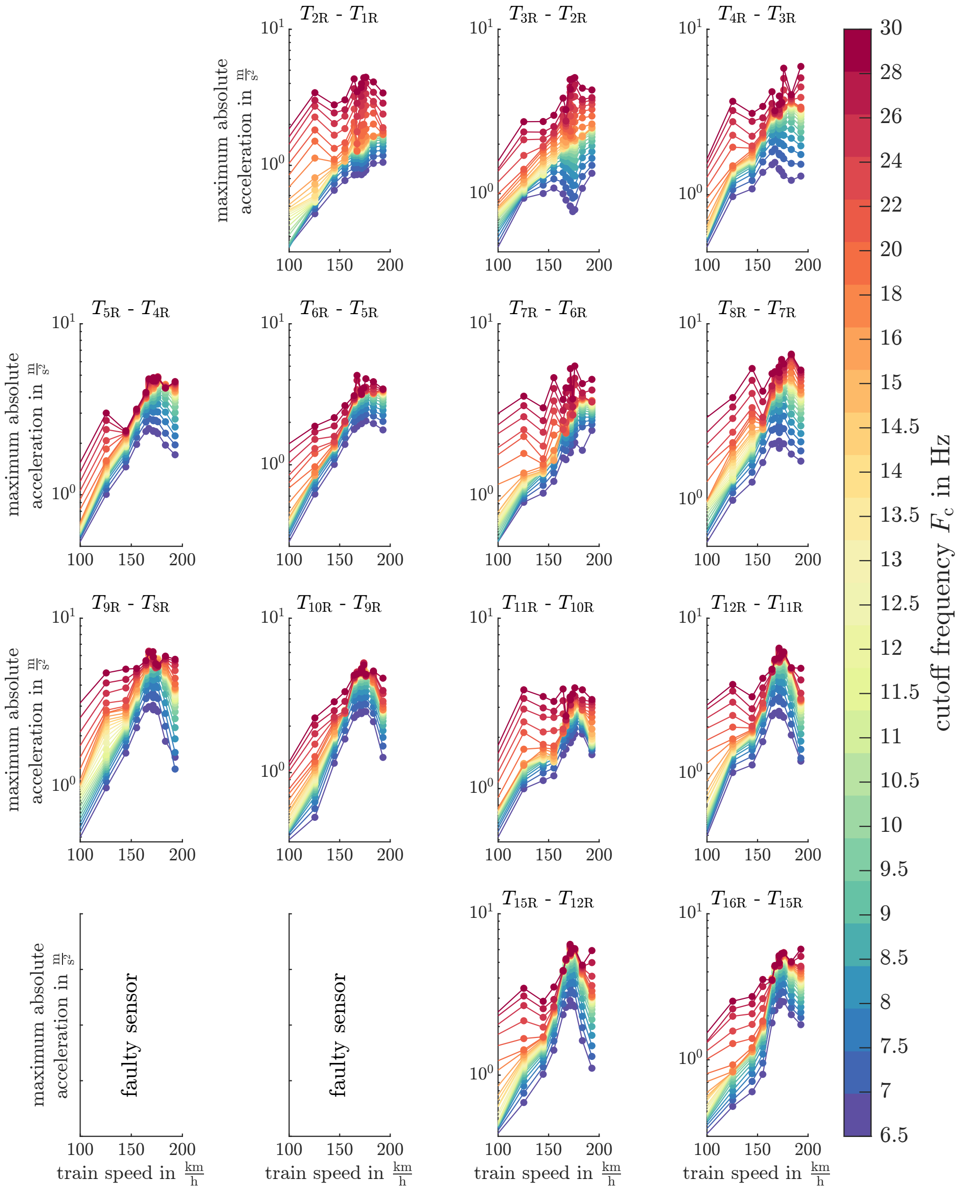

Figure B.33 Influence of the cut-off frequency F_c on the resonance curve with the maximum absolute values of the accelerations of the residual signals to the preceding axle 200

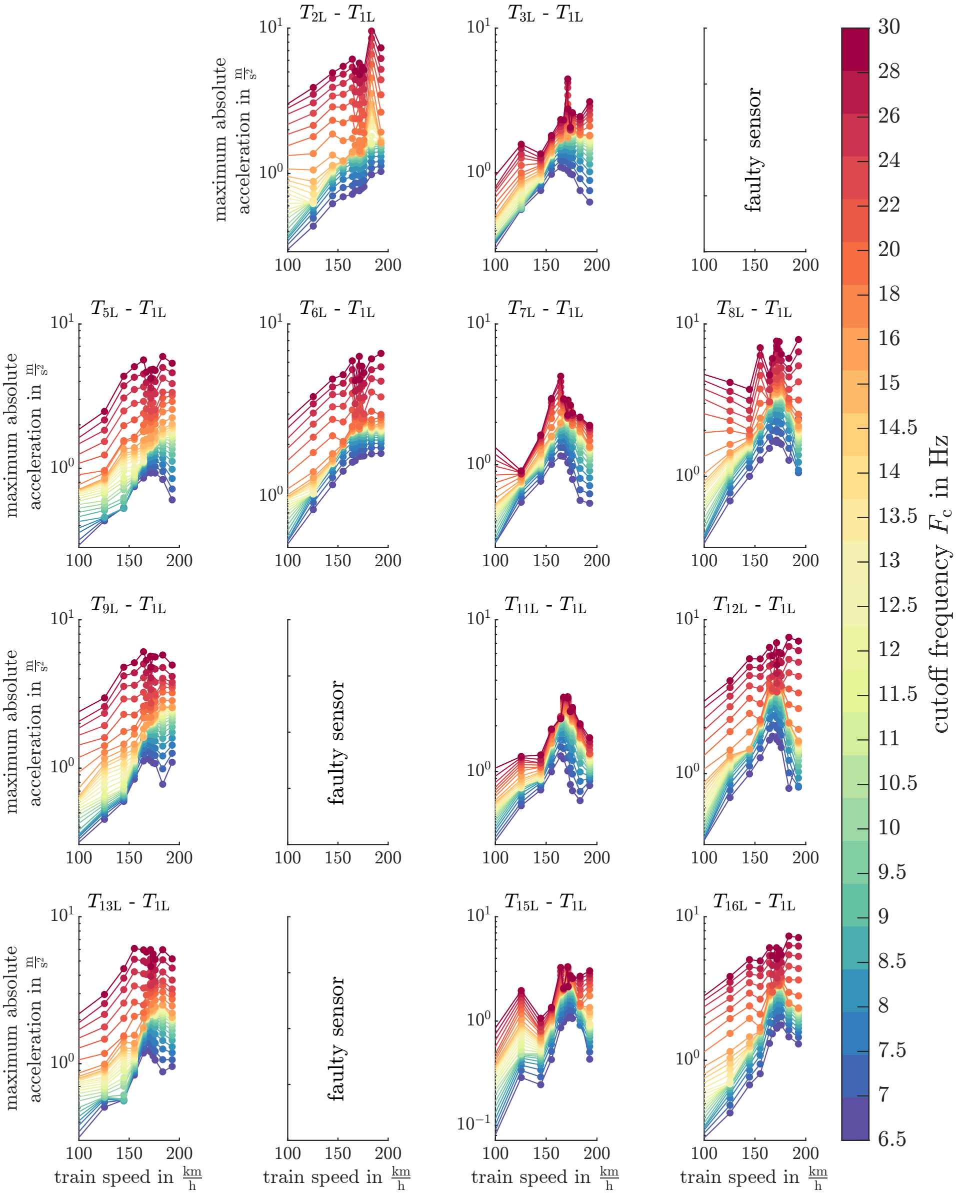

Figure B.34 Influence of the cut-off frequency F_c on the resonance curve with the maximum absolute values of the accelerations of the residual signals to the first axle 100

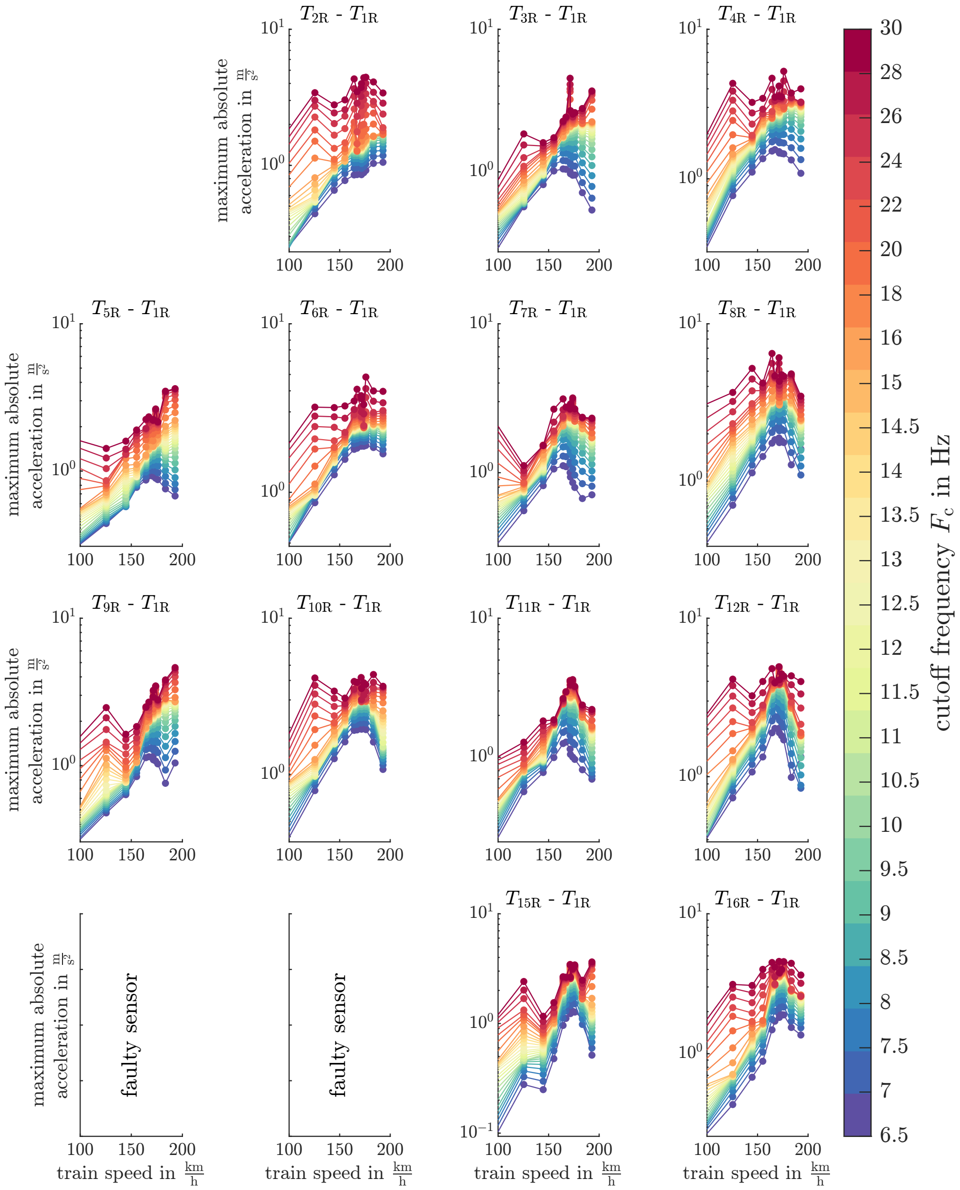

Figure B.35 Influence of the cut-off frequency F_c on the resonance curve with the maximum absolute values of the accelerations of the residual signals to the first axle 200